

EAEC - CONAT 2024

The International Congress of Automotive and
Transport Engineering

Dragoş Sorin Dima · Răzvan Gabriel Boboc ·
Eugen Valentin Butilă
Editors

EAEC - CONAT 2024

The International Congress of Automotive and
Transport Engineering



Transilvania
University
Press

2024

Editors

Dragoş Sorin Dima
Department of Automotive and Transportation Engineering
Transilvania University of Braşov
Romania

Răzvan Gabriel Boboc
Department of Automotive and Transportation Engineering
Transilvania University of Brasov
Romania

Eugen Valentin Butilă
Department of Automotive and Transportation Engineering
Transilvania University of Brasov
Romania

ISSN 2069-0401 (print)
ISSN 2069-0428 (e-book)

Publisher: Transilvania University Press, Brasov, Romania

© 2024

This work is subject to copyright. All rights are reserved by Authors.

The use of general descriptive names, registered names, trademarks, service marks, etc. in this publication does not imply, even in the absence of a specific statement, that such names are exempt from the relevant protective laws and regulations and therefore free for general use.

The publisher, the authors and the editors are safe to assume that the information in this book are believed to be true and accurate at the date of publication. Neither the publisher nor the authors or the editors give a warranty, express or implied, with respect to the material contained herein or for any errors or omissions that may have been made.

Table of Contents

| | |
|--|----------|
| Foreword..... | IX |
| Scientific Committee..... | XI |
| Main Section..... | 1 |
| Software Applications, Equipment and Procedures used for the Acquisition and Processing of Experimental Data in Case of Road Accidents..... <i>Claudiu Nedelescu Anghel Chiru, Radu Iulian Negrila, Paul Mihai Vrabie, and Daniel Dragoş Truşcă</i> | 3 |
| Contributions to the Modelling of Gasoline Injection in the Spark Ignition Engines..... <i>Mihai Blaga, Tudor Mitran, Alexandru Rus, George Dragomir, Horia Beles and Vasile Blaga</i> | 19 |
| The Impact of Bullbar Devices on Dynamics and Consequences Vehicle-Pedestrian Road Accidents..... <i>Ioan Ciobanu, Anghel Chiru and Alexandru Ionuţ Radu</i> | 39 |
| Continuously Variable Planetary Transmission..... <i>Victor Sivu</i> | 53 |
| Analysis of Braking Force and Absolute Deceleration using Data Obtained from Measurements on the Brake Stand..... <i>Mădălin-Florin Popa, Bogdan-Manolin Jurchiş and Nicolae Burnete</i> | 67 |
| Optimization of Road Infrastructure Safety Management by Analyzing Statistical Data of Serious Road Accidents in Urban Areas. Case study: Streets of Bucharest..... <i>Corneliu Ioan Dimitriu and Gheorghe Frăţilă</i> | 75 |
| Contributions to the Strengthening of the National Legislative Framework for Road Infrastructure Safety Management in Romania. Case Study on the Evolution of National Regulations in the Context of the Implementation of EU Directives..... <i>Corneliu Ioan Dimitriu and Gheorghe Frăţilă</i> | 87 |
| Experimental Research Concerning the Decreasing of the State of Charge from the Traction Battery for an Electric Vehicle used in Urban Driving Conditions..... <i>Valentin Nişulescu, Florian Ivan, Marius Toma, Cristian Renţea, Gheorghe Bancă</i> | 95 |

| | |
|---|-----|
| Flying Taxis as a Solution for the Future..... | 103 |
| <i>Arghirescu Marius and Spiridon Lucian</i> | |
| Biography of Prof. univ.eng. Radu-Emil Mărdărescu - the Creator of the Automobiles and Engines School at the Braşov Institute of Mechanics..... | 115 |
| <i>Vladimir Mărdărescu and Marius-Daniel Călin</i> | |
| Student Section | 133 |
| Designing A Lightweight and Ergonomic Formula Student Pedal Box Assembly Using Finite Element Analysis..... | 135 |
| <i>Robert-Cristian Iridon, Tiberiu Andrei Boborean, Marius Pop-Călimanu</i> | |
| Study of Gas Exchange of a Supercharged, Two Stroke, Opposed Piston Engine..... | 149 |
| <i>Costin Ene</i> | |
| Design and Manufacturing of the Drive Shaft using CFRP for the Formula Student Car..... | 155 |
| <i>Andrei Casian Borza, Andrei Tiberiu Boborean, Sergiu-Valentin Galaţanu</i> | |
| Aerodynamics in Karting..... | 163 |
| <i>George Octavian Onaca, Dragos Maxim, Florin Scurt and Casian Alexandru Toth</i> | |
| Efficiency of the Design of a Formula Student Chassis based on an Architecture in CATIA..... | 171 |
| <i>Daniel Ursache, Alexandru George Pantiru, Robert Adrian Chiscop, Ştefan Grigorean</i> | |
| Fixed Air Quality Monitoring Station in Road Traffic..... | 183 |
| <i>Sorin Ionascu, Alexandru Şopron, Cosmin Hâncu and Robert Perianu</i> | |
| Implementation and Evaluation of the Bearing Monitoring System in the EV Field using Vibrations Sensors in the Context of Maintenance Engineering..... | 187 |
| <i>Dumitrel Barbu, Raul Ferchiu and Valentin Silivestru</i> | |
| Global Positioning and Data Synchronisation System..... | 197 |
| <i>Aurora Țurcanu, Cristina-Corina Chihaia and Ruben Drăgan</i> | |
| Outriggers for Vehicle Testing and Concepts of Lateral Stability..... | 203 |
| <i>Elena-Dorina Dumitru</i> | |
| Construction and Mechanical Design of a Four Rotor Wankel Engine..... | 215 |
| <i>Mihai Bălăşescu</i> | |

| | |
|--|-----|
| Study of Gas Exchange and Acoustical Supercharging of the Wankel Engine..... | 223 |
| <i>Maria Dimache</i> | |
| Analysis of Brake Energy Recovery Potential in Flywheels..... | 231 |
| <i>Mânza Radu-Cristian</i> | |
| Lithium Iron Phosphate Battery Pack for Hybrid Drive Applications..... | 239 |
| <i>Andrei Cristian Grigore, Jan-Alexandru Văduva</i> | |
| Evaluation of the Tire Influences on the Dynamics of a Formula Student Type Single-Seater..... | 249 |
| <i>Bogdan-Tudor Gal and Adrian Todoruț</i> | |
| Development of an Electric Powertrain for a Formula Student Vehicle..... | 267 |
| <i>Ionuț-George Moldovan and Mihai-Alexandru Bilici</i> | |

Foreword

The 21st-century automobile is the result of continuous innovation, creativity, and experimentation by a global community of researchers, scientists, designers, and manufacturers. These efforts have integrated cutting-edge advancements in materials, technologies, and systems spanning mechanical, hydraulic, pneumatic, electrical, and electronic domains. In today's era, the focus on sustainable development and the decarbonization of the automotive industry, driven by stringent environmental regulations and the finite nature of fossil fuel reserves, necessitates an in-depth evaluation of the energetic, dynamic, economic, and ecological attributes of vehicles. This encompasses a diverse range of power sources, from traditional internal combustion engines to hybrids, electric vehicles, and alternative fuels like decarbonized options, eco-hydrogen, fuel cells, and electricity. Moreover, the rise of electromobility, connectivity, autonomous vehicle technology, and digitization is driving profound transformations within the automotive sector.

The vision for sustainable development in the automotive industry, as outlined by the European Commission, requires a strategic balance between enhancing the competitiveness of automobile manufacturers and adhering to environmental protection standards. In addressing the major challenges faced by the automotive industry, the authors of the papers presented in the technical sections of the CONAT 2024 International Congress offer their vision and solutions in areas such as:

- Advanced Powertrain Systems;
- Automobile and Environment;
- Advanced Engineering Methods;
- Vehicle Dynamics and Vehicle Systems;
- New Materials and Manufacturing Technologies;
- Advanced Transport Systems;
- Accident Research and Analysis;
- History of automotive technics and technologies.

A total of 108 papers were presented and published, selected from 268 submitted proposals. These papers were developed by over 200 specialists from 19 countries. An international scientific committee carried out the assessment and organization of the presentations, analyzing the novelty and scientific content, as well as the layout of each paper, in accordance with the requirements set by FISITA, SIAR, SAE International, and the publisher.

This volume includes 12 of the selected papers, along with 15 papers presented in the Students' Section of the Congress. The students' papers were also peer-reviewed by a scientific committee.

The initiation, implementation, and completion of activities for preparing, collecting, and finalizing the volume containing the Proceedings of the CONAT 2024 Congress were made possible through the involvement and professionalism of Dr. Dinu Covaciu, the Coordinator of the Congress Technical Programme. We extend our gratitude to him for all his efforts.

X

We also extend our appreciation to our colleagues from Transilvania University, the members of the Scientific Committee and reviewers, as well as to the organizers and partners from the companies Schaeffler, Siemens, Star Assembly, Autoliv, Albeca Engineering, HaynesPro, Sebert Trillingstechnik B.V., FEV, Mercedes, INAS, AVL, AKA, Exclusiv Auto, Spectromas, Rădăcini Motors, and Beciul Domnesc for their support and involvement in all activities required for organizing the XIIIth Edition of the International Congress of Automotive and Transport Engineering, CONAT 2024..

Assoc. Prof. Dragoş Sorin Dima

Member of the CONAT 2024 Students Committee

Lect. Răzvan Gabriel Boboc

Member of the CONAT 2024 Organizing Committee

Dr. Eugen Valentin Butilă

Member of the CONAT 2024 Organizing Committee

Scientific Committee

Presidents of the Scientific Committee

Professor Anghel Chiru
Transilvania University of Brasov, Romania
Professor Cornel Stan
West Saxon University of Zwickau, Germany

Scientific Committee Members

Professor Csaba Antonya
Transilvania University of Brasov, Romania

Professor Ion Boldea
Politehnica University Timisoara, Romania

Professor Silviu Butnariu
Transilvania University of Brasov, Romania

Professor Michael Butsch
University of Applied Sciences Konstanz, Germany

Professor Dan Centea
McMaster University Hamilton, Canada

Professor Giovanni Cipolla
DECET, Italy

Professor Dragos Ciuparu
Petroleum – Gas University of Ploiesti, Romania

Professor Paul Cizmas
Texas A&M University, USA

Professor Adrian Clenci
National University of Science and Technology POLITEHNICA, University
Center of Pitesti, Romania

Professor Corneliu Cofaru
Transilvania University of Brasov, Romania

Professor Mihai Dimian
University Stefan Cel Mare of Suceava, Romania

Professor Ilie Dumitru
University of Craiova, Romania

Professor Helmut Eichlseder
Graz University of Technology, Austria

Professor Santiago Ferrandiz
Universitat Politècnica de València, Spain

Professor Nicolae Filip
Technical University of Cluj-Napoca, Romania

Professor Paul Gümpel
Institut für Werkstoffsystemtechnik WITg, Germany

Professor Elena Helerea
Transilvania University of Brasov, Romania

Professor Alexandre Herlea
Université de Technologie de Belfort-Montbéliard, France

Professor Daniel Iozsa
National University of Science and Technology POLITEHNICA, University
Center of Bucharest, Romania

Professor Nicolae Ispas
Transilvania University of Brasov, Romania

Professor Manuel Loewer
University of Wuppertal, Germany

Dr. Christoph Menne
FEV Europe GmbH, Germany

Dr. Simona Silvia Merola
CNR-STEMS, Institute of Science and Technology for Sustainable Energy and
Mobility, Italy

Professor Céline Morin
Université Polytechnique Hauts-de-France, France

Professor Dana Motoc
Transilvania University of Brasov, Romania

Professor Constantin Pana
National University of Science and Technology POLITEHNICA, University
Center of Bucharest, Romania

Professor Ion Preda
Transilvania University of Brasov, Romania

Professor Ismael Saadoune
Mohammed VI Polytechnic University, Morocco

Professor Corina Sandu
Virginia Tech, USA

Professor Eran Sher
Technion, Israel

Professor Adrian Soica
Transilvania University of Brasov, Romania

Assoc.Professor Stelian Tarulescu
Transilvania University of Brasov, Romania

Beside the members of the Scientific Committee listed here, the papers were reviewed by a total number of 68 reviewers from academic institution, research centers and industry.

Main Section

Software Applications, Equipment and Procedures used for the Acquisition and Processing of Experimental Data in Case of Road Accidents

Claudiu Nedelescu¹, Anghel Chiru¹^[0009-0004-7769-6736], Radu Iulian Negrila², Paul Mihai Vrabie¹, and Daniel Dragos Trusca¹

¹ Transilvania University of Brasov, Department of Automotive and Transport Engineering, 29 Eroilor Blvd, 500036 Brasov, Romania

{claudiu.nedelescu, achiru, paul.vrabie, d.trusca}@unitbv.ro

² Aurel Vlaicu University, Str. George Cosbuc no.1-3, 310018, Arad, Romania
radu.negrila@premiermotors.ro

Abstract. This paper presents the software applications, equipment and procedures used for the acquisition and processing of experimental data obtained from crash tests. Experimental research involves simulating accidents through crash tests to study the impact forces, vehicle behavior, and the effectiveness of safety features. The illustration of the use of the applications was carried out following some experimental research on crash tests, highlighting the work methodologies for their correct use. Also, the most common measurement errors were presented, as well as filtering methods after the data were acquired.

Keywords: Experimental data, Acquisition equipment, Crash tests.

1 Introduction

People live in a modern society that is continuously developing based on its distinctive features. These characteristics have echoes in numerous fields of research that explore the complex links between environment and life.

To date, the importance of the motor vehicle has increased greatly, having multiple roles and significantly influencing transport on public roads.

Due to the increase in the number of road accidents resulting in bodily injuries or deaths, special attention is given to the analysis of road events with the aim of discovering the causes that produce the collisions and to reduce the number of road accidents as much as possible [1].

The first road accident occurred in England in 1896, and in 1899 the first death caused by a motorized vehicle was registered in the USA [2]. In 1935, the first publication related to reconstruction of road accidents appeared in Germany [3].

Road safety has become an international priority, and the optimization of the automobile has registered a significant increase from this point of view, thus imposing the need to improve reconstruction methods.

Experimental analyzes can be used to validate the methods used in the reconstruction process. This aspect is necessary due to the complexity of a collision, because there are numerous parameters that can vary and influence the event, as well as various materials that are used in the manufacture of motor vehicles [4].

Therefore, kinematic parameters (displacement, velocity and acceleration) that describe the movement of the vehicle or the occupants can be estimated theoretically, but for a better accuracy of the results, experimental research is needed, using various equipment and software applications for acquisition and calculation of these parameters.

The main objective of the paper is to offer alternatives to the existing methods and procedures for the acquisition and processing of experimental data in case of road accidents.

2 Equipment Used for Experimental Data Acquisition

2.1 Velocity Measurement with GPS System

Velocity of the vehicle can be acquired with the GPS system. The hardware components that make up the GPS system are a Venus GPS device, an antenna ANT-555 and a laptop.

The Venus GPS board (Fig. 1) is based on the chip GPS receiver 638FLPx-L. The update rate is up to 20 Hz, and requires a regulated 3.3V supply to operate in a temperature range from -40°C to $+85^{\circ}\text{C}$ [5].

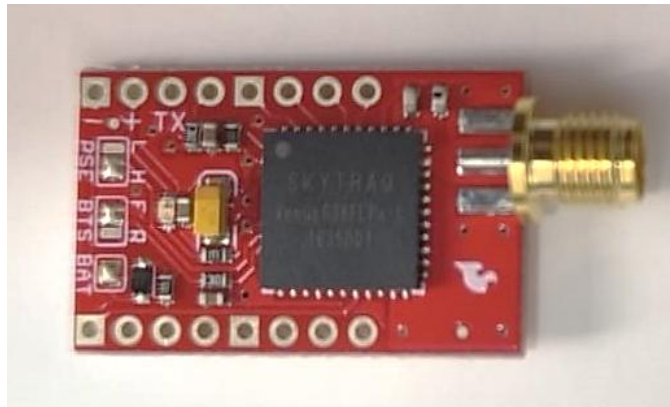


Fig. 1. Venus GPS board.

The ANT-555 antenna (Fig. 2) is used to capture the radio signal (electromagnetic wave) from air and to transform the signal into electrical signal. It includes protection circuits to avoid electrostatic discharge. It works with very low power consumption and can also be used at different temperatures between -40°C and $+85^{\circ}\text{C}$. The attachment of the antenna to the vehicle is magnetic and the length of the cable can vary from 2 m to 5 m.



Fig. 2. The ANT-555 antenna

Other characteristics of the ANT-555 antenna are that it has a weight of 80 g, a height of 14 mm and a length, respectively a width of 46.5 mm. The supply voltage is between 2.7 and 3.3 V, and the operating frequency is 1575.42MHz +/-1.023MHz [6].

The GPS system provides accurate position, velocity data and has multiple applications, being used for vehicle navigation systems, automatic vehicle location systems or for various operations with other types of machinery. The GPS receiver (Venus 638FLPx-L) uses the antenna ANT-555 and the circuit transforms the electrical signal taken from the antenna into data (binary or text). The simplified scheme for interconnecting the equipment constituting the GPS system is presented in Fig. 3.

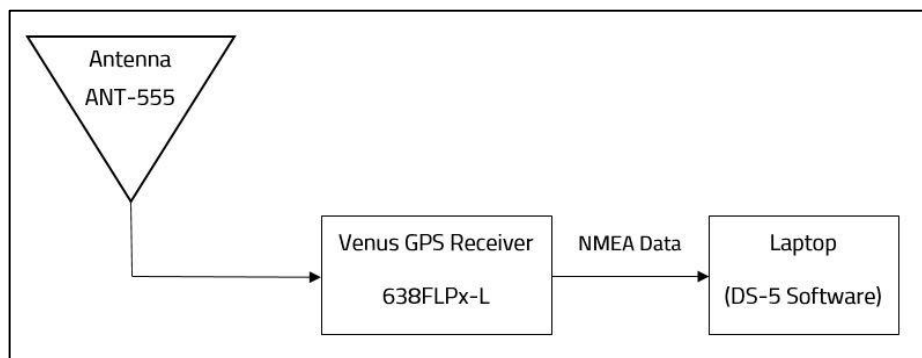


Fig. 3. Simplified scheme of the GPS system

In Fig. 4 it can be seen that the antenna is positioned on the automobile roof. The GPS receiver and the laptop are placed inside the vehicle.



Fig. 4. Antenna mounted on the vehicle roof

The data received from the GPS are represented as NMEA codes. The default transfer rate of NMEA codes is 9600 bps, but it can be adjusted to 115200 bps. Some of the identification codes and their meanings are presented as follows:

- \$GPGGA - 3D position and accuracy information;
- \$GPRMC - minimum recommended positioning data as well as speed and time information;
- \$GPVTG – information about heading and ground speed in km/h and knots [7].

In experimental accidentology tests, the velocity is found using the NMEA sequence \$GPRMC. The data is saved in text files, according to the NMEA 0183 standard. An example of the NMEA sequence is shown below:

```
$GPRMC,130352.4,A,4540.20355,N,02536.46533,E,000.02,185.4,200310, ,E*51
```

The meaning of the fields is as follows: Identifier, UTC time, Status (A= data valid, V=data not valid), Latitude, N/S indicator (N=north, S=south), Longitude, E/W indicator (E=east, W=west), Speed over Ground (unit knots), Course over ground (unit degrees), Date (ddmmyy), Checksum [8].

2.2 Measurement of Vehicle and Occupant Accelerations

Pic DAQ systems are data acquisition platforms for recording dynamic data, through which accelerations and angular velocities can be measured. The platforms are developed by the Austrian company DSD and these are intended for impact, braking or cornering tests.

In Fig. 5 is shown the Pic DAQ 5 accelerometer which can be used to acquire the occupant's accelerations.



Fig. 5. Data acquisition platform - PicDAQ 5.

The system has a maximum weight of 500 grams with the following dimensions: length 135 mm, width 130 mm and thickness 40 mm. The data acquisition platform has 15 analog input channels, as well as 4 digital inputs which are available on a 12-bit resolution. The multiple analog input channels are needed to cover a wide range of uses, such as steering wheel angle measurement, wheel rotations etc. The user can select the number of samples obtained per second for each channel up to a rate of 1 kHz. Another feature is that the card memory allows the recording of approximately 500 braking tests. Tests that simulate the collision, as well as those for brake dynamics, are carried out by means of two triaxial accelerometers ($\pm 1.5g$ and $\pm 200g$), and roll, pitch and yaw movements are measured by means of a triaxial angular velocity sensor (± 300 deg). The acquisition time is up to five minutes. In Fig. 6 is shown where the PicDAQ 5 accelerometer is mounted inside the dummy's thorax.



Fig. 6. PicDAQ 5 mounted inside the dummy's thorax

Another data acquisition platform is the Pic DAQ 4 accelerometer (Fig. 7) which can be used to acquire vehicle accelerations.

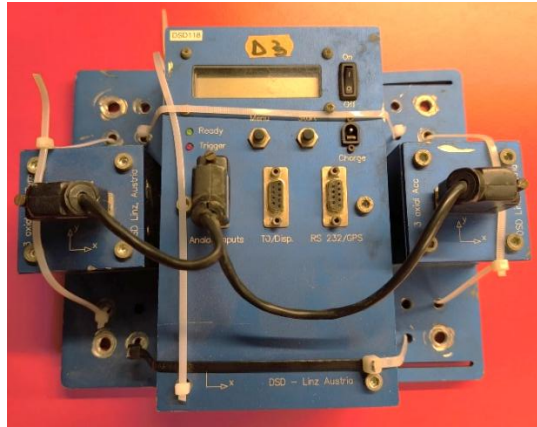


Fig. 7. Data acquisition platform - PicDAQ 4.

It consists of the main control unit and two blocks with sensors. The main unit includes the control buttons, display and connectors. One of the sensor blocks includes three axial acceleration sensors for small values (5 g range) and 3 angular velocity sensors (150 degree/second range). The other sensor block includes 3 axial acceleration sensors for high values (up to 50 g). In the case of braking and cornering tests, acceleration sensors in the 5 g range and angular velocity sensors are used, and for impact tests, sensors in the 50 g range are used. In Fig. 8 is shown where the Pic DAQ 4 accelerometer is mounted inside the vehicle.



Fig. 8. PicDAQ 4 mounted inside the vehicle.

The graphical interface is divided into several sections, one of which is a control area in the upper-left part of the window that contains various buttons for starting or stopping recording, connecting or disconnecting; another section on the left side of the window is called "Quality" (it refers to the quality of the signal); in the lower-left part there is a marking area with the "Mark point" button that refers to the current position and an area where numbers for the gear can be entered; an area named "Date" that displays the date in DDMMYY format, the current time, latitude, longitude, speed, respectively the number of records, these being the data provided in real time by GPS; an area with a white background on the right side of the screen that represents the real-time evolution of the speed, being represented graphically by means of a red curve; at the bottom is an area where the NMEA codes received from the GPS are displayed, the information is redundant in this case, but it is useful for data verification [7].

3.2 Processing of Acceleration Parameters

The files recorded through the PicDAQ systems are processed through the PocketDaq Analyzer software application. It can be accessed from a personal computer.

The measured accelerations can be influenced by the effect of gravity, but the software application has an interesting feature that it takes into account the installation area of the platform, thus neglecting the gravitational acceleration.

To import the data acquired by the accelerometer, the orientation of the sensors must be chosen. Next, the use of the sensor is set, namely "CRASHTEST" for accidentology tests. Within the application there is also the "BRAKETEST" option, which represents braking tests. Specific to these two options is that for the first option accelerometers with a high g level are used, while the second option uses accelerometers with a low g level. A period is set to perform the automatic correction, calculating the average of the measured values and the data file can be imported.

Channel Frequency Class (CFC) is a parameter used in signal processing to filter accelerometer data in crash analysis. This filtering smooths the data by reducing high-frequency noise, enhancing the clarity of significant trends and events in the data. When acquiring acceleration data for dummies, the acquisition frequency is set to 1 kHz, and the filter applied in this case will be CFC60. For the vehicle, the frequency 0.5 kHz can be used, filtering the data with CFC30. The correlation is performed according to the SAE J211 standard.

In Fig. 10 is displayed an example of the graphic obtained after the data acquisition by the sensor mounted inside the dummy. For a detailed viewing, the graph of dummy's acceleration is cut within an interval of interest. After successive reductions, the graph can be obtained.

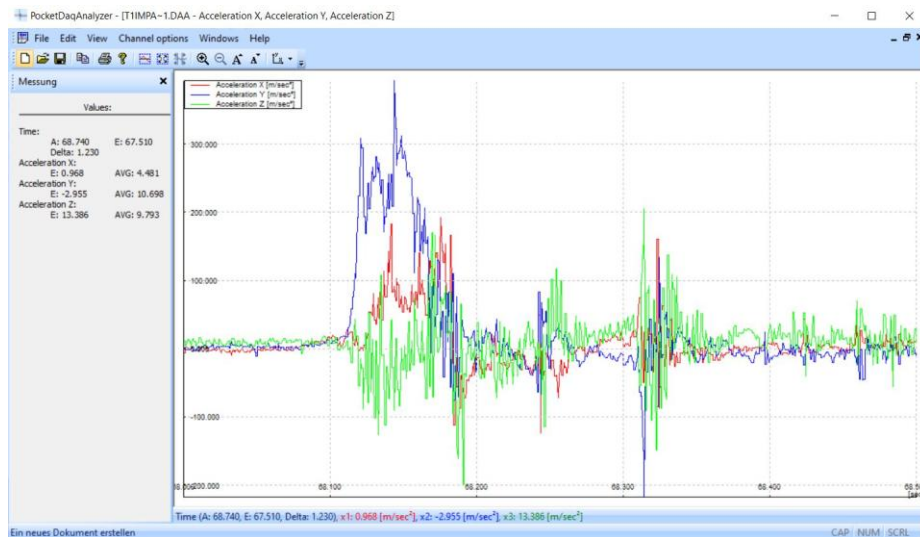


Fig. 10. Magnified view of the cropped graph section.

3.3 Processing of Video Evidence

Tracker is a free video analysis tool developed using the Open Source Physics (OSP) Java framework. It is designed for introductory physics courses, enabling detailed study of motion through features like manual and automated object tracking, center of mass tracks and interactive vector overlays [10].

The processing of the video samples and the display of the obtained kinematic parameters (displacement, velocity and acceleration) can be done through the Tracker application software.

Video samples that were filmed with a high-speed camera are used. In Fig. 11 is shown the graphical interface of the application after opening a video sample.

The frames per second are chosen depending on the video sample, for example 600 frames/s. An interval is also chosen in which the application will analyze and collect the data. It is necessary to establish the axis system for measurements to be made against an absolute reference system. The measurements are carried out by means of mass points of the analyzed bodies. Mass points refer to the conceptualization of a mass as being concentrated at a single point. These will be fixed on the marks applied to the bodies before the experiment is performed. When the bodies will move, the points will follow the movement of the markers applied to the vehicle and the thorax, respectively the head of the occupant (Fig. 12).

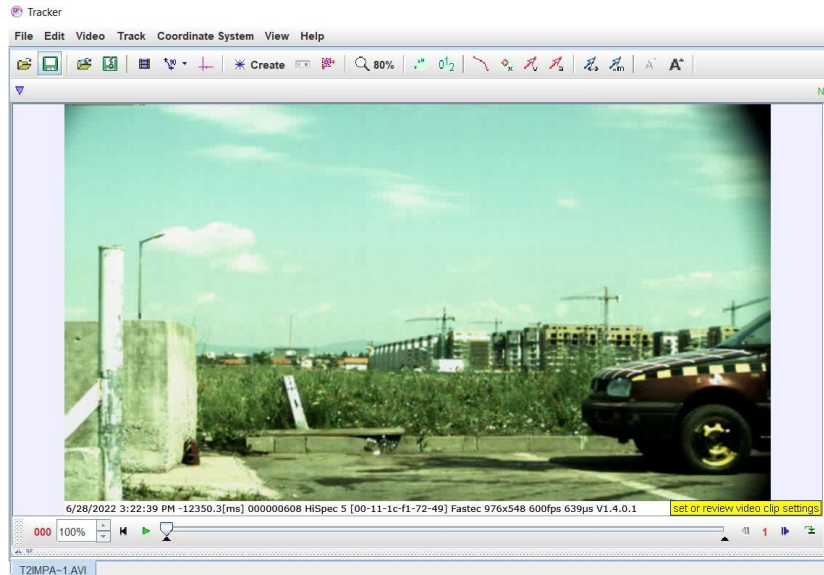


Fig. 11. The graphical interface of the Tracker software application.

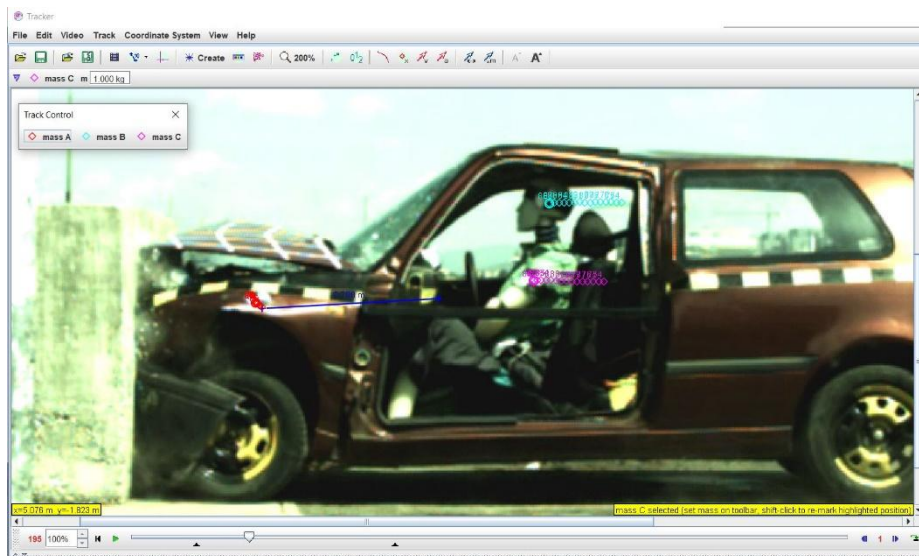


Fig. 12. Analysis of the movement through the mass points.

Finally, the parameters (displacement, velocity, acceleration) will be obtained after performing the video analysis. In Fig. 13 is an example for the graph of the velocity parameter of the occupant's head which is displayed in Tracker:

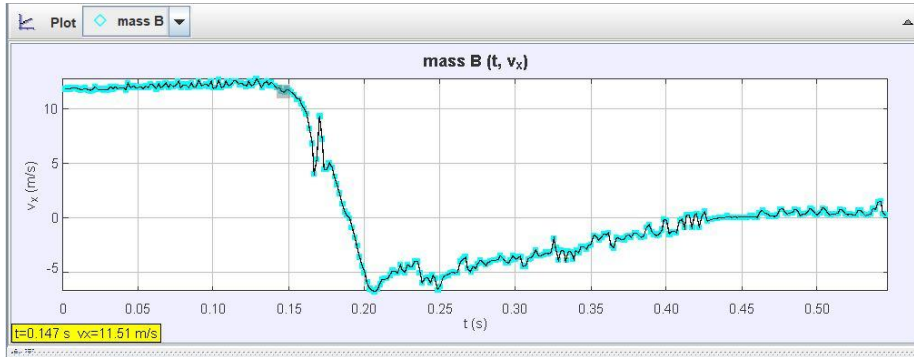


Fig. 13. Graph of the velocity parameter

Acquired data for all parameters (x - displacement; v – velocity, a - acceleration) are displayed in Tracker in the tabular form (Fig. 14):

| t (s) | x (m) | v (m/s) | a (m/s ²) |
|-------|-------|---------|-----------------------|
| 0.000 | 1.208 | | |
| 0.002 | 1.229 | 11.85 | |
| 0.003 | 1.248 | 11.91 | 85.45 |
| 0.005 | 1.269 | 11.85 | 108.2 |
| 0.007 | 1.287 | 11.95 | 61.48 |
| 0.008 | 1.308 | 11.99 | 75.25 |
| 0.010 | 1.327 | 11.86 | 152.2 |
| 0.012 | 1.348 | 11.78 | 76.50 |
| 0.013 | 1.367 | 11.80 | 65.16 |
| 0.015 | 1.387 | 11.91 | 73.67 |
| 0.017 | 1.406 | 11.78 | 141.9 |
| 0.018 | 1.427 | 11.67 | 81.26 |
| 0.020 | 1.445 | 11.79 | 31.95 |
| 0.022 | 1.466 | 12.02 | 71.23 |
| 0.023 | 1.485 | 11.80 | 94.03 |
| 0.025 | 1.505 | 11.82 | 42.51 |
| 0.027 | 1.525 | 11.76 | 23.00 |
| 0.028 | 1.544 | 11.83 | 22.31 |

Fig. 14. Displaying the acquired data in Tracker in the tabular form

4 Data Processing Procedures

4.1 Measurement Errors of Experimental Data

A road accident is influenced by several factors that determine measurement errors which may lead to useless data, some of the factors being the weather condition, the road condition, the condition of the vehicle, as well as the wrong recording of the experimental data due to the human error that may occur during data acquisition [11]. Therefore, measurement errors are of two types: errors caused by the incomplete acquisition of experimental data, as well as those generated by the lack of precision in data collection [12].

An important aspect of measurement errors refers to the uncertainties that characterize them, which are related to the parameters used for the reconstruction calculations,

usually when there is a variation in their values. For example, a vehicle equipped with ABS traveling at speed v , brakes suddenly until all wheels are locked. In this case, braking will be accompanied by skidding until the vehicle comes to a complete stop. If the velocity and distance are measured with a radar device, respectively a self-adhesive measuring tape, then the determination of the frictional drag coefficient (f_d) can be performed starting from the relationship for calculating the velocity when skidding occurs:

$$v = \sqrt{2 \cdot f_d \cdot x \cdot g} \quad (1)$$

$$f_d = \frac{v^2}{2 \cdot x \cdot g} \quad (2)$$

Where:

v – velocity of the vehicle;

x – skid distance;

g – gravitational acceleration.

In this case, the determination of the frictional drag coefficient can be influenced by the accuracy of the measurement of the travel velocity or the skid distance. It is obvious that any deviation in the velocity or distance measurements leads to variations in the frictional drag coefficient. If two self-adhesive measuring tapes are used, and one of them has a finer scale, the values $f_{d1}=0.434$ and $f_{d2}=0.43$ can be obtained. However, it is difficult to assess whether the difference is an error or not. In certain situations, measurement errors are not mistakes, but a difference in the measurement resolution between the measured value of the frictional drag coefficient and its actual value. A low accuracy can be caused by the measurement tools as previously presented or the way the measurement is performed, for example if the radar device is located at different places or distances from the vehicle for the two measurements (E.g. Placed at points such as the start and end of the track). Also, the time period between the two measurements is important, because a longer period can cause a change in the weather through the occurrence of meteorological phenomena or there can be influences caused by external factors that can alter the existing skid marks on the road.

Therefore, to quantify the uncertainties, the bias or systematic error can be determined. The bias can be calculated based on the following formula:

$$b = B \pm \Delta b \quad (3)$$

Where:

b - the calculated or measured quantity, for example the value of the frictional drag coefficient or velocity;

B – reference value;

Δb – the variation of the b value;

$b - B$ = bias or systematic error [13].

4.2 Data Filtering Methods

Origin is a comprehensive data analysis and graphing software widely used in scientific and engineering fields. It offers a robust suite of tools for tasks such as Peak Analysis,

Statistics, Signal Processing, Image Processing and 3D Surface Fitting. Chosen for its versatility and user-friendly interface, Origin is ideal for processing and visualizing complex data sets. In particular, it has proven effective for filtering raw data from crash tests, providing precise and reliable analysis critical for research and development. A signal obtained experimentally, by measurement, must be adjusted during its processing because filtering enhances the clarity of the signals of interest. This is essential for identifying specific events or characteristics within the crash test data, such as the exact moment of impact, peak values of velocities or accelerations. Filtering data makes it more suitable for graphical representation. Smooth data plots are easier to read and interpret, which is essential for communicating results to stakeholders. Origin provides several methods that can be used when smoothing raw experimental data, such as Fast Fourier Transform (FFT), Savitzky-Golay, Adjacent-Averaging, Binomial, Loess and Lowess. To filter the data obtained in the field of accidentology, a filter that uses FFT can be used.

The algorithm on which the FFT filter tool is based involves in the initial step the calculation of the FFT transform, then the user will select the frequencies. Afterwards a filter (Low-Pass / High-Pass / Band-Pass / Band-Block / Low-Pass Parabolic) is applied. The last step is to apply the Inverse FFT transformation [14].

The access path of FFT filter tool is Analysis-Signal Processing – Smooth - Open Dialog. Fig. 15 shows the dialog with the chosen options.

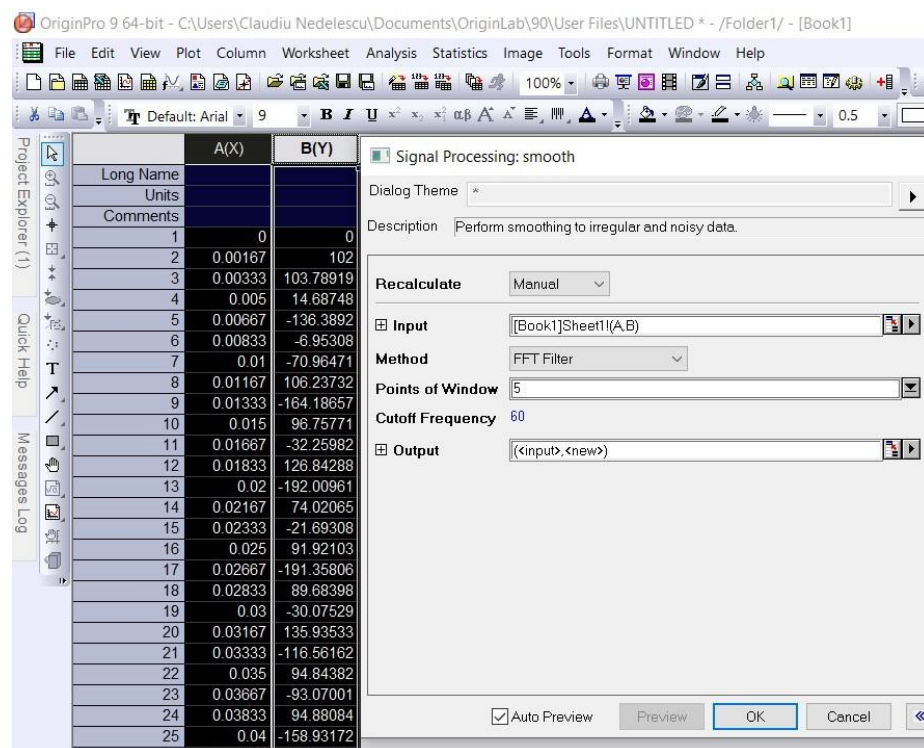


Fig. 15. The dialog with the chosen options when performing smoothing.

The window allows the number of window points to be specified, and the cutoff frequency changes automatically, thus controlling the degree of smoothing.

In Fig. 16 is the graph that contains the raw and smoothed data.

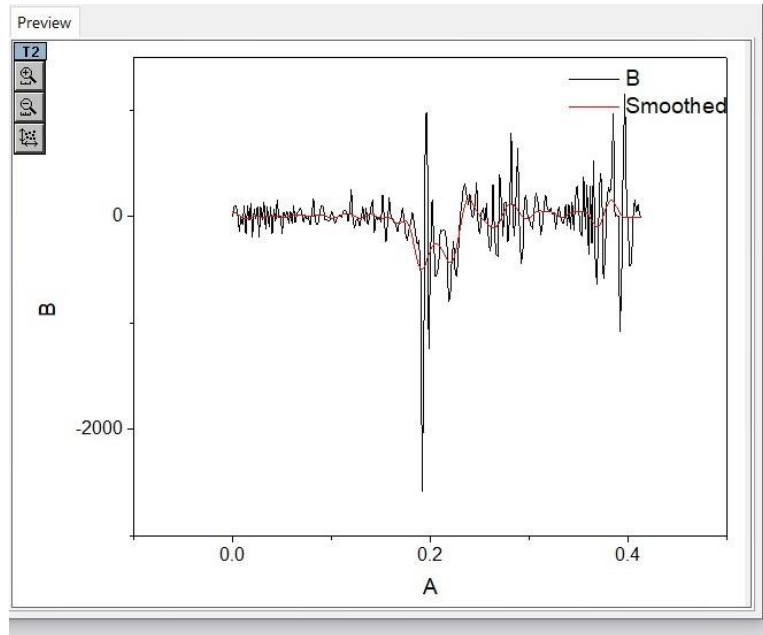


Fig. 16. Graph with the raw and smoothed data

5 Conclusions

The paper presented equipment and software applications used in crash tests, which are necessary for the acquisition and interpretation of data obtained. The velocity parameters of the vehicle can be acquired with the GPS system, and the accelerations of the vehicle and the occupant can be recorded with the PicDAQ systems. Also, the kinematic parameters (displacement, velocity, acceleration) of the vehicle and occupants can be determined in the Tracker application using video samples.

The presentation of the applications was carried out following some experimental research by creating simulations of the situations in which road accidents occur, both from the perspective of vehicle collisions and with regard to occupant behavior during an impact, illustrating suggestive images during the use of the software applications.

Various aspects of the software applications were highlighted, such as: the graphic interface of the applications used, as well as the work methodologies for their correct use. Also, the most common measurement errors were presented, as well as filtering methods after the data were acquired.

A future direction of research would be to assess by comparison the acquisition of data with the PicDAQ5 accelerometer when it is mounted inside, as well as outside the dummy's thorax, observing the influence of the deformations on the recorded data. Another future direction is to study other equipment or methods which can be used to determine the forces applied to the occupant's neck or thorax, as well as to measure the deformation of the dummy's thorax and neck during an impact.

References

1. Durlut, C., Ionescu, H. Automotive technical expertise (in romanian: Expertiza tehnică auto), (1980).
2. Todoruț, A. Dynamics of road accidents (in romanian: Dinamica accidentelor de circulație), U.T.PRESS, Cluj-Napoca (2008).
3. Schneider, E., Lossagk, H. Traffic accidents: A handbook for their processing and investigation for police, gendarmerie, courts and drivers. Fellowship, (1935).
4. Bobos, B. Research on motor vehicle collision reconstruction (in romanian: Cercetări privind reconstituirea coliziunii autovehiculelor), Risoprint, Cluj-Napoca (2008).
5. SparkFun Homepage, <https://www.sparkfun.com/>, last accessed 2024/07/26.
6. Mouser ANT-555 Technical Data, <https://www.mouser.com/datasheet/2/287/ANT555-2011-1839506.pdf>, last accessed 2024/05/25.
7. Covaciu, D., Preda, I., Ciolan, G., Campian, O. V. Data acquisition system based on GPS technology, for vehicle dynamics analysis. In CONAT 2010, Press Transilvania University of Brasov, Brasov (2010).
8. NMEA Reference Manual, Version 2.1, 2007.
9. DSD PicDAQ Technical Data, http://www.dsd.at/index.php?option=com_content&view=article&id=16:pic-daq&catid=37&Itemid=159&lang=en, last accessed 2024/06/03.
10. Physlets Homepage - Tracker Video Analysis and Modeling Tool, <https://physlets.org/tracker/>, last accessed 2024/07/25.
11. Ahmed, A., Sadullah, A. F. M., Yahya, A. S. Errors in accident data, its types, causes and methods of rectification-analysis of the literature. *Accident Analysis & Prevention*, **130**, 3-21 (2019).
12. Wang, X., Liu, Q., Guo, F., Xu, X., & Chen, X. Causation analysis of crashes and near crashes using naturalistic driving data. *Accident Analysis & Prevention*, **177**(106821), (2022).
13. Brach, M., Mason, J., Brach, R. M.: Vehicle accident analysis and reconstruction methods. 3rd edn. SAE International, Warrendale (2022).
14. OriginLab Homepage, <https://www.originlab.com/>, last accessed 2024/06/03.

Contributions to the Modelling of Gasoline Injection in the Spark Ignition Engines

Mihai Blaga¹, Tudor Mitran¹, Alexandru Rus¹, George Dragomir¹,
Horia Beles¹ and Vasile Blaga¹

¹Mechanical Engineering and Automotive Department, University of Oradea, 1 University
Street, Bihor County, Romania
mihaibлага332@gmail.com

Abstract. The operation of the closed loop motor with lambda transducer and catalyst makes the coefficient λ to be kept as close as possible to $\lambda = 1$ (stoichiometric dosage). Based on their own model, the authors performed the analytical calculation of the pressure in the intake manifold p_{ga} and the inlet pressure p_a . The equations of the model of operation of the spark ignition engine equipped with electronic fuel injection, introduced on the computer, have been determined. For modeling the ICE, with the petrol injection the initial data, the expressions of temperatures and pressures in the characteristic points are noted. The post-combustion volume increase ratio δ , the exhaust gas temperature T_e , the flue gas coefficient γ_r , reaching the determination of the injection duration, the cycle ends with the temperature at the end of the intake T_a . All these expressions were calculated analytically and correlated with each other so that they could be entered into the computer. The computer received the command to repeat these operations until the ICE parameters were obtained with an imposed error; in Annexes A and B. After making the engine parameter diagrams made with the help of the program, they are compared with the experimental diagrams raised on the experimental engine test installation and compared. In this paper a comparison is made between the calculated external characteristic and the one raised on the experimental engine test installation.

Keywords: inlet manifold pressure, inlet pressure, gas resistance coefficient, post-combustion volume increase ratio, fuel mass, injection duration.

1 Calculation of the pressure in the intake manifold and the inlet pressure

The flow of fresh fluid through the intake system is accompanied by pressure losses. These are linear pressure losses (due to friction with the walls of the intake manifold pipes) and local pressure losses (due to variations in flow section or flow rate direction). The intake process takes a short time, so for the gas flow through the intake system, the Bernoulli equation written for inlet section 0-0 and inlet section 1-1 applies (Fig. 1) [1]. If the density of the motor fluid is variable, Bernoulli's relationship between sections 0-0 and 2-2 is written for a case closer to reality.

This calculation is developed in two variants:

a. If the density of fresh fluid is constant (ambient temperature is constant)

b. The case where the density of the motor fluid ρ is variable. This variant is used in Matlab calculation.

In this case, Bernoulli's relationship between sections 0-0 and 2-2 becomes:

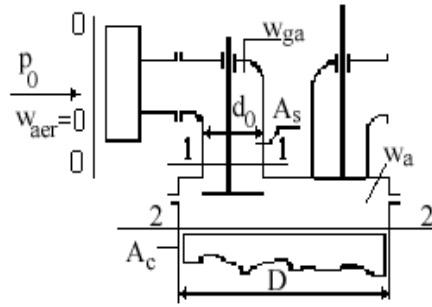


Fig. 1. Diagram for the analytical calculation of p_{ga} and p_a

$$p_o = p_a + (1 + \xi_a) \frac{\rho_a}{2} \cdot W_a^2 [Pa]; \quad (1)$$

where: - p_a - pressure at the end of the intake stroke (considered to be constant during the intake stroke);

$$\rho_a = \frac{p_a}{RT_a} [kg/m^3]; \quad - \text{density of fresh fluid at the end of the intake stroke;}$$

The speed of sound in the fresh fluid:

$$a_{sa} = \sqrt{k_a \cdot R \cdot T_a} [m/s]; \quad (2)$$

where: - $k_a = 1.4$ - the adiabatic exponent of the admission process, which comes from:

$$RT_a = \frac{a_{sa}^2}{k_a};$$

and, further:

$$\rho_a = \frac{k_a}{a_{sa}^2} \cdot p_a [kg/m^3];$$

Entering in (1), it results:

$$p_o = p_a + (1 + \xi_a) \cdot \frac{k_a}{2} \cdot \frac{1}{a_{sa}^2} \cdot p_a \cdot \left(\frac{4}{30 \cdot \pi}\right)^2 \cdot \left(\frac{V_s}{D^2}\right)^2 \cdot n^2 [Pa]; \quad (3)$$

and:

$$p_o = p_a \left[1 + (1 + \xi_a) \cdot \frac{k_a}{2} \cdot \left(\frac{4}{30 \cdot \pi}\right)^2 \cdot \left(\frac{V_s}{D^2}\right)^2 \cdot \left(\frac{n}{a_{sa}}\right)^2 \right] [Pa]; \quad (4)$$

or:

$$p_a = \frac{1}{1 + (1 + \xi_a) \frac{k_a}{2} \left(\frac{4}{30 \cdot \pi}\right)^2 \cdot \left(\frac{V_s}{D^2}\right)^2 \cdot \left(\frac{n}{a_{sa}}\right)^2} \cdot p_o = k_1 \cdot p_o [Pa]; \quad (5)$$

$$\text{where: } -k_1 = \frac{1}{1+(1+\xi_a) \cdot \frac{k_a}{2} \cdot \left(\frac{4}{30\pi}\right)^2 \cdot \left(\frac{V_s}{D^2}\right)^2 \cdot \left(\frac{n}{a_{sa}}\right)^2}; \quad (6)$$

Bernoulli's equation between sections 0-0 and 1-1 is:

$$p_o = p_{ga} + (1 + \xi_{ga}) \cdot \frac{p_{ga}}{2} \cdot w_{ga}^2; \quad (7)$$

where: $-\rho_{ga} = \frac{p_{ga}}{R \cdot T_{ga}} = \frac{p_{ga}}{RT_o} [kg/m^3]$; - engine fluid density in the intake manifold;

- T_o [K] - ambient temperature;

- T_{ga} [K] - temperature in the intake manifold, considered to be equal to the ambient temperature (T_o);

Applying the relation of the continuity of the mass flow between sections 1-1 and 2-2 (fig. 1), it results:

$$W_{ga} \cdot A_s \cdot \rho = W_a \cdot A_c \cdot \rho_a [m/s]; \quad (8)$$

Intake manifold gas flow rate:

$$W_{ga} = \frac{A_c}{A_s} \cdot \frac{\rho_a}{\rho_{ga}} \cdot W_a = \frac{\pi \cdot D^2}{4} \cdot \frac{4}{\pi \cdot d_o^2} \cdot \frac{p_a}{p_{ga}} \cdot \frac{R \cdot T_o}{R \cdot T_a} \cdot W_a [m/s]; \quad (9)$$

or:

$$W_{ga} = \frac{D^2}{d_o^2} \cdot \frac{p_a}{p_{ga}} \cdot \frac{T_o}{T_a} \cdot \frac{4}{30\pi} \cdot \frac{V_s}{D^2} \cdot n = \frac{4}{30\pi} \cdot \frac{p_a}{p_{ga}} \cdot \frac{T_o}{T_a} \cdot \frac{V_s}{d_o^2} \cdot n [m/s]; \quad (10)$$

Enter (10) in Bernoulli's equation written for sections 0 = 0 and 1 = 1 (7) and result:

$$p_o = p_{ga} + (1 + \xi_{ga}) \frac{p_{ga}}{2RT_o} \cdot \left(\frac{4}{30\pi}\right)^2 \cdot \left(\frac{p_a}{p_{ga}}\right)^2 \cdot \left(\frac{T_o}{T_a}\right)^2 \cdot \left(\frac{V_s}{d_o^2}\right)^2 \cdot n^2 \quad (11)$$

and, further:

$$p_o = p_{ga} + (1 + \xi_{ga}) \frac{1}{2RT_a} \cdot \left(\frac{4}{30\pi}\right)^2 \cdot \frac{p_a^2}{p_{ga}} \cdot \frac{T_o}{T_a} \cdot \left(\frac{V_s}{d_o^2}\right)^2 \cdot n^2; \quad (12)$$

Replace in (12): $RT_a = \frac{a_{sa}^2}{k_a}$; and obtain:

$$p_o \cdot p_{ga} = p_{ga}^2 + (1 + \xi_{ga}) \frac{k_a}{2a_{sa}^2} \cdot \left(\frac{4}{30\pi}\right)^2 \cdot k_1^2 \cdot p_o^2 \cdot \frac{T_o}{T_a} \cdot \left(\frac{V_s}{d_o^2}\right)^2 \cdot n^2; \quad (13)$$

It is noted $p_a = k_1 \cdot p_o$; $p_{ga}^2 - p_o \cdot p_{ga} + k_2 \cdot p_o^2 = 0$

Solve the equation of degree two with the unknown p_{ga} where:

$$k_2 = \frac{k_a}{2} \cdot k_1^2 \cdot (1 + \xi_{ga}) \cdot \left(\frac{4}{30\pi}\right)^2 \cdot \frac{T_o}{T_a} \cdot \left(\frac{V_s}{d_o^2}\right)^2 \cdot \left(\frac{n}{a_{sa}}\right)^2; \quad k_2 > 0; \quad (14)$$

$$p_{ga_{1,2}} = \frac{p_o \pm \sqrt{p_o^2 - 4 \cdot k_2 \cdot p_o^2}}{2} = \frac{p_o \pm p_o \sqrt{1 - 4 \cdot k_2}}{2} = \frac{p_o(1 \pm \sqrt{1 - 4 \cdot k_2})}{2}; \quad k_2 > 0; \quad (15)$$

From (14) it is observed that if $n = 0$ rot / min, $k_2 = 0$ and $p_{ga} = p_o$. In other words, losses in the intake pathway occur only as a result of fresh fluid flowing through the intake gallery.

The solution of equation (15) is:

$$p_{ga} = \frac{1 + \sqrt{1 - 4k_2}}{2} p_o = k_3 \cdot p_o; \text{ where: } -k_3 = \frac{1 + \sqrt{1 - 4k_2}}{2}. \quad (16)$$

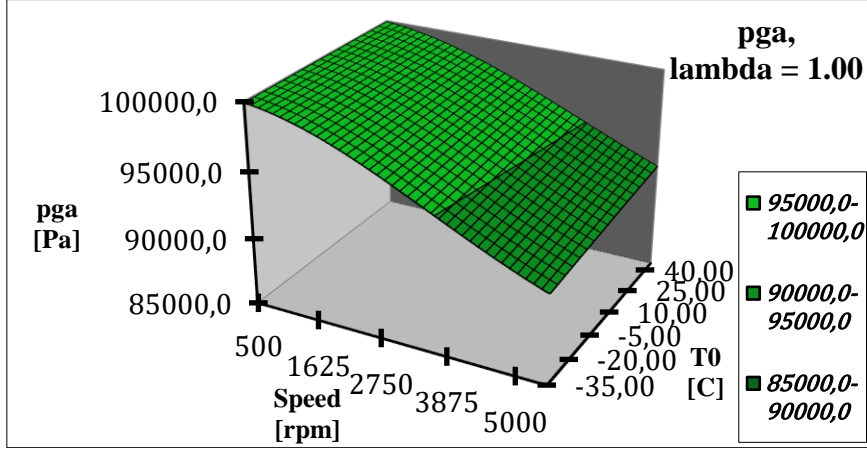


Fig. 2. Variation of pressure in the intake manifold p_{ga} as a function of speed (n) and ambient temperature (T_0), for an excess air coefficient $\lambda = 1$

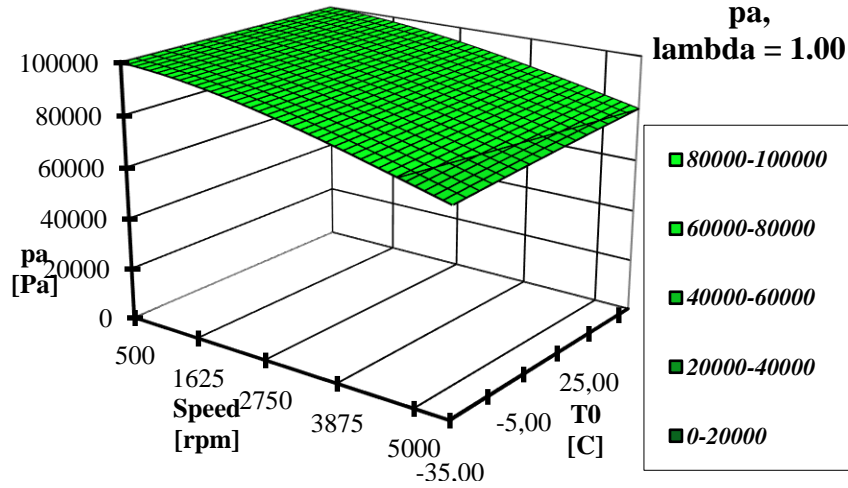


Fig. 3. Variation of inlet pressure p_a as a function of speed (n) and ambient temperature (T_0), for an excess air coefficient $\lambda = 1$

By calculating p_{ga} and p_a , all the data needed to enter the spark ignition engine cycle are determined with gasoline injection.

It is determined:

$$\psi_o = \frac{\Delta p_a}{p_o} = \frac{p_o - p_a}{p_o} = 1 - \frac{p_a}{p_o};$$

$$\psi_1 = \frac{\Delta p_r}{p_r} = \frac{p_r - p_o}{p_r} = 1 - \frac{p_o}{p_r}; \psi = \frac{p_a}{p_r}.$$

The polytropic exponent of the admission process is:

$$n_a = 1 - \frac{k_a - 1}{\varphi_a}; \quad \varphi_a = 1,05; \quad k_a = 1,458 - 0,525 \cdot 10^{-4} (T_0 + T_a). \quad (17)$$

where φ_a is the coefficient that characterizes the deviation of the work process at admission in relation to the adiabatic process. Given the average temperature at the end of the intake $T_a = 322\text{K}$. Determine the temperature at the end of compression: $T_c = T_a \cdot \varepsilon^{n_c-1}$. The polytropic exponent of the n_c compression process can be expressed as a function of the adiabatic exponent k_c and the coefficient that takes into account the heat released by the agent to the cylinder walls during this process:

$$n_c = 1 + \frac{k_c - 1}{\varphi_c}; \quad \varphi_c = 1,06;$$

φ_c - coefficient that characterizes the deviation of the working process in relation to the adiabatic process at compression.

The coefficient φ_c is a consequence of the energy balance equation applied to the compression process;

$$\varphi_c = 1 - \frac{Q_{pc}}{\Delta U} = - \frac{L_{a-c}}{U_c - U_a} = \frac{L_{a-c}}{U_a - U_c}; \quad (18)$$

At the absolute mechanical work of compression[7]; $\Delta U = U_c - U_a$ is the variation of the internal energy of the fresh mixture during this process.

It is obvious that since $Q_{pc} < 0$ and $\Delta U > 0$ the coefficient φ_c is supraunitary, so $n_c < k_c$. Under the conditions of the compression process the adiabatic exponent k_c is obtained with the relation:

$$k_c = 1,438 - 0,525 \cdot 10^{-4}(T_a + T_c) \quad (19)$$

The pressure at point c is:

$$p_c = p_a \cdot \varepsilon^{n_c} \quad (20)$$

Determine the temperature T_z :

$$p_z \cdot V_z = m \cdot R \cdot T_z \text{ și } p_c \cdot V_c = m \cdot R \cdot T_c;$$

and; $V_z = V_c$; by division it results:

$$\frac{p_z}{p_c} = \frac{T_z}{T_c} = \alpha; ;$$

Where: $T_z = \alpha \cdot T_c$ and $p_z = \alpha \cdot p_c$. (21)

Temperature in point u of post-burn stage T_u are calculated:

$$T_u = T_z \cdot \delta^{1-n_u}; \quad n_u = 0,9; \quad [5] \quad (22)$$

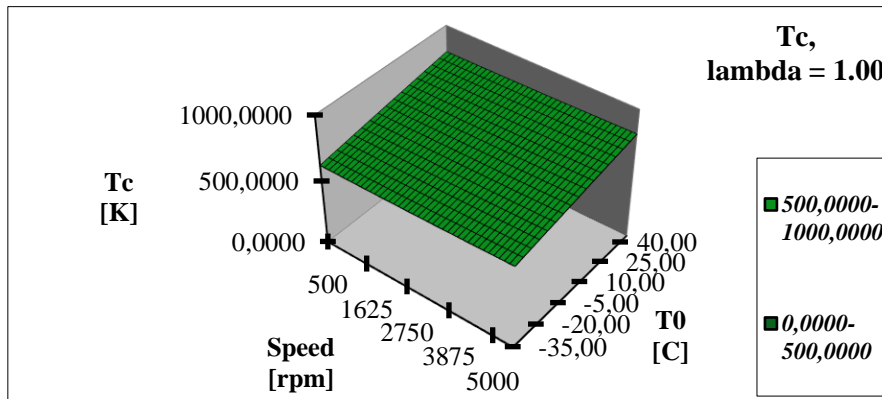


Fig. 4. Tc temperature variation with ambient speed and temperature

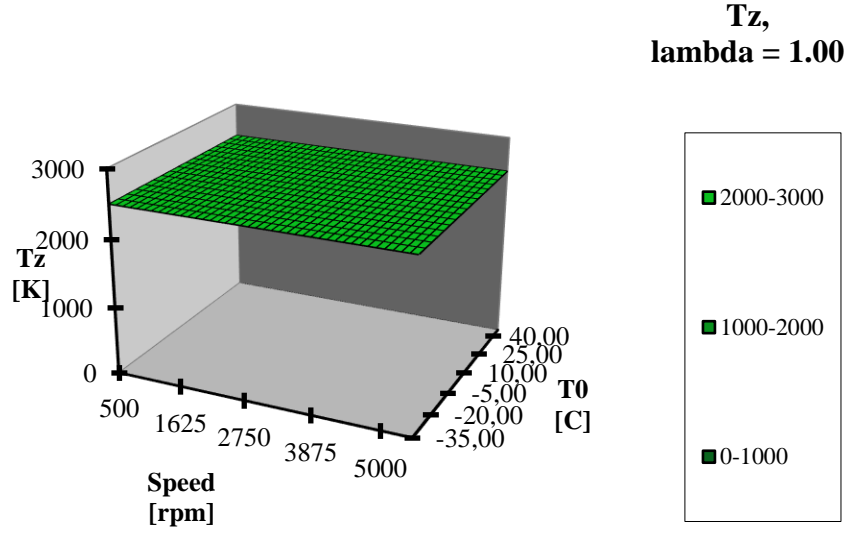


Fig. 5. T_z temperature variation with ambient speed and temperature

The mean adiabatic exponent at post-combustion k_u is determined by the relation [5]:

$$k_u = 1,268 - \frac{0,035}{\lambda} + \frac{126}{T_z + T_u}. \quad (23)$$

end of expansion temperature:

$$T_d = T_u \left(\frac{\delta}{\varepsilon} \right)^{n_d - 1}. \quad (24)$$

The polytropic exponent n_d of the expansion is calculated by the relation:

$$n_d = 1 + \frac{k_d - 1}{\varphi_d}. \quad (25)$$

The adiabatic exponent k_d , results [1]:

$$k_d = 1,268 - \frac{0,035}{\lambda} + \frac{126}{T_u + T_d}; \quad (26)$$

where: $\varphi_d = 0,92$ is the coefficient that characterizes the deviation of the work process at relaxation, in relation to the adiabatic process [1].

The temperature at point d_1 is calculated by the relation:

$$T_{d_1} = T_d \left[\frac{\left(\frac{\varepsilon}{\delta} \right)^{n_d} \cdot \delta^{n_u}}{\psi \cdot \alpha \cdot \varepsilon^{n_c}} \right]^{\frac{k_e - 1}{k_e}} \quad (27)$$

The temperature at point r is:

$$T_r = \frac{T_{d_1}}{\varphi_r} \quad (28)$$

where: $\varphi_r = 1,04$ is the coefficient that characterizes the deviation of the working process on the portion $d_1 - r$, in relation to the adiabatic process (ratio of temperatures in forced evacuation).

Temperature at point r_1 :

$$T_{r_1} = T_r \cdot \psi^{k_e - 1/k_e} \tag{29}$$

The adiabatic exponent k_u results from:

$$k_e = 1,268 - \frac{0,035}{\lambda} + \frac{126}{T_d + T_{r_1}} n_e = 1 + \frac{k_e - 1}{\varphi_e} \tag{30}$$

where: $\varphi_e = 0,92$ is the coefficient that characterizes the deviation of the working process at evacuation in relation to the adiabatic process.

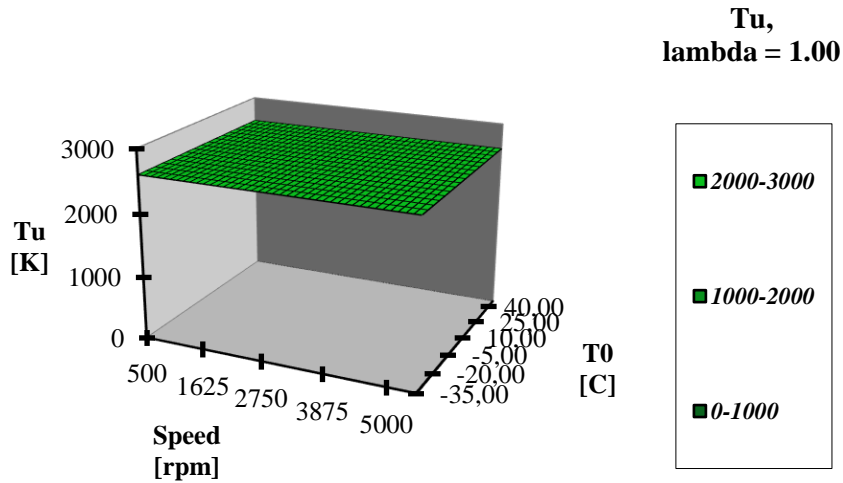


Fig. 6. Temperature variation at the end of post-combustion T_u with the speed and temperature of the environment

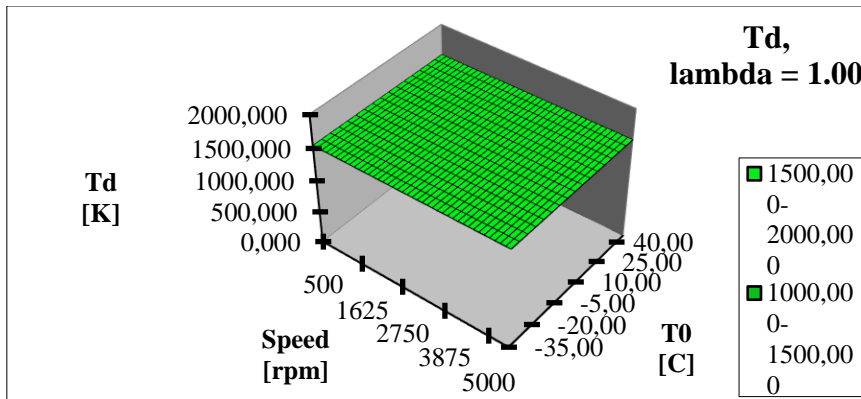


Fig. 7. Temperature variation at the beginning of T_d free discharge with ambient speed and temperature

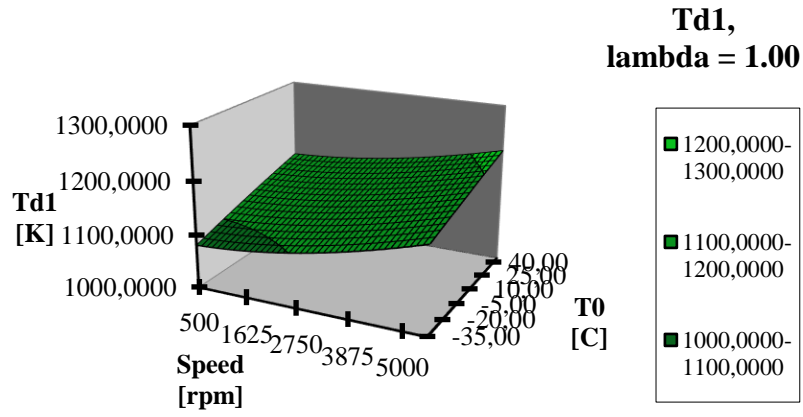


Fig. 8. Temperature variation at the end of the forced discharge T_{d1} with the speed and temperature of the environment.

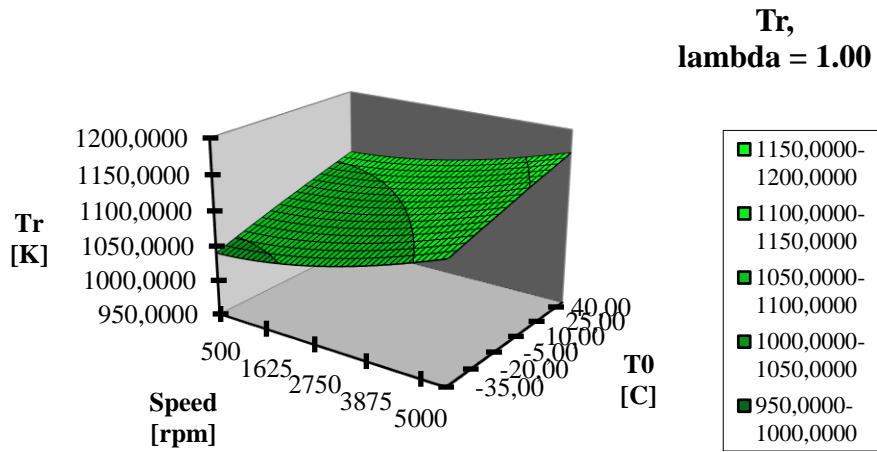


Fig. 9. Variation of gas temperature at the end of T_r discharge with ambient speed and temperature.

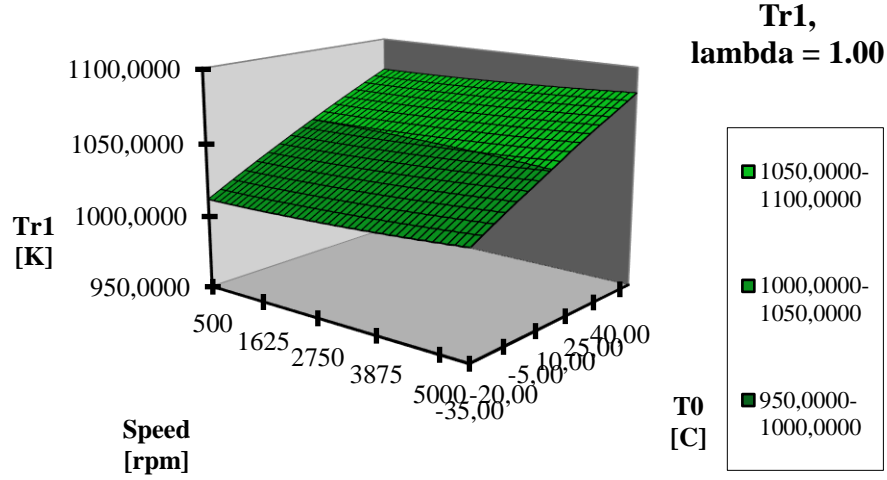


Fig. 10. Temperature variation at the end of the isentropic expansion of the waste gas T_{r1} with the speed and temperature of the environment

2 Calculation of the thermal load q_{cb} of the cylinder

In order to establish the equations that allow the correlation of the heat developed by the combustion of the fuel with the characteristic parameters of the cycle, we start from the energy efficiency of the combustion.

It is note: $\xi = \frac{m_{aer}}{m_{ad}}$; $d = \frac{1}{\lambda \cdot L_0}$; (31)

where: - m_{ad} [kg] - mass of fresh fluid in the cylinder at the end of the intake process;
 - d - dosage, which characterizes the air-fuel mixture;

$$m_{cb} = \xi \cdot m_{ad}. \quad (32)$$

Degree of filling:

$$\eta_v = \frac{m_{ad}}{m_{Vs}} = \frac{m_a - m_r}{\frac{p_0 V_s}{R T_0}}; \quad (33)$$

where: - m_a [kg] - mass of working fluid in the cylinder at the end of the intake process;

- m_r [kg] - mass of residual flue gas remaining in the cylinder from the previous cycle;

It follows from (33):

$$m_{ad} = \eta_v \cdot m_{Vs} = \eta_v \cdot \rho_0 \cdot V_s \quad (34)$$

Substituting in (32) results:

$$m_{cb} = \xi \cdot d \cdot \eta_v \cdot \rho_0 \cdot V_s \quad (35)$$

where: $\rho_0 = p_0 / R \cdot T_0$ [kg/m³]; density of air at pressure p_0 and temperature T_0 of the environment;

Amount of fuel that can be burned in the unit volume of the unit cylinder:

$$m_{cb}^{Vs} = \frac{m_{cb}}{V_s} = \xi \cdot d \cdot \eta_v \cdot \rho_0 \left[\frac{kg_{comb}}{m^3} \right]. \quad (36)$$

Entering these values of ξ into calculations leads to an increase in the calculation accuracy of the following relations:

$$Q_{cb} = m_{cb} \cdot Q_i \quad (37)$$

Replacing relation (35) with relation (37), results in:

$$Q_{cb} = \xi \cdot d \cdot \eta_v \cdot \rho_o \cdot V_s \cdot Q_i \text{ [J / cycle]} \quad (38)$$

Based on the last relation, the thermal input of the engine cylinder unit is obtained:

$$q_{cb} = \frac{Q_{cb}}{V_s} = \xi \cdot d \cdot \eta_v \cdot \rho_o \cdot Q_i; \left[\frac{\text{J}}{\text{m}^3} \right]$$

The expression for the fill factor is:

$$\eta_v = (1 - \psi_o) \cdot \frac{\varepsilon}{\varepsilon - 1} \left[1 - \left(1 + \frac{1}{n_a} \cdot \frac{k_a - k_e}{k_e - 1} \right) \cdot \frac{1}{\varepsilon} \cdot \frac{1}{\psi^{1/k_e}} \right]; \quad (39)$$

where: - k_e - the average adiabatic exponent of the evacuation process;

- n_a - the average polytropic exponent of the admission process;

- $\varphi_a = 1.05$ [1] - coefficient that characterizes the deviation of the work process at admission in relation to the adiabatic process; $k_a = 1,458 - 0,525 \cdot 10^{-4} (T_o + T_a)$.

$$n_a = 1 + \frac{k_a - 1}{\varphi_a}; \quad (40)$$

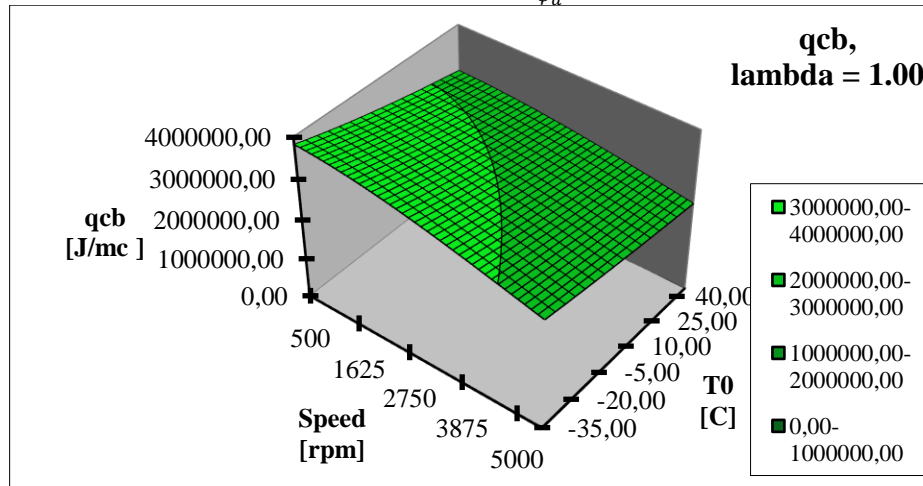


Fig. 11. Variation of thermal loads of the cylinder q_{cb} as a function of speed (n) and ambient temperature (T_0), for an excess air coefficient $\lambda = 1$

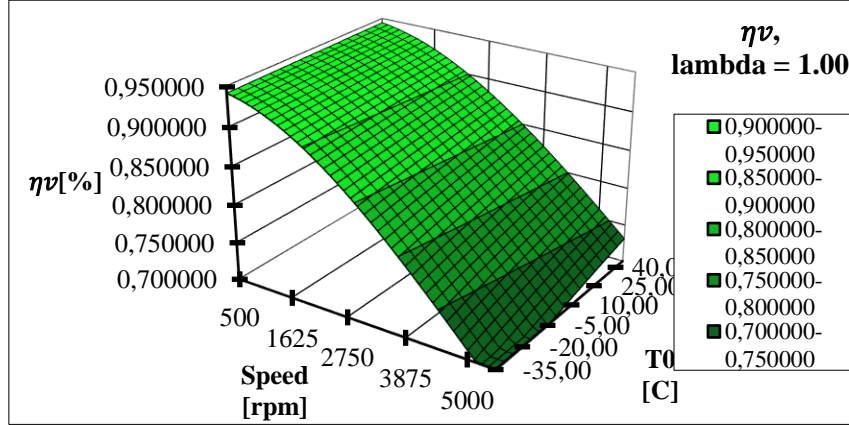


Fig. 12. Variation of the filling coefficient η_v depending on the speed (n) and the ambient temperature (T_0), for an excess air coefficient $\lambda = 1$

3 Determination of the equation of the ratio of increase in pressure at isocorous combustion α and of the equation of the ratio of increase of volume in post-combustion volume δ

The establishment of these equations is based on the idea of correlating the heat developed during combustion at constant volume, respectively after combustion, with the parameters of the thermal agent that takes over this heat.

To calculate the heat input in constant volume combustion, write the equation:

$$Q_v = m_c \cdot c_{vg} (T_z - T_c); [J] \quad (41)$$

where: - m_c [kg] - mass of working fluid in the cylinder at the end of the compression stroke - c_{vg} [J/kgK] - average specific heat at constant volume of flue gas: $c_{vg} = R/k_v - 1$; T_z [K] - temperature at the end of combustion at constant volume; T_c [K] - temperature at the end of the compression stroke; k_v - average adiabatic exponent, which characterizes the temperature range ($T_z - T_c$);

Developing Equation (41) and considering that:

$$m_c = p_c V_c / RT_c \text{ [kg]}, T_z / T_c = \alpha; V_s = V_a - V_c; [\text{m}^3] \text{ (Vs unit cylinder);}$$

the heat input of the combustion chamber volume unit results in:

$$q_v = \frac{p_c \cdot V_c}{(V_a - V_c)} \cdot \left(\frac{T_z}{T_c} - 1 \right) \frac{1}{k_v - 1} \quad (42)$$

and further:

$$q_v = \frac{Q_v}{V_s} = \frac{p_c}{\varepsilon - 1} \left[\frac{\alpha - 1}{k_v - 1} \right]; \quad (43)$$

Because: $q_v = q_{cz} = \xi_0 \cdot q_{cb}$; $q_{cz} = \xi_0 q_{cb} = \frac{p_c}{\varepsilon - 1} \cdot \frac{\alpha - 1}{k_v - 1}; k_v = 1,268 - \frac{0,035}{\lambda} + \frac{126}{T_c + T_z}$;
then:

$$\alpha = 1 + \frac{\xi_0 \cdot q_{cb} \cdot (\varepsilon - 1) (k_v - 1)}{p_c}; \quad (44)$$

δ - the ratio of volume increase in post-combustion has the relation.

$$\delta = \left[1 + \frac{\varepsilon-1}{\varepsilon^{nc}} \cdot \frac{1-n_u}{p_o(1-\psi_o)} \cdot \frac{k_u-1}{k_u-n_u} \cdot \frac{q_u}{\alpha} \right]^{\frac{1}{1-n_u}} \quad (45)$$

Fig. 13. shows the dependence of α , calculated according to the speed and temperature of the environment. depending on the speed and temperature of the environment, for an excess air coefficient $\lambda = 1$ [5]. Fig. 14. shows the variation of δ , calculated according to the speed and temperature of the environment, for an excess air coefficient $\lambda = 1$ [5].

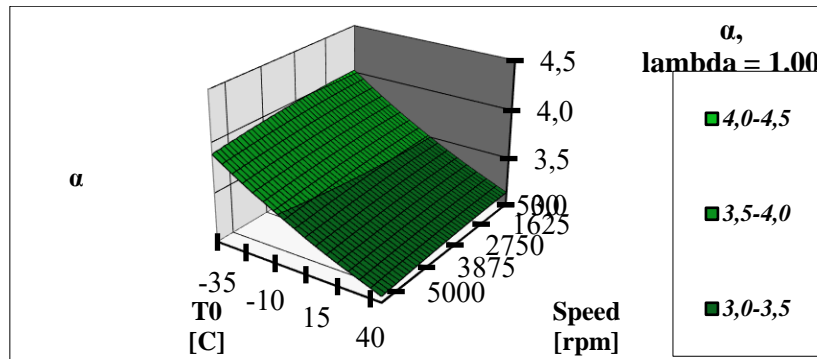


Fig. 13. Variation of the coefficient α with the speed and temperature of the environment

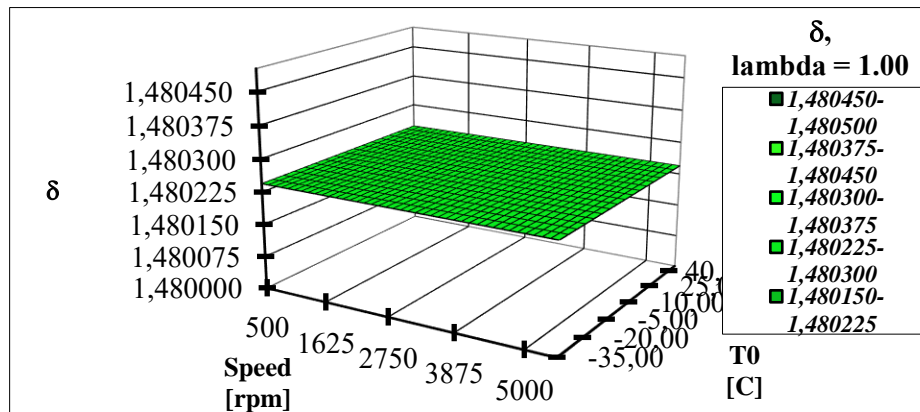


Fig. 14. Variation of the volume increase ratio in post-firing δ with the speed and temperature of the environment.

4 Determination of gasoline flow and injection duration

The fuel flow through the injector flow section is calculated by the relation:

$$Q_b = \mu_i \cdot A_i \sqrt{\frac{2(p_b - p_{ga})}{\rho_b}}; \quad (46)$$

where: μ_i - flow coefficient in the section provided by the needle; $\mu_i = 0,8 - 0,93$;

Taking into account the relation:

$$p_b = K_r + p_{ga} \quad [5] \quad (47)$$

$$Q_b = \mu_i \cdot A_i \sqrt{\frac{2K_r}{\rho_b}} \quad (48)$$

where: A_i is the injector flow section; p_b - gasoline pressure at the inlet to the injector; p_{ga} - air pressure in the intake manifold; ρ_b - gasoline density ; K_r - pressure regulator constant, Q_b - gasoline flow. On the other hand, it is known from the flow definition relation that it is the volume of combustion drained in the unit of time.

You can write:

$$Q_b = \frac{V_b}{t_i} = \frac{m_{cb}}{\rho_b \cdot t_i} \quad (49)$$

From the equality of relations (48) and (49) results the injection duration, t_i :

$$t_i = \frac{m_{cb}}{\rho_b} \cdot \frac{1}{\mu_i \cdot A_i \cdot \sqrt{\frac{2K_r}{\rho_b}}} = \frac{m_{cb}}{\mu_i \cdot A_i \cdot \sqrt{2K_r \cdot \rho_b}}; \quad d = \frac{1}{\lambda \cdot L_o} = \frac{m_{cb}}{m_{aer}};$$

$$m_{cb} = \frac{m_{aer}}{\lambda \cdot L_o} = \frac{m_{aer}}{m_{ad}} = \frac{m_{ad}}{\lambda \cdot L_o} = \xi \cdot d \cdot m_{ad}; \quad \xi = \frac{m_{aer}}{m_{ad}};$$

where ξ is the coefficient that represents the ratio between the amount of air required to burn m_{aer} and the amount of fuel mixture allowed m_{ad} .

Result:

$$t_i = \frac{\xi \cdot d \cdot m_{ad}}{\mu_i \cdot A_i \cdot \sqrt{2K_r \cdot \rho_b}} \quad [s] \quad (50)$$

where: m_{cb} is the mass of fuel; m_{aer} - engine suction air mass; m_{ad} - mass permissible fuel mixture; d - dosage.

Finally, by going through the Matlab calculation, the injection time is determined with the speed and temperature of the environment for $\lambda = 1$ (stoichiometric mixture), Fig. 15

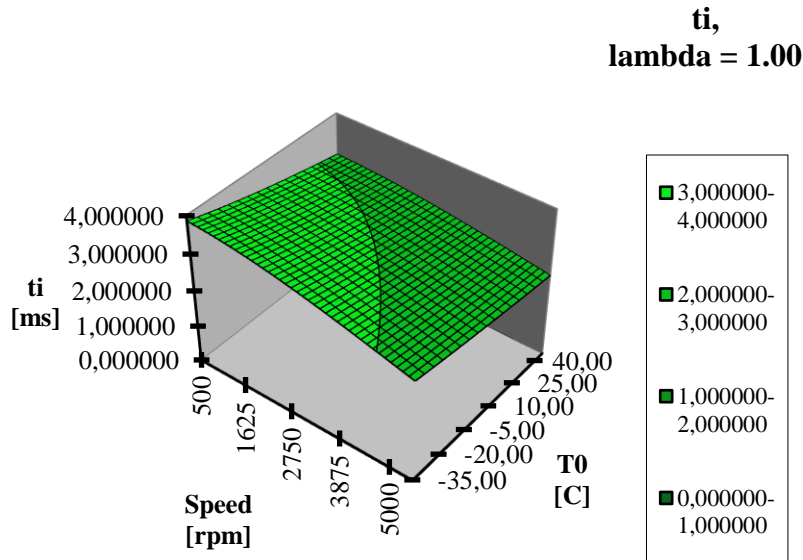


Fig. 15. Variation of injection time with speed and ambient temperature

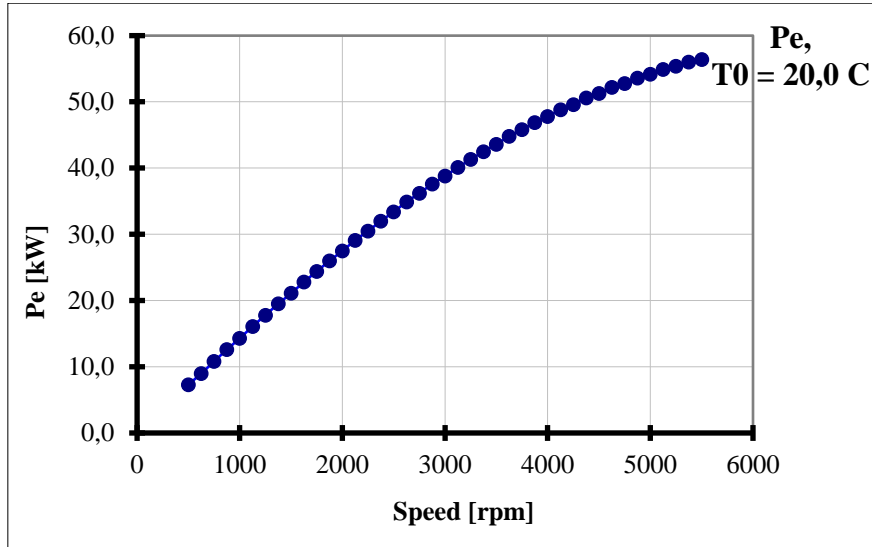


Fig. 19. Variation of effective power calculated with speed

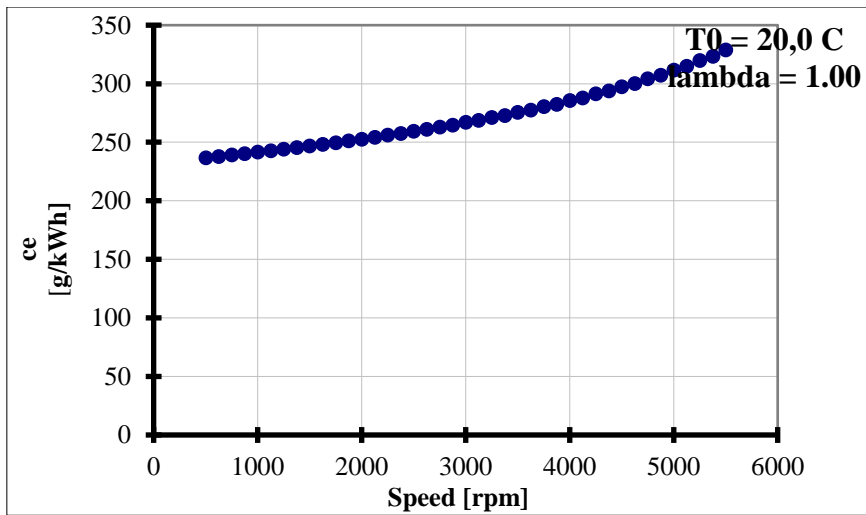


Fig. 20. Variation of effective specific consumption calculated with speed

5 The real indicated diagram

The test bed used to determine the engine's parameters is shown in fig. 21. Its main components are:

- the engine that equips a 1.6l Logan car, which is mounted on a frame fixed in a foundation;
- torquemeter type Honeywell 1604-1K;
- data acquisition system AVL INDIMICRO;
- a transducer to measure the instantaneous pressure inside the cylinder type AVL GH14D;

Table 1 Calculated and measured values from external engine characteristics

| n[rpm] | Mec [Nm] | Mem [Nm] | Pec [kW] | Pem [kW] | cec [g/kWh] | cem [g/kWh] |
|--------|-------------|-------------|-------------|-------------|----------------|----------------|
| 500 | 138 | 134 | 6,65 | 6,45 | 240 | 249 |
| 1000 | 130 | 126 | 11,9 | 11,65 | 245 | 252 |
| 1500 | 125 | 122 | 20 | 19,34 | 248 | 256 |
| 2000 | 120 | 117 | 26 | 25,28 | 252 | 261 |
| 2500 | 115 | 113 | 34 | 33,5 | 263 | 270 |
| 3000 | 109 | 107 | 39,5 | 38,1 | 270 | 280 |
| 3500 | 100 | 97,8 | 45 | 43,5 | 278 | 286 |
| 4000 | 95 | 92 | 49 | 47,21 | 290 | 297 |
| 4500 | 90 | 87,4 | 52 | 51,07 | 300 | 310 |
| 5000 | 80 | 77 | 54 | 52,62 | 315 | 325 |
| 5500 | 78 | 76 | 55 | 52,99 | 330 | 340 |



Fig. 21. The test bed

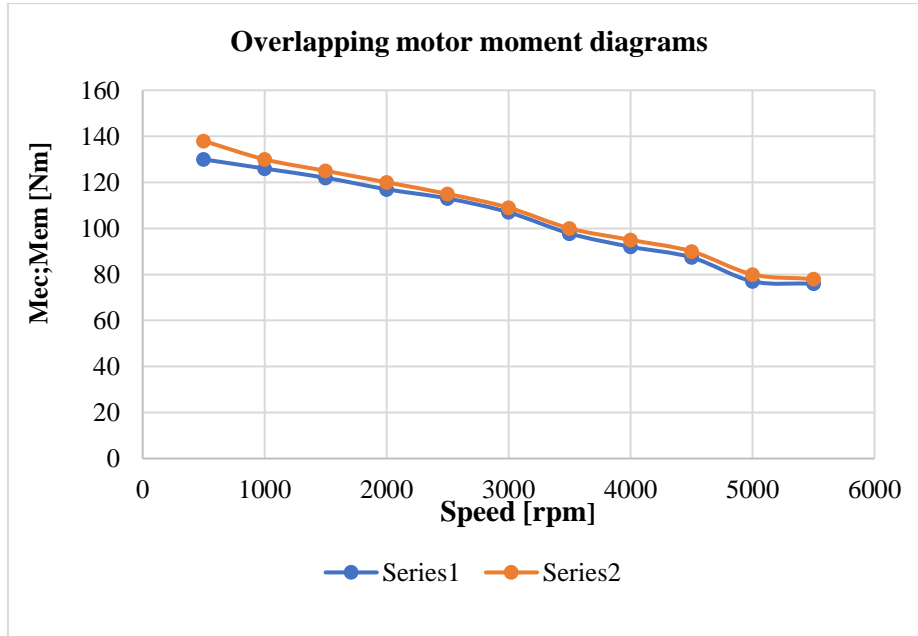


Fig. 22. Overlapping, calculated and measured motor torque diagrams

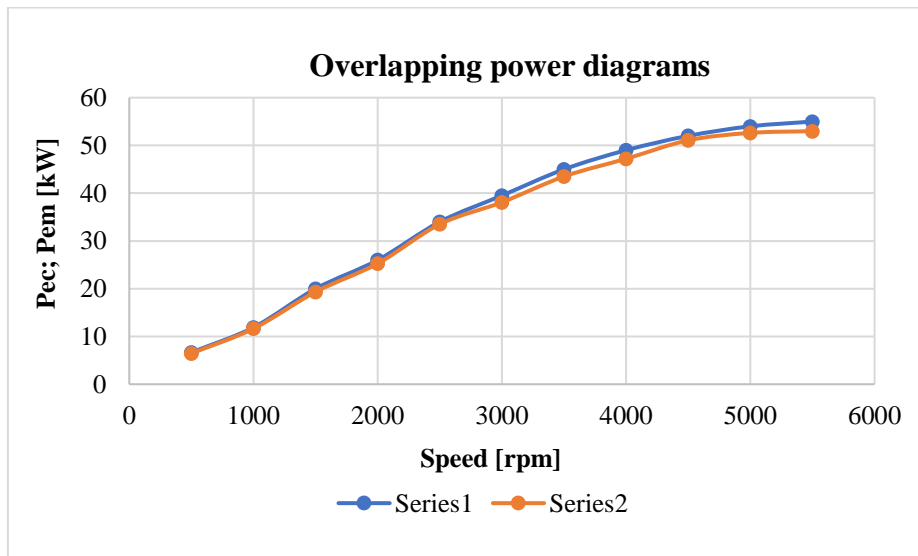


Fig. 23. Overlapping effective, calculated and measured power diagrams

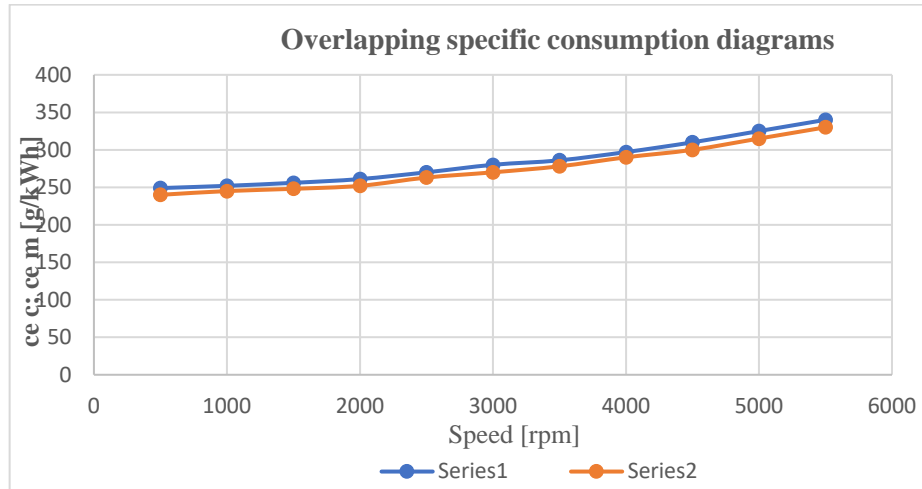


Fig. 24. Overlapping calculated and measured specific consumption diagrams

Conclusions

A model was proposed for a direct gasoline injection system, adopted on the given car. The technical data of the 1.6 l Logan car engine were introduced in Matlab.

Intake manifold pressure and inlet pressure were calculated taking into consideration two cases: when the density of the engine fresh charge is constant and the case, closer to reality, when the density of the fresh fluid is variable. The calculated parameters were determined using the relationships for the second case [1].

The calculation algorithm proposed by the authors to determine the parameters of the engine cycle is a part is auxiliary for the simulation of the gasoline injection [1].

The program for the calculus of the parameters of the spark ignition engine is structured in 10 procedures and functions. Some of the constants are declared as initial data at the beginning of the program. Other initial data were chosen from statistical data: $T_{ao}=322$ K; $T_{zo}=2530$ K; $T_{uo}=2660$ K; $k_{uo}=1.2$; $k_{do}=1.3$ and $k_{eo}=1.3$.

The variables are the temperatures between which the thermal process evolve. These temperatures depend on the adiabatic coefficients. The computational cycle runs until these coefficients become constant, the error being 0.000009. The cycle ends when the error for constant temperature T_a is below 1.5K.

The calculation algorithm consists of the following steps:

- 1) The initial relations T_{ao} , T_{zo} , T_{uo} and k_{co} , k_{vo} , k_{uo} , k_{do} , k_{eo} for a speed are taken as parameters.
- 2) The cycle is completed, resulting in new values for the coefficients k and temperatures T_a , T_z , T_u .
- 3) The differences are made between the old values and the new calculated values (Δk , ΔT).

4) If the differences (Δk , ΔT) are smaller than the imposed errors, then the new calculated values are valid and the cycle moves on to the next value of the speed and repeat points 1-4.

5) If the differences (Δk , ΔT) are above the imposed errors, then the cycle is followed by recalculating the values of the adiabatic coefficients and the temperatures, considering the new values as initial parameters. This re-run is performed until the differences (Δk , ΔT) fall below the imposed errors.

It should be noted that the program calculates the characteristic quantities of a thermodynamic cycle in general only by restricting the energy efficiency of combustion η_{ar} and the heat utilization coefficient in the combustion stage at constant volume ξ_o , which defines it as a powerful means of study.

Finally, comparing the injection time obtained with the program on the computer with the one determined on the engine stand, it can be seen that they are of almost identical values.

Table 2. Ratio of measured and calculated quantities from external engine characteristics

| n[rpm] | Mem/Mec | Pem/Pec | cec/cem |
|--------|---------|---------|---------|
| 500 | 2,9% | 3,01% | 3,62% |
| 1000 | 3,08% | 2,11% | 2,78% |
| 1500 | 2,4% | 3,3% | 3,13% |
| 2000 | 2,5% | 2,77% | 3,45% |
| 2500 | 2,74% | 3,3% | 2,6% |
| 3000 | 1,84% | 3,55% | 3,58% |
| 3500 | 2,2% | 3,34% | 2,8% |
| 4000 | 3,16% | 3,66% | 2,36% |
| 4500 | 2,89% | 1,79% | 3,23% |
| 5000 | 3,75% | 2,56% | 3,08% |
| 5500 | 2,57% | 3,66% | 2,95% |

From the table 2 results the differences between the calculated and the measured data are in the interval 1.79 -3,75 %.

The following conclusions can be drawn from the overlapping of the measured and calculated load diagrams of the total load, the errors found are within acceptable limits, especially since the engine under test was five years old. The values of the engine energy indices were totally higher in the case of their determination with the program presented above, compared to the sizes determined on the motor stand. The values of the actual specific fuel consumption, calculated with the help of the program, are totally lower than those measured on the engine stand. In conclusion, the presented calculation program can be adapted to any type of aspirated or supercharged engine, regardless of whether it is a spark-ignition engine or a compression-ignition engine, obtaining superior technical-economic indices.

References

1. Blaga V 2005 *Engines with Gasoline Injection* (Oradea: University of Oradea Publishing House)
2. Delanette M 1989 *Les Motors a Injection* (Edition Tehniques pour L'automobile et L'industrie)
3. Grunwald B 1980 *The Theory, the Calculus and the Constuction of the Engines for Road Vehicles* (Bucharest: Didactic and Pedagogical Publishing House)
4. Mitran T, Blaga V and Moca S 2017 *The Calculation Algorithm for the Determination of the Intake Stroke for GDI Engines* (Brasov: International Congress of Automotive and Transport Engineering) pp 311-318
5. Blaga V 2000 *Contributions to the Modelling of the Gasoline Injection at the SI Engines Cluj- Napoca: PhD Thesys*
6. Blaga V, Beles H, Dragomir G, Vlad I, Vlad M and Timar M 2009 *The Theoretical Contribution Modelling Gasoline Injection at Spark Lightening* (Viena: DAAM International Scientific Book) pp 43-58
7. Radcenko V 1977 *Criteria for the Optimization of the Thermal Processes* (Bucharest: Technical Publishing House)
8. Blaga V 2013 *Processes and Characteristics of the Internal Combustion Engines* (Oradea: University of Oradea Publishing House)
9. Blaga V, Bara L, Bara C, Bara V and Domuta C 2008 *The Experimental Stand of Engines with Gasoline Injection* (Viena: DAAM International Scientific Book) pp 109-110
10. V Blaga, T Mitran, A Rus, H Beles and G Dragomir *A comparative study of calculated and experimental indicated diagrams of a S.I. Engine* AITS 2021 (Chisinau: IOP Conf. Series: Materials Science and Engineering); 1220 (2022) 012016

The Impact of Bullbar Devices on Dynamics and Consequences Vehicle-Pedestrian Road Accidents

Ioan Ciobanu¹, Anghel Chiru¹ and Alexandru Ionuț Radu¹

¹ Transilvania University, Brașov 500024, Romania
ioan.ciobanu@unitbv.ro

Abstract. This article presents an analysis of the effect of installing a bullbar device on a vehicle involved in a vehicle-pedestrian accident. Emphasizing comparative analysis, this study evaluates the differences between accidents where vehicles had bullbars installed and those where they did not. The impact of bullbar devices on the dynamics and consequences of vehicle-pedestrian road accidents is a complex subject in road safety. This article will address aspects such as: assessing the risk of injury to pedestrians by highlighting the impact of bullbars on pedestrian injuries in road accidents and investigating how they influence impact dynamics and energy absorption in a vehicle-pedestrian crash. Software such as PC-Crash will be used for simulations to evaluate the structural behavior of bullbars in various impact scenarios. Road Safety Regulations will also be presented, analyzing how the use of bullbars affects vehicle compliance with road safety standards and regulations. Possible discrepancies or gaps in existing regulations can be identified, and modifications or updates can be proposed. The article will conclude by presenting the risks of pedestrians in the event of an impact with a vehicle equipped with a bullbar and also the severity of injuries caused to pedestrians depending on the speed of the impact.

Keywords: vehicle-pedestrian accident, bullbar, road safety, safety systems.

1 Introduction

Road traffic accidents involving vehicles and pedestrians represent a major public safety issue, with severe consequences on both human health and economic costs. Bullbars, devices mounted on the front of vehicles for protection in collisions, have sparked intense debate due to their impact on the dynamics of accidents and the severity of injuries incurred by pedestrians. This article explores the history, evolution, current uses, benefits and disadvantages of bullbars, as well as their effects on safety and the environment.

The aim of this study is to assess and analyze how the presence of bullbars on vehicles influences the nature and severity of road accidents involving pedestrians. The study seeks to provide an in-depth understanding of the physical interactions between bullbars and human victims during collisions, as well as to identify trends related to the types of injuries these devices cause.

The significance of this study arises from the increased need to balance the safety requirements of drivers with pedestrian protection in both urban and rural settings. While bullbars may offer additional protection for vehicles and their occupants against certain types of impacts, serious concerns exist regarding the heightened risk of severe or even fatal injuries to pedestrians in the event of an accident. Therefore, the outcomes of this study are crucial for developing effective policies and regulations that ensure a balance between various aspects of vehicular and pedestrian safety.

In addition to contributing to the academic literature and knowledge base, this study aims to inform policymakers and vehicle manufacturers about the potential effects of bullbars on pedestrian safety, encouraging the development of safer alternatives and innovative designs that minimize associated risks.

2 History and Evolution of Bullbars

2.1 The origin and original use of bullbars

Bullbars were initially developed in the early decades of the 20th century, primarily for use on military and off-road vehicles. The main purpose of these devices was to protect the front of the vehicle against collisions with large obstacles, such as tree trunks, rocks, and other solid objects on rugged terrains. The first bullbars were made of solid steel, featuring a simple yet robust construction, ensuring vehicle protection in challenging conditions. These devices proved extremely useful during World War I and World War II, when military vehicles needed to navigate inhospitable terrains. [1]

2.2 Development and diversification of bullbar design

As off-road vehicles gained popularity beyond military contexts in the 1950s and 1960s, bullbars began to be used on commercial and recreational vehicles. During this period, the design of bullbars evolved, and the materials used became more diverse. Steel remained the predominant material, but aluminum alloys and composite materials were introduced to reduce weight and enhance performance [1].

The 1980s and 1990s saw a significant rise in the popularity of off-road vehicles and SUVs, leading to even greater diversification in bullbar design. Manufacturers began to develop bullbars with aerodynamic shapes that better integrated with the overall design of the vehicle. Additionally, modular bullbars were introduced, allowing users to add or remove components according to specific needs, such as winch mounts or extra lights [2].

2.3 Current uses and types of vehicles equipped with bullbars

Today, bullbars are utilized on a wide range of vehicles, from SUVs and pickup trucks to commercial trucks and emergency vehicles. Current uses include:

- Off-road and recreational vehicles: Bullbars are essential for protecting vehicles operating in rough terrains, where collisions with natural obstacles are common.
- Commercial and delivery vehicles: Many trucks and vans are equipped with bullbars to protect the vehicle in low-speed collisions and to minimize damage in loading and unloading zones.

- Emergency vehicles: Ambulances, fire trucks, and police vehicles may be equipped with bullbars to facilitate rapid movement through obstacles and provide additional protection in critical situations.

- Rural vehicles: In areas where collisions with wildlife are frequent, bullbars provide extra protection against impacts with large animals such as deer, kangaroos, or elk.

Besides their functional uses, bullbars have also become an aesthetic accessory for many vehicle owners, who view them as a way to give their vehicle a robust and rugged appearance. This trend has contributed to the diversification and customization of bullbar designs, offering a variety of styles, colors, and finishes to meet individual user preferences.

3 Regulations and Standards Regarding Bullbars

3.1 International and local legislation relating to bullbars

The legislation regarding the use of bullbars varies considerably between different countries and regions. These regulations are designed to ensure that bullbars not only protect the vehicle but also minimize the risk of injury to pedestrians and cyclists.

European Union (EU)

Regulation (EC) No. 78/2009: This regulation sets requirements for the protection of pedestrians and other vulnerable road users in the event of collisions with vehicles equipped with bullbars. It includes specifications for the design of bullbars and the materials used to ensure that they absorb part of the impact energy [8].

Australia

Australian Design Rule (ADR) 42/04: This regulation establishes the requirements for all vehicles equipped with bullbars, including design specifications and impact absorption requirements. Australian regulations are among the strictest, due to the high frequency of collisions with large animals [9].

State Legislation Various Australian states have implemented additional regulations for bullbars, banning the use of certain types of bullbars in urban areas to protect pedestrians.

United States of America (USA).

Federal Motor Vehicle Safety Standards (FMVSS): Although there are no specific federal regulations for bullbars, the vehicle safety standards of the National Highway Traffic Safety Administration (NHTSA) include general requirements for pedestrian protection, which may influence bullbar designs [10].

3.2 Safety standards and impact tests

To ensure bullbars comply with safety regulations, they are subjected to rigorous impact tests and must meet certain standards:

Frontal Impact Tests evaluating the performance of bullbars in frontal collisions with a crash test dummy to measure the forces transmitted to it and assess the risk of injury. Testing the deformability of the bullbar to ensure it can absorb part of the impact energy, thus reducing the severity of injuries.

Low-Speed Impact Tests testing bullbars at lower speeds, which are typical for collisions in urban environments, to evaluate how they protect pedestrians and cyclists in such scenarios.

Material Analysis analyzing the materials used to manufacture bullbars to ensure they are sufficiently deformable and can absorb impact energy without breaking or causing additional injuries.

Regulation (EC) No. 78/2009: Requires that bullbars be made from energy-absorbing materials and pass rigorous impact tests. These regulations have led to the development of bullbars with advanced designs that reduce the risk of injury to pedestrians and cyclists [8].

ADR 42/04: Specifies requirements for bullbars, including that they must be mounted in such a way that they do not interfere with the operation of airbags and do not reduce the driver's visibility. Additionally, the regulations prohibit the use of protruding bullbars in urban areas.[9]

Regulations and standards concerning bullbars play a crucial role in ensuring the safety of all road users. By implementing strict regulations and rigorous impact tests, authorities can minimize the risks associated with the use of bullbars and promote the use of innovative and safe designs. It is essential that these regulations are applied consistently and updated as new technologies and materials become available.

4 The Impact of Bullbars on Pedestrian Safety

4.1 Risk analysis of vehicle-pedestrian collisions and pedestrian injury statistics

Bullbars are designed to protect vehicles during collisions with large obstacles; however, this protection can have serious consequences for pedestrian safety. Bullbars, particularly those made from rigid materials such as steel, are not engineered to effectively absorb shock in collisions involving pedestrians, thereby transferring the impact force directly to the human body. This can lead to severe injuries, such as fractures, cranial trauma, and internal injuries.

Multiple studies have investigated the impact of bullbars on the severity of injuries suffered by pedestrians. A study conducted by Ritchie and colleagues in 2007 demonstrated that pedestrians struck by vehicles equipped with bullbars are at an increased risk of fatal injuries compared to those hit by vehicles without bullbars [3]. Another study, conducted by Georgiades et al. in 2017, examined the risk of cranial trauma in collisions involving vehicles with bullbars. The findings indicated that pedestrians hit by vehicles with bullbars face a significantly higher risk of sustaining severe head injuries due to the rigidity and lack of shock absorption of the bullbar [4].

To better understand the impact of bullbars, a comparison with vehicles without these devices is useful. Modern vehicles are designed with crumple zones and other safety features intended to minimize injuries to pedestrians in collisions. These features include deformable hoods, front bumpers that absorb impact energy, and an overall design that reduces the risk of severe injuries.

4.2 Comparative analysis of vehicles with and without bullbar

In contrast, vehicles equipped with bullbars exhibit:

1. Increased rigidity: Bullbars, being made from hard materials, do not deform during an impact, leading to the direct transfer of force to the pedestrian.
2. Reduced contact surface: Bullbars often have a smaller contact area compared to the front of a vehicle without a bullbar, concentrating the impact force on a smaller area of the pedestrian's body, which can result in more severe injuries.
3. Lack of energy absorption: While modern vehicles are equipped with systems that absorb impact energy to protect pedestrians, bullbars lack this capability, increasing the risk of severe injuries.

Studies have shown that the likelihood of death and serious injuries significantly increases in collisions involving vehicles with bullbars. For example, research conducted by the University of Adelaide concluded that the risk of pedestrian death increases by up to four times in the event of a collision with a vehicle equipped with a bullbar, compared to one without a bullbar.

Pedestrian injuries are a major cause of death worldwide and account for 65 percent of the 1.2 million annual road traffic deaths [5]. The installation of rigid, aggressive bars for protection against wildlife or merely for aesthetic reasons has been highlighted as a cause for concern in many countries [5],[6]. It has been argued that these bars are essential safety elements that protect occupants in the event of such collisions; however, there has been much debate about their use in densely populated urban areas, where pedestrians are often the only victims they come into contact with [7].

5 Comparative simulations and results

5.1 Head Injury Criterion

HIC, or Head Injury Criterion, is a measure used to assess the likelihood of head injury arising from an impact. It is primarily used in the automotive industry to evaluate the safety performance of vehicles during crashes. HIC quantifies the risk of head injury by analyzing the acceleration experienced by the head during a collision and the duration of that acceleration. The formula for calculating HIC is based on the acceleration-time history recorded during a crash test, focusing on the most severe continuous period of acceleration.

Formula for HIC Calculation:

The average value \bar{a} of the acceleration $a(t)$ over the time interval t_1 to t_2 is given by:

$$\bar{a} = \frac{1}{t_2 - t_1} \int_{t_1}^{t_2} a(t) dt$$

For the HIC, this was modified (based on experimental data) as follows:

$$\text{HIC} = \max \left\{ (t_2 - t_1) \cdot \left[\frac{1}{t_2 - t_1} \int_{t_1}^{t_2} a(t) dt \right]^{2.5} \right\} \quad [15],[16]$$

where:

- t_1 and t_2 are the start and end times, respectively, of the worst impact duration in seconds,
- $a(t)$ is the acceleration at time, [15]

Usage: HIC is utilized in various safety testing scenarios, such as Automobile Crash Tests, Helmet Testing and Regulatory Compliance.

5.2 Variation head acceleration as a function of impact velocity

The comparative simulations were carried out with the help of the PC Crash program, choosing for the impact simulation a car frequently equipped with a bullbar, a Suzuki Grand Vitara shown in the image below.



Fig. 1. Suzuki Grand Vitara III [14]

The simulations are carried out with the same vehicle, from the same direction, under the same adhesion conditions, using the same pedestrian model to compare and present conclusions regarding the influence of the bullbar in the case of vehicle-pedestrian impact.

In the following we will analyze a pedestrian vehicle type impact. In the first situation the vehicle will not be equipped with bulbar, in the following it will be equipped with bulbar.

Pedestrian impact with a vehicle without bullbar

The dynamics of the impact of the pedestrian with the vehicle equipped without bullbar, according to the computer simulation carried out using the PC-Crash program for $V=20$ km/h, the braking sequence of the vehicle manifests itself from the moment of the impact with the pedestrian is presented in Figure 2.

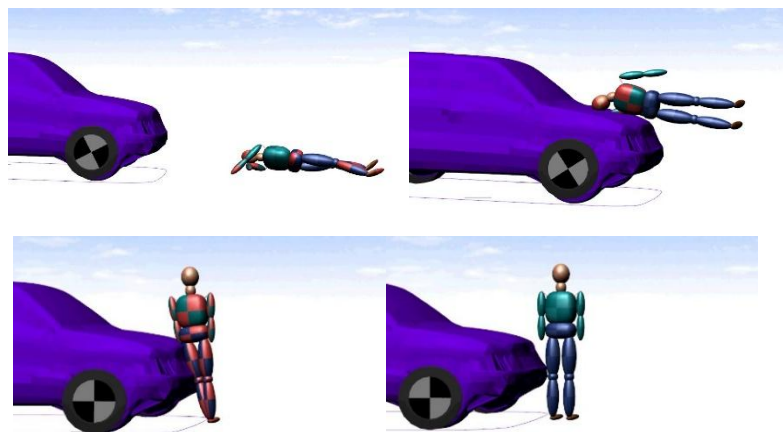


Fig. 2. The dynamics of the impact of the pedestrian with the vehicle without bullbar

The following graph shows head acceleration during simulated impact at 20 km/h without bullbar. It represents the acceleration in three axes: X, Y, and Z, as well as the resultant acceleration, which is the combined effect of the three components. The vertical axis (Y) represents acceleration in m/s^2 and the horizontal axis (X) represents time in seconds.

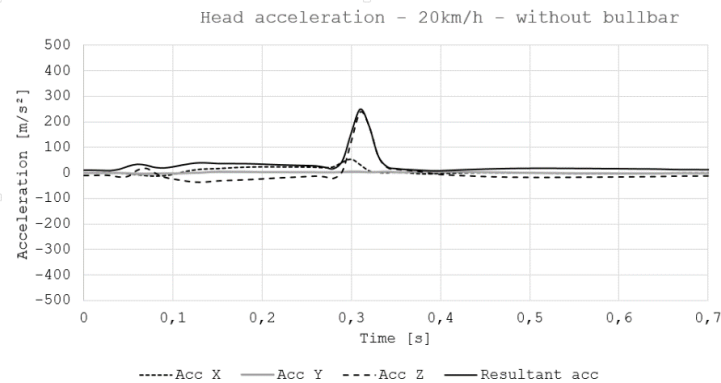


Fig. 3. The variation of the head acceleration during the impact time with a vehicle without bullbar, impact speed of 20 km/h

At about 0.3 seconds, there is a significant increase in acceleration values, with the resulting acceleration reaching nearly 250 m/s^2 . It marks the moment of impact, when the head experiences maximum force. Acc Y (solid line) appears to dominate, showing the highest values during impact, suggesting that most of the force is directed along the Y axis. Acc X (dashed line) and Acc Z (dotted line) show smaller contributions, indicating smaller acceleration forces in these directions. After the peak, the acceleration drops rapidly to near zero, suggesting that the head decelerates rapidly once the primary impact force has been absorbed.

The high peak acceleration, particularly along the Y-axis, suggests that this direction experiences the most significant impact force, which could lead to potential head injuries. The absence of other peaks implies that the impact is a single, sharp event without multiple collisions. The following graph shows head acceleration during an impact at a speed of 50 km/h without a bullbar.

Around 0.1 seconds, the resulting acceleration spikes to approximately 600 m/s^2 . This indicates the moment of the highest force applied to the head during the impact, with a sharp increase and rapid decline following the peak. Acc X (dashed line) and Acc Z (dotted line) show significant contributions to the resulting acceleration, indicating that the impact forces are more spread across these directions compared to the previous graph at 20 km/h. Acc Y (solid line) is slightly lower than Acc X and Acc Z but still plays a role in the overall impact.

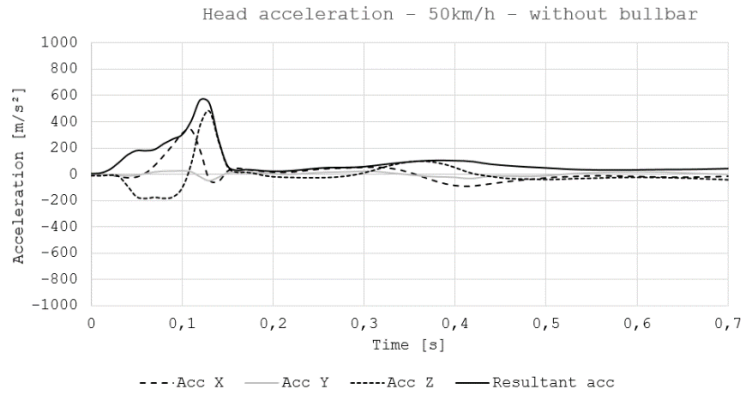


Fig. 4. The variation of the head acceleration during the impact time with a vehicle without bullbar, impact speed of 50 km/h

After the peak, the acceleration values in all directions return to near zero by around 0.2 seconds, suggesting that the primary force of impact is short-lived. However, there are some smaller fluctuations indicating minor movements after the initial impact.

The forces are more distributed across all three axes (X, Y, and Z), suggesting a more complex interaction during the collision compared to a lower-speed impact. The graph highlights the risk of severe head injuries due to the high accelerations encountered at this speed, even without a bullbar.

Pedestrian impact with a vehicle equipped with bullbar

For the simulations in PC-Crash, a metallic bullbar with a length of 0.710 m, a thickness of 0.147 m and a height of 0.461 m was used. The bullbar was mounted on the vehicle at a height of 0.371 m.

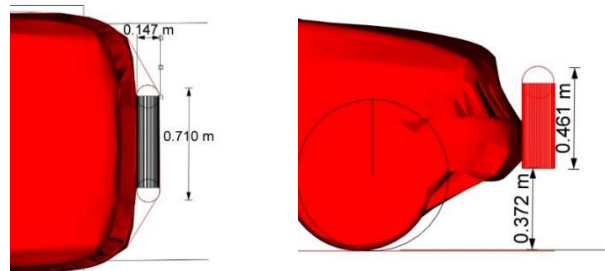


Fig. 5. Bullbar shape and dimensions

The dynamics of the impact of the pedestrian with the vehicle equipped with bullbar, according to the computer simulation carried out using the PC-Crash program for $V=20$ km/h, the braking sequence of the vehicle manifests itself from the moment of the impact with the pedestrian is presented in figure 5.2.8.

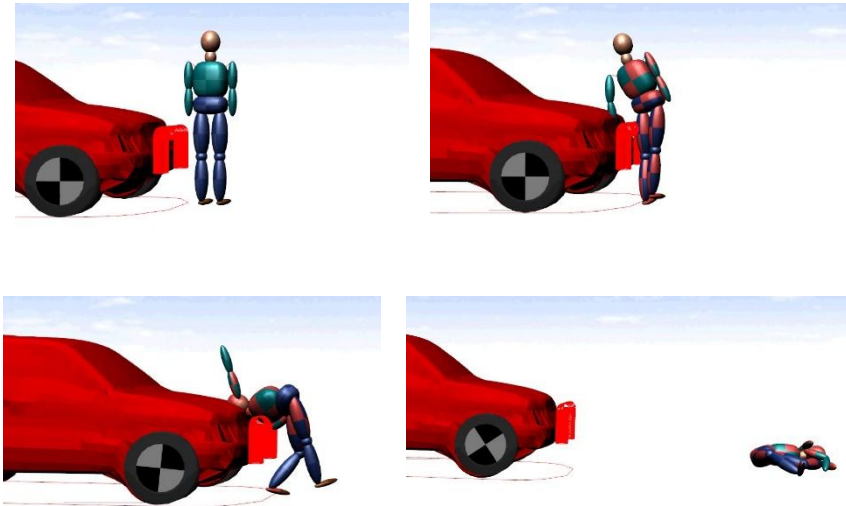


Fig. 6. The dynamics of the impact of the pedestrian with the vehicle vehicle equipped with bullbar

The following graph shows head acceleration during an impact at a speed of 20 km/h with bullbar installed on the vehicle.

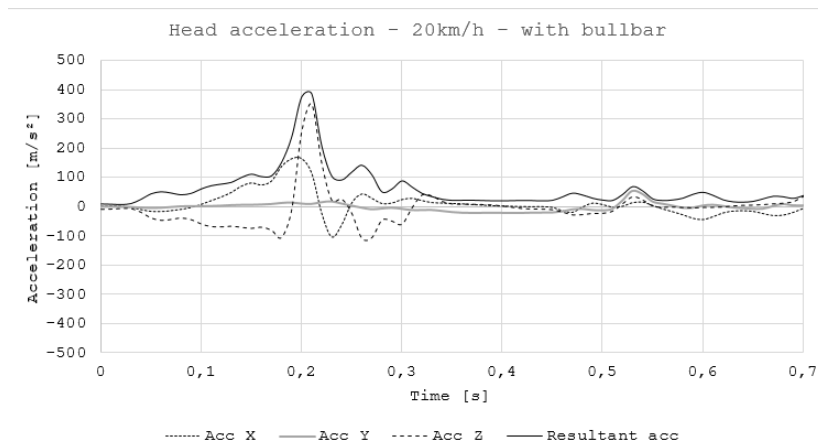


Fig. 7. The variation of the head acceleration during the impact time with a vehicle with bullbar installed on the vehicle, impact speed of 20 km/h

At about 0.2 seconds, the resulting acceleration reaches its highest value, peaking at about 400 m/s². This suggests a significant force applied to the head during impact caused by the presence of the bullbar. Acc Y (solid line) contributes the most to the resultant acceleration, meaning that the primary force acts along the Y axis. Acc X (dotted line) and Acc Z (dashed line) also show notable contributions, but remain smaller than the Y-axis values. There are secondary fluctuations after the initial spike, particularly on the Y and Z axes, indicating further interactions (such as possible head bouncing or secondary impacts).

After the main peak, the acceleration values do not immediately return to zero. Instead, there are smaller peaks and oscillations, indicating more complex dynamics in this scenario compared to the no-bullbar case. This could suggest that the bullbar causes additional impacts or prolongs the interaction during the collision.

The graph shows that the presence of a bullbar during a 20 km/h collision results in significantly higher head acceleration, indicating a higher risk of injury.

The following graph shows head acceleration during an impact at a speed of 50 km/h with bullbar installed on the vehicle.

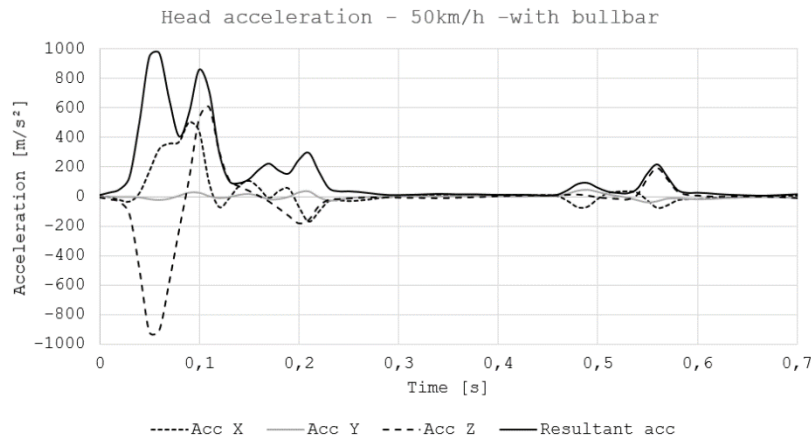


Fig. 8. The variation of the head acceleration during the impact time with a vehicle with bullbar installed on the vehicle, impact speed of 50 km/h

The resulting acceleration peaks very high early in the timeline, with the largest peak occurring around 0.05 to 0.1 seconds. This peak is close to 1000 m/s², indicating an extremely strong impact. Several smaller peaks are seen after the first major, suggesting that the head experiences a series of impacts or vibrations after the initial impact. Acc X (dashed line) and Acc Z (dotted line) both contribute significantly to acceleration, with Acc Z showing a sharp early negative peak followed by a rapid recovery. This suggests that the head could rotate or experience complex movement due to the collision. Acc Y (solid line) also shows significant values, but is somewhat less dominant compared to the other axes in this case. The forces in the X and Z directions are more

prominent. Fluctuations in the Z-axis (acceleration along the vertical axis) indicate potential bounces or lifts during impact.

After the initial impact, the accelerations gradually decrease, but exhibit smaller oscillations up to about 0.3 seconds. These oscillations may indicate residual motion as the head comes to rest, suggesting multiple contacts or a prolonged interaction during the collision.

Secondary spikes following the initial impact suggest that the bar is not causing just one impact, but rather a series of impacts or movements, potentially exacerbating the overall head injury. Significant forces along the X and Z axes indicate that the head may experience complex motion, such as rotation or jumping, during the collision. This suggests that the presence of a bullbar leads to more dynamic and unpredictable interactions during impact.

The graph demonstrates that at 50 km/h, the presence of a bullbar results in extremely high acceleration forces on the head, increasing the likelihood of serious head injuries.

6 Conclusion

Bullbars, while useful in protecting vehicles against collisions with large obstacles, pose significant risks to pedestrian safety. Bullbars made from hard materials transfer the impact force directly to pedestrians, leading to serious injuries and, in some cases, fatalities. Common injuries include cranial trauma, multiple fractures, and internal injuries due to the concentration of impact force on small areas of the body.

At the impact speed of 20 km/h a significant difference in peak of acceleration is observed. The presence of the bullbar results in a peak resultant acc that is approximately 1.6 times greater than without the bullbar. This indicates a significantly increased risk of head injury when a bullbar is used, even if the impact speed is only 20 km/h.

Peak acceleration in this scenario (with a bullbar) is significantly higher compared to a similar impact without a bullbar. The higher peak and more complex post-impact oscillations imply that the bar increases the severity of the collision for the pedestrian's head. Oscillations after the initial peak suggest that the bar may cause secondary impacts or alter the way the head interacts with the vehicle after the initial impact, resulting in multiple accelerations.

The bullbar changes the dynamics of impact, causing not only greater peak force, but also additional movement or impact after initial contact. This highlights the potential for increased injury severity when bars are present in pedestrian collisions.

An impact speed of 50 km/h results in a much higher initial resultant acc peak (about 1000 m/s²) compared to the no bullbar scenario (about 600 m/s²). This substantial increase highlights the increased crash severity due to the bullbar, which is counterproductive to pedestrian safety.

The resulting acceleration reaching almost 1000 m/s² shows an extremely high impact force, indicating a serious risk of head injury. This force is considerably greater than in the lower speed scenarios or no-bar impacts, highlighting the increased hazard when a bar is present at higher speeds. Multiple peaks and high acceleration values in

different directions (especially X and Z) indicate that the bar is exacerbating the dynamics of the impact, causing complex and potentially more damaging motions. This highlights the need for further research and improved design to reduce the risk of serious injury in such collisions.

Both graphs demonstrate that at 50 km/h the risk to pedestrians is considerably increased by using a bullbar. The increased severity and complexity of impacts can lead to a much greater chance of catastrophic injury.

Even at an impact speed of 50 km/h, in the case of the bullbar equipped vehicle, the severe acceleration values recorded indicate that the current designs are not to ensure the safety of pedestrians at higher speed impacts. This highlights the need for continued research, development and testing to create safer roll bar designs that better protect pedestrians without compromising the roll bar's effectiveness in protecting the vehicle and its occupants.

The analysis of the impact of bullbars on pedestrian safety clearly indicates that these devices can exacerbate the severity of injuries in vehicle-pedestrian collisions. While the bullbars protect the vehicle and its passengers in certain scenarios, it is essential that their design be reviewed and regulated to minimize risks to pedestrians. Vehicle manufacturers and regulatory authorities must collaborate to develop bullbars that balance vehicle protection with pedestrian safety, using deformable materials and innovative designs that absorb impact energy and reduce the severity of injuries.

References

1. R.M. Ogorkiewicz "Fighting Vehicle Design and Development", DOUBLEDAY (1968)
2. Gianpiero Mastinu și Manfred Ploechl „Off-Road Vehicle Dynamics", CRC Press; 1er edición (6 Enero 2014)
3. Ritchie, Euan G., et al. "The Performance of Vehicle Bullbars in Reducing Collision Damage to Wildlife." *Biological Conservation* 135.4, pp. 506-516 (2007)
4. Georgiades, Stelios, et al. "Effect of Bullbar Design on Pedestrian Head Trauma Risk in Vehicle Collisions." *Accident Analysis & Prevention* 103, pp. 50-57 (2017)
5. Peden M, Scurfield R, Sleet D, et al. *World Report on Road Traffic Injury Prevention*. Geneva, Switzerland: World Health Organization (2004)
6. Higgins T. Why do motorists fit bull bars? In: Griffiths MJ, Jones CJ, eds. *Proceedings of Bull Bar Safety Workshop*. Sydney, Australia: Road Safety Bureau, Roads and Traffic Authority NSW, pp.68-72 (1994)
7. Attewell R, Glase K. *Bull Bars and Road Trauma*. Canberra, Australia: Australian Transport Safety Bureau (2004) Report CR200.
8. European Parliament Council. Regulation (EC) No. 78/2009 of the European Parliament and of the Council of 14 January 2009 on the type approval of motor vehicles with regard to the protection of pedestrians and other vulnerable road users, amending Directive 2007/46/EC and repealing Directives 2003/102/E and 2005/66/EC (2009)
9. Australian Design Rule (ADR) 42/04
10. Federal Motor Vehicle Safety Standards (FMVSS)
11. Monash University Accident Research Centre. "Evaluation of Bullbars and Their Impact on Pedestrian Safety." MUARC Report No. 215 (2011)
12. European Transport Safety Council. "Bullbars and Road Safety." ETSC Report (2009)

13. Chapman, Simon. "Vehicle Bullbar Construction for Animal Collision Protection: A Review of Design Requirements, Fabrication Methods, and Material Performance." *Applied Sciences* 10.1 (2020)
14. <https://www.arb.com.au/suzuki-grand-vitara-2008-2011/bull-bars/>
15. McHenry, Brian G. *Head Injury Criteria and the ATB* (2004)
16. "Crash Tests and the Head Injury Criterion" (PDF). Archived from the original (PDF) on 2011-07-06. Retrieved 2009-11-03.
17. Anderson RWG, Doecke S, Van Den Berg AL, Searson DJ, Ponte G. *The Effect of Bull Bars on Head Impact Kinematics in Pedestrian Crashes*. Adelaide, South Australia: Centre for Automotive Safety Research (2009) Report CASR059
18. Anderson RWG, Ponte G, Doecke S. *A Survey of BullBar Prevalence at Pedestrian Crash Sites in Adelaide, South Australia*. Adelaide, South Australia: Centre for Automotive Safety Research (2008)
19. Bowd D. Impact of bull-bars on pedestrians. In: *Proceedings from the Inaugural International Conference on Accident Investigation, Reconstruction, Interpretation and the Law*. pp. 389–400 (October 16–19, 1995) IRRD 868526
20. Bowd D. Trends in fatalities associated with bull-bars, 1990–1992. Paper presented at: *International Conference on Accident Investigation, Reconstruction, Interpretation and the Law*; (September 22 1997); Brisbane, Queensland, Australia
21. Chiam HK, Tomas JA. *Investigation of the Effect of Bull Bars on Vehicle Pedestrian Collision Dynamics*. Canberra: Department of Transport Australia, Office of Road Safety (1980) Report CR13
22. Doecke SD, Anderson RWG, Ponte G. Bull bar prevalence among types of vehicles in metropolitan Adelaide. In: *Proceedings 2008 Australasian Road Safety Research, Policing and Education Conference*. Adelaide, Australia: Causal Productions (2008)
23. Kloeden CK, White K, McLean AJ. *Characteristics of Fatal and Severe Pedestrian Accidents in South Australia*. Adelaide, Australia
24. Kratzke S. *Regulatory History of Automatic Crash Protection in FMVSS 208*. Warrendale, Pa (1995) SAE Paper No. 950865
25. Peden M, Scurfield R, Sleet D, et al. *World Report on Road Traffic Injury Prevention*. Geneva, Switzerland: World Health Organization (2004)

Continuously Variable Planetary Transmission

Victor Sivu¹

¹Transilvania University of Brasov
victor.sivu@gmail.com

Abstract. The Continuously Variable Planetary Transmission (CVPT) invention has a continuous variation of the transmission ratio from the ratio of 2.5 to 0.4. It does not use friction elements, elastic traction elements. The CVPT consists of two planetary gears connected by a disk with a differential role, which makes possible the continuous variation of the ratio. The transmission ratio is achieved by varying the distance between the gearing areas and the imaginary axis of the differential disc. If at the input gear this size decreases, at the output gear the size increases. The power required to actuate the system to vary the transmission ratio is a maximum of 1% of the transferred power, it does not use hydraulic systems and high-pressure forces. The CVPT invention meets all the conditions for electric vehicle transmission. It has no power flow interruptions and has the ability to instantly transmit any level of power provided by the electric motor. The invention proposed (for which I hold an invention patent since 2023) contributes significantly to this process of reducing pollution by at least 12%-14%. In addition to this reduction, there is also the reduction obtained from the production process, where the consumption of materials and energy are much reduced compared to the solutions used now and pollution reduction can reach a threshold of at least 20%. The invention has no applicability limits only in the vehicle transmission systems, moreover, it has applicability in agriculture and in renewable energy systems (wind turbines). It can offer a wide range between the minimum and maximum transmission ratio.

Keywords: Gearbox, Continuously variable planetary transmission, Transmission ratio.

1 Introduction

Until this moment, all the cars produced use a gearbox to be able to adapt the power provided by the engine to the dynamic and traction needs of the cars. The only gearbox that comes close to the IDEAL gearbox is the CVT type. But no gearbox (mounted up to this moment on vehicles) doesn't fulfill the ideal theoretical conditions for transmission of traction force.

The desired of any propulsion system or generator are:

- Energetic efficiency;
- Compaction;
- Full automation capability at the lowest possible costs.

In the case of ICE engines (even EV ones), operating in energy efficiency

mode means keeping the engine within certain parameters, as can be seen in the optimal energy efficiency curve in Fig. 1.

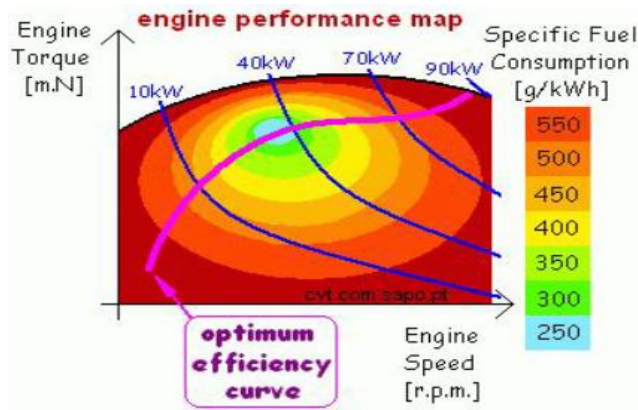


Fig. 1. Optimum efficiency curve

In Fig. 2 represents the energy efficiency point at a maximum load.

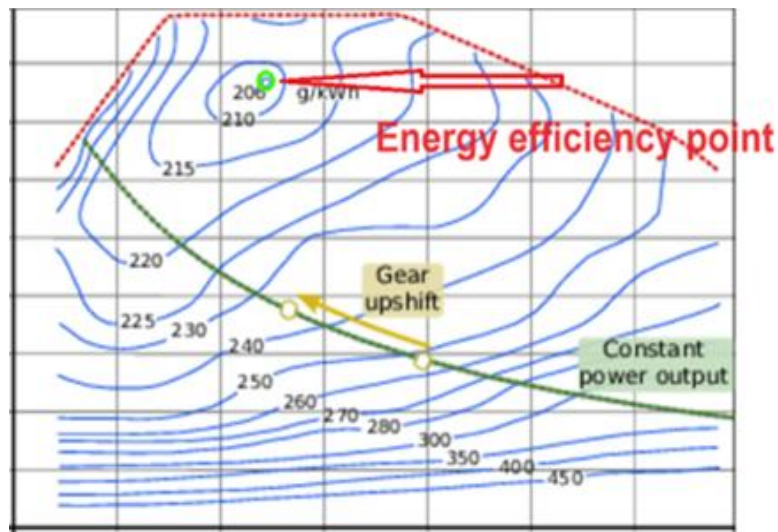


Fig. 2. Energy efficiency point

For the same reason, the established manufacturers are assiduously looking for solutions to make the systems more efficient, especially CVTs, because they are the transmission option nearest of ideal transmission for vehicles.

In Fig. 3, the positioning of the CVT system can be seen as the optimal option compared to all gearbox systems used up to this point in the industry.

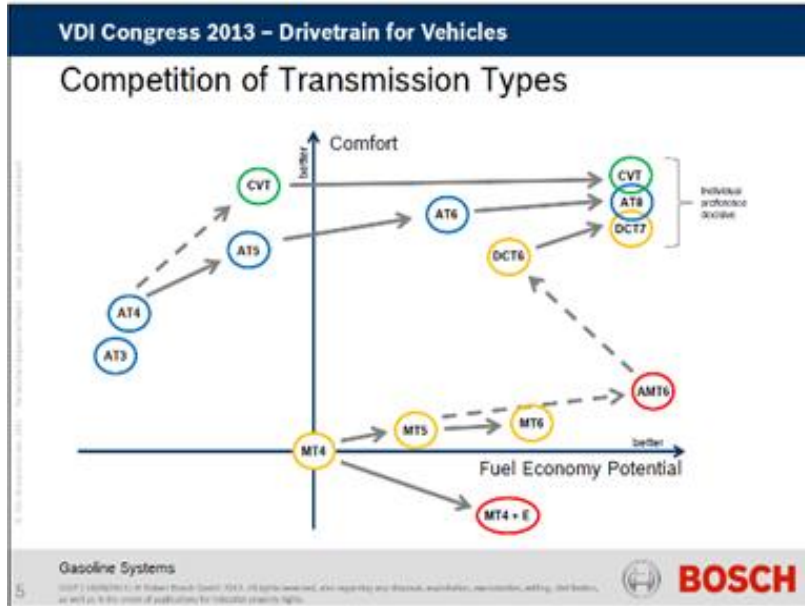


Fig. 3. transmission abilities: comfort - fuel economy

Fig. 4 illustrates the behavioral tendency of customers to opt for such CVT type gearboxes.

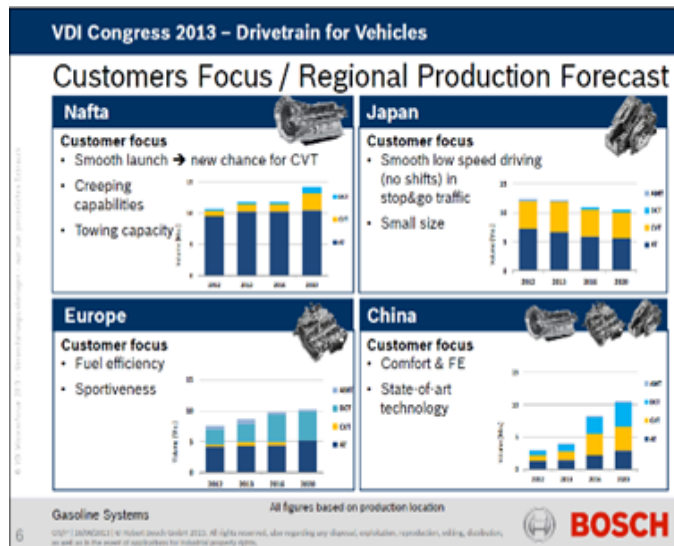


Fig. 4. Customer trends towards CVT gearboxes

Analyzing the products on the market, my invention is **the only solution that meets the ideal conditions for transmission of the traction force**, thus solving the current problems

In “The Innovation” Chapter you can see why my invention defeats all the models of gearboxes used now. My invention, the CVPT, achieves a reduction in fuel consumption of at least 12%.

In accordance with the global demands for a massive reduction in pollution as well as the tendency of consumers to purchase cars with a Continuously Variable Transmission type gearbox, it is the right time to market my invention, CVPT.

2. The proposed solution

My invention is “Unique-Smart-Simple” and combines all the advantages of manual and automatic gearboxes in steps, eliminating all their disadvantages:

- **UNIQUE:** worldwide, it is the only technical solution, and we hold a patent for it.
- **SMART:** realizes a continuous variation of the transmission ratio through 2 planetary groups.
- **SIMPLE:** low number mechanical parts, command simple system with low energy consumption.

In the polygonal diagram (Fig. 4), the main characteristics of the CVPT are presented with a yellow line. Also, the CVPT fulfills the ideal (theoretical) traction curve according to the graph in Fig. 5 and it is better mechanical solution.

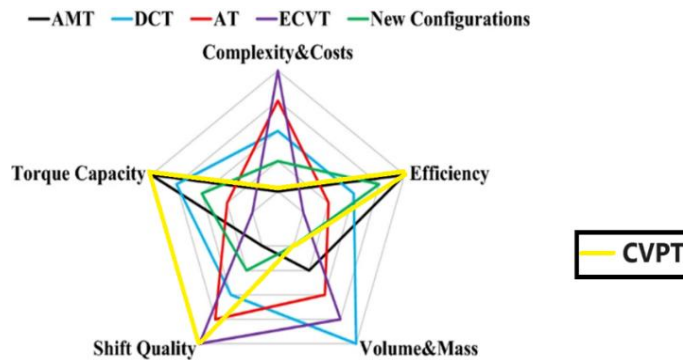


Fig. 4. Main characteristics of CVPT

The name Variable Planetary Transmission comes from the fact that the satellites are not permanently equidistant, the distance between them varies depending on the chosen transmission ratio. At the extreme values of the transmission ratio, the distance between the satellites also varies from a minimum to a possible maximum.

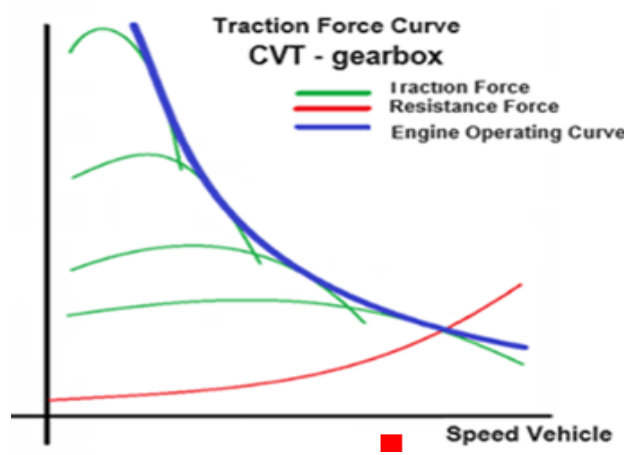


Fig. 5. Traction curve - CVT

The operating principle of the CVPT is: the traction force generated by the engine is transferred to the input planetary group (planetary group of shades in red colors). The satellites transfer the force to the central differential disc through their axes only in the gearing area of the crown.

In Fig 6 (a and b) the gear position is for starting the vehicle.

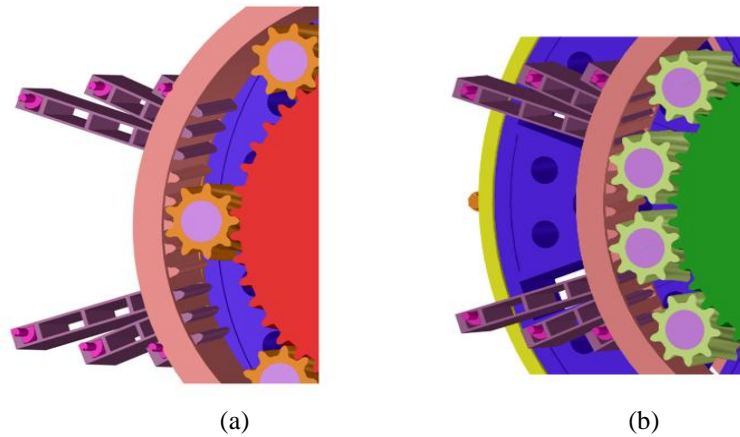


Fig. 6. (a) Input gear area; (b) Output gear area

Fig. 7 shows 3 main positions of the CVPT:

- Ration 2.5:1 is for the moment the vehicle starts moving.
- Ration 1:1 when the distances between the satellite axes are identical.
- Ration 0.4:1 when the vehicle can get maximum speed.

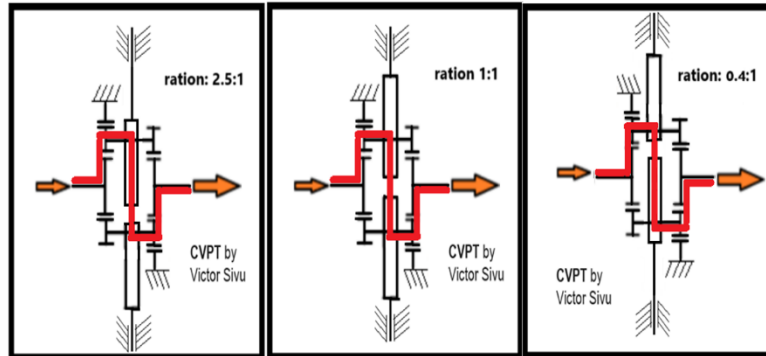


Fig. 7. Main positions of the CVPT

The mobile central disk (central differential disc) transfers the traction force to the satellites of the output planetary group (the planetary group in shades of green) through their axes only in the gearing area of the satellites of the output planetary group that is diametrically opposite towards input gearing area.

By moving the mobile central disc, a leverage ratio is created between the engagement position of the input satellites, the imaginary center of rotation of the mobile central disk and the respective engagement position of the output satellites (Fig. 8). It is exactly the principle of the seesaw presented in Fig. 9.

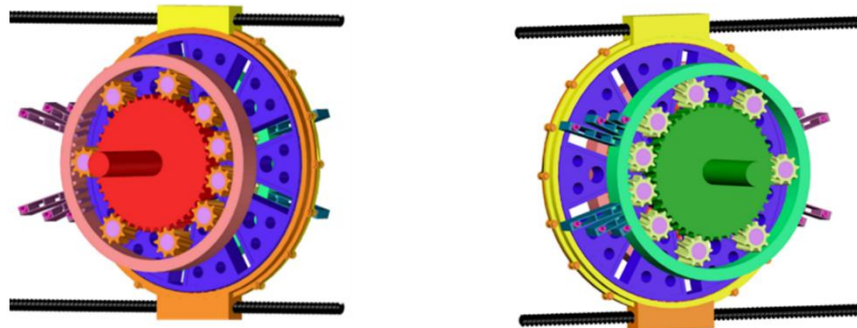


Fig. 8. The input and output planetary gears in the starting position of the vehicle

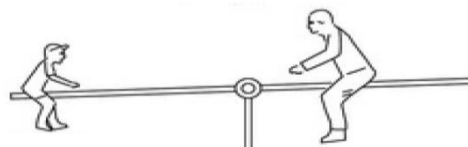


Fig. 9. Seesaw principle

3. Breakthrough potential

It is the only gearbox that can be successfully adapted to vehicles with electric propulsion systems.

In Fig. 10, my achievements at the laboratory prototype level can be seen, as well as some of my project promotion actions.

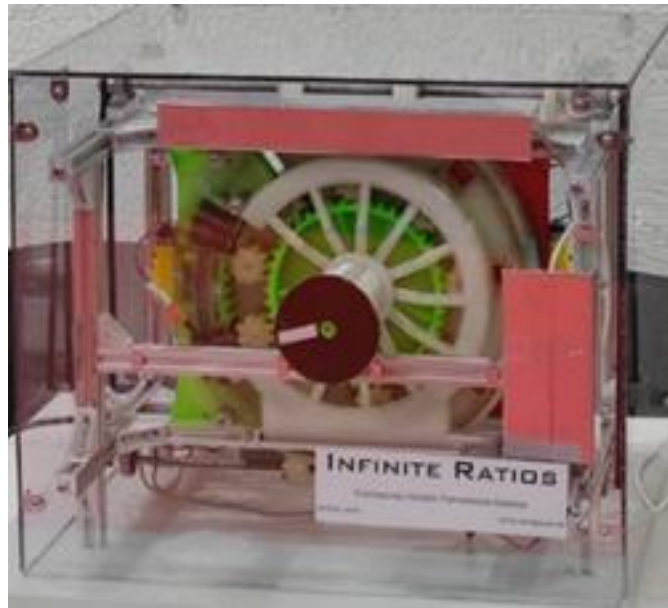


Fig. 10. Laboratory prototype of the CVPT

Following the laboratory studies (on the laboratory prototype) the advantages found are clearly superior, thus concluding:

- simpler like a manual gearbox.
- it does not present moments of interruption of the torque transfer.
- the transmission ratio variation is quite completely automated.
- it does not require a complex control module such as that of today's automatic and CVT gearboxes.
- It's so compact.
- behavior like a planetary mechanism, meaning simple mechanism.
- NO limits to transfer a high torque.
- rigid mechanism and structure.
- no friction surface or pulley-belt to transfer traction force.
- low production costs.
- low production time.
- the highest reliability in operation due to the constructive simplicity.
- minimal fuel consumption compared to other types of gearboxes (high performance/efficiency).

- increased safety in traffic by instantly reacting to the driver's commands.
- can be used on cars, SUVs, trucks, buses, even ships, wind power mechanical system and more.
- reducing fuel consumption, implicitly reducing pollution

The CVPT has a large range of changes in the transmission ratio, from multiplier to demultiplier, its ratio being symmetrical with respect to these two extremes.

For example: as a force multiplier it can start from the ratio of 2.5:1, go through 1:1 and reach a demultiplication ratio of 0.4:1

For a comparison with the best ATs used now (8 or 9 gears), please see the following table (as an example, I took the characteristic of the transfer ratios of the gearbox model 9G-Tronic from Mercedes Benz).

| | TR 1 | TR 2 | TR 3 | TR 4 | TR 5 | TR 6 | TR 7 | TR 8 | TR 9 |
|-------------|--------|--------|--------|--------|--------|--------|--------|--------|--------|
| 9G-Tronic | 5,5032 | 3,3333 | 2,3148 | 1,6611 | 1,2106 | 1,0000 | 0,8651 | 0,7167 | 0,6015 |
| CVPT | 2,5 | | | | | | | | 0,4 |
| CVPT+R | 5 | | | | | | | | 0,8 |
| CVPT + CVPT | 6,25 | | | | | | | | 0,16 |

Through a simple comparison of the kinematic sketches of a 9G-Tronic gearbox by Mercedes Benz and my invention (see Fig. 11), the minimalist degree of my invention can be seen.

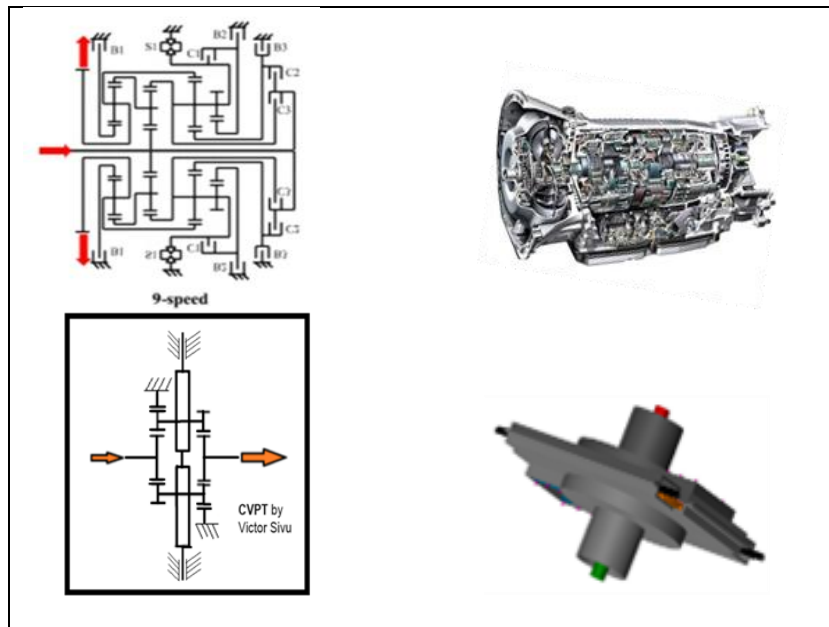


Fig. 11. 9G-Tronic gearbox vs CVPT

From a constructive point of view, the invention is a compact solution that can be adapted to any type of vehicle.

The degree of compaction is at least 40% more compact than an automatic gearbox and at least 20% more compact than a manual gearbox.

For special vehicles where a higher driving force multiplication ratio is needed, it is possible to successfully insert 2 or more CVPTs without imposing significant structural changes to them.

Even if the major direction of the investments is towards electrification, between the electric motor and the wheels we find a gearbox with at least one step or two.

Research in the field has shown that EVs also need a gearbox to create an efficient vehicle: smaller engine, smaller battery or greater range.

This can only be achieved in an EV with a CVT gearbox. Belt CVTs cannot transmit the high torques of electric motors, so it is not compatible with the operating regimes of an electric motor.

The only gearbox with continuous variation of the transmission ratio, without any big disadvantages, is my invention called CVPT and it is also perfectly compatible with the electric motor.

4. Market and Competition Market

My invention addresses a wide market in the field of motor vehicle production, the energy field and more, as follows:

1. Vehicles:
 - cars (annual production of at least 89 million units in 2022);
 - heavy trucks, light trucks (over 2 million heavy units and over 91.5 million light units sold annually);
 - buses, minibuses, trams, trolleybuses (more than 1 mil unit);
 - railway trains;
 - agricultural tractors (over 2 million units annually);
 - heavy and light construction equipment (over 1.5 million units produced annually)

In conclusion, we have a total of 187,140,000 units produced per one year.
2. Land trains.
3. Maritime: maritime vessels (all categories).
4. Energetic:
 - wind: first half 2023 is of 69.5GW installed power, means: around 140k units;
 - hydropower.
5. Industrial:
 - machine tools where a continuous variation of the transmission ratio is required: lathes, mills, etc. CVPT brings added value to machine tools through the simplicity and rapid automation of the transmission ratio.

The market I am addressing is made up of big car manufacturers as well as the manufacturers of transmission systems.

The major car manufacturers I deal with are: Stellantis Group (Peugeot, Citroen, Fiat, Opel, Fiat, s.a.), Volkswagen Group (VW, Audi, Skoda, Seat, s.a.), Ford, BMW and more.

The major manufacturers of transmission systems that I address are: ZF Transmission, Jatco (V-Belt), CVTCORP (toroidal transmission), Van Doorne's transmission (V-Belt), LuK Transmission (CVT through chain for AUDI), Xtronic CVT (Nissan – Renault: Push – belt), Aisin (AT – planetary gearbox).

Another large European manufacturer of auto components, Bosch AG, is doing in-depth studies to introduce CVT transmission systems on the market for vehicles with electric propulsion (with the Bosch CVT4EV study: Push Belt for EV).

As you can see, all examples of CVT are solutions that transfer engine torque through Frictional Force, solutions that are not viable for contemporary high-performance engines.

This means that the competitors and the market I am addressing are one and the same. Even so, I have no direct competitors, because my invention has a totally different operating principle from the solutions used.

The only thing I will have to do, to convince them, is to complete the CVPT study and its implementation, and here I mean the creation of a complete transmission system mounted on the vehicle. Upon completion of this study, I have all the elements to convince the car manufacturers as well as the transmission system manufacturers.

The advantages with which I convince clients to buy my CV over the suppliers of classic CVTs are and not only:

- The CVPT is a simple and rigid mechanical system.
- Compact construction,
- Smaller construction even than a manual gearbox.
- Engine torque transmission through rigid mechanical components: transfer is not made through friction surfaces and/or elastic elements.
- Transmission efficiency at the manual gearbox level
- 100% automation of CVPT
- It does not limit the value of the engine torque transmitted to the wheel.
- 100% integration on hybrid cars
- 100% integration and justification on EV cars
- Very easy adaptation to existing vehicle structures
- The possibility of customization for each car manufacturer by simply modifying the software.
- Easy creation of models for different ranges of motor torque required to be transmitted to the wheel.
- It does not negatively influence the dynamic behavior of the vehicle: being able to maintain the dynamic characteristic even in EV vehicles.
- CVPT production can be adapted to customer needs very easily due to the constructive simplicity of the system.

5. Broad impacts

They are major elements that impact the environment and society:

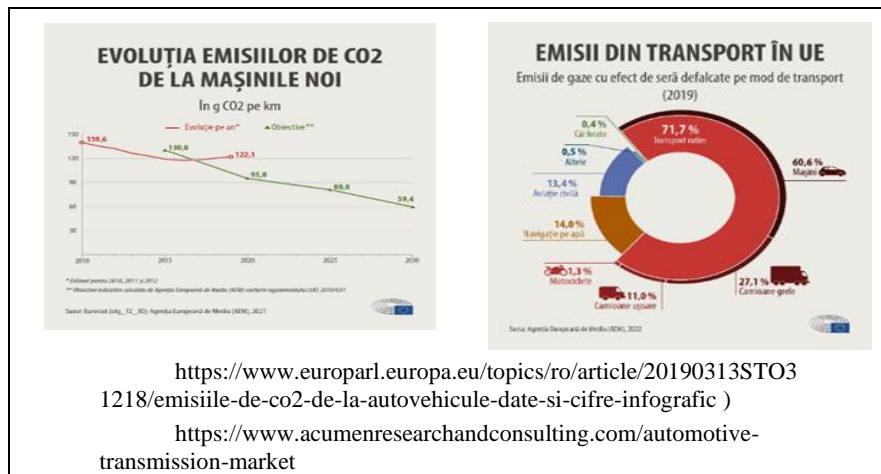
- Reduction of CO₂ emissions by using CVPTs on vehicles, determining their energy efficiency by at least 12%: (see the table below).
- CO₂ reduction through the production process: simple construction that requires short production time and simple production processes. Also, the non-use of non-ferrous materials (e.g.: multi-disc clutches from classic ATs): CO₂ emissions are at least 30% lower (production + use) than in the case of automatic gearboxes.
- 100% recyclable:
- Low amount of waste: it requires a reduced amount of lubricating oil (less than 60% compared to the automatic gearbox), as well as the time of use is equivalent to the lifetime of the vehicle.

From the first business period, I only consider the production of CVPTs for the automotive field.

The studies carried out by the major companies in the field highlight the trends in the automotive industry, and here I am referring to the increase in production of at least 15% until 2030 (a global increase of 21 million units produced compared to 2020) and a reduction in CO₂ emissions by minimum 50% until 2030.

By restricting the market only to European car production, where car production was 10,769,893 units in 2022 and considering the proposed target (of 0.1% in the first year of production), we have:

- 0.1% market share in the first year of production: represents production of 10,000 CVPT units
- minimum 0.4-0.6% in the 2nd year of production.
- minimum 1.0% in the 3rd year of production



In the following table we have a simple analysis of CO₂ reduction only by using CVPTs on vehicles, thus:

- The fuel reduction achieved by the CVT gearboxes is between 10% and 15% compared to the respective MT and AT.
- Considering the number of vehicles sold in the last 5 years and the trend of increasing demand for ATs (minimum 50% of ATs compared to MTs, I can consider, without having negative margin deviations, an efficiency of fuel consumption of at least 12% by using CVPT.
- We have considered a mileage of at least 15,000Km/year, we have the following CO₂ reduction over the next 5 years
- in 2019, the CO₂ production generated by new cars is 122.1g/km.
- using CVPT results in a reduction of at least 14.5g CO₂/km (12%):

Evaluating all aspects from production to a use of at least 10 years, it can be seen from the table above, the major positive impact in CO₂ reduction.

| Year | CVPT sale | Annually km | CO ₂ reduced [kg] |
|--------------|------------------|---------------------------|------------------------------|
| a | b | c | d |
| | | =15,000 * b | =c * 12 / 1000 |
| 1 | 100.000 | 1.500.000.000 | 18.000.000 |
| 2 | 200.000 | 3.000.000.000 | 36.000.000 |
| 3 | 300.000 | 4.500.000.000 | 54.000.000 |
| 4 | 400.000 | 6.000.000.000 | 72.000.000 |
| 5 | 500.000 | 7.500.000.000 | 90.000.000 |
| Total | 1.500.000 | 52.500.000.000 | 630.000.000 |
| | | =c1*5+c2*4+c3*3+c4*2+c5*1 | |

6. Conclusions

- The CVPT is a simple and rigid mechanical system.
- Compact construction.
- Smaller construction even than a manual gearbox.
- Engine torque transmission through rigid mechanical components: transfer is not made through friction surfaces and/or elastic elements.
- Transmission efficiency at the manual gearbox level.
- 100% automation of CVPT.
- It does not limit the value of the engine torque transmitted to the wheel.
- 100% integration on hybrid cars.
- 100% integration and justification on EV cars.
- Very easy adaptation to existing vehicle structures.
- The possibility of customization for each car manufacturer by simply modifying the software.

- Easy creation of models for different ranges of motor torque required to be transmitted to the wheel.
- It does not negatively influence the dynamic behavior of the vehicle: being able to maintain the dynamic characteristic even in EV vehicles.
- CVPT production can be adapted to customer needs very easily due to the constructive simplicity of the system.
- It does not present moments of interruption of the torque transfer.
- The transmission ratio variation is quite completely automated.
- It does not require a complex control module such as that of today's automatic and CVT gearboxes.
- Behavior like a planetary mechanism, meaning simple mechanism.
- NO limits to transfer a high torque.
- No friction surface or pulley-belt to transfer traction force.
- Low production costs.
- Low production time.
- The highest reliability in operation due to the constructive simplicity.
- Minimal fuel consumption compared to other types of gearboxes (high performance/efficiency).
- Increased safety in traffic by instantly reacting to the driver's commands.
- Can be used on cars, SUVs, trucks, buses, even ships, wind power mechanical system and more.
- Reducing fuel consumption, implicitly reducing pollution.

References

1. Transmisii Automate, Automatizate si Continue pentru Automobile – Autori: MACARIE Tiberiu Nicolae, VIERU Ionel, BĂDĂRĂU Șușter Helene, Editura: Editura PIM, Iași 2018.
2. Dinamica Autovehiculelor - Autori: Prof. Ing. C. GHIULAI, Prof. Dr. Ing. CH. VASILIU, Editura: Editura Didactică și Pedagogică Bucuresti, 1975; Subcap 4.2.2.1. Hiperbola de Tracțiune și transmisiile progresive, pag 167.
3. Calculul și Construcția Automobilelor - Autori: Prof Dr. Ing. Marin UNTARU, Prof. Dr. Ing. Nicolae SEITZ, Conf Dr. Ing. Ghorghie FRAȚILĂ, Conf Dr. Ing. Ghorghie poțincu, Conf Dr. Ing. Ghorghie PEREȘ . Editura Editura Didactică și Pedagogică Bucuresti, 1982; Cap 3.1.2. Clasificarea cutiilor de viteze, pag 105; Cap 3.4. Cutii de viteze mecanice cu variație continua a raportului de transmitere, pag 245
4. Construcția și Calculul Automobilelor - Autori: Prof Dr. Ing. Marin UNTARU, Conf. Dr. Ing. Vasile CAMPAN, Dr. Ing. Calin HILOHI, Ing. Victor VĂRZESCU. Editura: Editura Tehnica, 1974;; Cap 3.1. Bilanțul de tracțiune și de putere al automobilului, pag 56; Cap 9.3. Construcția și calculul cutiilor de viteze cu variație continua a raportului de transmitere, pag 221.
5. Dinamica Autovehiculelor pe Roți, Aplicații Numerice - Autori: Cristian ANDREESCU, Cornelia STAN, Ana-Maria MANEA. Editura: AGIR, 2022 Cap 3.1. Bilanțul de tracțiune și de putere al automobilului, pag 56; Cap 9.3. Construcția și calculul cutiilor de viteze cu variație continua a raportului de transmitere, pag 221.

6. Bosch Automotive: <https://www.bosch-mobility.com/en/solutions/transmission-technology/transmission-cvt4ev>
7. Bosch Automotive: <https://innovate-bosch.com/submit/supplier-innovations.html>
8. https://en.wikipedia.org/wiki/Mercedes-Benz_9G-Tronic_transmission
9. Capitol 4_Transmisii prin frictiune - Transmisii Mecanice.doc
10. Hybrid Transaxle Prius (eCVT)
11. Hybrid Planetary Gear, CVT
12. www.jatco.com
13. International VDI Congress “DriveTrain for Vehicles” – Schaeffler June 18, 2013
14. International VDI Congress “DriveTrain for Vehicles” – Bosch June 18, 2013
15. Progress in Automotive Transmission Technology: Xiangyang Xu^{1,2} · Peng Dong^{1,2} · Yanfang Liu^{1,2} · Hui Zhang^{1,2}; Automotive Innovation (2018) 1:187–210
<https://doi.org/10.1007/s42154-018-0031-Y>
16. Solving the Powertrain Puzzle: 10th Schaeffler Symposium April 3/4, 2014, SCHAEFFLER
17. A Review on Automobile Gear Transmission Mechanism, International Research Journal of Engineering and Technology, February 02, 2020

Analysis of Braking Force and Absolute Deceleration using Data Obtained from Measurements on the Brake Stand

Mădălin-Florin Popa¹, Bogdan-Manolin Jurchiș¹ and Nicolae Burnete¹

¹ Technical University of Cluj-Napoca, Department: Road Vehicles and Transports, B-dul Muncii street, No. 103-105, 400641, Cluj-Napoca, Romania
madalin.popa@live.com

Abstract. This study presents experimental results for braking on the roller brake stand but also presents a series of analytical calculations of some braking parameters based on the general equations of motion. Using the data obtained from the experimental bench tests, the main trends in the values of specific braking force and relative deceleration for commercial vehicles are obtained. The study combines measurements on the roller brake stand, with calculations based on equations from specialized works and aims to analyse the variation of these parameter values, when using real data of braking forces and weights on wheels and axles, all these forces taken from experimental tests on the roller brake stand.

Keywords: brake, roller brake stand test, deceleration, commercial vehicles.

1 Introduction

Currently, in the field of road transport of goods, there is a continuous pressure on the maximum efficiency of transport, with a minimum consumption of fuel, of energy or resources, but at the highest possible capacities and at the same time respecting the safety rules of traffic on public roads. In this regard, depending on the needs, different types of commercial vehicles are used. The analysis of the main parameters of the braking performance of these vehicles can go beyond the domain of classical mechanics, because there is a wide range of external influences on the braking system itself.

In the operation of motor vehicles, the analysis of the entire braking process [1 – 4], including both the mechanical system of the motor vehicle and the physiological reactions of the driver, can be divided into four groups of factors:

- calculations for mechanical braking (friction coefficients, mechanical resistances, materials, adhesion coefficients, production technologies, bench tests, measurements);
- calculations for dynamic parameters (decelerations, wheel/axle force distributions);
- analyses related to external factors such as: driver reaction times (physiological reactions) or road conditions, driving style, driving path;
- calculation algorithms for electronic driving and braking assistance systems.

In this sense, it is possible to carry out: experimental analysis, analytical calculations, or simulations, to include the widest possible range of aspects related to the entire braking process.

2 Experimental determinations on the roller brake stand

2.1 Tests on the brake stand

In the current study, roller brake bench tests were performed on a total of 70 commercial vehicles. Then the obtained data were entered into calculation formulas to highlight their variations and trends according to the vehicles in the study.

The performance analysis on the brake stand highlights the trends in the distribution of obtained braking force at each wheel/axle, depending on the constructive parameters of the analysed vehicle and the test conditions.

The brake stand used, allowed the identification of an important number of parameters as shown in the report in figure 1, (where: A are stand identification data; B – vehicle input data; C – stand identifier; D – number of axles and type of the tested brake system; E – data measured and generated by the stand).

| <p style="text-align: center;">Camion</p> <p>Nume/Co.: Strada: Cod postal, oras Telefon: Data: 03/04/2024 Ora: 10:36</p> <p style="text-align: right;">A</p> | <p style="text-align: center;">Camion</p> <p>Nr. inmatriculare: S. .V Kilometri: 284800 Inreg.init: Producator vehicul: MB Tip vehicul: cap tractor Nr. Sasiu Veh. WDB96340310 Numar axe: 2</p> <p style="text-align: right;">B</p> | <p style="text-align: center;">EUROSYSTEM LKW V 3.15.036</p> <p style="font-size: 2em; font-weight: bold; text-align: left;">C</p> | | | | | | | | | | | | | | | | | | | | | | | | | | | | | | | | | | | | | | | | | | | | | | | | | | | | | | | | | | | | | | | | | | | | | | | | | | | | | | | | | | | | | | | | | | | | | | | | | | | | | | | | | |
|---|---|--|-----------|--------------|--------------|-------------------|---------|---------|--|--|-----------------------|----------|----------|----------|-----|------------------------|-------|-------|--|--|------------|--------|--------|--------|-----|-----------------------|--------|--------|--------|-----|------------------------|--------|--------|--------|-----|---------------------------|--|--|--|--|-------------|--------|---------|-----------|--------------|----------------|------|------|------|-----|-----------------|------|------|------|-----|-----------------|------|------|------|-----|--------------|------|--|--|--|----|--------|--|--|----------|----|--------|--|--|--|--|--|--|--------|---------|-----------|--------------|-------------------|---------|---------|--|--|-----------------------|---------|---------|----------|-----|------------------------|-------|-------|--|--|------------|--------|--------|--------|------|-----------------------|--|--|--|--|
| MAHA-TEST FRINA | | | | | | | | | | | | | | | | | | | | | | | | | | | | | | | | | | | | | | | | | | | | | | | | | | | | | | | | | | | | | | | | | | | | | | | | | | | | | | | | | | | | | | | | | | | | | | | | | | | | | | | | | | | |
| Test frina cap tractor | | | | | | | | | | | | | | | | | | | | | | | | | | | | | | | | | | | | | | | | | | | | | | | | | | | | | | | | | | | | | | | | | | | | | | | | | | | | | | | | | | | | | | | | | | | | | | | | | | | | | | | | | | | |
| <p style="font-weight: bold; font-size: 1.1em;">1. Axa Frina de serviciu</p> <table border="1" style="width: 100%; border-collapse: collapse;"> <thead> <tr> <th></th> <th style="text-align: center;">Stinga</th> <th style="text-align: center;">Dreapta</th> <th style="text-align: center;">Axa total</th> <th style="text-align: center;">Dezechilibru</th> </tr> </thead> <tbody> <tr> <td>Forța de frinare:</td> <td style="text-align: center;">0.51 kN</td> <td style="text-align: center;">0.57 kN</td> <td></td> <td></td> </tr> <tr> <td>Rezistența la rulare:</td> <td style="text-align: center;">17.53 kN</td> <td style="text-align: center;">17.10 kN</td> <td style="text-align: center;">34.63 kN</td> <td style="text-align: center;">2 %</td> </tr> <tr> <td>Max. Forța de frinare:</td> <td style="text-align: center;">-- kN</td> <td style="text-align: center;">-- kN</td> <td></td> <td></td> </tr> <tr> <td>Ovalitate:</td> <td style="text-align: center;">2.51 t</td> <td style="text-align: center;">2.38 t</td> <td style="text-align: center;">4.89 t</td> <td style="text-align: center;">5 %</td> </tr> <tr> <td>Greutate axa statica:</td> <td style="text-align: center;">2.67 t</td> <td style="text-align: center;">2.67 t</td> <td style="text-align: center;">5.34 t</td> <td style="text-align: center;">0 %</td> </tr> <tr> <td>Greutate dinamica axa:</td> <td style="text-align: center;">2.67 t</td> <td style="text-align: center;">2.68 t</td> <td style="text-align: center;">5.34 t</td> <td style="text-align: center;">0 %</td> </tr> <tr> <td>Greutate dinamica max.axa</td> <td></td> <td></td> <td></td> <td></td> </tr> <tr> <td>Eficacitate</td> <td style="text-align: center;">Stinga</td> <td style="text-align: center;">Dreapta</td> <td style="text-align: center;">Axa total</td> <td style="text-align: center;">Dezechilibru</td> </tr> <tr> <td>Efic. statica:</td> <td style="text-align: center;">71 %</td> <td style="text-align: center;">73 %</td> <td style="text-align: center;">72 %</td> <td style="text-align: center;">3 %</td> </tr> <tr> <td>Efic. dinamica:</td> <td style="text-align: center;">67 %</td> <td style="text-align: center;">65 %</td> <td style="text-align: center;">66 %</td> <td style="text-align: center;">3 %</td> </tr> <tr> <td>Efic. din. max:</td> <td style="text-align: center;">67 %</td> <td style="text-align: center;">65 %</td> <td style="text-align: center;">66 %</td> <td style="text-align: center;">3 %</td> </tr> <tr> <td>Forța pedala</td> <td style="text-align: center;">-- N</td> <td></td> <td></td> <td></td> </tr> <tr> <td>Pm</td> <td style="text-align: center;">-- bar</td> <td></td> <td></td> <td style="text-align: center;">E</td> </tr> <tr> <td>Px</td> <td style="text-align: center;">-- bar</td> <td></td> <td></td> <td></td> </tr> </tbody> </table> | | Stinga | Dreapta | Axa total | Dezechilibru | Forța de frinare: | 0.51 kN | 0.57 kN | | | Rezistența la rulare: | 17.53 kN | 17.10 kN | 34.63 kN | 2 % | Max. Forța de frinare: | -- kN | -- kN | | | Ovalitate: | 2.51 t | 2.38 t | 4.89 t | 5 % | Greutate axa statica: | 2.67 t | 2.67 t | 5.34 t | 0 % | Greutate dinamica axa: | 2.67 t | 2.68 t | 5.34 t | 0 % | Greutate dinamica max.axa | | | | | Eficacitate | Stinga | Dreapta | Axa total | Dezechilibru | Efic. statica: | 71 % | 73 % | 72 % | 3 % | Efic. dinamica: | 67 % | 65 % | 66 % | 3 % | Efic. din. max: | 67 % | 65 % | 66 % | 3 % | Forța pedala | -- N | | | | Pm | -- bar | | | E | Px | -- bar | | | | <p style="font-weight: bold; font-size: 1.1em;">2. Axa Frina de serviciu</p> <table border="1" style="width: 100%; border-collapse: collapse;"> <thead> <tr> <th></th> <th style="text-align: center;">Stinga</th> <th style="text-align: center;">Dreapta</th> <th style="text-align: center;">Axa total</th> <th style="text-align: center;">Dezechilibru</th> </tr> </thead> <tbody> <tr> <td>Forța de frinare:</td> <td style="text-align: center;">0.38 kN</td> <td style="text-align: center;">0.26 kN</td> <td></td> <td></td> </tr> <tr> <td>Rezistența la rulare:</td> <td style="text-align: center;">7.54 kN</td> <td style="text-align: center;">7.64 kN</td> <td style="text-align: center;">15.18 kN</td> <td style="text-align: center;">1 %</td> </tr> <tr> <td>Max. Forța de frinare:</td> <td style="text-align: center;">-- kN</td> <td style="text-align: center;">-- kN</td> <td></td> <td></td> </tr> <tr> <td>Ovalitate:</td> <td style="text-align: center;">1.19 t</td> <td style="text-align: center;">1.02 t</td> <td style="text-align: center;">2.21 t</td> <td style="text-align: center;">14 %</td> </tr> <tr> <td>Greutate axa statica:</td> <td></td> <td></td> <td></td> <td></td> </tr> </tbody> </table> | | | Stinga | Dreapta | Axa total | Dezechilibru | Forța de frinare: | 0.38 kN | 0.26 kN | | | Rezistența la rulare: | 7.54 kN | 7.64 kN | 15.18 kN | 1 % | Max. Forța de frinare: | -- kN | -- kN | | | Ovalitate: | 1.19 t | 1.02 t | 2.21 t | 14 % | Greutate axa statica: | | | | |
| | Stinga | Dreapta | Axa total | Dezechilibru | | | | | | | | | | | | | | | | | | | | | | | | | | | | | | | | | | | | | | | | | | | | | | | | | | | | | | | | | | | | | | | | | | | | | | | | | | | | | | | | | | | | | | | | | | | | | | | | | | | | | | | |
| Forța de frinare: | 0.51 kN | 0.57 kN | | | | | | | | | | | | | | | | | | | | | | | | | | | | | | | | | | | | | | | | | | | | | | | | | | | | | | | | | | | | | | | | | | | | | | | | | | | | | | | | | | | | | | | | | | | | | | | | | | | | | | | | | |
| Rezistența la rulare: | 17.53 kN | 17.10 kN | 34.63 kN | 2 % | | | | | | | | | | | | | | | | | | | | | | | | | | | | | | | | | | | | | | | | | | | | | | | | | | | | | | | | | | | | | | | | | | | | | | | | | | | | | | | | | | | | | | | | | | | | | | | | | | | | | | | |
| Max. Forța de frinare: | -- kN | -- kN | | | | | | | | | | | | | | | | | | | | | | | | | | | | | | | | | | | | | | | | | | | | | | | | | | | | | | | | | | | | | | | | | | | | | | | | | | | | | | | | | | | | | | | | | | | | | | | | | | | | | | | | | |
| Ovalitate: | 2.51 t | 2.38 t | 4.89 t | 5 % | | | | | | | | | | | | | | | | | | | | | | | | | | | | | | | | | | | | | | | | | | | | | | | | | | | | | | | | | | | | | | | | | | | | | | | | | | | | | | | | | | | | | | | | | | | | | | | | | | | | | | | |
| Greutate axa statica: | 2.67 t | 2.67 t | 5.34 t | 0 % | | | | | | | | | | | | | | | | | | | | | | | | | | | | | | | | | | | | | | | | | | | | | | | | | | | | | | | | | | | | | | | | | | | | | | | | | | | | | | | | | | | | | | | | | | | | | | | | | | | | | | | |
| Greutate dinamica axa: | 2.67 t | 2.68 t | 5.34 t | 0 % | | | | | | | | | | | | | | | | | | | | | | | | | | | | | | | | | | | | | | | | | | | | | | | | | | | | | | | | | | | | | | | | | | | | | | | | | | | | | | | | | | | | | | | | | | | | | | | | | | | | | | | |
| Greutate dinamica max.axa | | | | | | | | | | | | | | | | | | | | | | | | | | | | | | | | | | | | | | | | | | | | | | | | | | | | | | | | | | | | | | | | | | | | | | | | | | | | | | | | | | | | | | | | | | | | | | | | | | | | | | | | | | | |
| Eficacitate | Stinga | Dreapta | Axa total | Dezechilibru | | | | | | | | | | | | | | | | | | | | | | | | | | | | | | | | | | | | | | | | | | | | | | | | | | | | | | | | | | | | | | | | | | | | | | | | | | | | | | | | | | | | | | | | | | | | | | | | | | | | | | | |
| Efic. statica: | 71 % | 73 % | 72 % | 3 % | | | | | | | | | | | | | | | | | | | | | | | | | | | | | | | | | | | | | | | | | | | | | | | | | | | | | | | | | | | | | | | | | | | | | | | | | | | | | | | | | | | | | | | | | | | | | | | | | | | | | | | |
| Efic. dinamica: | 67 % | 65 % | 66 % | 3 % | | | | | | | | | | | | | | | | | | | | | | | | | | | | | | | | | | | | | | | | | | | | | | | | | | | | | | | | | | | | | | | | | | | | | | | | | | | | | | | | | | | | | | | | | | | | | | | | | | | | | | | |
| Efic. din. max: | 67 % | 65 % | 66 % | 3 % | | | | | | | | | | | | | | | | | | | | | | | | | | | | | | | | | | | | | | | | | | | | | | | | | | | | | | | | | | | | | | | | | | | | | | | | | | | | | | | | | | | | | | | | | | | | | | | | | | | | | | | |
| Forța pedala | -- N | | | | | | | | | | | | | | | | | | | | | | | | | | | | | | | | | | | | | | | | | | | | | | | | | | | | | | | | | | | | | | | | | | | | | | | | | | | | | | | | | | | | | | | | | | | | | | | | | | | | | | | | | | |
| Pm | -- bar | | | E | | | | | | | | | | | | | | | | | | | | | | | | | | | | | | | | | | | | | | | | | | | | | | | | | | | | | | | | | | | | | | | | | | | | | | | | | | | | | | | | | | | | | | | | | | | | | | | | | | | | | | | |
| Px | -- bar | | | | | | | | | | | | | | | | | | | | | | | | | | | | | | | | | | | | | | | | | | | | | | | | | | | | | | | | | | | | | | | | | | | | | | | | | | | | | | | | | | | | | | | | | | | | | | | | | | | | | | | | | | |
| | Stinga | Dreapta | Axa total | Dezechilibru | | | | | | | | | | | | | | | | | | | | | | | | | | | | | | | | | | | | | | | | | | | | | | | | | | | | | | | | | | | | | | | | | | | | | | | | | | | | | | | | | | | | | | | | | | | | | | | | | | | | | | | |
| Forța de frinare: | 0.38 kN | 0.26 kN | | | | | | | | | | | | | | | | | | | | | | | | | | | | | | | | | | | | | | | | | | | | | | | | | | | | | | | | | | | | | | | | | | | | | | | | | | | | | | | | | | | | | | | | | | | | | | | | | | | | | | | | | |
| Rezistența la rulare: | 7.54 kN | 7.64 kN | 15.18 kN | 1 % | | | | | | | | | | | | | | | | | | | | | | | | | | | | | | | | | | | | | | | | | | | | | | | | | | | | | | | | | | | | | | | | | | | | | | | | | | | | | | | | | | | | | | | | | | | | | | | | | | | | | | | |
| Max. Forța de frinare: | -- kN | -- kN | | | | | | | | | | | | | | | | | | | | | | | | | | | | | | | | | | | | | | | | | | | | | | | | | | | | | | | | | | | | | | | | | | | | | | | | | | | | | | | | | | | | | | | | | | | | | | | | | | | | | | | | | |
| Ovalitate: | 1.19 t | 1.02 t | 2.21 t | 14 % | | | | | | | | | | | | | | | | | | | | | | | | | | | | | | | | | | | | | | | | | | | | | | | | | | | | | | | | | | | | | | | | | | | | | | | | | | | | | | | | | | | | | | | | | | | | | | | | | | | | | | | |
| Greutate axa statica: | | | | | | | | | | | | | | | | | | | | | | | | | | | | | | | | | | | | | | | | | | | | | | | | | | | | | | | | | | | | | | | | | | | | | | | | | | | | | | | | | | | | | | | | | | | | | | | | | | | | | | | | | | | |

Fig. 1. Braking report sheet on the brake stand for a truck



Fig. 2. Vehicle on the stand (from the category light commercial vehicles)



Fig. 3. Heavy commercial vehicle on stand test (Truck category)

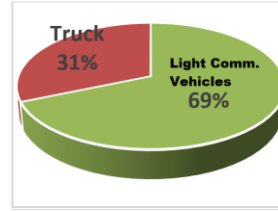


Fig. 4. Distribution of vehicles in the experimental study

The commercial vehicles used in the study were grouped into two categories. Figure 2 shows the testing on the stand of a light commercial vehicle, from the category of those with a maximum authorized mass of up to 5 tons (*light commercial vehicles*) and figure 3 shows the testing of a semi-trailer truck (from the *Truck* category). Figure 4 shows the distribution of vehicles in the study.

2.2 Obtained results

The distribution of the values obtained for the maximum braking force, represented a first step in the data analysis. The maximum braking values (per axle) obtained for the service brake and for the parking brake (see Fig. 5) were between 8 ... 109 kN for the service brake (FS) and between 3,5 ... 73 kN for the parking brake (FP). The value of the measured force increases proportionally with the increase in the vehicle load, which is why the division into two categories was made.

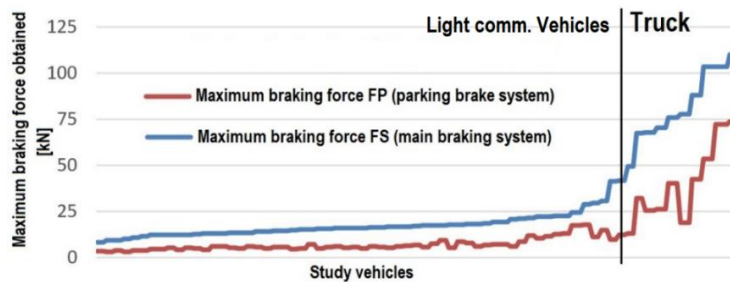


Fig. 5. Values of the braking force (per axle) for the service brake and for the parking brake (for all vehicles in the study)

On the brake stand, a series of differences in the application of braking forces on the wheels/axles were also observed. These differences are shown in figures 6 – 8 and are very important in the occurrence and evolution of uneven wear in the braking system.

It was observed that equal values of the forces, measured at the wheels of the same axle, are very difficult to obtain and small values of the left-right difference are quite reduced. However, the force values differ within certain limits, and the highest frequency are differences in the range of 0,1 ... 0,5 kN, (caused by uneven wear or different

force distributions on the wheels and axles [5 – 7]) which they do not create problems in operation, being differences that can be corrected in operation.

Cases in which the difference is greater than 0.5 kN, also have a significant weight, representing 38,5% of cases. These situations require extra attention because they can cause damage to the elements in the braking system [5 – 7].

The identified differences were divided into three categories, according to importance (see Fig. 6). The first category includes the smallest differences (up to 0.1 kN), which can be neglected (these cases have a share of up to 20% for light commercial vehicles and 30% on trucks). The middle category includes the differences measured in the range 0.1 ... 0.5 kN, these differences must be monitored but from this stage can be corrected (even automatically) during operation.

The differences greater than 0.5 kN have been classified in the last category and these necessarily increased attention, because in most cases, in this stage, appear some unexpected wears and the normal wear can no longer be maintained within the permissible limits. In this range of values, most defects are encountered in the braking system [5 – 7].

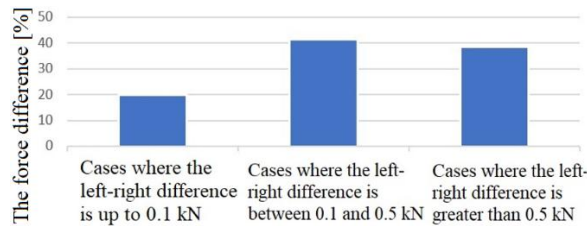


Fig. 6. Differences of the values measured on the brake stand for the braking force on each axle in relation to all measured cases

Moving from the comparison of the values measured to the left wheel, with those measured at the right wheel (at the same axle), the data obtained at the first axle are compared with second axle and third axle (in case of vehicles with more than two axle).

It has been observed that, for trucks, the differences measured when applying the braking force, differ significantly from the other categories (see Fig. 7). In this case the values fall in the category of differences greater than 0.5 kN in proportion of 50% of cases (for the 3rd axle) and up to 91% of cases (for the first axle). The graph in figure 7 do not show the values for the 4th axle due to the reduced number of tests.

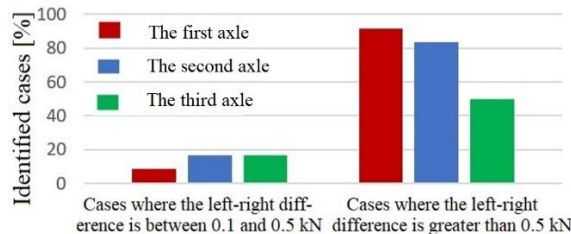


Fig. 7. Differences measured to braking force (left / right) on each axle, for heavy trucks

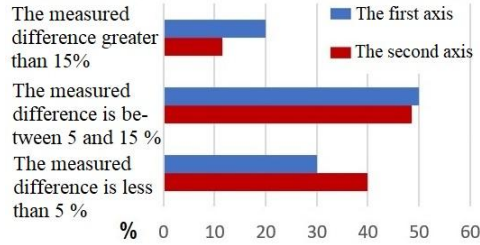


Fig. 8. Differences of the braking force measured on the stand (at the same axle)

For the total number of vehicles studied, the distribution is shown in Figure 8, where it can be seen that there is a predominant range between 5 and 15 %, with a higher number of vehicles falling into this range.

3 Calculations based on data obtained on brake stand

The analysis of the link between the data obtained on the stand and the values obtained by calculation was carried out. Based on the data obtained on the stand (braking forces on axles and wheels), the following parameters were calculated: the *specific braking force* (γ_f) and relative deceleration ($a_{f\ rel}$) [1].

Starting from the braking forces measured on the braking force measured on the braking stand, it is not possible to estimate exactly how the vehicle will brake on the road (on the braking stand the grip is maximum; the adjustment system that redistributes the braking moments between the wheel/axle is not present; other interactions related to the dynamic distribution of forces at the wheels/axle are missing). However, a series of calculations have been attempted in order to observe the main trends of the possible deceleration.

In specialized studies [1 - 4], the most used parameters for appreciating and comparing braking performance are: absolute deceleration ($a_f = -dv/dt$) or relative deceleration ($a_{f\ rel}$), braking time (t_f) and minimum braking space (S_f). In this part of study only the decelerations were analysed, for light commercial vehicles and trucks.

In [1], starting from the relationship of the tangential force and by analogy to the specific traction force, the relation (1) for the *specific braking force* (γ_f) is indicated: (ratio between the *braking force* F_f and the *total weight* of the vehicle G_a):

$$\gamma_f = \frac{F_f}{G_a} \tag{1}$$

For the quantitative assessment of the braking qualities, the *relative deceleration* can be used. This represents the ratio between the absolute deceleration of the vehicle (a_f) and the gravitational acceleration (g) [1]:

$$a_{f\ rel} = 100 \frac{a_f}{g}, \% \tag{2}$$

Using these calculation relationships [1 – 4], based on the bibliography in the specialized studies and using the values measured on the stand for the braking force and the weight on wheels and axle, the values for the *specific braking force* and for the absolute decelerations were obtained.

Figure 9 shows the values calculated for the specific braking force for the vehicles in the study. The average value calculated for all vehicles is $\gamma_f = 0.343$. The average value for light commercial vehicles is $\gamma_{f \text{ light}} = 0.35$ and for trucks there is a slight decrease in average value to $\gamma_{f \text{ truck}} = 0.34$.

The values for the braking force, obtained on the stand, were lower than the maximum possible ones so the values of the deceleration obtained through these calculations can be even higher.

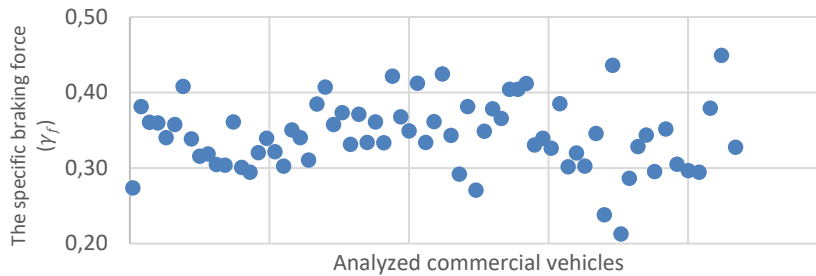


Fig. 9. Values calculated for the specific braking force (γ_f)

Deceleration values below 5 m/s^2 were also obtained in [2]. In [8], for automatic braking, (at a capacity of only 50% of the maximum capacity) a deceleration of 3 m/s^2 is obtained. However, values of deceleration (for trucks), greater than 5 m/s^2 have also been encountered in other studies. In [9] the maximum value of the deceleration is 7.41 m/s^2 and in [10], in case of emergency brake the values can reach up to 8.33 m/s^2 .

The maximum value encountered for deceleration is found in [11], where in dry asphalt conditions, at emergency braking, 12 m/s^2 is obtained. For vehicles in [12] decelerations fall between 7.35 and 9.3 m/s^2 .

The distribution of the values calculated for the relative decelerations, divided into the two categories, are presented in figure 10.

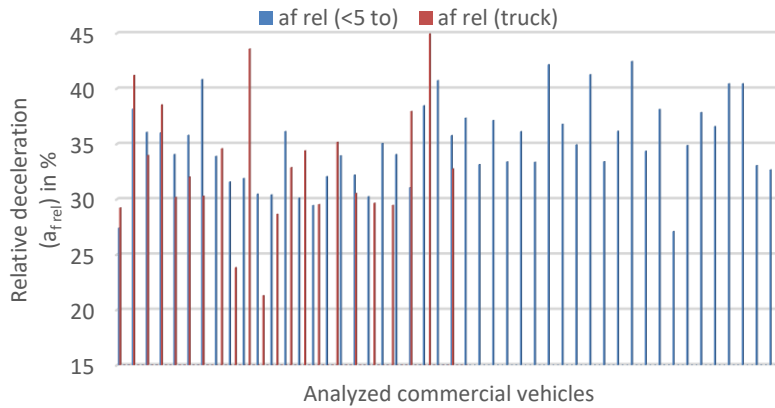


Fig. 10. Values obtained for relative deceleration ($a_{f\ rel}$)

It was observed that in only 14.3% cases, the relative deceleration was less than 30%. Of the other cases remaining in 41.4 % of them, decelerations were registered greater than 35 %. The maximum calculated value being 44.93 % for a 4 -axle truck.

4 Conclusions

Data obtained experimentally on the roller brake stand were analysed, and the distribution of braking forces at wheels and axles for two categories of commercial vehicles were analysed in particular.

The results indicated the appearance of differences in the application of the braking force at the wheels of the same axle (left/right differences) but also to the axle depending on their type and position. It has also been observed that the difference intervals in the application of forces to the wheels, vary according to the type of vehicle. The predominant interval in which most vehicles fall, when analysing the application of braking force on the same axle wheels, is between 0.1 and 0.5 kN. It has also been observed that there is a predominant interval between 5 and 15 % representing the difference in applying the braking force on the wheels of the same axle (left -right differences).

Identifying the appearance of differences in the application of forces to the wheels is of major importance in controlling wear in the system, but also in traffic safety, because in many cases these defects are not noticed and cannot be interpreted by the sensors in the system. The factors that cause defects of this type must be analysed and eliminated by adapting new control systems for the elements in the braking system. Moreover, the effect of these variations of the braking force do not bring visible changes in the deceleration calculation, except in the field of large differences (as shown in the graphs).

Average deceleration for heavy trucks was below 5.5 m/s^2 . Other values of the decelerations in the specialized literature were analysed, and the conclusion was that they can vary in a wide range and can frequently reach 8 m/s^2 in case of emergency brake.

The calculations made, based on the data obtained on the stand, highlighted the values of the minimum decelerations for the two categories of vehicles. These values are very useful in the process of analysing the dynamic parameters at braking or in the analysis of defects in the braking systems of the different types of commercial vehicles.

The values obtained when measuring the braking force on the stand have varied a lot and were lower than the maximum values indicated by the manufacturer for the analysed trucks, which means that in the formulas of deceleration the result will be even bigger values than obtained.

References

1. M., Untaru, Gh., Poșincu, A., Stoicescu, Gh., Pereș, I. Tabacu, *Dinamica autovehiculelor pe roți*, Editura didactică și pedagogică, Bucuresti (1981)
2. Șt., Tabacu, I., Tabacu, T., Macarie, E., Neagu, *Dinamica Autovehiculelor. Îndrumar de proiectare* Editura Universității din Pitești (2004)
3. T., Macarie, H., Suster-Bădărău, *Dinamica Autovehiculelor. Îndrumar de laborator*, Pitești (2012)
4. C. Andreescu, *Curs Dinamica Autovehiculelor*, Universitatea Politehnica din București, Facultatea de Transporturi, <https://transporturi.curs.pub.ro> (2017)
5. M., POPA, B., Jurchiș, Analysis of the Wear Process of the Elements in the Braking System of Heavy Trucks, *The Annals of "DUNAREA DE JOS" university of Galati fascicle IX. Metallurgy and materials science*, No4 - 2021, ISSN 2668-4748; e-ISSN 2668-4756, (2021)
6. M., Popa, N., Burnete, Analysis of operating defects in current braking systems of heavy commercial vehicles in the context of future generations of road vehicles, *Ingineria Automobilelor*, ISSN 1842-4074, NR 63/ JUNE 2022
7. M., Popa, D., Capătă, N., Burnete, Aspects of measuring brake parameters on heavy trucks using a roller brake stand, *ICOME Craiova* (2022)
8. ***Mercedes-Benz Homepage, <http://group.mercedes-benz.com>
9. S., Ramireddy, V., Ala, K., Ravishankar, A., Mehar, Acceleration and Deceleration Rates of Various Vehicle Categories at Signalized Intersections in Mixed Traffic Conditions, *Periodica Polytechnica Transportation Engineering*, 49(4), pp. 324–332, (2021)
10. L., Rost, J., Sallberg, What are the effects of AEBs on collision avoidance? Master's thesis in Engineering Mathematics and Computational Science and Applied Physics, Chalmers University Of Technology Goteborg, Sweden (2019)
11. D., K., Murthy, Emergency Braking in Compact Vehicle Platoons: A Cyber-Physical Design, Dissertation, Fakultät für Informatik an der Technischen Universität Chemnitz
12. N., Kudarauskas, Analysis of emergency braking of a vehicle, *TRANSPORT – 2007*, Vol XXII, No 3, 154–159, ISSN 1648-3480 online TRANSPORT

Optimization of Road Infrastructure Safety Management by Analyzing Statistical Data of Serious Road Accidents in Urban Areas. Case study: Streets of Bucharest

Corneliu Ioan Dimitriu^{1,2}[0000-0001-9433-8165] and Gheorghe Frățilă²[0000-0002-6740-5403]

¹ Romanian Road Authority - ARR, Bucharest, Romania

² National University of Science and Technology POLITEHNICA Bucharest, Romania
cydimitriu@yahoo.com

Abstract. The paper presents a methodology for analyzing road infrastructure safety on urban roads, intended for planning, organizing, and conducting road safety inspections as well as for training specialized personnel. The main causes of serious accidents in urban compared to rural areas are identified. The relationship between the configuration of intersections on urban roads and the frequency of serious accidents is analyzed. For Bucharest, the results of road safety inspections carried out by ARR auditors on category I and II streets are examined. The breakdown of provisions of road safety inspection reports (CSRs) shows the nature of the specific risks involved. The research uses the database of serious road accidents in Romania, recorded by the Traffic Police during 2017-2022. The aim of the research is to present a working model for urban inspections, documented on the analysis of infrastructure deficiencies according to the type of risks.

Keywords: Road Safety, Serious Accidents, Road Infrastructure.

1 Introduction

Road safety in urban environments is an essential aspect for the mobility and well-being of the population. The World Health Organization (WHO) Global State of Road Safety Report 2023 shows that more than half of road fatalities are vulnerable road users: pedestrians, cyclists, and motorcyclists [1]. A similar statistic at European level indicates that 47% of people killed in accidents are vulnerable road users [2].

The National Road Safety Strategy – 2022-2030 shows that Romania successively registers one of the highest rates of road deaths among Member States [3]. According to data published by the National Institute of Statistics – INS in the last 10 years there has been a constant increase both in the number of road vehicles registered in circulation (INS-TRN 102B) and in their mileage, expressed in „thousand vehicles-km” (INS-TRN 104) [4].

In the context of increasing the motorization rate, accelerated urbanization of localities and insufficient development of the street network, in Romania, the management and improvement of existing road infrastructure, especially in large cities such as

Bucharest, are major priorities for the authorities. Starting from these realities, optimizing the management of road safety inspections through the analysis of serious road accidents is crucial for identifying major problems and implementing effective solutions to increase safety on urban roads. A new approach is needed for staff designing, planning, and organizing road safety inspections. It is essential for those carrying out road safety inspections, as provided for in Directive (EU) 2019/1936 and Law no. 265/2008 updated, on road infrastructure safety management [5].

In recent years, the number of serious road accidents registered in urban areas has become a major concern in Romania. About 75% of these accidents occur in localities (streets and transit roads), and Bucharest is no exception. The research performs the analysis and evaluation of road safety on urban roads as well as on category I and II streets in Bucharest [6]. In the light of road safety criteria, based on which the sorting of provisions to remedy infrastructure nonconformities is carried out, the results of road safety inspections carried out by the Road Authority Romanian – ARR on some category I and II streets in Bucharest are analyzed [7].

The aim of this new approach to road safety inspections is to increase the effectiveness of measures to counter existing road risks on urban streets and roads in Romania.

2 Distribution of serious accidents according to road traffic environment

The analysis of the distribution of serious accidents registered at national level during 2017-2022 shows that the proportion of accidents produced in urban areas compared to those produced in rural areas remains constant, being 3 to 1 according to the data in Table 1.

Table 1. Dynamics of serious accidents in rural and urban areas.

| Serious accident | 2017 | 2018 | 2019 | 2020 | 2021 | 2022 | Total |
|------------------|--------|--------|--------|--------|--------|--------|--------|
| rural | 24.11% | 23.23% | 22.30% | 23.29% | 24.93% | 23.14% | 23.42% |
| urban | 75.89% | 76.77% | 77.70% | 76.71% | 75.07% | 76.86% | 76.58% |

In the urban traffic environment, high traffic values are observed, there are many complex intersections, vehicles move at low speeds, and there are many pedestrians and cyclists. To increase road safety, it is necessary to manage traffic flows, clear signage, and constant maintenance of vertical and horizontal road signals.

In rural traffic environments, traffic is scarcer, but speeds are higher, and visibility and lighting are often reduced. Roads follow less demanding road environments for drivers, but measures are needed to control speed and improve visibility and predictability.

Adapting safety measures to the specifics of each road traffic environment is essential to reduce accidents and improve road safety.

Given that approx. 75% of serious accidents are recorded on public roads belonging to the urban traffic environment, the study shows what are the relationships between serious accidents and their consequences (deaths and serious injuries).

Fig. 1 shows the percentage distribution of serious accidents, road deaths and serious injuries registered in Romania between 2017 and 2022 in both urban and rural traffic areas.

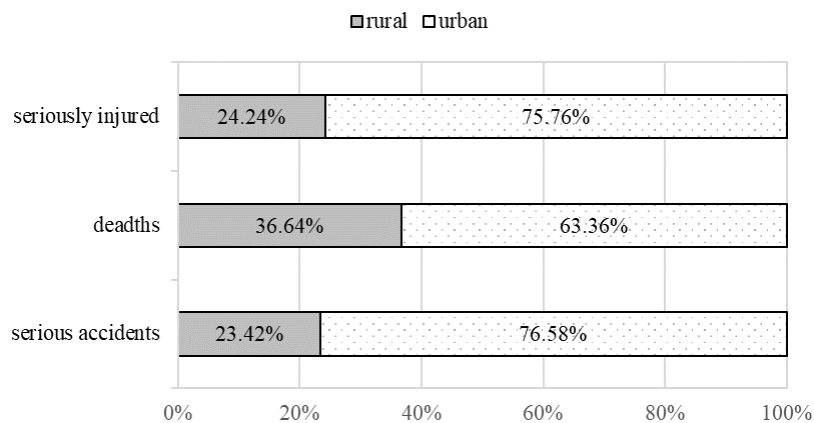


Fig. 1. Distribution of serious accidents in Romania and consequences (2017-2022).

The proportion of 1/3, which represents accidents in rural versus urban areas, is also found in the case of „seriously injured”. In the case of „deaths” the proportion is 1/1.7.

It shows that although accidents are more common in localities, accidents in rural areas tend to generate more deaths, possibly due to higher speeds as well as longer response times of emergency services.

3 Causes of serious accidents in urban traffic environments

„Speed not adapted to road conditions” is the main cause of serious accidents in Romania. (EAEC-cases). It is responsible for the highest number of deaths and serious injuries recorded on the road network.

3.1. Peculiarities of circulation in urban areas

The particularities of urban traffic generate conflict situations different from rural areas, such as [8]:

High traffic density - in cities, the large number of vehicles and road users (pedestrians, cyclists, public transport) can increase the likelihood of serious accidents.

Complex intersections – in urban areas there is a higher density of multiple and complex intersections, where the risk of collisions is higher due to frequent maneuvers and changes of direction. and due to the lack of guide markings, signaling and storage spaces for left turns.

Variable speed - in localities, vehicles are frequently forced to alternate between high and low speeds, which can lead to accidents. if the speed does not adapt to traffic and visibility conditions

Large number of pedestrians and cyclists - in urban areas, there are many pedestrians and cyclists who share road space with vehicles, which increases the risk of accidents.

Heavy public transport - buses, trams and other forms of public transport contribute to the complexity of traffic and can create dangerous situations.

Irregular parking - vehicles parked illegally or in inappropriate places can obstruct visibility and create additional hazards for all road users.

Distraction – distractions caused by bright advertisements, pedestrian congestion, cell phone use, and other inappropriate activities while driving are more common in urban environments.

Lack of adequate infrastructure - road infrastructure may be insufficient or inadequate for traffic volume, leading to unsafe traffic conditions, especially in conditions of accelerated urbanization of localities.

The situation in the urban traffic environment is analyzed. The graph in Fig. 2 shows the result of data filtered by „urban” criterion.

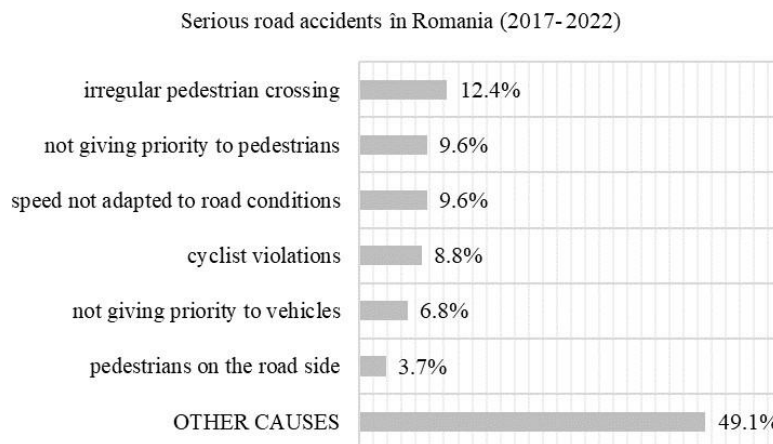


Fig. 2. Distribution of serious accidents by cause in urban areas.

The main causes of serious accidents, on the streets and roads that take over the street function when transiting localities in Romania, are ordered differently from the situation at the level of the national road network.

3.2. Causes of serious accidents in Bucharest

The study highlights the differences between the main causes of accidents at national level (Fig. 2) and in Bucharest (Fig. 3).

The percentage distribution by main causes of serious road accidents registered in Bucharest during 2017-2022 is shown in Fig. 3.

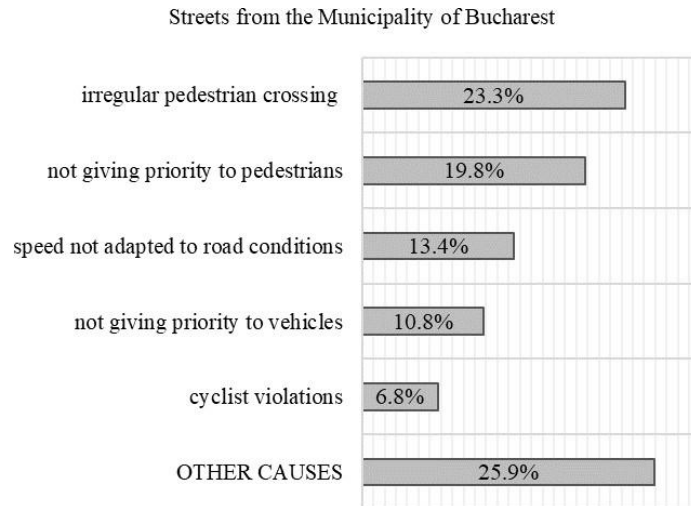


Fig. 3. Percentage distribution of serious accidents by cause (2017-2020).

The order in descending order of the share of serious accidents registered in urban areas, by main causes, shows that the first five causes are the same both nationally and in Bucharest. However, at national level, these five causes are responsible for approximately 51% of serious accidents, compared to approximately 74% in Bucharest. This suggests that, although the main causes of accidents are similar, their impact is much more pronounced in Bucharest, indicating a more urgent need for road safety measures specific to the Romanian capital.

The particularity of the administrative organization (the General City Hall of the Capital and the mayors for each administrative sector) is that most streets have different administrators, which leads to different road safety policies.

Different road safety policies between administrators may result in [9]: Inconsistency: inconsistencies in signage and traffic rules.

Low efficiency: uncoordinated and less effective safety measures. Increased risk of accidents: confusion for drivers and pedestrians. Coordination issues: delays and duplication of efforts.

Inefficiently used resources: inefficient allocation of financial and human resources.

Reduced accessibility: variable standards affect vulnerable users.

Information fragmentation: incomplete data and difficulties in addressing problems.

4 Influence of road characteristics on road safety

Road characteristics play a crucial role in determining road safety. The distribution of serious accidents, deaths, and serious injuries according to different street configura-

tions is analyzed, comparing data from Bucharest with those at national level. Table 2 shows the distribution of percentages for analysis.

Table 2. Distribution of percentages of serious accidents, deaths, and serious injuries by road characteristics in urban areas.

| Characteristics of the street | The city of Bucharest | | | Romania | | | Characteristics of the street |
|-------------------------------|-----------------------|--------|-------------------|-------------------|--------|-------------------|-------------------------------|
| | serious accidents | deaths | seriously injured | serious accidents | deaths | seriously injured | |
| free | 55.07% | 60.57% | 54.06% | 68.06% | 70.86% | 65.95% | free |
| intersection | 44.09% | 37.14% | 45.26% | 19.37% | 13.12% | 20.45% | intersection |
| curve | 0.36% | 1.14% | 0.28% | 11.67% | 14.22% | 12.75% | curve |
| on bridge | 0.19% | 0.57% | 0.14% | 0.44% | 0.76% | 0.41% | on bridge |
| in the tunnel | 0.16% | 0.29% | 0.14% | 0.27% | 0.93% | 0.22% | CFR pass |
| under the bridge | 0.10% | 0.29% | 0.07% | 0.15% | 0.06% | 0.17% | in the tunnel |
| CFR pass | 0.03% | 0.00% | 0.04% | 0.05% | 0.04% | 0.05% | under the bridge |

Considering the characteristics of the street infrastructure and the percentage distribution of serious accidents, road deaths and serious injuries in Romania, compared to Bucharest, according to the data in the table presented, the following conclusions can be drawn regarding road safety:

„Free” characteristic (streets in alignment). In Bucharest, this characteristic represents a significant proportion of serious accidents (55.07%), deaths (60.57%) and serious injuries (54.06%). Nationally, these proportions are even higher, with 68.06% serious accidents, 70.86% fatalities and 65.95% seriously injured. This indicates that the "free" characteristic are common places for serious accidents both in Bucharest and in the rest of Romania. The higher percentages at urban-national level can be explained by higher traffic speeds in transit zones through localities and weaker road infrastructure. Compared to the situation in Bucharest, at national level, the delayed intervention of emergency services may be a factor that also contributes to a higher percentage of deaths.

„Intersection” characteristic. Intersections account for 44.05% of serious accidents, deaths, and serious injuries in Bucharest, compared to 19.37% nationwide. This suggests that urban intersections, especially in Bucharest, are critical points where many serious accidents occur. This could be due to dense traffic and complex maneuvers required at intersections in the city. Intersections are much more dangerous in Bucharest's urban area than in the rest of the country, indicating the need for additional safety measures, such as efficient traffic lights and improved infrastructure for pedestrians and cyclists and increased visibility.

„Curve” characteristic. In Bucharest, curves account for only 0.36% of serious accidents, 1.14% of deaths and 0.28% of serious injuries. Nationally, these percentages are much higher: 11.67% serious accidents, 14.22% fatalities and 12.75% seriously injured. This indicates that curved roads are much more dangerous outside dense urban environments, where speed and visibility can be significant factors in accidents.

3.3. The distribution of serious accidents in the administrative sectors

The root cause of serious accidents varies from sector to sector. In Sector 1, the main cause is „speed not adapted to road conditions”, followed by „failure to give priority to pedestrians”; in sectors 2, 3, 5 and 6, most serious accidents are caused by „irregular pedestrian crossing” followed by „failure to priorities pedestrians”; and in Sector 4, most serious accidents are caused by „failure to give priority to pedestrians”, followed by „irregular pedestrian crossing”.

The analysis of the distribution of serious accidents shows that in sectors 1 and 2 of the municipality occur approx. 40% of all accidents recorded in. The percentages allocated to each administrative sector are shown in Fig. 4.

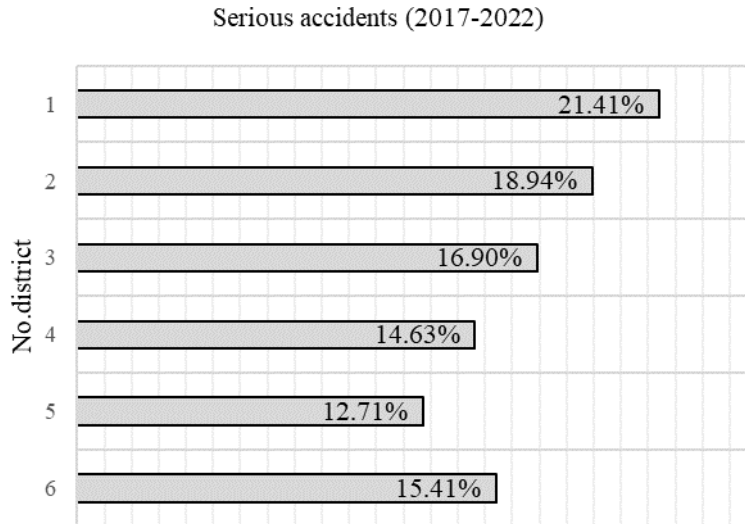


Fig. 4. Distribution of serious accidents by sectors in Bucharest (2017-2022).

Compared to the situation at national level, where the main cause of serious accidents is „failure to adapt speed to road conditions”, in urban areas the peculiarities of road traffic generate different problems for road users, thus, the main cause of serious accidents on urban roads is "irregular pedestrian crossing" followed by „failure to give priority to pedestrians”. In third place is „failure to adapt speed to road conditions”.

If at national level, the main cause of serious accidents is „failure to adapt speed to road conditions”, in urban areas in Romania, the peculiarities of road traffic generate different problems for infrastructure users. In urban areas, the main cause of serious accidents is „irregular pedestrian crossing” followed by „failure to priorities pedestrians”. In third place is „failure to adapt speed to road conditions”, a situation that is also found in Bucharest. These differences suggest that road safety measures need to be adapted to the specific context of each traffic environment.

5 Influence of intersection configuration on road safety

Analysis of the distribution of serious accidents on urban streets and roads, depending on road configuration, is presented in Table 3. It is the Romanian police who are responsible for classifying each serious accident according to the specific configuration of the place where it occurred.

„Free” configuration (streets in alignment). In both Romania and Bucharest, this configuration accounts for many serious accidents, deaths, and serious injuries on urban roads. The percentages are very close: 54.91% serious accidents in Bucharest and 56.03% in Romania.

„Simple T” configuration (three-link intersections). The analysis shows that these types of intersections are most dangerous in urban road traffic environments. In Bucharest, this configuration accounts for 16.61% of serious accidents, compared to 8.42% nationwide. This suggests that T-junctions are more dangerous in Bucharest's dense urban environment.

„Cross” configuration (four-link junctions). In Bucharest, serious accidents at this type of intersections represent 14.14%, compared to 5.75% at national level. This indicates a significant challenge in managing intersections in Bucharest, where traffic density is higher.

These conclusions highlight the importance of an adapted management of road safety inspections, considering the specificities of road traffic in the urban environment. The management of three- and four-arm intersections and speed control on urban roads, such as Bucharest streets, require specific measures to reduce the associated risks.

The analysis of the remedial actions (through the provisions of inspection reports) of road safety auditors employed by ARR, can show what type of actions are needed to reduce and eliminate road risks.

Table 3. Distribution of percentages of serious accidents, deaths, and serious injuries by configuration of intersections in urban areas.

| Configures of the street | The city of Bucharest | | | Romania | | | Configures of the street |
|--------------------------|-----------------------|--------|-------------------|-------------------|--------|-------------------|--------------------------|
| | serious accidents | deaths | seriously injured | serious accidents | deaths | seriously injured | |
| free | 54.91% | 61.43% | 53.77% | 56.03% | 58.42% | 54.33% | free |
| simple T | 16.61% | 15.71% | 16.72% | 8.42% | 6.23% | 8.76% | simple T |
| cross | 14.14% | 11.43% | 14.56% | 5.75% | 3.85% | 6.11% | cross |
| double T | 2.47% | 1.14% | 2.69% | 1.27% | 0.63% | 1.38% | roundabout |
| roundabout | 0.55% | 0.57% | 0.60% | 0.96% | 0.68% | 0.99% | double T |
| in Y | 0.49% | 0.57% | 0.46% | 0.73% | 0.57% | 0.79% | in Y |
| in the star | 0.23% | 0.00% | 0.25% | 0.10% | 0.04% | 0.11% | in the star |
| curve | 0.35% | 0.29% | 0.36% | 6.55% | 8.13% | 7.32% | curve |
| other | 10.18% | 8.86% | 10.52% | 16.59% | 17.59% | 16.64% | other |
| - | - | - | - | 3.42% | 3.26% | 3.42% | NULL |

6 Road safety inspections in Bucharest

During 2020-2021, a few 21 road safety inspections were carried out on category I and II streets according to the service contract concluded between the Road Authority Romanian - ARR and the Streets Administration of Bucharest – ASB [6].

According to the street classification established by Government Ordinance no. 43/2017, updated, regarding the regime of roads, in Bucharest there are 58 streets of category I, 147 of category II and 3 streets include sections that fall into both classifications, I and II [10].

Following road safety inspections on category I and II streets in Bucharest, the auditors of the Romanian Road Authority -ARR recorded in their reports a series of road

risks directly related to factors specific to the urban environment, which can explain the higher rate of serious accidents.

The inspection reports shall contain instructions to the road manager to carry out mandatory works aimed at remedying the deficiencies found [11]. Table 4 presents the results of the analysis for the distribution of provisions by road traffic safety assessment criteria [12].

Table 4. Distribution of provisions based on road risk criteria (RTS).

| Street name | V | P | M | D | C | R | A | Total provisions |
|-----------------------|--------------|--------------|--------------|-------------|-------------|-------------|-------------|------------------|
| St. Calea Crângași | 39 | 12 | 2 | 4 | 5 | 1 | 9 | 72 |
| Bd. Constructorilor | 14 | 7 | 1 | 0 | 4 | 0 | 1 | 27 |
| Bd. Dimitrie Cantemir | 39 | 15 | 2 | 5 | 0 | 1 | 0 | 62 |
| St. Drumul Sării | 29 | 10 | 17 | 13 | 4 | 0 | 0 | 73 |
| Bd. Libertății | 21 | 10 | 8 | 2 | 5 | 6 | 0 | 52 |
| Bd. Regina Elisabeta | 24 | 10 | 1 | 1 | 2 | 0 | 0 | 38 |
| St. Vasile Lascăr | 35 | 19 | 14 | 8 | 0 | 8 | 0 | 84 |
| St. Vatra Luminoasă | 100 | 1 | 20 | 10 | 3 | 1 | 1 | 136 |
| Total | 301 | 84 | 65 | 43 | 23 | 17 | 11 | 544 |
| % | 55.3% | 15.4% | 11.9% | 7.9% | 4.2% | 3.1% | 2.0% | 100.0% |

It is found that the provisions allocated to the "Visibility" criterion represent 55.3% of the total remedial provisions, highlighting that visibility problems between road users and road infrastructure elements are the most common and require greater attention. It suggests that road safety auditors have identified numerous road risks arising from road infrastructure non-compliances and requiring significant improvements in visibility on urban roads to reduce the risk of accidents.

In comparison, on the DN 2-E85 road, a rural road known for the highest number of deaths in Romania, the provisions allocated to the "Visibility" criterion represent 49.6% of the total remedial provisions, compared to 55.3% is the percentage of Bucharest [7].

This comparison shows that, although visibility is a major problem in both urban and rural areas, the need to address these problems is more acute in urban areas, where traffic density and infrastructure complexity increase risks for road users.

The analysis is essential to priorities work to remedy the deficiencies found. The action plan should provide, chronologically, for the first interventions on road infrastructure to be targeted at measures leading to immediate improvements in road safety. Thus, initial interventions should focus on vision problems and other critical deficiencies that can rapidly reduce the risk of accidents. The implementation of a struc-

tured and well-prioritized plan will ensure an efficient use of resources and will significantly contribute to increasing safety on urban roads.

7 Conclusions

The analysis and optimization of road infrastructure safety management by analyzing statistical data of serious accidents in urban areas highlights the need for urgent and coordinated measures to improve road safety on the streets of Bucharest and at national level.

In Bucharest, the main causes of serious accidents are irregular pedestrian crossing and failure to give priority to pedestrians, followed by failure to adapt speed to road conditions. At national level, inadequate speed is the main cause, followed by the same pedestrian problems. These differences suggest that safety measures need to be adapted to the specificities of each traffic environment.

In urban environments, traffic complexity and high density of vehicles, pedestrians and cyclists increase the risk of serious accidents. In rural areas, high speed and poor visibility are the main problems. These observations indicate the need for specific measures for each type of environment.

Vision problems account for a significant proportion of deficiencies identified in road safety inspections. Addressing these problems should be a priority in order to reduce the risks of serious accidents in urban environments.

Differences in road safety policies between administrations of different sectors in Bucharest can lead to inconsistencies in signaling and traffic rules, reducing the effectiveness of safety measures and increasing the risk of accidents. Better coordination between authorities is essential to implement uniform and effective policies.

It is necessary for authorities to train road safety auditors to guide the provisions of inspection reports towards remedying the most serious deficiencies. This will ensure that resources are used efficiently and that the measures implemented will have the maximum impact on road safety.

To improve road safety, it is crucial that authorities work closely together, implement uniform policies, and focus on remedying the most serious deficiencies identified in inspection reports. Adequate training of road safety auditors and prioritization of intervention measures will significantly contribute to reducing the number of serious accidents and increasing safety on urban roads in Romania.

Disclosure of Interests. The authors do not have competing interests to declare that are relevant to the content of this article.

References

1. World Health Organization. (2023, December 13). Global status report on road safety 2023. Retrieved April 10, 2024, from WHO: <https://www.who.int/publications/i/item/9789240086517>

2. European Parliament, Council of the European Union. (2019, November 26). Directive (EU) 2019/1936 amending Directive 2008/96/EC on road infrastructure safety management. (p.–1. OJ L 305, Ed.) Retrieved February 10, 2024, from <https://eur-lex.europa.eu: http://data.europa.eu/eli/dir/2019/1936/oj>
3. The Government of Romania. (2022, May 31). Annex to Government Decision no. 682/2022 for the approval of the National Road Safety Strategy for the period 2022-2030. The Official Monitor of Romania, I(535 bis), pp. 3-74.
4. National Institute of Statistics - INS, Romania. (2023). TEMPO ONLINE - Road transport. Retrieved May 12, 2024, from <https://insse.ro/cms/ro: http://statistici.insse.ro:8077/tempo-online/#/pages/tables/insse-table>
5. The Romanian Parliament. (2012, August 23 07). Law no. 265/2008, republished and updated with subsequent amendments, regarding the management of traffic safety on the road infrastructure. The Official Monitor of Romania, I(608), pg. 6- 18.
6. Romanian Road Authority - A.R.R. (2022). Pre luat pe February 10, 2024, de pe www.arr.ro: https://www.arr.ro/arr_doc_230_rapoarte-si-studii_pg_0.htm
7. Dimitriu, C. I., & Frățilă, G. (2024, March 27). The influences of human factors on road accidents in Romania in the period 2013 – 2022. IOP Conference Series: Materials Science and Engineering, Economicity, Safety and Reliability for Motor Vehicles Congress (and SIAR International Automotive and Transport Engineering Congress) 02/11/2023 - 04/11/2023 Bucharest, Romania(1303), 8. doi:10.1088/1757-899X/1303/1/012048
8. Costescu, D., Bujor, C. R., & Ifrim, A. M. (2024, March 27). Methodology for assessing the road traffic risk in urban areas. IOP Conference Series: Materials Science and Engineering, Economicity, Safety and Reliability for Motor Vehicles Congress (and SIAR International Automotive and Transport Engineering Congress) 02/11/2023 - 04/11/2023 Bucharest, Romania(1303), 8. doi:10.1088/1757-899X/1303/1/012049
9. U.S. Department of Transportation. (2009, 04 06). <https://highways.dot.gov/>. Retrieved 02 28, 2024, from <http://www.highwaysafetymanual.org/>
10. Bucharest City Hall. (1992). Streets in administration. Pre luat pe March 28, 2024, de pe Bucharest Streets Administration - ASB: <https://aspmb.ro>
12. Ministry of Transport of Romania. (2017, June 19). Order no. 606/2017, with subsequent changes and additions, for the approval of some measures regarding the road safety inspection. The Official Monitor of Romania, I(457), pg. 6-13.
13. International Permanent Association of Road Congresses, PIARC. (2019). Road Safety Evaluations Based on Human Factors Method. Road Safety, PIARC, Technical Committee, Paris. Retrieved 02 25, 2024, from <https://www.piarc.org/en/order-library/31358-en->

Contributions to the Strengthening of the National Legislative Framework for Road Infrastructure Safety Management in Romania. Case Study on the Evolution of National Regulations in the Context of the Implementation of EU Directives

Corneliu Ioan Dimitriu^{1,2}[0000-0001-9433-8165] and Gheorghe Frățilă²[0000-0002-6740-5403]

¹ Romanian Road Authority - ARR, Bucharest, Romania

² National University of Science and Technology POLITEHNICA Bucharest, Romania
cydimitriu@yahoo.com

Abstract. As part of the 2018 Europe on the Move package, the European Commission set targets for reducing road deaths and injuries by 2050, proposing a new framework for 2020-2030 based on the 'safe system'. It requires multisectoral collaboration to improve infrastructure and use new technologies. Also, the Romanian legislation must be harmonized with European standards to manage road risks more efficiently. In the field of road safety, the legislative and managerial context in Romania is crucial for the prevention and reduction of serious accidents. The implementation of EU directives, such as Directive 2008/96 (EC) and the amendments brought about by Directive (EU) 2019/1936, significantly influences national legislation. The research focuses on the evolution of the Romanian legislative framework, highlighting the changes introduced by OG no. 3/2022.

Keywords: Road Infrastructure, Safety Management, National Regulations.

1 Introduction

As part of the 'Europe on the Move' package of 17 May 2018, the European Commission introduced a new approach to EU policy on road safety management, accompanied by a medium-term strategic action plan [1]. This staff working document details how this new policy will be implemented in practice, the Safe System Approach. The document stresses the importance of an integrated approach to road safety, which prevents deaths and serious injuries by creating multiple layers of protection and compensating for human error. The legislative proposals include new mandatory vehicle safety measures and improved road infrastructure safety management.

Resolution A/RES/74/299 adopted by the UN General Assembly on 31 August 2020 underlines the importance of improving road safety globally, recognizing that road accidents are a major public health problem and an economic burden [2]. The document calls on member states to adopt comprehensive legislation to address key risk factors

and improve road infrastructure. The need for public education and awareness on road safety is emphasized. The resolution encourages Member States to develop public policies that include international standards and good practices in road safety.

The Commission Communication of 20 July 2010 set out the EU's strategic objectives of halving road deaths by 2020 compared to 2010 and achieving 'zero fatalities' by 2050. Progress has stalled recently and the Council, through its conclusions of 8 June 2017 and the Valletta Declaration, set a new interim target: halving the number of serious injuries by 2030 compared to 2020 [3]. Further efforts are needed to achieve these goals.

Road safety in the EU has made significant progress, with a 43% reduction in deaths between 2001 and 2010 and a further 19% decrease between 2010 and 2016, but the mortality rate has recently stagnated. The Commission is proposing a new framework for the period 2020-2030, based on a 'safe system', which aims to prevent deaths and serious injuries by improving road infrastructure, reducing speeds and using new technologies. This approach requires improving road infrastructure management, through multisectoral actions and the collaboration of all stakeholders to create a safer road environment and save lives.

Road safety in the EU has made significant progress, with a 43% reduction in deaths between 2001 and 2010 and a further 19% decrease between 2010 and 2016, but the mortality rate has recently stagnated. The Commission is proposing a new framework for the period 2020-2030, based on a 'safe system', which aims to prevent deaths and serious injuries by improving road infrastructure, reducing speeds and using new technologies. This approach requires improving road infrastructure management, through multisectoral actions and the collaboration of all stakeholders to create a safer road environment and save lives.

The proposal extends the scope of the directive to motorways and main roads, which cover 15% of the length of the road network but account for 39% of fatal accidents. The impact assessment shows that this combination of measures could save more than 3,200 lives and avoid 20,700 serious injuries between 2020 and 2030, with the costs being limited compared to the benefits. The new procedures, road-wide assessment and the introduction of performance requirements for markings and signaling, with a focus on the protection of vulnerable users, will ensure better road safety across the Union.

2 Amendments to primary legislation by transposing the provisions of Directive (EU) 2019/1936

The research focuses on the main amendments of Law no. 265/2008 [4], updated by Government Ordinance no. 3/2022 [5], for the transposition of the provisions of Directive (EU) 2019/1936 [6] amending Directive 2008/96 (EC) [7].

2.1 Management of "black spots"

The National Road Safety Strategy 2022-2024 aims to reduce the number of black spots/hotspots in urban and interurban areas by 48% by the second quarter of 2026,

compared to 2019. This objective will be achieved through the implementation of projects financed by the European Investment Bank, PNRR and POT, totaling investments of 216 million euros for the treatment of the 267 locations identified as black spots in the period 2015-2019. The funding includes feasibility studies and specific technical measures to eliminate these danger points [8].

On the website of the Romanian Road Authority – ARR is presented the method of establishing the "black spot" using one or more attributes from the database of serious road accidents [9].

In letter n), art. 3, of Law no. 265/2008, the definition of "black spot" was given. This definition is repealed by Art. I. OG no. 3/2022 for amending and supplementing Law no. 265/2008. The lack of definition is an aspect also noted by the Special Report of the European Court of Auditors, p.38, [10].

The road traffic indicator (A55) that signals car users to the approach of a road sector with a high risk of accidents – "black dot" – is represented in the Romanian standard [11]. This indicator is not found in ANNEX No. 2, A, "Warning Road signs" of the normative act GEO 195/2002 on road traffic, being found on national roads in Romania [12].

The repeal of the definition of the "black spot" in Law no. 265/2008 by Government Ordinance no. 3/2022 and the lack of the A55 indicator in the specific legislation regulating road traffic may have important implications on the implementation of the National Road Safety Strategy 2022-2024. Without a clear definition in the legislation, identifying and managing these danger points could become more difficult.

This implies the need to correlate and update the terminology, as well as the methodologies used in the National Road Safety Strategy. It is necessary to revise the legislation and the criteria for identifying and evaluating black spots, adapting action plans and allocating financial resources, to ensure the coherence and efficiency of measures to reduce road accidents according to the new legal regulations.

2.2 Addressing road safety in tunnels and adjacent areas

Article 1, paragraph 3 of Law no. 265/2008, updated, transposes the provisions of Directive (EU) 2019/1936 on the non-applicability of procedures on roads passing through tunnels subject to Law 277/2007. Thus, tunnels in Romania that are less than 500 m long are excluded from a competent assessment.

It is important that road sections passing over bridges and tunnels are regulated regarding road safety (preamble 5, [6]). The road area comprising these elements of road architecture encompasses several road risks. For example, when passing through the tunnel, the road environment and traffic conditions change rapidly. Infrastructure needs to provide predictability for users, vehicles and vulnerable users.

It is necessary to clearly specify this sensitive category of roads, sections adjacent to tunnels, to be included in the regulatory scope of how the joint inspection is carried out by the ARR auditors together with the ISC inspectors. The inspection reports prepared by the ARR auditors contain findings regarding visibility problems in the tunnel area, inadequate lighting, deficiencies in rainwater drainage and protection of vulnerable users (pedestrians and cyclists).

2.3 Limitations in the application of road infrastructure safety management procedures (RISM)

By Article 1, paragraph (5), Law no. 265/2008, updated by Government Ordinance no. 3/2022, the structure of the national road network subject to the scope of the Directive was established. Subsequently, Law 265/2008 was amended by GEO no. 109/2022 and county roads have been completely removed from the scope of the directive for road safety impact assessment (EISR) and road safety audit (ASR) procedures.

This provision implies the obligation to execute the RISM procedures on the entire network, but without considering that the efficient allocation of resources should be made only on those roads that require investment. For this, Member States may exclude from the application of the Directive low-risk roads, justified by traffic volumes and accident statistics, and may include roads not mentioned in the Directive (UE) 2019/1936, Art.1, Alin. 4, &1 and &2.

The provision of the Directive requiring the application of procedures, including EISR and ASR, to other roads or road infrastructure projects outside urban areas, financed by the European Union, is not fulfilled. By doing so, the EU ensures that funds allocated to Member States are not used for the construction of unsafe roads, (preamble 10 and Art. 1, Alin. 3, [6]).

2.4 Road Infrastructure Safety Management

According to Law no. 265/2008, updated on 31.01.2022, the periodic road safety inspection was carried out by road safety auditors, employees of ARR, on the road network subject to the Law. According to the contracts with the road manager, the inspection reports, which included provisions to remedy non-conformities and deficiencies in the road infrastructure, were sent to the contracting party. At the end of the period allotted for compliance with the provisions, the ARR carried out a follow-up inspection to ascertain compliance with the provisions within the time limit. Otherwise, the road administrator could be sanctioned for failure to comply with the provisions within the established term, Art.23, letter c) of the law.

By implementing the provisions of Directive (EU) 2019/1936, the objectives of road safety inspections have been reorganized. Table 1 shows the evolution of the national approach on how to implement the provisions of the Directives for road safety inspections.

Table 1. Comparative table of road inspections according to the legislation.

| No. Crt. | Type of inspection | Directive 96/ Lege 265/2008 | Directive 1936/ OG 3/2022 | Observations |
|----------|--------------------------------------|-----------------------------|---------------------------|--|
| 1 | Periodic inspection | Yes | Yes* | *Only for findings aimed at remedying deficiencies through road infrastructure maintenance works |
| 2 | Additional Fatal Accident Inspection | Yes* | - | *Were carried out upon notification of the Romanian Police according to Annex 4 of the law |

| | | | | |
|---|---------------------------------|------|------|---|
| 3 | Additional Follow-Up Inspection | Yes* | - | *To verify the fulfilment of remedial measures |
| 4 | Joint inspection (ARR with ISC) | - | Yes* | *On road sections adjacent to tunnels with a length > 500 m |
| 5 | Specific inspection | - | Yes* | *On dangerous sections resulting from the road network assessment |

The approach of Law no. 265/2008, updated on 30.01.2022, met the quality management requirements according to the PDCA cycle, Fig. 1-A.

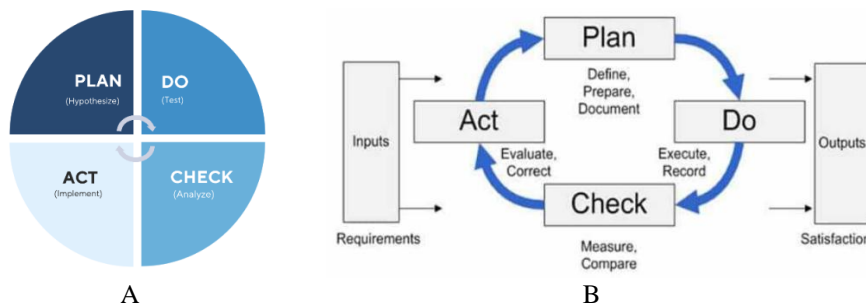


Fig. 1. PDCA Cycle Chart (Plan Do Check Act).

By amending Law no. 265/2008 with OG no. 3/2022, the PDCA cycle of road safety inspection processes were affected. The final part of the cycle, "Check" and "Act", Fig. 1-B, was left to the discretion of the road administrator. The Ministry of Transport and Infrastructure - MTI, through the ARR, no longer has the legal possibility to inspect on the ground the remedy of the deficiencies found by carrying out the ordered measures. The table shows the amendments to the law that altered the PDCA cycle.

The road administrator periodically reports "the degree of implementation of the deficiency remedy plan" and "the proof of implementation of the measure ordered by the report", leaving room for interpretation of these obligations for each road administrator. Currently, these attributions are the responsibility of the 41 county councils (for county roads) and the National Company for Road Infrastructure Administration – CNAIR (for national roads, expressways and highways).

Table 2 shows the consequences of changes to some provisions.

These changes diminished the force of the administrative act, by transferring responsibility to the 41 county councils and CNAIR for the different categories of roads (Art. I, pct.19, [5])

Between 2018 and 2022, through the inspections carried out, the ARR inspectors identified numerous road risks generated by the lack of maintenance of the national roads under the administration of CNAIR. Also, many road accidents resulting in deaths on county roads, administered by county councils, have been attributed to the same problems of insufficient maintenance. The recent amendments to Law no. 265/2008 by OG no. 3/2022 affected the PDCA cycle of road safety inspections, leaving it to the discretion of the road administrator to verify and remedy the deficiencies found, which can lead to various interpretations of the obligations and, implicitly, to the maintenance

of road risks. This shortcoming is amplified by the outsourcing of inspections that focus solely on maintenance issues. There is no legal possibility for periodic inspections to be carried out with priority on the most dangerous sections, sections identified by the ARR following the road network safety assessment.

Table 2. Comparison of the provisions of Law no. 265/2008 and OG no.3/2022 in the field of inspections.

| No. crt. | Law 265/2008, updated 30.01.2022 | Provision content | OG 3/2022 | Provision content | Observations |
|-----------------|---|--|---------------------------|--|--|
| 1 | Art.1, para. (6) | Determines the road network on which further inspection is carried out | Art. I, item 2, amendment | The specific inspection procedure is introduced | The additional inspection procedure of follow-up and inspection of fatal accidents is eliminated |
| 2 | Art.3, let. p) | Definition of additional inspection | Art. I, item 4 | The definition of specific inspection is introduced | The definition of additional follow-up inspection is deleted |
| 3 | Art.23, let. c) | The administrator's obligation to remedy the deficiencies found by carrying out the measures ordered within the deadline | | The obligation of the administrator to transmit within the deadline the degree of implementation of the measures ordered | It is left to the discretion of the administrator to assess the fulfillment of the provisions/measures ordered to remedy the deficiencies |
| 4 | | | Art. I, pct.30, lit. h) | The obligation of the administrator to implement remedial measures is introduced | Failure to comply with the obligation cannot be sanctioned by the ARR because the additional field tracking inspection procedure has been eliminated |

3 Conclusions

The implementation of the systematic approach to road safety in the EU, inspired by the medium-term action strategy, highlights the importance of multiple prevention and mandatory measures for the safety of vehicles and infrastructure.

The National Road Safety Strategy 2022-2024 aims to significantly reduce the "black spots", but the elimination of the definition and the non-inclusion of the A55 indicator in OUG 195/2002 could complicate their management.

The updated legislation excludes tunnels shorter than 500 m from competence assessments, highlighting the need for clear regulations for these areas in view of the increased risks.

The exclusion of county roads from the EISR and ASR procedures could affect the efficient allocation of resources and safety on these roads, despite EU funding.

The legislative changes transferred the responsibility for checking and fixing deficiencies to the administrators, eliminating the additional inspections carried out by the ARR and thus diminishing the effectiveness of the PDCA process.

These conclusions underline the importance of a coherent and integrated approach in road infrastructure safety management, highlighting the need for clear definitions and well-distributed responsibility to ensure the effective implementation of safety measures.

Disclosure of Interests. The authors do not have competing interests to declare that are relevant to the content of this article.

References

1. Bucharest City Hall. (1992). Streets in administration. Preluat pe March 28, 2024, de pe Bucharest Streets Administration - ASB: <https://aspm.ro>
2. Costescu, D., Bujor, C. R., & Ifrim, A. M. (2024, March 27). Methodology for assessing the road traffic risk in urban areas. IOP Conference Series: Materials Science and Engineering, Economicity, Safety and Reliability for Motor Vehicles Congress (and SIAR International Automotive and Transport Engineering Congress) 02/11/2023 - 04/11/2023 Bucharest, Romania(1303), 8. doi:10.1088/1757-899X/1303/1/012049
3. Dimitriu, C. I., & Bujor, C. R. (2022). The integrated methodology for assessing the safety of the road network infrastructure in Romania. IOP Conference Series - Materials Science and Engineering (p. 8). Timisoara, EAEC MVT: IOP Publishing Ltd. Retrieved from <http://www.siarcongress.eu/index.php/mvt/2022>
4. Dimitriu, C. I., & Frățilă, G. (2022). Top causes of road traffic accidents in Romania. IOP Conference Series - Materials Science and Engineering (p. 8). Timisoara, EAEC MVT: IOP Publishing Ltd. Retrieved from <http://www.siarcongress.eu/index.php/mvt/2022>
5. Dimitriu, C. I., & Frățilă, G. (2024, March 27). Road infrastructure safety assessment using the integrated method - case study DN2. IOP Conference Series: Materials Science and Engineering, Economicity, Safety and Reliability for Motor Vehicles Congress (and SIAR International Automotive and Transport Engineering Congress) 02/11/2023 - 04/11/2023 Bucharest, Romania(1303), 8. doi:10.1088/1757-899X/1303/1/012052

6. Dimitriu, C. I., & Frățiță, G. (2024, March 27). The influences of human factors on road accidents in Romania in the period 2013 – 2022. IOP Conference Series: Materials Science and Engineering, Economicity, Safety and Reliability for Motor Vehicles Congress (and SIAR International Automotive and Transport Engineering Congress) 02/11/2023 - 04/11/2023 Bucharest, Romania(1303), 8. doi:10.1088/1757-899X/1303/1/012048
7. European Parliament, Council of the European Union. (2019, November 26). Directive (EU) 2019/1936 amending Directive 2008/96/EC on road infrastructure safety management. (p.–1. OJ L 305, Ed.) Retrieved February 10, 2024, from <https://eur-lex.europa.eu: http://data.europa.eu/eli/dir/2019/1936/oj>
8. International Permanent Association of Road Congresses, PIARC. (2019). Road Safety Evaluations Based on Human Factors Method. Road Safety, PIARC, Technical Committee, Paris. Retrieved 02 25, 2024, from <https://www.piarc.org/en/order-library/31358-en-Road%20Safety%20Evaluations%C2%A0Based%20on%20Human%20Factors%20Method>
9. Ministry of Transport of Romania. (2017, June 19). Order no. 606/2017, with subsequent changes and additions, for the approval of some measures regarding the road safety inspection. The Official Monitor of Romania, I(457), pg. 6-13.
10. National Institute of Statistics - INS, Romania. (2023). TEMPO ONLINE - Road transport. Retrieved May 12, 2024, from <https://insse.ro/cms/ro: http://statistici.insse.ro:8077/tempo-online/#/pages/tables/insse-table>
11. Romanian Police. (2022). Graphs of the main statistical indicators regarding police activity - Statistics Archive. Retrieved July 07, 2023, from www.politiaromana.ro: https://www.politiaromana.ro/ro/utile/statistici-evaluari/statistici
12. Romanian Road Authority - A.R.R. (2022). Preluat pe February 10, 2024, de pe www.arr.ro: https://www.arr.ro/arr_doc_230_rapoarte-si-studii_pg_0.htm
13. Technical Committee on Road Safety , PIARC. (2003). Search: Road Safety Manual. Preluat pe April 29, 2024, de pe www.piarc.org: https://www.piarc.org/en/search.htm?q=Manual&l=current
14. The Government of Romania. (2022, May 31). Annex to Government Decision no. 682/2022 for the approval of the National Road Safety Strategy for the period 2022-2030. The Official Monitor of Romania, I(535 bis), pp. 3-74.
15. The Romanian Parliament. (2012, August 23 07). Law no. 265/2008, republished and updated with subsequent amendments, regarding the management of traffic safety on the road infrastructure. The Official Monitor of Romania, I(608), pg. 6-18.
16. U.S. Department of Transportation. (2009, 04 06). <https://highways.dot.gov/>. Retrieved February 28, 2024, from <http://www.highwaysafetymanual.org/>
17. World Health Organization. (2018, June 17). Global status report on road safety 2018. Licence: CC BY-NC-SA 3.0 IGO, Social Determinants of Health. Geneva: WHO. Retrieved July 07, 2023, from www.who.int: https://www.who.int/publications/i/item/9789241565684
18. World Health Organization. (2023, December 13). Global status report on road safety 2023. Retrieved April 10, 2024, from WHO: <https://www.who.int/publications/i/item/9789240086517>

Experimental Research Concerning the Decreasing of the State of Charge from the Traction Battery for an Electric Vehicle used in Urban Driving Conditions

Valentin Nişulescu¹, Florian Ivan², Marius Toma¹, Cristian Renţea¹, Gheorghe Bancă¹

¹National University of Science and Technology Politehnica Bucharest, Romania.

²National University of Science and Technology Politehnica Bucharest, Pitesti University Center, Romania.

nisulescu.valentin@yahoo.com

Abstract. Currently, electric cars enjoy a major interest among users and potential buyers. As a result, the offer of manufacturers has become very varied and generally adapted to the needs of customers. The major challenge for these manufacturers is the range between two successive charges of the traction battery. This parameter plays a decisive role when purchasing a certain type of electric vehicle. At this moment, an autonomy that fully satisfies reasonable mobility needs has not been reached. According to the regulations applicable at international level, the autonomy of an electric vehicle is determined in laboratory conditions following certain test cycles. Unfortunately, laboratory tests cannot faithfully reproduce real operating conditions. Considering these aspects, the authors developed experimental research in urban driving conditions intended to identify the concrete causes of reduction of the state of charge (SOC) of the traction battery during the journey. In the first part of the paper, are presented the particularities of the test, the specific technical data of electric vehicle tested and the details regarding the acquisition of experimental data from the vehicle. The fundamental goal pursued was to highlight the parameters that define the state of charge of the traction battery. In the second part of the paper, the results of the experimental research are presented and interpreted. Also, are established conclusions regarding the decreasing of the state of charge from the traction battery and the circumstances under which it occurred. At the same time, specific measures are proposed to improve the overall autonomy of such a vehicle.

Keywords: Electric vehicle, State of charge, Traction battery, Urban driving.

1 Introduction

In the last period, the number of road vehicles equipped with the electric energy source has increased, experiencing a spectacular evolution. This is also due to the fact that the electric infrastructure for charging the traction batteries has developed progressively, ensuring the need for mobility in this segment of electric vehicles [1]. Even if for the moment there has not yet been a development of the charging infrastructure that would fully meet the needs, the evolution is continuous and sustained [2].

Also, the performance of traction batteries has increased, knowing the fact that, with a traction battery that has a higher energy storage capacity, the range increases considerably [3]. It is known that, in addition to the power of the battery, the range is dependent on many factors such as, the materials used in the construction of the battery, the outside temperature, the mass of the vehicle, the way of use, the speed or its destination [4] [5].

The legal provisions applicable currently at the European level require that, in the case of electric vehicles the range to be obtained by repeated driving under laboratory conditions. Thus, after charging the traction battery to 100%, the vehicle runs continuously following the speed allure of the WLTC cycle (World-wide harmonized Light duty Test Cycle) until the battery is completely discharged [7].

After obtaining the range, it is communicated together with the technical characteristics of the electric vehicle in the technical data sheets and commercial brochures of the product. As is known, at the current moment the testing of vehicles in laboratory conditions using the dynamic bench where, all the particular conditions regarding temperature, humidity and others. can be easily achieved, manage to reproduce to a great extent but not entirely the real operating conditions of the vehicle.

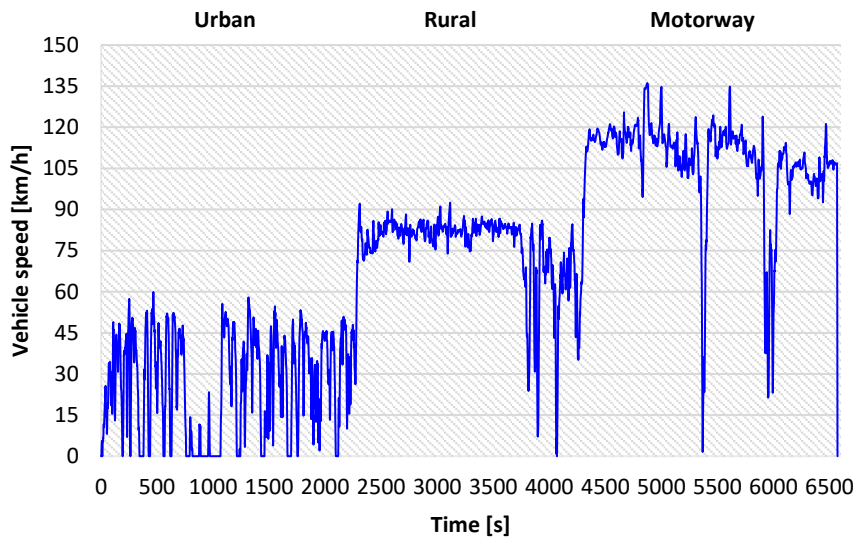


Fig. 1. The vehicle speed obtained using the testing in real driving conditions [6]

Considering the previously mentioned, through this paper the authors proposed to obtain scientific information based on experimental research concerning the decrease of the state of charge of the traction battery but in real driving conditions. To carry out the experimental research, the RDE (Real Driving Emissions) test was selected. After this type of testing can be obtained an allure of vehicle speed as shown in fig.1. This test method in real driving conditions is currently applicable for vehicles with thermal engines in order to determine the pollutant emissions.

Knowing the fact that most current electric vehicles generally run in urban areas, the research will be limited only to the urban driving area. The urban driving area is characterized by vehicle speeds lower than or equal to 60 km/h and the minimum distance operation shall be 16 km. From the total duration of the cycle the urban driving shall however never be less than 29%. Also, the average speed including stops of the urban driving should be between 15 and 40 km/h [8].

2 Experimental Research

The experimental tests were carried out using an electric vehicle with 5 seats. After fully charging of the traction battery the vehicle was parked outside, the value of the outside temperature being between 20°C and 30°C. During the tests the vehicle's comfort system was permanently switched on to create optimal conditions in the passenger compartment. Also, two people were permanently in the electric vehicle, the driver and the person who monitored the data acquisition equipment. The main technical characteristics of the vehicle under research are:

- Maximum speed: 140 km/h;
- Own weight: 1500 kg;
- Front traction;
- Maximum power: 65 kW;
- Maximum torque: 200 Nm;
- Traction battery technology: Li-Ion, (NMC) Lithium-Nickel-Mangan-Cobalt 400V.
- Traction battery power: 22 kWh;
- Type of charging applied to the traction battery: single-phase slow charging, power 2.3 kW/h.

From all these tests, the 2 most representative results were selected for presentation, being indicated in graphic form the urban speed profile obtained and the evolution of the state of charge of the traction battery.

Table 1. Specific test parameters

| | Urban [Test 1 Fig.4] | Urban [Test 2 Fig.5] |
|-----------------------------|--------------------------------|--------------------------------|
| Duration (s) | 2281 | 2154 |
| Distance (km) | 16.71 | 20.59 |
| Average speed (km/h) | 26.38 | 34.42 |

In table 1 are indicated for the 2 representative tests, the resulting regarding the duration of the test, the distance traveled and the average speed obtained, and can be observed that in the case of both tests the imposed test conditions are met, which validates the test conditions. Also, to highlight the way in which the electric vehicle was subjected to the test from a dynamic point of view, using special equipment during the testing period certain information of interest was permanently acquired from the electronic

control units. Perhaps the most important parameter that indicates the dynamic loading of electric vehicles is the information regarding the position of the accelerator pedal

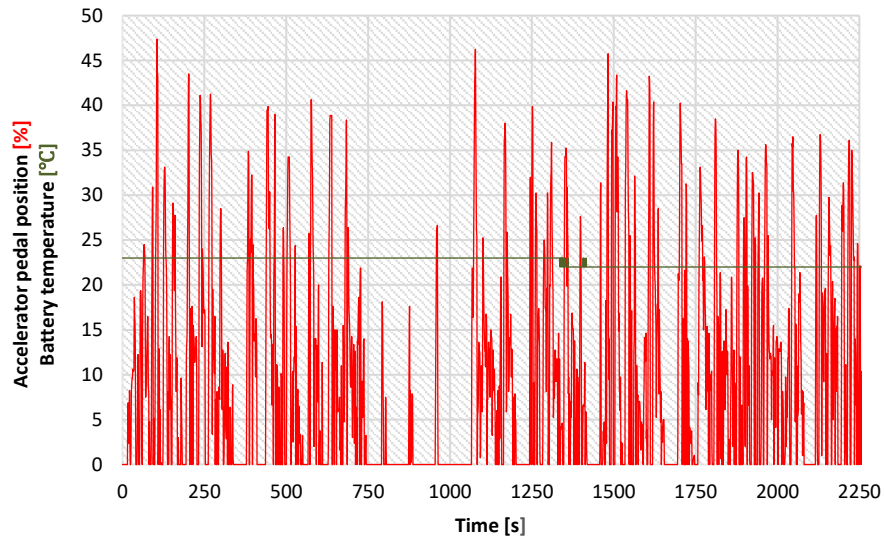


Fig. 2. The accelerator pedal position and the temperature of the traction battery during test 1

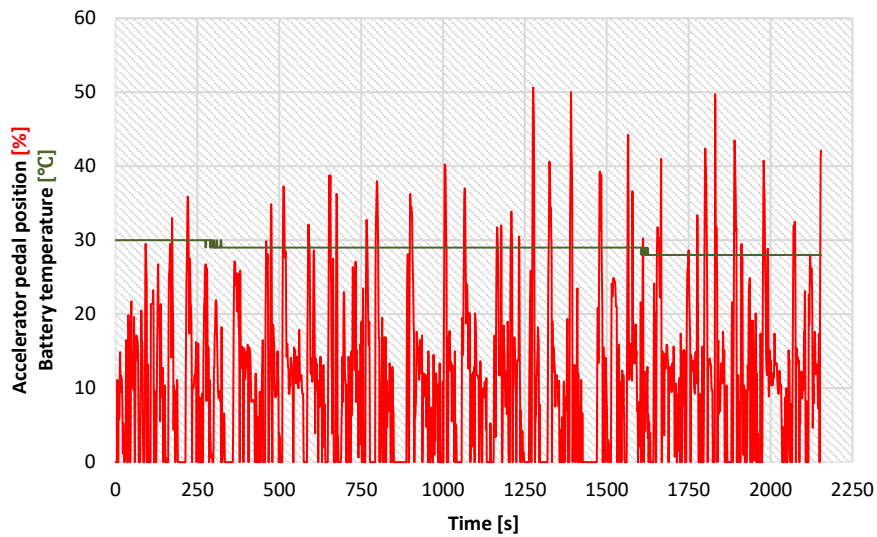


Fig. 3. The accelerator pedal position and the temperature of the traction battery during test 2

In Figures 2 and 3, can be observed the position of the accelerator pedal during each test, which, in addition to information on the dynamic loading of the vehicle show and information regarding the restrictions imposed by the traffic condition, which cannot be the same every time. At the same time, to corroborate the information regarding the load to which the vehicle is subjected and the decreasing of the state of charge from the traction battery, information concerning the internal temperature of the traction battery was also acquired.

3 Results and discussions

As a result of experimental tests carried out in the urban driving area, was highlighted the mode of decrease of the state of charge from the traction battery, being presented in graphic form for both tests the evolution of the speed of the electric vehicle and the state of charge of the traction battery.

In the case of both tests indicated in figures 4 and 5, it is observed that the mode of decrease of the state of charge from the traction battery is linear and progressive. It can be observed that, in the case of the test 1, after a single run in the urban driving area specific to the test in real conditions, the state of charge of the traction battery decreased by only 6.5%, so an electric power consumed from the battery of approximately 1.43 kWh. In the case of test 2, the situation is similar, the state of charge of the traction battery decreased by only 7.3%, so an electric power consumed from the battery of approximately 1.60 kWh.

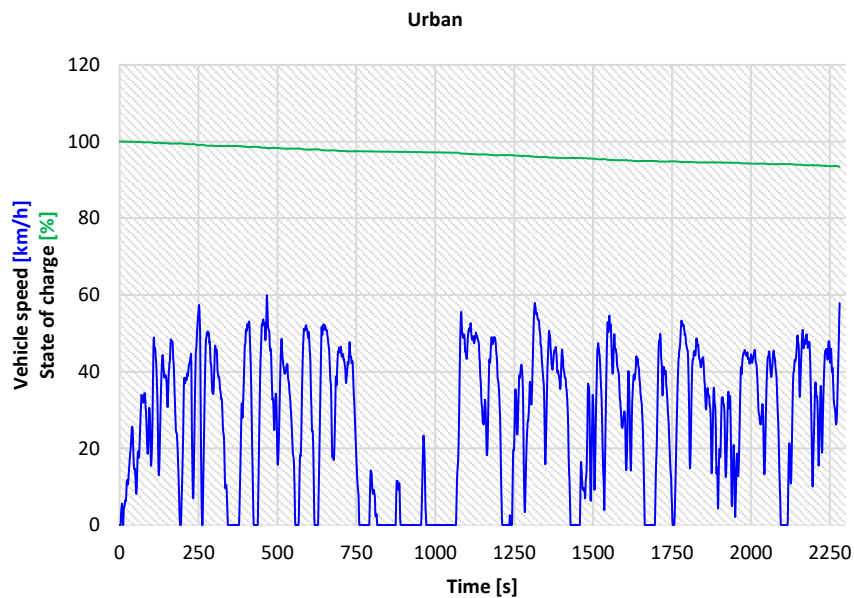


Fig. 4. Evolution of SOC of the traction battery in the case of urban driving, test 1

Thus, even if the vehicle has not been driven until the battery was completely discharged because the objectives of the work were different, by analogy knowing the values obtained after a single test, we can estimate that, in the same conditions to discharge such a battery, characterized by a power of 22 kWh, it would have been necessary of approximately 14 urban test cycles.

Obviously, the linear and progressive decrease of the state of charge of the traction battery corroborated with the reduced consumption of electric power it is also explained by the fact that in urban driving conditions there are many situations in which energy can be recovered, it is practically the most favorable running mode to ensure the recovery of electrical power.

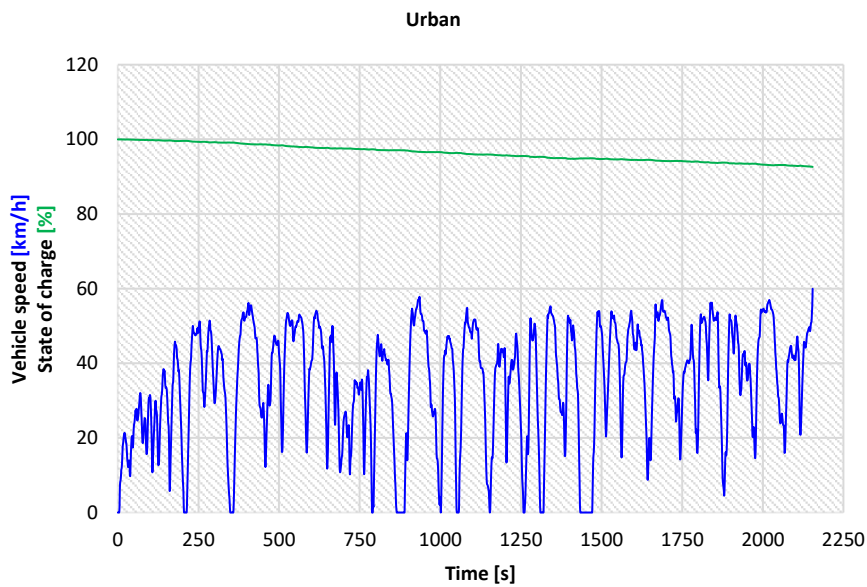


Fig. 5. Evolution of SOC of the traction battery in the case of urban driving, test 2

Analyzing the variation of the accelerator pedal position, it can be seen that during both tests, there are many moments when the accelerator pedal is released, occasion with which the electric power is recovered in the traction battery. From a graphical point of view, the state of charge status displayed as a percentage, has only a decreasing allure but in reality, energy recovery is present, practically increasing the time allocated to each percentage of charge.

Also, regarding the internal temperature of the traction battery, it can be seen that in the case of both tests, this remains at approximately the same value but this aspect can be influenced by the value of the outside temperature, the temperature of the asphalt, and where it is the case by the additional cooling method applied to the battery. In the present case the battery is additionally cooled with cold air from the air conditioning system. Based on the results obtained, it can be easily observed that electric vehicles

respond very well to use in urban conditions, situation favored by low energy consumption but also as a result of the multiple energy recovery conditions. All this, in the case of urban use, makes the electric vehicle a solid alternative to vehicles that use other energy sources.

4 Conclusions

Both tests presented in the paper, indicates that the decrease of the state of charge of the traction battery is linear and progressive. It can be observed that, in the case of the test 1, after a single run in the urban driving area, the state of charge of the traction battery decreased by only 6.5%, so an electric power consumed from the battery of approximately 1.43 kWh. In the case of test 2, the situation is similar, the state of charge of the traction battery decreased by only 7.3%, so an electric power consumed from the battery of approximately 1.60 kWh.

The linear and progressive decrease of the state of charge of the traction battery corroborated with the reduced consumption of electric power it is explained by the fact that in urban driving conditions there are many situations in which energy can be recovered, it is practically the most favorable running mode to ensure the recovery of electrical power.

Regarding the internal temperature of the traction battery, it can be seen that in the case of both tests, this remains at approximately the same value but this aspect can be influenced by the value of the outside temperature, the temperature of the asphalt, and where it is the case by the additional cooling method applied to the battery.

Current electric vehicles respond very well to use in urban conditions situation favored by low energy consumption but also as a result of the multiple energy recovery conditions. All this, in the case of urban use, makes the electric vehicle a solid alternative to vehicles that use other energy sources.

References

1. Buchmann, I.: Batteries in a Portable World, 2nd end. Cadex Electronics Inc. (2001).
2. Paul, D., Stănescu, O., Electric, hybrid and fuel cell cars, Politehnica, Timișoara (2015)
3. Jeong, N.T., Yang, S.M., Urban driving cycle for performance evaluation of electric vehicles. *Int. J. Automot. Technol* 17(1), 145-151 (2016)
4. Bamban, V., et al.: Analysis of range extender electric vehicle performance using vehicle simulator. *Energy Procedia* 68, 409-418 (2015)
5. Shi, Q., et al.: The study of a new method of driving cycles construction. *Procedia Eng.* 16,79-87 (2011)
6. V Nisulescu et al, Experimental research regarding the autonomy of electric cars in real driving conditions, *IOP Conf. Ser.: Mater. Sci. Eng.* 1303 012001 (2024)
7. EUR-Lex Homepage, <http://data.europa.eu/eli/reg/2017/1151/oj>, last accessed 2024/06/21
8. EUR-Lex Homepage, <https://eur-lex.europa.eu/eli/reg/2018/1832/oj>, last accessed 2024/06/25

Flying Taxis as a Solution for the Future

Arghirescu Marius¹ and Spiridon Lucian²

¹ OSIM, Bucharest, RO; GCI-DLMFS-Romanian Acad.

² CRIFST-Romanian Acad., RO

marius.arghirescu@osim.gov.ro

Abstract. It is known that the development of the electric car and rechargeable electric battery industry has also led to the creation of prototypes of flying taxis by private companies, commonly defined as passenger drones also known as 'urban air mobility vehicles', which can also travel 1-6 people over inter-urban distances, usually. The paper presents the main technical solutions known for flying taxis, built or designed by various companies, differentiated mainly by the use/non-use of airplane wings in connection with propulsion assemblies: electric motor-propellers and by the way they are arranged and oriented in relation to the main body, of command and passenger transport. The issue of producing more efficient electric batteries, usable by such vehicles, as well as the possibility of using the Coanda effect for the vertical ascent of some electric flying taxi vehicles are also analysed.

Keywords: flying taxi, electric propulsion, Coandă effect.

1 Introduction: The tendency of flying taxis development

1.1 The main known companies of flying taxis

In most cases, the flying taxis have the form of super-sized, passenger-carrying drones, known as electric vertical take-off and landing (eVTOL) aircraft.

Most flying taxis, constructed or only designed, use more than two propellants in form of assemblies: electric motor-propeller and can usually carry 1-5 persons.

There are more than 20 companies involved in the development of air taxi technology:

Joby Aviation, (US); Volocopter and Lilium, (Germany); Airbus, (European multinational Comp.); Archer Aviation, (San Jose, US); Vertical Aerospace, (Bristol, England); Wisk, (Mountain View, US); EHang Holdings, (China); Urban Air Port Limited, (Coventry, UK); Beta Technologies, (Vermont, US); Hyundai (South Korea); Jaunt Air Mobility, (US + Canada); Terrafugia Transition, (China); Ascendance Flight Technologies, (Airbus, Toulouse, FR); BOEING Company, (US); Eve Air Mobility, (Brazil); Overair, (Santa Ana, CA); Flying taxis, (Archer&Joby Aviation); VerdeGo Aero Inc., (Daytona beach, US); VIA Transportation Inc., (New York, US); SkyDrive (Toyota city, Japan).

Also, NASA's Ames Research Center in California's Silicon Valley is interested in developing of flying taxis technology, in collaboration with Joby Aviation [1].

1.2 The main known solutions of flying taxis

In can be identified 3 general types of flying taxis:

- a) Without wings, having only electric propellants, as that made in China, (Fig. 1), using at least six sets of two contra-rotated propellers, or that planned for Dubai, (fig. 2), using more than ten simple electric propellants [2].



Fig. 1. Air taxi without wings, [1].



Fig.2. Volocopter, [2].

A particular case is that of a model chosen by the company SkyDrive Inc. (Toyota city, Japan), using only four sets of contra-rotated electric propellants for a light air taxi [3] (Fig. 3, Fig. 5), a similar solution being adopted also by a variant designed by Airbus Helicopters, but for a heavier air taxi, having high diameter propellers (Fig. 4).



Fig. 3. Air taxi of comp. SkyDrive Inc., [3].



Fig. 4. Air taxi of comp. Airbus Helicopters.



Fig. 5. a), b). Air taxi of comp. IndiGo and Archer, [4].

b) With wings and electric propellants.

In this category, we can identify two sub-groups of flying taxi models:

b1) with two pairs of wings and at least four electric propellants for ascension, as that designed by IndiGo owned by InterGlobe Enterprises and by the firm Archer, supported by Boeing (Fig. 6), [4], at least two electric propellants having rotatable orientation;

b2) with a single pair of fixed wings having attached electric propellants with adjustable orientation (Fig. 7), [5];

b3) with a single pair of orientable wings having attached electric propellants with fixed orientation in report to the corresponding wing (Fig. 8), [6];

b4) mixed variants (with a pair of fixed electric propellants attached to fixed wings and at least a pair of electric propellants with adjustable orientation)



Fig. 6. a), b) Flying taxi with two pairs of wings and orientable electric propellants, [4].



Fig. 7. a), b), Flying taxi designed by Archer Aviation, [5].



Fig. 8. a), b) Airbus' flying taxi tested in Eastern Oregon- US, [6].

1.3 Remarks regarding the electric batteries usable by a flying taxi

An air-craft battery must function well at low temperatures and a rapid rate of discharge.

The used electric batteries for air taxis are usually the lithium-ion aircraft batteries, but rechargeable sodium-ion batteries (SIBs) are considered as the most appealing alternative to lithium-ion batteries (LIBs) regarding the limited natural abundance and increasing consumption of Li resources, [7], because similar to LIBs, Na⁺ can be the charge carrier to achieve electrochemical energy storage in SIBs. However, sluggish mobility of Na ions results in relative lower energy density and poorer kinetics than LIBs. NASA is also interested in research for high-performance battery cells and safety testing aimed at advanced air mobility (AAM) uses and space applications, in collaboration with Archer Aviation [8]. Archer recently announced plans to start air taxi operations in Abu Dhabi and Dubai in 2026.

Also, the company AMSL Aero plans to use the \$3.6 million grant from the Australian Renewable Energy Agency (ARENA) to develop a fuel cell system to power electric aerial vehicle (EAV –figure 9), designed to aid first responders and emergency personnel in reaching Australians living in regional and remote areas [9].



Fig. 9. EAV model of AMSL Aero, [9].

Other types of solution for electric batteries are: Lithium Oxy-halide; Lithium/Fluorinated carbon; Silver-Zinc; Silver-Aluminum; Nickel-Metal Hydride; Nickel-Cadmium.

2. Un-conventional types of flying taxis

There are few types of un-conventional solutions of flying taxis:

2.1. The company Jump Aero recently received \$3.6 million in contracts from the U.S. Air Force to accelerate the company's technology development. Part of the funding is targeted to fund the first full-scale prototype, JA1 Pulse, (Fig. 10), [9].

The first orders for the JA1 Pulse electric aerial vehicles (EAV) came from Falck Ambulance Service, which is a global first-response business with operations in 26 countries. The JA1 Pulse, in development since 2019, is intended to fly with emergency equipment to unimproved landing zones in rural areas with the aim of reducing emergency response times. The company promises a speed of up to 458 km/h.

The JA1 Pulse model uses two pairs of wings with attached electric propellants, symmetrically disposed in report to the air taxi's body, as in Fig. 10. **2.2.** In April 2017

the Munich-based startup Lilium demonstrated the first flight of its two-seater prototype VTOL (vertical take-off and landing jet –fig. 11), which could reach speeds of 297 km/h powered by 36 electric jet engines smaller than the electric rotors used by other flying taxis..



Fig. 10. The JA1 Pulse model, [9] (credit: Jump Aero).

EAV jet maker Lilium recently announced that ArcosJet DMCC is going to purchase 10 of its electric jets and become the exclusive dealer for its private jets in the region, [10].



Fig. 11. a), b). Lilium’s electric VTOL jet, [10].

The technical solution for this variant of air taxi is the including a set of 12 and of 6 electric propellants in a single structure rotatable attached on the back part of two pairs of wings, as in Fig. 12.

2.3. Another un-conventional type of flying taxi looks like a normal airplane with two wings and a main propellant in the air-plane’s nose, with the difference that in a relative large hole of each wing it has an electric propellant for airplane’s ascension, (Fig. 12), [11].



Fig. 12. Air taxi with electric propellants included in wings, [11].

3. The possibility of Coandă effect's use for flying taxis

3.1. Coandă lenticular aerodyne

The lenticular aerodyne - made by the Romanian inventor Henry Coandă (1886-1972) based on the Coandă effect, represents a discoid-shaped device, where the lifting force is obtained by sending a fluid (air, steam) under pressure along the lenticular-shaped aerodynamic profile of its body so as to achieve both an increased dynamic pressure, necessary for the production of levitation bearing force by the local decrease of the static pressure, according to Bernoulli's law, ($p_s + p_d = \text{constant}$), as well as the attraction inside this fluid of a quantity of surrounding air that increases the total flow rate and the lifting force, increasing the dynamic pressure above the aerodynamic profile and by creating a propulsive jet of fluid below the ship (Fig. 13; Fig. 14, Fig. 15, a), 1970, [12].

For the flight controls, some fins with a vertical axis and a kind of ailerons with a horizontal axis can be used, to deflect the jet of air sucked in from above the ship and sent along an aerodynamic body to the bottom of the ship, as in the model made by GFS-UAV (Fig. 15, b), [13].



Fig. 13. Coandă aerodyne, FR 796.843/1932, [12]. Fig. 14. Coandă aerodyne, 1965.



Fig. 15. a),b). Coandă aerodyne: a) of "D. Leonida" museum [12]; b) tested by J.L. Naudin

3.2. Types of drones or aircraft using experienced Coandă effect

A functional drone with Coandă effect is the one tested by Jean Louis Naudin, (Fig.15, b, Fig. 16, a), [13]. Another drone with a similar Coanda effect, was made and tested in Romania as part of a MEDIAS-UAV project (national grant: 2008, Galati-Iași-Bacău (Fig. 16, b), [14], which has as a novelty the provision of a toroidal camera with helium.

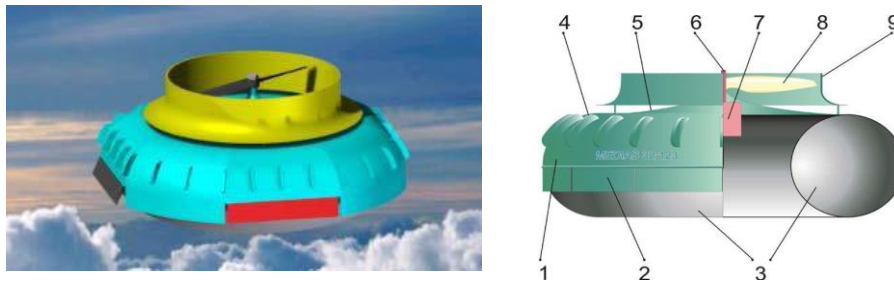


Fig. 16. Aerodyne type drone, without or with He chamber: a) Experimented by J. L. Naudin; b) MEDIAS-UAV -type.

To these drones, the air is sucked from above the drone and sent to the profile of the upper part through the circular slot generated between the drone casing and a cylindrical part above it, the Coandă effect being generated at the surface of the casing. For horizontal movement manoeuvres, magneto-electrically controlled flaps were provided at the edge of the drone's 'skirt', as in Fig. 15, b) and Fig. 16, a).

In 2007, Geoffrey Hutton and GFS Projects Ltd., with the invention of patent document GB2424405/2005, won a contract with the US government with an aerodyne project like that experienced by J. L. Naudin, (figure 16, a), but with the particularity that it used an electric motor built into the upper part of the drone housing, (Fig. 17), [15]. A craft having a rotor 9A producing a flow over an aerodynamic (e.g. domed) surface 1, to create lift or thrust, the gyroscopic effect of the rotor, when driven at full power, is such as to give the craft positive stability. The rotor may comprise part of a radial flow fan 2, having blades 9C, and a heavy annular magnet 9B cooperating with fixed coils 7A for effecting drive of the rotor. The resulting angular momentum of the rotor may afford gyroscopic stability enabling the craft to hover close to the ground or a vertical surface. Pitch and roll control may be achieved by vanes PV1, PV2, RV1, RV2 controlled electronically in response to rotation sensed by optical gyroscopes S1, S2 and taking gyroscopic precession into account.

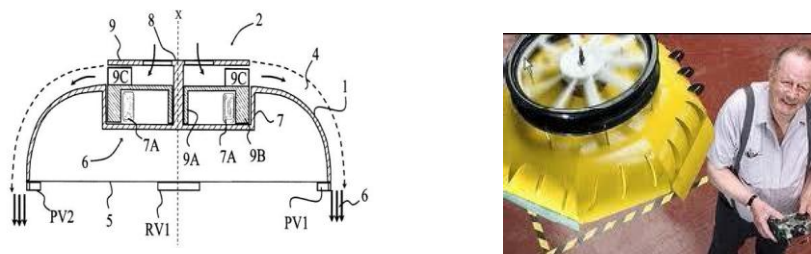


Fig. 17. Aerodyne with Coanda effect made by G. Hutton.

A 'flying saucer' variant with a pilot, with operation based on the Coanda effect, was tested by the US Army and by the Canadian AVROCAR project (1956- figures 18, 19, [16]), but they were not considered perspective solutions. In this variant, the air was sucked in axially and sent to the edges of the lower part of the casing, but also in the axial direction (Fig. 19).

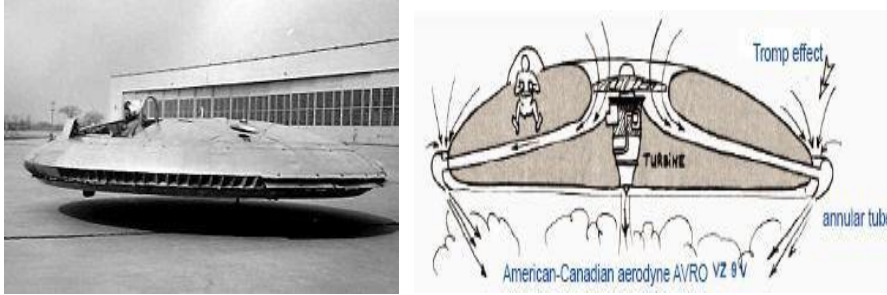


Fig. 18. The Avrocar variant- in testing. Fig.19. The Avrocar variant – functioning scheme.

3.3. The Liciar Cyclonoid

The Liciar method of achieving a useful traction of over 10,000 kgf/m using a 50 HP engine, uses a rotor that instead of rotor blades, has concentric rings of progressive diameters (overlapping rotary ring systems), with small rectangular blades with the length parallel to the rotor axis and with the width at an angle to the tangent to the rotor circle, through which, during rotation, the air from the inner area is sent to the surface of the air foil type of a lenticular aircraft, thus creating a vacuum above it that generates a propulsive force, which in the case of using this Liciar turbine (Fig. 20, a) is obtained with a higher yield even than that obtained by Henri Coandă through the system used by him, [17].

Such a propeller is very light, does not occupy more than 1.5 square meters and it was experimentally created and tested in Romania in the presence of an OSIM referent and of a Soviet commissar who took the invention in the USSR. Liciar obtained patent RO21370 for his invention (Fig. 20, b).

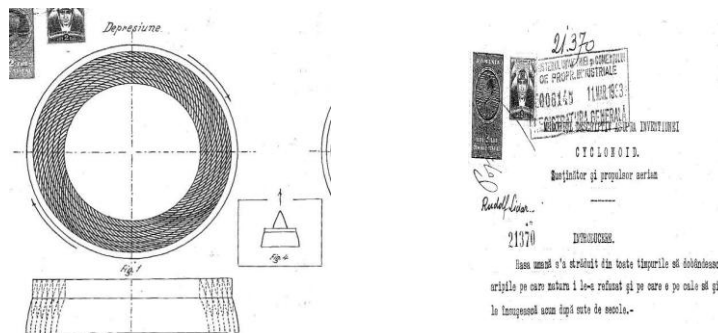


Fig. 20. Liciar-type propeller (patent document).

3.4. Un-tested solutions for drones/aircraft using the Coandă effect and Liciar-type propeller

A technical un-tested solution using the Liciar type propeller was proposed by the first author in the patented invention “Solar drone”, (RO132245 B1, [18]), which relates to the use of photovoltaic batteries with plastic support on the upper part of a drone’s frame and of the Coandă effect, (fig. 21, a), the main novelty part consisting in the using of at least one propellant with mixed, axial-radial suction, for generating axial airflow, made of simple or double funnel-shaped bodies and an electric motor rotating a propeller of mixed type, with a part with thin radial blades fixed to an edge part with rectangular slots and some small rectangular blades forming a Liciar type turbine, for air intake both from above and from the side, as in Fig. 21, b.

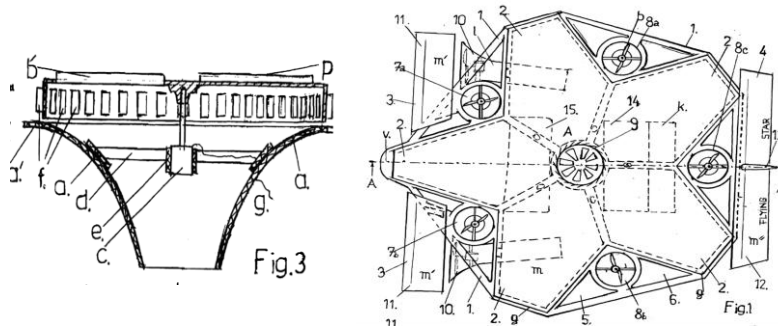


Fig. 21. Solar drone (RO2016-00298) using a thruster generating Coandă effect.

Two un-tested variants for the use of Coandă effect for a flying taxi using thrusters with axial-radial air aspiration were proposed in two patent applications of the first author: RO2018-00290 (Fig. 22, Fig. 23) [19], and RO2023-0019 (Fig. 24) [20].

The solution presented in Fig. 22 uses a propeller with mixed, axial-radial suction, realized as in figure 23, with radial blades having attached as in their top a shorter blade oriented in angle of 30°-35° related to the tangent of the rotation' circle and in another angle β related to the rotation axis, which increases the flow of air ejected downstream by also collecting air from the level of a discoidal aerodynamic profile, with the generation of the Coandă effect.

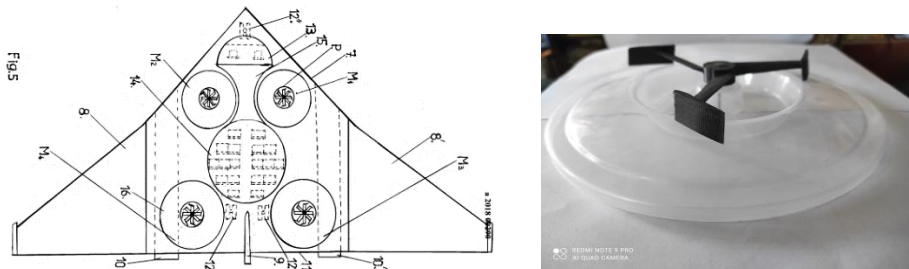


Fig. 22. Air taxi having Coandă effect propellants. **Fig. 23.** Propellant using Coandă effect .

Another un-tested solution, presented in Fig. 24, was proposed by the first author in the patent application RO2023-00019 with the title: “Reactive hybrid thruster with Coandă effect and flying taxi type aircraft that use it”, uses the Coandă effect through propellers with optimized radial-axial air intake and with a mixed engine: electric- for starting and thermo-reactive for ascent - a stage in which the engine their electric generator becomes a dynamo for producing electric current to re-charge the electric batteries needed for electric thrusters for horizontal advancement (stage in which the lift force is generated through the wings -figures 24, a), b)).

However, the proposed solutions of Fig. 23 and Fig. 24 present as a disadvantage the fact that the thrusters using the Coandă effect can only be used for ascent, not for horizontal flight.

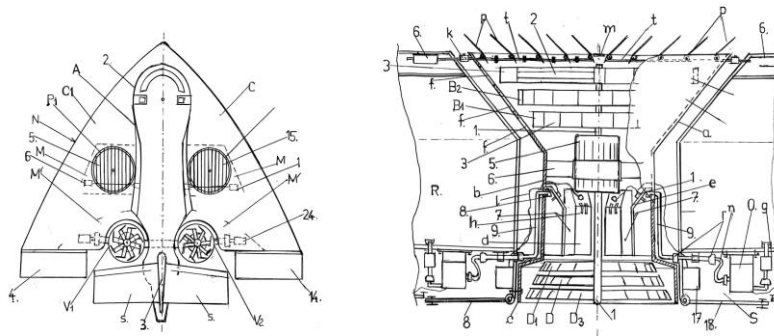


Fig. 24. Air taxi using Coandă effect and a hybrid engine: electric and thermo-reactive.

A flying taxi solution, proposed by the first author, which can use the two thrusters with the Coanda effect, provided for ascent, and for horizontal flight, is the one presented in Fig. 25, in which is provided also the possibility of rotating the assembly: electric motor-mixed propeller relating to the plane of the wings and of the aerodynamic profile generating the Coandă effect. The aerodynamic profiles for Coandă effect can also contain rubber chambers with He, usable and as safety means.

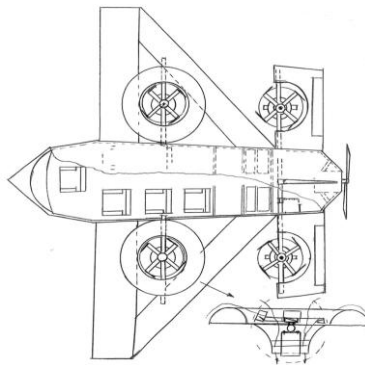


Fig. 25. Flying taxi which uses two thrusters with Coandă effect, provided for ascent but also for horizontal flight.

4. Conclusions

The variants of flying taxis presented in the paper show that there are already solutions of the future, competitive and from a financial point of view with the usual means of land transport, which, unlike current airplanes and helicopters, can be realized with ecological engines, electrically powered by accumulator batteries or high-performance fuel cells.

It results also that all flying taxi variants designed or already made by companies interested in the development of these transporting machines use conventional means of obtaining ascent, without the use of the Coandă effect.

In Ref. [21] it was shown that with the current prototype using Coandă effect, with the air flowing down on aerodynamic profile, only a small amount of lift can be achieved, which would not be sufficient for the unmanned aerial vehicle (UAV) to take off, even if the introduction of Coanda jets should, in theory, increase the amount of entrainment from above the wing, one proposed experiment involving the use of a fan to increase the velocity of air circulation around the wing, as we know that lift increases with air velocity squared, the conclusion being that the feasibility of using the Coanda Effect for a commercial UAV as AVROCAR variant is more apparent.

However, in Ref. [22] it was shown that the Coandă effect is not yet used at its full potential and capabilities, because some Coandă effect applications developed so far proved to be very efficient from energetic point of view, specific experiments [22] indicating that for the same energy available P_0 in order to obtain the highest force possible for an available used energy it is preferable to put into motion the highest amount of fluid possible with the lowest speed possible instead of a small amount of fluid put into motion with a high speed.

We can conclude on the base of this experimental result that a variant of flying taxi as that presented in figures 22-25, using propellers with mixed axial-radial air suction, could be of practical interest in correlation with the need to combine flight performance with the passenger safety requirements.

References

1. <https://www.jobyaviation.com/>
2. www: „Air taxis launched in Dubai” /TimesofIndia.com /Travel News, May 12, (2024)
3. <https://en.skydrive2020.com/>
4. <https://www.news18.com/explainers/flying-taxis-to-cut-travel-time-between-delhi-and-gurugram-to-7-minutes-how-will-it-work-explained-8883551.html>
5. Arindam M., “Come '26, hailing an air taxi may become a reality”, The Economic Times, 20 Apr. (2024)
6. Banse, T., „In The Skies Of Eastern Oregon, An Autonomous Robo Taxi Takes Flight” PB News, 10 Oct. (2019)
7. Gaddam, R. R.; Zhao, G., Handbook of Sodium-Ion Batteries, (2023).
8. Martin, C., “Flying Taxi Company Moving to Production; Final Testing Next”, IOT World Today, 7 Feb., (2024)

9. Martin, C., "Flying Vehicle Startup Funded for Air Ambulance; Hydrogen-Powered", IOT World Today, 20 Nov., (2023)
10. Martin, C., "Flying Taxi Company Sells 10 Electric Jets; Customers in Mideast", IOT World Today, 16 Nov., (2023). <https://lilium.com/>
11. Stokel-Walker, C., "UK plans for flying taxis by 2026 pie in the sky, expert says" UKTN News, Tue 19 Mar (2024).
12. Berbente C., "Scientific personality of Henri Coanda", Anniv. Session "Celebrating 100 year of the first jet aircraft invented by Henri Coanda", Romanian Acad., 15 December 2010, Bucharest, Romania; INCAS BULLETIN, Volume 2, Number 4/ 2010, pp. 3 – 10.
13. <http://jlnlabs.online.fr/gfsuav/index.htm>
14. Florin NEDELCUȚ –, "Coandă Effect aerodyne – a new platform concept for a fluvial and ecological remote sensing aerial vehicle", Univ. „Dunărea de Jos” Galați, CEDREN Seminar on UAV-based remote sensing in fluvial research Trondheim, Nov. 13, (2014).
15. Patent GB2424405/2005
16. <https://www.nationalmuseum.af.mil/Visit/Museum-Exhibits/Fact-Sheets/Display/Article/195801/avro-canada-vz-9av-avrocar/>
17. Lucian Cosma, "The Secret Science", Edit. Obiectiv, (2002)
18. Patent RO132245 B1
19. Patent application RO2018-00290
20. Patent application RO2023-0019.
21. Chris Barlow, Darren Lewis „Investigating the use of the Coanda Effect to create novel unmanned aerial vehicles" oai:eprints.soton.ac.uk:342110, 1 Dec. (2009).
22. Cârciu, I., Dinea, S., „Review of Applications on Coandă Effect. History, Theories, New Trends", Henri Coanda 100 - Celebrating 100 years from the first jet flight, Bucharest, Jan. (2010).

Biography of Prof. univ.eng. Radu-Emil Mărdărescu - the Creator of the Automobiles and Engines School at the Braşov Institute of Mechanics

Vladimir Mărdărescu and Marius-Daniel Călin

Transilvania University of Braşov, RO 500036, Romania
vlady.mardarescu@unitbv.ro

Abstract. The paper addresses the main biographical data about Prof. univ.eng. Radu-Emil Mărdărescu, respectively his family and education, professional experience, original contributions in the scientific engineering field and his academic activity. Radu-Emil Mărdărescu was born in Bucharest on February 19, 1907, in a family of intellectuals. In 1948, Radu E. Mărdărescu began teaching activity, focusing on the teaching courses in mathematics, mechanics and the strength of materials at the Forestry Institute in Braşov. In 1949, he founded the Department of Automobiles and Tractors within the Faculty of Mechanics. On this occasion, together with the engineer Silviu Crişan, he founded the Institute of Mechanics in Braşov. As a professor, head of department, he has a collaborative activity with the factories in Braşov, performing the first approvals for SR 101 engines and then partial approvals for SR 211 in the Engine Laboratory of the Braşov Polytechnic Institute. During his activity, Radu E. Mărdărescu obtained several invention patents in collaboration with the academia and industry factories. Professor Radu Mărdărescu's main passions, besides internal combustion engines, were: mathematics, astronomy, symphonic music, organic chemistry, classical Greek philosophy, the life of scientists, symmetry in nature and sports. He often said that a sports champion or a great performer of symphonic music is for us a model in terms of self-transcendence, which is the condition of human evolution.

Keywords: Mechanics, I.A.R. Braşov, Motor-Vehicles.

1 Family and Education

Radu-Emil Mărdărescu was born in Bucharest on February 19, 1907, in a family of intellectuals (Fig. 1).

His father, Emil Mărdărescu, a graduate of the University of Freiburg, was an university lecturer at the University of Iaşi, where he taught mining and processing technology courses oil and after the First World War became the owner of wells and oil lands and in 1910 he obtained an invention patent in the field of airplane propellers and two other patents dealing with rotary drilling.



Fig. 1. Professor Radu-Emil Mărdărescu (1907-1968)

His mother also comes from a family of intellectuals from which the names of his sister Margareta Cosăceanu-Lavrillier, a sculptor in Paris (where she worked in the workshops of the great masters Rodin, Brâncuși and Bourdelle) and his cousin, the great scientist Gogu Constantinescu, the inventor of sonicity, are worth mentioning.

In the Figure 2 it is highlighted the family of Radu Mărdărescu.



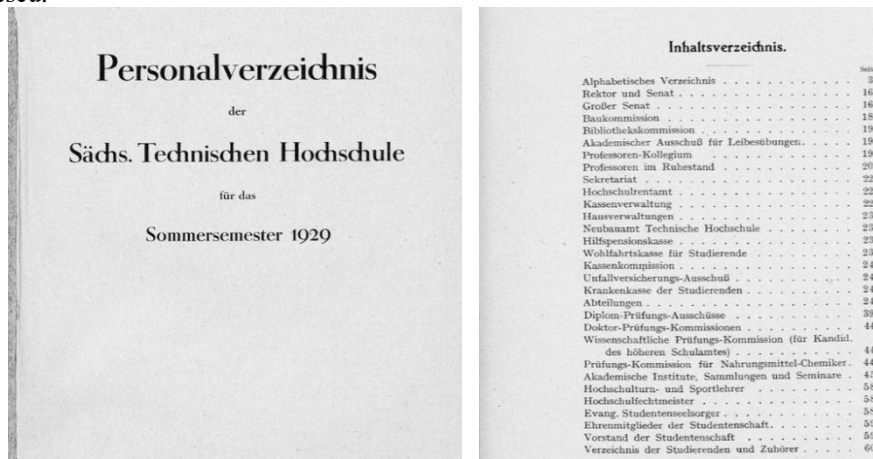
Fig. 2. Radu Mărdărescu with his family in Germany (from right to left: Radu Emil Mărdărescu, Emil Mărdărescu-father, Zoe Mărdărescu-mother, Vladimir Mărdărescu-brother)

During 1925-1926 he graduated from the 12th grade and obtained his baccalaureate at Gheorghe Lazăr High-school in Bucharest.

Growing up in this environment, Radu E. Mărdărescu asserted himself as a good mathematician during school, especially on the occasion of taking the Baccalaureate exam at the Gheorghe Lazăr High School in Bucharest, where he impressed the president of the committee, Professor Țițeica, by solving problems related to the satellites movement around the planets.

After finishing high school, he enrolled at the Faculty of Mathematics in Bucharest, where in the period 1926-1927, during one academic year of studies, he passed the exams for graduation up to the third year inclusive. Simultaneously, he completed his military internship at the Military School of Genius – as reserve officers. Here, together with his brother, he studies the problems of specific layouts of the front line, locations of warehouses, the construction of bridges for infantry, and locations for defense. At the Faculty of Mathematics, he formed a close friendship with the later great mathematician Grigore Moisil. In 1928, he went to the Dresden Polytechnic, where he was admitted after completing the internship for a year in all fields of engineering, from iron and steel industry to electrical engineering. Students were admitted here only after obtaining the appropriate qualifications for all the engineering fields in which they practiced. This year of practice was in fact a verification of the skills specific to the engineering fields, followed by the elimination of those who could not fit into the system of requirements of the University of Dresden.

Figure 3 shows the student catalogue of the Technischen Hochschule Dresden from 1929, in which Radu Mărdărescu name appears with his brother name - Vladimir Mărdărescu.



— 101 —

| Name | Geburtsort (bzw. Staatsangehörigkeit) | Studium | Imma- triku- liert | Wohnung++ |
|----------------------|--|---------|--------------------------|---------------------------|
| 1. | 2. † | 3. ** | 4. | 5. |
| Mannl, Walter | Dresden | B. | M 25 | Franklinstr. 25, II. |
| Manß, Gerhard | Chemnitz | B. | M 28 | Chemnitzer Str. 75, I. r. |
| Marangosoff, Nikolaj | Radewzi (Bulgar.) | H. | M 28 | Winckelmannstr. 43. |
| Marbach, Elisabeth | Stenn | M.N. | O 29 | Kl. Wolmsdorf, Gasthof. |
| Marcinkowski, Walter | Stettin | M.N. | O 25/28 | Schnorrstr. 70, I. r. |
| Marcus, Hans | Zeitz (Prß.) | M. | M 28 | Münchner Str. 1, I. |
| Mardarescu, Radu | Bukarest (Rum.) | M. | M 28 | Canalettostr. 28, Eg. |
| Mardarescu, Wladimir | Bukarest (Rum.) | M. | M 28 | Canalettostr. 28, Eg. |
| Crisan, Silvius | Neu-Arad (Rum.) | M. | O: 4/9 | Bendemannstr. 3, II. |
| Crome, Karl | Damme (Oldbg.) | H. | M 28 | Münchner Platz 2, I. |
| Cronstedt, Nils | Helsingfors (Finnl.) | M. | M 18/23 M 24 | Hübnerstr. 17, I. |

Fig. 3. The student's catalogue files of the Technischen Hochschule Dresden from 1929

The catalogue from Fig. 3 include the students name Radu Mărdărescu, Vladimir Mărdărescu (from pp. 101) and Silviu Crişan (from pp. 68).

Their colleague at the same university was Silviu Crişan, who after graduation worked at IAR Brasov, where he became Director of Manufacturing. In 1949, on the occasion of the establishment of the Institute of Mechanics in Brasov, Silviu Crişan founded the Machine Tools Department.

In 1935, Radu E. Mărdărescu was selected in the German North Pole exploration team. After a few months of training in polar climate conditions on the islands of the Nordic archipelago of Norway, he embarks on the expedition to the North Pole organized by the University of Dresden, where he was responsible for the research equipment of high-energy particles from the universe passing through the Earth's atmosphere, the main source of these particles being the Sun. In the same year, his father Emil Mărdărescu passed away and he was forced to interrupt the expedition.

In the Figure 4 it is highlighted the engineering diploma obtained by Radu E. Mărdărescu in 1936 at the Technischen Hochschule Dresden.

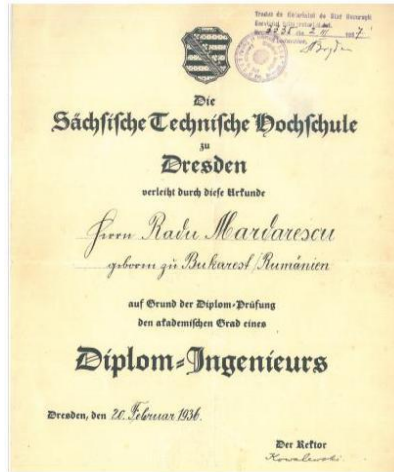


Fig. 4. Engineering diploma obtained in 1936 at the Technischen Hochschule Dresden

2 Professional Experience

In 1936, after obtaining his engineering degree, he returned to the country and joined the IAR-Braşov Aircraft and Engine Factories, where successively held the following positions:

- engineer, 1936;
- head of engine project office, 1939;
- head of engine research tests (experience) section, 1940;
- head of engine testing service, 1941;
- head of general engine design studies service, 1944;
- director of studies, 1947;
- chief construction engineer, 1949.

During this period, Radu E. Mărdărescu developed many technical solutions:

- Establishing the optimal distribution of the 1050 HP engine with 14 cylinders in double star type IAR 1000 A;
- Constructive studies of a series of 7 and 9 cylinder radial engines with powers between 250-400 HP.

In 1938, he proposed the construction of an 14 cylinders radial engine of 1500 HP, which represents as a novelty the construction of the compressor and the assembly of the crankshaft. On this occasion, tests are carried out on a single-cylinder engine to check combustion (identification of detonating regimes) and separately, on a specialized test bench, the parameters of the compressor are determined. The results being very good, the documentation is forwarded to the Ministry of War to obtain the necessary funds to build the functional model. The Ministry refuses to grant the funds and the project is handed over, based on the collaboration agreement, to the Gnome-Rhone company from France, which had granted the first aircraft engine manufacturing license to the IAR-Brasov company.

The engines are successfully made in France, but the Second World War breaks out and the Gnome-Rhone Factories are requisitioned by the German Army, which will equip the Gigant and Fokewolf planes with such engines. In 1944, Radu E. Mărdărescu led the design and construction of IAR 7M engine of 370 HP/ 2700 rpm (Fig. 5), one of the most efficient radial engines ever made, from the point of view of specific consumption and specific power.

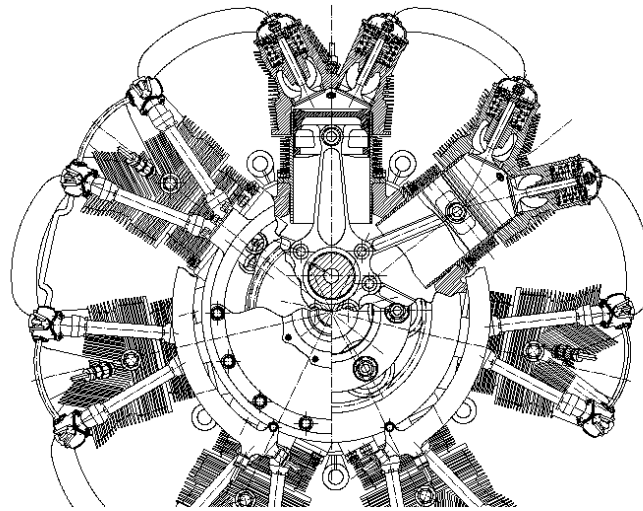


Fig. 5. Cross section through the IAR 7M engine

The main parameters of the IAR 7M engine are:

- Operating cycle SI 4 strokes;
- Bore 122 mm;
- Stroke 116 mm;
- Number of cylinders: 7 (radial);
- Mechanical Centrifugal Compressor Intake;
- Compressor drive ratio 9.62:1;
- Maximum supercharging pressure 1.5 bar;
- Power 370 HP;
- Nominal speed 2700 rpm.

In 1948, Radu E. Mărdărescu began teaching activity, teaching courses in mathematics, mechanics and the material resistance at the Forestry Institute in Braşov. In 1949, he founded the Department of Automobiles and Tractors within the Faculty of Mechanics. On this occasion, together with the engineer Silviu Crişan, he founded the Institute of Mechanics in Braşov.

In this period, under his leadership, the tractors IAR 22, IAR 23 were produced in approx. 16,000 copies, the IAR 002 prototype car in two variants and the IAR 003 moto-compressor. It should be noted that the IAR 002 engine with a displacement of

approx. 1 liter, fitted with a Roots supercharger, was produced during tests at the IAR Plant in 1946, with the power of 102 HP at a speed of 5200 rpm (Fig. 6).

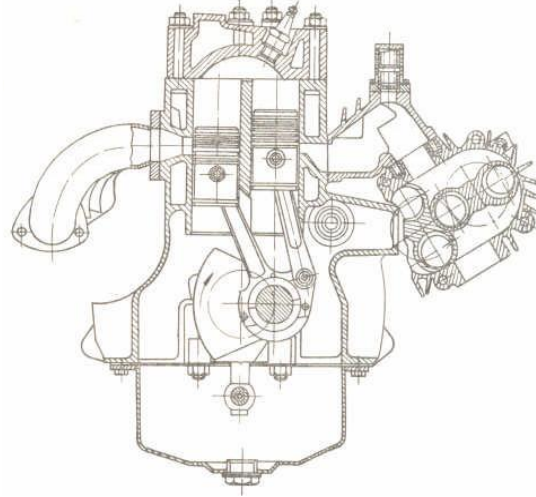


Fig. 6. Cross-section for the I.A.R. engine 002

In Figure 7, the drawing of the connecting rods for obtaining the optimal distribution diagram of the IAR 002 engine is represented.

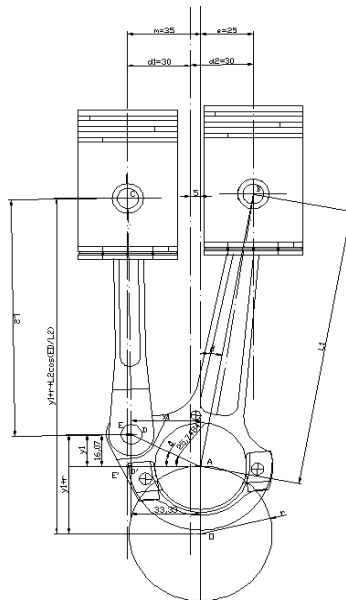


Fig. 7. The basic parameters of the articulated connecting rod solution at IAR 002 engine

The main parameters of the IAR 002 engine are (see Fig. 7):

- $L_1=140$ mm - antrax of the main connecting rod;
- $L_2=120$ mm - antrax of the secondary connecting rod;
- $r = 34.25$ mm - crank radius;
- $D=47.5$ mm - Cylinder bore.

In the Figure 8 it is shown the trajectories of the crank and the connecting rod joint relative to the axis of rotation of the crankshaft for the IAR 002 engine assembly.

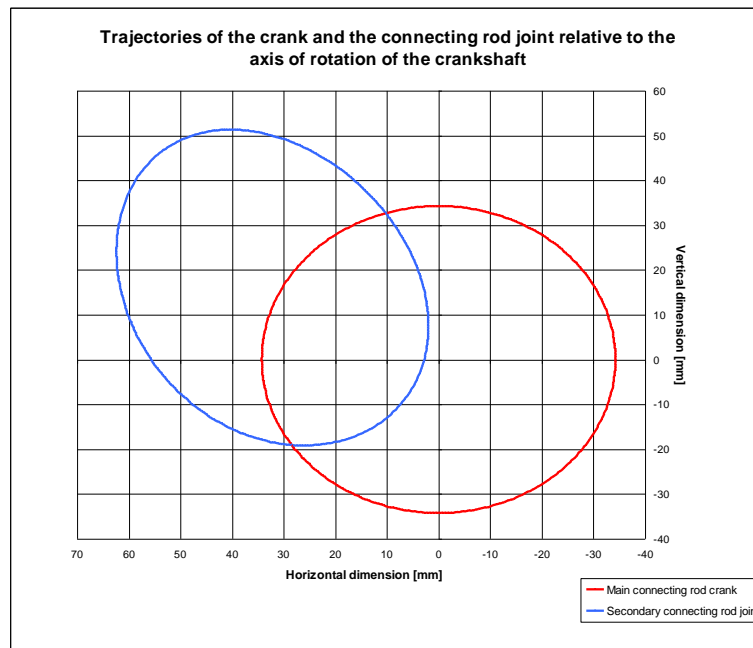


Fig. 8. Trajectories of the crank and the connecting rod joint relative to the axis of rotation of the crankshaft for the IAR 002 engine assembly

During 1945, the Management of the IAR Brasov plant decided to develop civilian production because the Soviet occupier prohibited the manufacture of military aircraft. The Management Staff of the Factory decided to produce automobiles, trucks and tractors. In 1946, two types of automobiles were produced, one sports and the other family, which were to go into mass production. The engines that equipped these automobiles were IAR 002 designed by engineer Radu Mărdărescu. As previously stated, the Soviet occupier decided only to manufacture tractors. The two prototypes of cars manufactured at IAR Brasov worked for 15 years in the service of the Tractorul Factory.

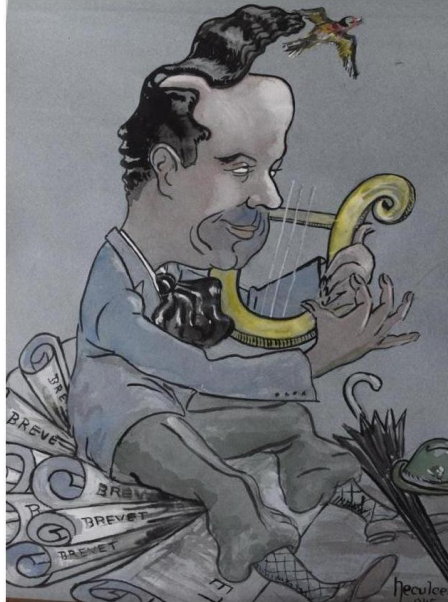


Fig. 8. Caricature of Eng. Radu Mărdărescu made by engineer I. Neculcea in 1945

Each engineer with an important contribution to the plant's activity received a caricature from engineer I. Neculcea, who in addition to good professional training also had a special talent in making caricatures. During this period, in 1945, engineer Radu Mărdărescu received from engineer I. Neculcea a caricature that defined him in the activity of Head of Motor Studies Office (see Fig. 8).

3 Original Contributions in the Scientific Field

Radu E. Mărdărescu developed original scientific works and studies, from which the following are highlighted:

1. The Thermotechnics Course from 1952, written to serve students specializing in the calculation and construction of engines for automobiles and tractors. The treatment is original and insists on the technical cycles of internal combustion machines, for which general formulas are given.

2. The Theory of Internal Combustion Engines - Course for Calculation and Construction of Automobile Engines, published in 1955 at Lithographia Invatamintului in Brasov (Fig. 9). This work is the first used in the didactic activity devoted to internal combustion engines. The structure of the work is based on the thermodynamics of internal combustion engines, the theoretical and real cycles of internal combustion engines, entropy, internal energy and enthalpy of gases, thermodynamic diagrams, indicated diagram, real heat balance, fuel combustion equations and considerations of the thermal process similarity theory etc.

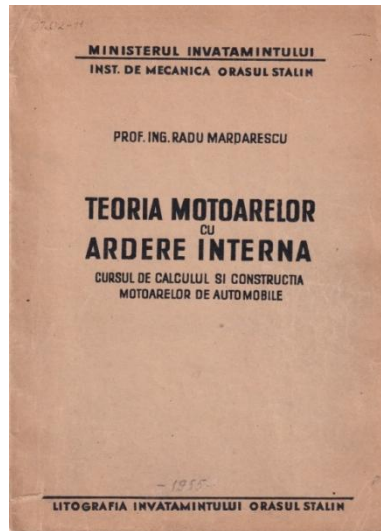


Fig. 9. Theory of internal combustion engines - Calculation and construction course of automobile engines, 1955, author Radu E. Mărdărescu

3. The specific sizes of internal combustion engines, scientific work in which, with the help of similitude method, the mechanical and thermal stresses in the engines are analyzed, giving the possibility to create new prototypes based on the results obtained on similar models (published in Rev. Metalurgia no. 4 of May 5, 1955).

4. The drive coefficient of the rotors of pumps and compressors depending on the number of blades and friction, in which the flows in the rotors of rotating hydraulic machines are treated, determining the drive factor of the fluid depending on the finite number of vanes, keeping taking into account the influence of the friction of the fluid against the walls of the channels. This work makes it possible to determine the dimensions of high-speed compressor rotors, depending on the number of vanes, where friction is an important factor. The established formulas give a closer approximation than those used previously.

5. The characteristic invariant of internal combustion engines. In this work, the conditions that must be met by a dimensionless number formed by the product of the numerical data imposed on the construction, conclude to be an invariant characteristic of each type of machine. As a result, the theory of the characteristic invariant of internal combustion engines is developed and the invader diagram is given depending on the thermal efficiency, which completely determines the optimal constructive characteristics and demands of the engine defined by the imposed data. The paper was presented at the Scientific Session of the Institute of Mechanics in Brașov in 1955.

6. Lubrication and wear of cylinders for internal combustion engines. It is a work of synthesis of the methods for determining the lubrication quality of cylinders of internal combustion engines, taking into account the laws of hydrodynamics and the chemical transformations of oils under the processes influence inside the engine.

7. Scientific principles of replacement of materials in the construction of machines, is also a synthesis work that takes into account the characteristics of the materials in the country. In the work, diagrams and numerical criteria are given for the replacement of deficient materials. The work was requested by ASIT Bucharest and was presented at the national consultation on the improvement of car construction in January 1955.

8. Fatigue resistance of cylinder liners for internal combustion engines. This work has an original character, establishing the similarity criteria for the variable stresses of cylinder liners and indicating a new method of material fatigue analysis for parts with certain stress characteristics. The paper also gives applications of the method on concrete cases.

9. The Internal Combustion Engine Theory course was written in 1955 for students involved in automobile and tractor construction. The theory of semi-ideal gases is extensively applied and a mathematical modeling of detonation in internal combustion engines is given. Applications of the similarity theory of internal combustion engines are also given.

10. Maximum compression ratio of spark ignition engines. In this work, the mixture detonation phenomenon is treated, taking into account the path traveled by the flame front and the ignition delay. This provides a functional link between the compression ratio, the final intake pressure and the cylinder diameter.

On this occasion, Professor Radu E. Mărdărescu established the relationship that defines the maximum compression ratio for spark ignition engines, as follows:

$$\varepsilon_{\max} = \frac{C_o}{a} \cdot \frac{\left(\frac{\lambda \cdot z}{V_H} \right)^{\frac{1}{9}}}{\sqrt[3]{p_A}} \quad (1)$$

where: C_o - octane number (Motor method);

a - constant defined by the constructive solution of the engine cylinder head;

λ - stroke/bore ratio of the engine;

z - number of engine cylinders;

V_H - engine displacement;

p_A - the final intake pressure in the cylinder.

The method was numerically verified on examples of engines from the country and abroad. The compression ratios of the SR-206, SR-207 and SR-211 engines were determined after this treatment, the results obtained being in accordance with reality.

11. Development of high peripheral speeds rotors based on dynamic similarity method. The scientific paper was elaborated together with Prof. Eng. Ioan Coșereanu from the Chair of Materials Resistance and was published in 2nd Volume of Scientific Works of the Polytechnic Institute of Brașov in 1957. The study raised the problem of determining the similarity criterion of resistance by analyzing the differential equation of moving rotors. By using the second similarity theorem, the invariant that determines

the points of the same resistance is deduced for similar rotors. By generalization, it results similar rotors that have equal stresses at corresponding points. As a result, normal rotors of equal resistance are determined. Finally, the transformation laws for series of affine rotors deduced from the normal rotor are deduced.

12. The propulsion efficiency of the terrestrial rocket. The paper was presented at the scientific session of the Polytechnic Institute of Brasov in 1957. By generalization, it is concluded that the propulsion efficiency of a rocket in a constant gravitational field is the ratio between the total energy stored by the rocket (kinetic and potential) and the kinetic energy of the fuel consumed. It results a formula of the general yield, compared to which the formulas used at that time in the specialized literature, represented a particular case. Also, calculation criteria of the rocket yield are established for constructive cases and the conclusion is reached that the maximum yield is a function of the gas ejection speed and the gravitational field. The optimal fuel utilization limits for the technical data of the modern rocket are indicated.

13. Vibration analysis on the intake manifold pipe of spark ignition engines. The paper was presented at the scientific session of the teaching staff of the Polytechnic Institute of Braşov in 1959. The purpose of the paper was to determine the resonance spectrum of the vibration of the intake gas column for establishing the optimal design of the intake pipe for a given engine. The differential equation of an elastic column with an infinite number of degrees of freedom (Riemann) is applied, adapting it to the boundary conditions of the considered case. For this, the pulsating phenomenon of the intake in the cylinder is developed in Fourier series. In conclusion, for the constructive case of the SR-203 engine, the proper frequencies of the intake column and hence the engine speeds that must be avoided in operation are determined. In addition to the obtained result, the paper also presents a method for analyzing vibrations in a column of fluid under periodic impulses and can be applied with some adaptations to other problems of this kind in the construction of car engines (vibrations in the fuel injection system).

14. Analysis of the temperature field in the piston of spark ignition engines. The work was presented at the scientific session of the teaching staff of the Polytechnic Institute of Braşov in 1959. Considering the limit values of a potential field of temperatures, values determined experimentally and statistically, by introducing some linear dependencies of these temperatures, the field of temperatures in the piston body. The work was prepared to establish the optimal constructive shape of the piston of the SR-203 engine, which, working after the gasoline injection cycle, requires a special profile. The temperature field thus determined is similar to the fields found experimentally and found in the literature. Knowing the variation of temperatures in the piston, conclusions can be drawn about its resistance and ensuring lubrication in good conditions. The work served to design the SR-203, 204, 205, 206, 207 and 211 prototype engines.

15. Automobile and Tractor Engines. The work appeared in 1959 and represents the extended course of engines for automobiles and tractors, from the Polytechnic Institute of Braşov, where it was lithographed in 2×800 copies of 1030 pages each (1st Volume and 2nd Volume, Fig. 10).



Fig. 10. Automobile and tractor engines - Volume I and II, 1959, author Radu E. Mărdărescu

The chapters required by the analytical program were provided, part I being the analytical part and part II the constructive part. In the theoretical part, the thermodynamics at high temperatures of internal combustion engine cycles are treated, taking into account the variation of specific heats with temperature, the dissociation of gases at cycle temperatures and heat losses, accurately establishing both the heat balance of the engine and its economy. Elements similar to internal combustion engines are also treated. In the constructive part, focus is on the calculation and construction of the engine organs, developing, among others, the calculation of the cylinder liners, the pistons, the segments, the motor shaft, the distribution, etc. Two-stroke and supercharged engines are also treated theoretically and constructively. In conclusion, the engine performance determination apparatus and the research methodology on the test bench are discussed. Most of the issues dealt with are accompanied by examples of calculation, of execution drawings that can be used in design or operation. The course was also purchased in the car manufacturing industry, so that only 350 copies were left for teaching use, and a re-edition of the course was necessary in 1961.

16. Endurance tests of automobile engines. A collaborative work, in which conclusions are drawn on the methods and results of long-term testing of automobile engines (Fig.11).

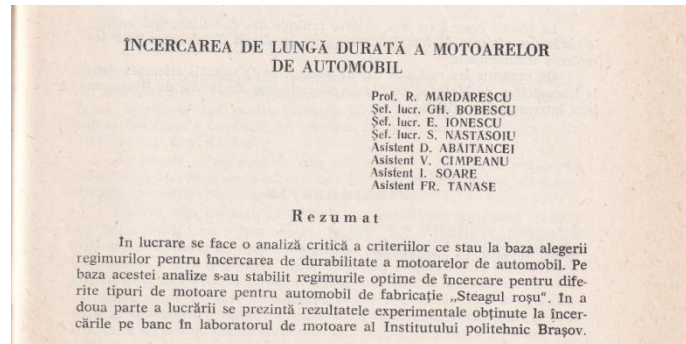


Fig. 11. Scientific paper 'Long-term testing of automobile engines', 1964

The work was awarded by the Ministry of Education in 1964.

17. Catoptric telescopic systems with technical profile mirrors. The paper was presented at the scientific session of the teaching staff of the Polytechnic Institute of Brașov in November 1960. The paper analyzes the technique and materials used in the construction of the mirrors of large optical telescopes. The author comes to the conclusion that the used Pyrex glass can be replaced with aluminum alloys that present manufacturing advantages. A new method for obtaining parabolic, hyperbolic and even sinusoidal profiles is presented. Profiles processed in this way are called technical profiles. More examples of optical systems with a technical profile are calculated further, analyzing the correction of optical errors by Seidel's iconal method. The work is of great interest for the possibility of building large optical instruments for astronomical observation.

18. Calculation of the thermomechanical stresses of the cylinder head. The paper was presented at the scientific session of the didactic staff of the Polytechnic Institute of Brașov, in November 1964. The paper indicates a method to calculate the fatigue stress of the material of the cylinder head, of an internal combustion engine, taking into account the variable stresses of the engine cycle and the thermal stresses due to the flow of heat in the cooling system (Fig. 12).

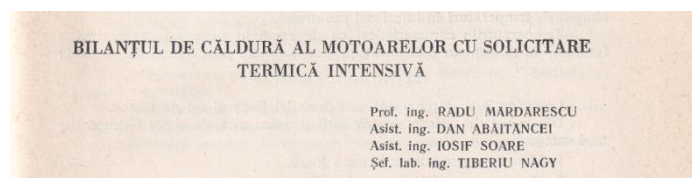


Fig. 12. Scientific paper 'The heat balance of engines with intensive thermal stress', 1964

The work was requested by the Brașov Truck Factories and deals with the calculation of the cylinder heads of two prototype engines of the factory. The method being general, can be applied to any type of piston engine.

19. Differential gas turbine. It is a theoretical paper that deals with a new gas turbine operation scheme, with suitable properties for application in road traction. The paper was presented at the republican session of automobiles and tractors from 1966, at Braşov.

20. Engines for Automobiles and Tractors, work written together with Prof. dr.eng. Dan Abaitancei and Prof. dr.eng. Victor Hoffmann, published in 1968 at the Didactic and Pedagogical Publishing House (Fig. 13).

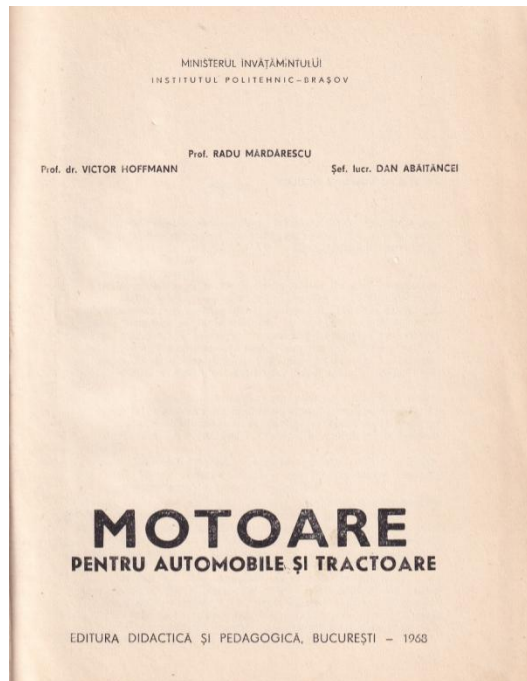


Fig. 13. Engines for automobiles and tractors - Compendium of calculation, construction and thermomechanical analysis of the main parts and components of the engine, 1968

4 Academic Activity

As a professor, head of department, Radu E. Mărdărescu had a collaborative activity with the factories in Braşov, performing the first approvals for SR 101 engines and then partial approvals for SR 211 in the Engine Laboratory of the Polytechnic Institute. In the course of his activity, Radu E. Mărdărescu obtained three invention patents in Germany, one in 1934 and two in 1938, where he worked at the Auto-Union and Daimler-Benz companies. Also, in 1938, he obtained two invention patents that returned to the IAR Factory, in the framework of the development of the 1500 HP engine. The two patents dealt with the construction and assembly of the crankshaft and the creation of the supercharging compressor in order to increase its effective efficiency. He obtained

also a patent in Romania in 1968, in collaboration with the collective of the Department of Motor Vehicles.

During his work at the Department of Automobiles and Tractors, he collaborated with the factories in Brasov at the Engines laboratory, where he led the homologation research for the SR 101 engine and the partial homologations for the SR 211 engines that equipped trucks produced in Brasov. He also collaborated with the Tractor factory in Brasov in order to solve technical development problems.

Figure 14 shows an image of the Automobiles and tractors promotion from 1956 of the Institute of Mechanics in Brasov.



Fig. 14. A suggestive picture with the fourth year Automobiles and tractors students from 1956 in front of building D of the Mechanics Institute in Brasov

In the course of his academic activity he write a course in Thermotechnics (1952), three courses in Internal Combustion Engines (1955, 1959, 1968) and other scientific studies published in journals and proceedings of scientific conferences.

Figure. 15 shows an image with the Mărdărescu family in Poiana Brasov resort, 1965.



Fig. 15. Radu E. Mărdărescu with the family in the Poiana Brasov resort, 1965

Professor Radu Mărdărescu's main passions, besides internal combustion engines, were: mathematics, astronomy, symphonic music, organic chemistry, classical Greek philosophy, the life of scientists, symmetry in nature and sports.

He often said that a sports champion or a great performer of symphonic music is for us a model in terms of self-transcendence - the condition of the human evolution.

Professor Mărdărescu's favorite maxim in Latin was "Naturae non imperatur nisi parendo" whose meaning is, one does not command nature without listening to it (Francis Bacon).

He died on September 10, 1968 in Brasov.

References

1. Mărdărescu, R.: Teoria motoarelor cu ardere internă, Cursul de calculul și construcția motoarelor de automobile (In English: The theory of internal combustion engines - the calculation and construction course of automobile engines). In: Litografia Invățământului Orașul Stalin (1955)
2. Mărdărescu, R.: Mărimile specifice ale motoarelor cu ardere internă (In English: Specific sizes of internal combustion engines), Metalurgia, **4(5)**, May 1955
3. Mărdărescu R.: Invariantul caracteristic al motoarelor cu ardere internă (In English: The characteristic invariant of internal combustion engines), Sesiunea Științifică a Institutului Politehnic din Brasov (1955)
4. Mărdărescu R.: Randamentul de antrenare al rachetei terestre (In English: The propulsion efficiency of the terrestrial rocket), Sesiunea Științifică a Institutului Politehnic din Brasov (1957)
5. Mărdărescu R.: Analiza vibrațiilor pe conducta de admisie a motoarelor cu explozie (In English: Vibration analysis on the intake pipe of explosion engines), Sesiunea Științifică a Institutului Politehnic din Brasov (1959)
6. Mărdărescu R.: Analiza câmpului de temperatura în pistonul motoarelor cu explozie (In English: Analysis of the temperature field in the piston of explosion engines), Sesiunea Științifică a Institutului Politehnic din Brasov (1959)

7. Mărdărescu, R.: Motoare de automobile și tractoare (In English: Automobile and tractor engines), Vol. I and II, Ministerul Învățămîntului și Culturii, Institutul Politehnic Orașul Stalin (1959)
8. Mărdărescu, R.: Sisteme telescopice catoptrice cu oglinzi de profil ethnic (In English: Catoptric telescopic systems with technical profile mirrors), Sesiunea Științifică a Institutului Politehnic din Brasov (1960)
9. Author, R. Mărdărescu: Calculul solicitărilor termomecanice ale capului de cilindru (In English: Calculation of the thermomechanical stresses of the cylinder head), Sesiunea Științifică a Institutului Politehnic din Brasov (1960)
10. Coeficientul de antrenare al rotoarelor de pompe și compresoare în funcție de numărul de palete și frecare (In English: The drive coefficient of the rotors of pumps and compressors depending on the number of blades and friction), Ministerul Învățămîntului, Institutul Politehnic Brașov: Lucrări Științifice Alese. Facultatea de Mecanică, Volumul VI (1964)
11. Mărdărescu, R.: Motoare pentru automobile și tractoare (In English: Engines for automobiles and tractors). In: Editura Didactică și Pedagogică, București (1968)
12. Sima, P.: Prof.univ. eng. Radu-Emil Mărdărescu. In: Revista Inv. Superior, May (1980)
13. Gheorghiu, C.C.: Fabricile de avioane românești în perioada interbelică (In English: Romanian aircraft factories in the interwar period). Editura Stiintifica si Enciclopedica, Bucuresti (1982)
14. Berențan, E.: Informare asupra motorului de avion în stea IAR-7M precum și necesitatea și posibilitatea fabricării de motoare de avion în țara noastră (In English: Information on the IAR-7M radial aircraft engine as well as the necessity and possibility of manufacturing aircraft engines in our country), Dactilogr. IAR Brasov (1991)
15. Salca, H.: Prof. univ. ing. Radu-Emil Mărdărescu - proiectant și constructor de motoare de avion (In English: Prof. Univ. Eng. Radu-Emil Mărdărescu - designer and builder of aircraft engines). In: Buletinul Științific al Universității „Transilvania” din Brasov (2004)
16. Mărdărescu, V.: Biografia profesorului universitar Radu-Emil Mărdărescu (In English: Biography of university professor Radu-Emil Mărdărescu). In: Fundatia Profesor Radu Mărdărescu, Brasov (2012)

Student Section

Designing A Lightweight and Ergonomic Formula Student Pedal Box Assembly Using Finite Element Analysis

Robert-Cristian Iridon¹, Tiberiu Andrei Borborean¹, Marius Pop-Călimanu¹

¹Polytechnical University of Timisoara, Timisoara, Romania

Abstract. The target of the paper is to follow the design process of a pedal box assembly with improved ergonomics with the help of finite element analysis. FEA simulation plays a key role in determining several factors that influence the weight of the assembly. Some of these factors are the possibility of executing strategically place cut outs to reduce the weight while maintaining the structural integrity; the minimization of the overall thickness of the components; the choice of materials, utilizing mostly ALU-6061 with only small shafts being manufactured out of C45 Steel. The ergonomics of the pedal box are to be improved by changing the position of the assembly itself in the single seater and of the gas and brake pedals themselves. Adding a sub system in the assembly that will allow the pilot to adjust position of the pedal box without the need for bolts will also improve the ergonomics. A position sensor and a stepper motor will be placed in the assembly and utilizing the data from two brake pressure sensors, placed on the front and back brake lines respectively, will allow the pilot to adjust the brake balance from the comfort of the cockpit. The expected results are a reduction in weight of approximately 15%, from the previous design, on top of the improved ergonomics, pilot comfort and viability of the assembly.

Keywords: FEA, Pedal Box, Lightweight, Ergonomics, Structural Analysis, Mechatronics, CAD, Ansys, Driver Comfort, Brake System

1 Introduction and initial thoughts

The braking system is responsible with the deceleration of the vehicle by transferring the pressure from the brake pedal to the calipers via the brake circuit composed of the master cylinder and brake lines with brake fluid. The pedal box is a crucial subassembly of the brake system and not only it also contains the gas pedal, this makes the pedal box assembly one of the systems that allow the driver to control the single seater but at the same time the pedal box assembly has to offer a certain level of comfort to the driver. This paper will present the process of designing, analyzing and improving a pedal box assembly for a Formula Student single seater. Formula Student being an international engineering contest I will focus also on the design choices and manufacturing methods not only on the ergonomics of the final system. Everything from the initial kinematic

calculations and dimensioning calculations to the FEA validation of the design and manufacturing process using FEA simulations will be presented below.

2 Kinematics of the brake pedal and initial calculations

2.1 Dimensioning of the master cylinder

Firstly, to determine the bore diameter of the master cylinder we had to calculate the braking torque. This will allow me to determine the pressure inside the brake circuit and by knowing the foot force of an average human to be around 1200 to 1400 N and the desired ratio of the brake pedal to be around 4.5 to 5 the bore diameter of the master cylinder can be determined.

First, we convert the speed to the international system units and calculated the deceleration resulting in a total deceleration of -8.8889 m/s^2 . Considering a 40 to 60 distribution between the front and rear we can deduce the moment needed to brake: $M_f = \frac{F \times 60}{100} \times r_r = \frac{1104 \times 470}{1000} = 518.88 \text{ Nm}$ (1)

Knowing the moment needed to brake also known as the braking torque, the radius of the disc and the coefficient of friction of the pads we can calculate the force in the caliper piston need to brake, force equal to 3470.769 N. Utilizing the area of the caliper piston and the force calculated above we can determine the pressure inside the brake system, pressure equal to 21.85 bar: $d_{master} = \sqrt{\frac{4 \times F_{foot} \times 4.5}{p \times \pi}} = \sqrt{\frac{4 \times 1300 \times 4.5}{21.85 \times \pi}} = 18.46 \text{ mm}$ (2)

This pre-dimensioning guided me to the choice of the Tilton [1] 780 series master cylinders with a $\frac{3}{4}$ inches bore diameter, which is equal to 19.05 mm, satisfying the condition of the minimal diameter determined above.

2.2 Initial calculations for the travel of the master cylinders

Table 1 contains the initial information needed to calculate the master cylinder travel needed to displace enough liquid to bring the single seater to a stop.

By dividing the brake system pressure to the area of the master cylinder, calculated from the diameter determined above, we obtain a force of 6227.754 N which represents the force needed to press the brake pedal.

The volume of liquid that needs to be displaced to bring the single seater to a stop is obtain by multiplying with 4 the produce between the area of the caliper cylinder and the distance traveled by the caliper piston when braking. This volume divided by the area of the master cylinder gives the length of travel needed by the brake pedal.

For this configuration of single seater an approximative of 14 mm of brake travel is needed to bring the car to a full stop.

Table 1. Initial information for calculating the master cylinder travel

| | | | |
|-------------------------------------|-------------|------|---------------------|
| Mass of the single seater | m_a | 288 | [kg] |
| Mass of the pilot | m_p | 80 | [kg] |
| Total mass | m_{total} | 368 | [kg] |
| Inertial force of the single seater | F | 3680 | [N] |
| Acceleration | a | 10 | [m/s ²] |
| Average rolling speed | v | 60 | [kmh] |
| Deceleration time | t | 3 | [sec] |
| Wheel radius | r_r | 470 | [mm] |
| Brake disk radius | r_d | 115 | [mm] |
| Caliper internal cylinder diameter | d_e | 31.8 | [mm] |

2.3 Kinematics schematic and multiplication ratio of the pedal

The brake pedal acts like a lever system, so to decrease the overall size of the pedal box assembly and improve the ergonomics the master cylinders have been moved to the back of the brake pedal. Another aspect to consider was the force required to press the pedal, in conventional systems this issue is avoided by lengthening the pedal or moving the point of pivot lower, for my system I came with a different approach. Using the principals of mechanical advantage I decided to approach this issue by placing the master cylinder behind the pedal on a slightly elevated position and at angle with the vertical axis. In this manner the brake pedal subsystem can be reduced to the following schematic (see figure 1).

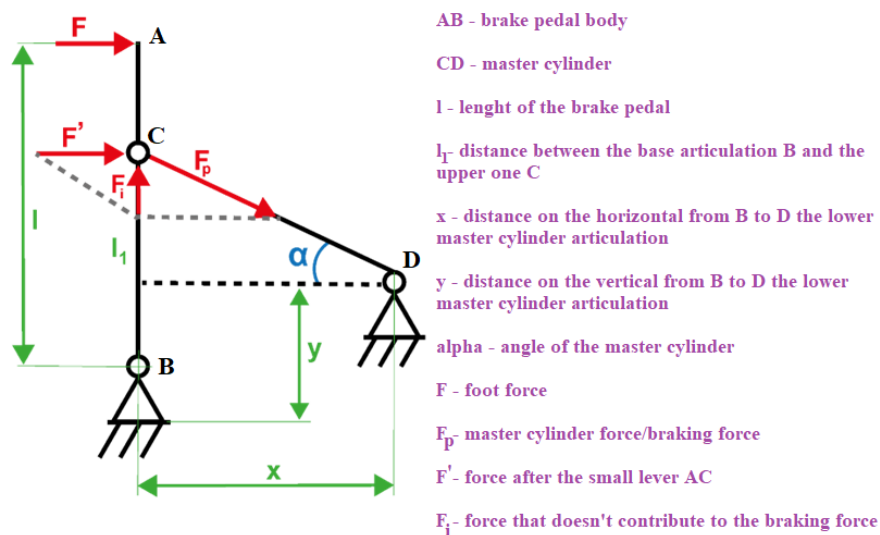


Fig. 1. Kinematic schematic of the brake pedal concept

The foot force is noted with F and is equal to about 1300 N and the other reaction forces, the one in the pumps and the one in the pedal can be determined using the next formulas:

$F_p = F \times \frac{l}{l_1} \times \frac{l_p}{x}$ (3) for the pump force and the $F_i = F \times \frac{l}{l_1} \times \frac{l_1 - y}{x}$ (4) for the force in the pedal. The ratio of multiplication in a normal pedal assembly is the given by the fraction between the distance from the pivoting point to the point of application of the force and the distance from the pivoting point to the point where the master cylinder is connected to the pedal. In the presented configuration the formula for the ratio can be reduced to the ratio between the foot force and the pump force or the formula $i_p = \frac{l \times l_p}{l_1 \times x}$ (5) where: l_1 is the distance from the pivot point to the point where the force is transmitted to the master cylinders, l_p represents the length of the uncompressed master cylinder, l is the overall length of the pedal and x is the abscissa of the pivot point of the master cylinder compared to the pivot point of the pedal. After creating a kinematic model in Catia V5 and experimenting with de values of the different lengths the final ratio of multiplication is approximative a 4.5:1 ratio, this means that the required force to push de brake pedal is reduce from the initial value calculated approve to only 1373 N.

3 Initial design the 3D modeling of the components [2,3]

The key word of the design phase was ergonomic, everything from the ideal position of the driver to the ability to adjust different components for different drivers. The previous version (*see figure 2*) had the master cylinders below, wasn't space efficient and the variety of drivers wasn't considered in the design phase.

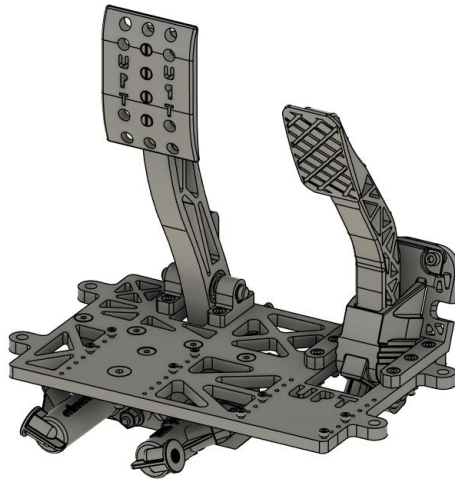


Fig. 2. Initial design

The main improvement from the previous versions is the integration of a positive locked adjustable system for changing the position of the entire pedal box assembly.

The distance between the gas and brake pedal was increased and a pair of adjustable Nylon infused with glass fibers 3D Printed heel rests were mounted in the front of the pedal box. The large amount of adjustment possibilities insures the pedal box's viability, ergonomics, and versatility. The main mounting plate of the assembly as well as most of the supports and mounts are manufactured from aluminum 6061 due to its great weight to strength ratio and the lower cost than the 7075 series aluminums. The shafts and the indexed rail, this is used to adjust the distance between the pedal box and the driver, are manufactured from C45 steel bar and S235 steel plate respectively. The final design of the pedal box is presented in the figures below (*see figure 3 and 4*).

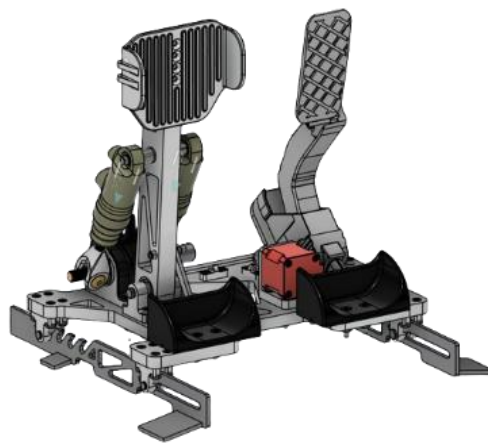


Fig. 3. Isometric view

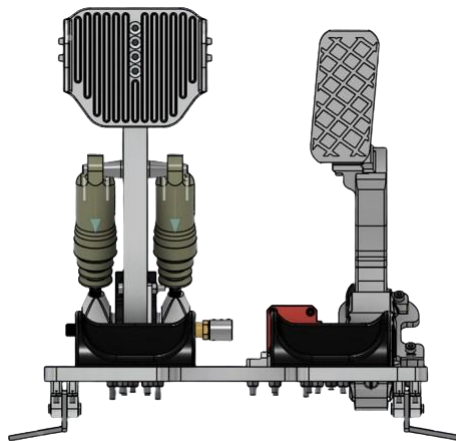


Fig. 4. Top view

4 Analysis of components using FEA simulations.

4.1 Analysis of the brake pedal in Formula Student regulations

The brake pedal is required by the Formula Student and FSAE [4] rules to withstand 2000N of force when actuated, keeping this in mind and the self-imposed requirements of the dimensions calculated in the kinematic section the final design was analysis in Ansys [5] with a mesh Tetrahedrons Patch Conforming with 98k nodes, average aspect ratio of 1.9 and a minimum element quality 0.27. The simulation presented below has, as boundary conditions (*see figure 5*), two remote displacements, both allow rotation only around the Z axis, and one remote force equal with 2000 N. The two remote displacement in combination with the second body, which plays the roll of the master cylinder and it is set a rigid body in the simulation, create the condition presented in the kinematic schematic presented above (*see figure 1*).

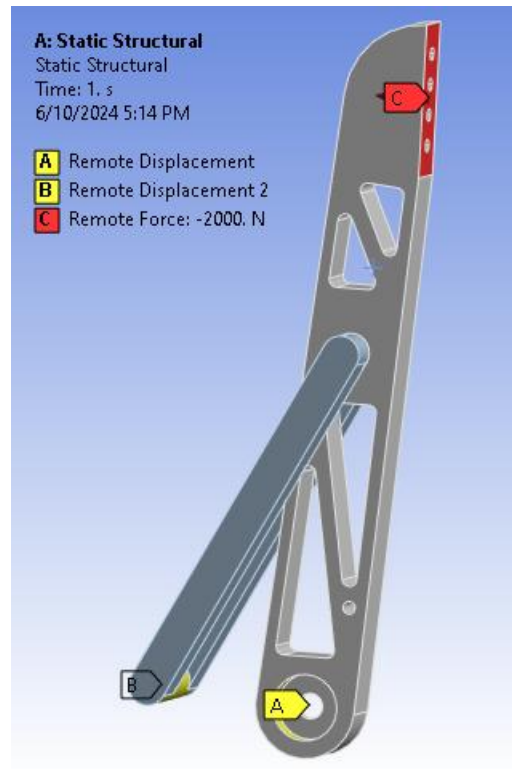


Fig. 5. Boundary conditions

The yield strength of aluminum 6061 is around 276 MPa and the ultimate tensile strength is around 310 MPa and from the result of the simulation presented below (*see figure 6*), the maxim stress in the brake pedal is only 152 MPa.

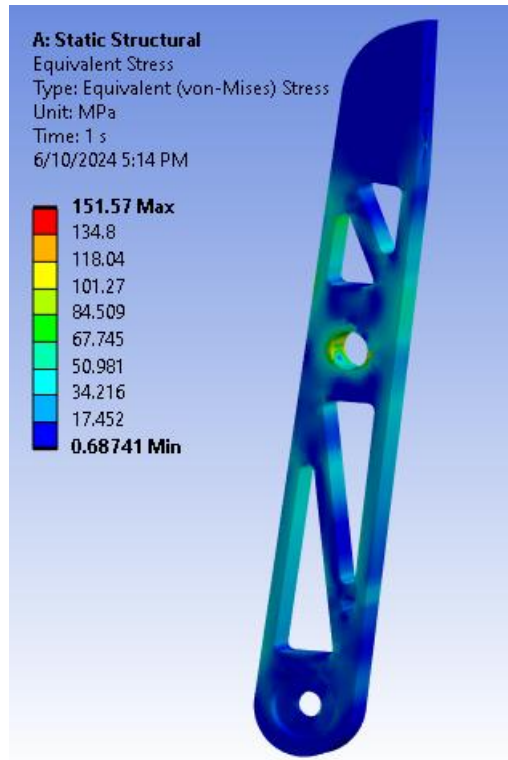


Fig. 6. Equivalent von-Mises Stress

From comparing the maximum stress in the brake pedal with the yield strength it results that no plastic strain appears in the component and also by calculating the safety factor by dividing the ultimate tensile strength to the maximum stress in the part it results in a safety factor equal to 2 with is more than sufficient. Next step was to verify that the design can withstand a large number of duty cycles, for that I created a fatigue analysis on the design with a Zero-Based cycle type, alternating from 0 to the maximum load, using a 0.6 strength factor as the initial condition and the Goodman theory as the mean stress theory. This results in fatigue life of around 43000 cycles and an average alternating stress of only 200 MPa.

4.2 Design of the indexed rail to minimize stress variations on different driving positions using Ansys Mechanical

Using FEA simulations, the indexed rail was optimized in such a way that between the maximum distance and the minimum one the variation of stresses, when utilizing the pedal box assembly, does not exceed 2.5%. This was done using strategically placed cutouts and moving the support brackets in such a way that the variation of stress is minimal. Each of the two indexed rails is exposed to half of the maximum braking force

generated by the driver while braking. This force is yet again distributed to the two pins, one sliding in the elongated slot and the other sitting on each of the angled half slots to lock the individual pedal box assembly in each position. This brings the force on each pin to be equal to about 1200 N and on each rail, there are to “Remote Force” loads equal with this calculated force, one is in the direction of the half slot and the other in the opposite direction on the elongated slot and the fixed distance determined by the pedal box assembly plate. The rails are fixed using “Fixed support” to represent the welds that will keep the rails fixed to the single seater. For the meshing strategy an Tetrahedron Patch Conforming with Quadratic elements resulting in 103k elements with a minim element quality of 0.2 and an average aspect ratio of 1.9.

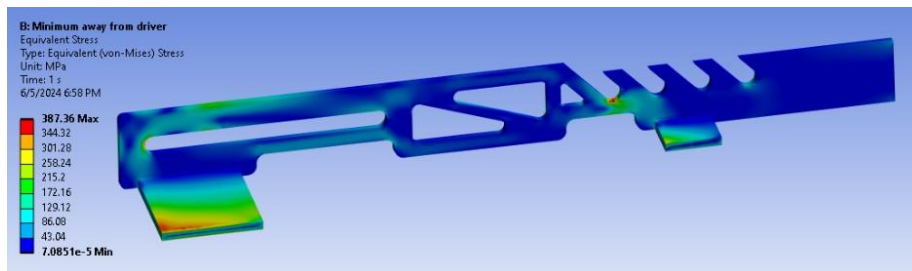


Fig. 7. Stress of one rail in the position closest to the driver

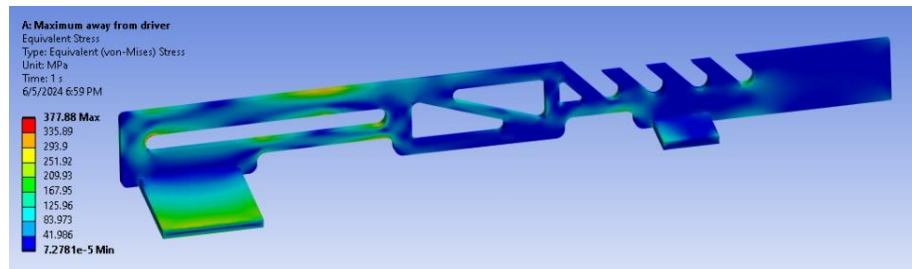


Fig. 8. Stress of one rail in the position furthest away from the driver

From the analysis it could also deduce that the part will only be elastically deformed being no plastics strains or permanent deformations present.

4.3 Predicting the flow of aluminum for the casting of the brake pedal face from aluminum using Moldex 3D [6]

Due to FSAE regulations and the complexity of the design of the brake pedal face the best approach was an aluminum casting in temporary molds. The casting in temporary molds is a highly volatile and unpredictable process, due to these aspects I design to create a 3d model of the mold and to create a FEA simulation not only to ensure the filling of the cavity of the mold but also to determine the internal stresses, that are an unavailable by-product of the casting process. The initial conditions of the simulation were the temperature of the aluminum 850 degrees Celsius and the temperature of the mold which was estimated to be around 25 degrees Celsius.

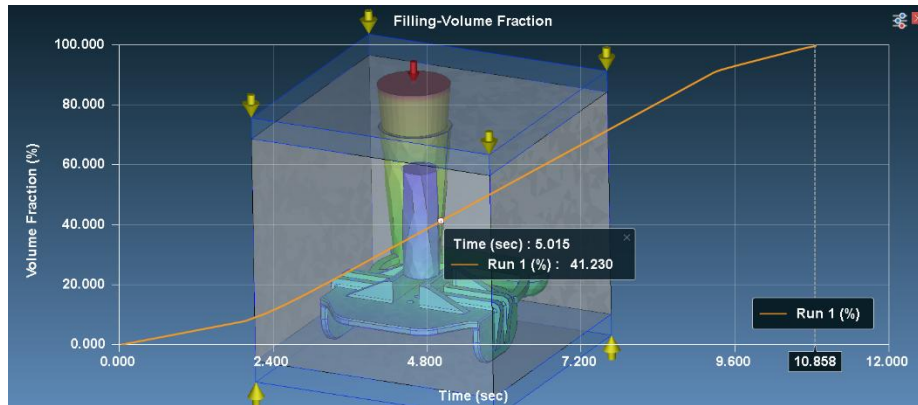


Fig. 9. Filling Volume graph of the mold

The graph above (see figure 9). presents the dependence of the overall filled volume in percentages of the cavity with time. The volume of the cavity is around 312 cc and for the simulation results that the entire volume is filled in 11 seconds, and by the first 5 seconds almost 42% of the volume was filled with aluminum. The flow rate of the liquid metal follows an accenting curve after which remains almost constant at around 41 cc/sec, while most of the cavity fills, and in the end, after the metal started its colling and the mold is almost filled, the flow rate descents rapidly (see figure 10).

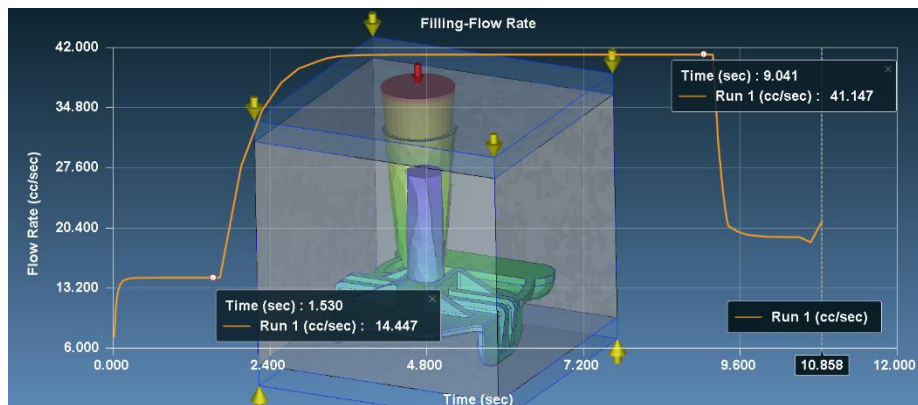


Fig. 10. Flow rate in the cavity of the mold

The last aspect to verify after ensuring the cavity will properly fill is to determine the value and location of the internal stresses resulted from the casting process. This was also determined using Moldex 3D and the results are presented below (see figure 11).

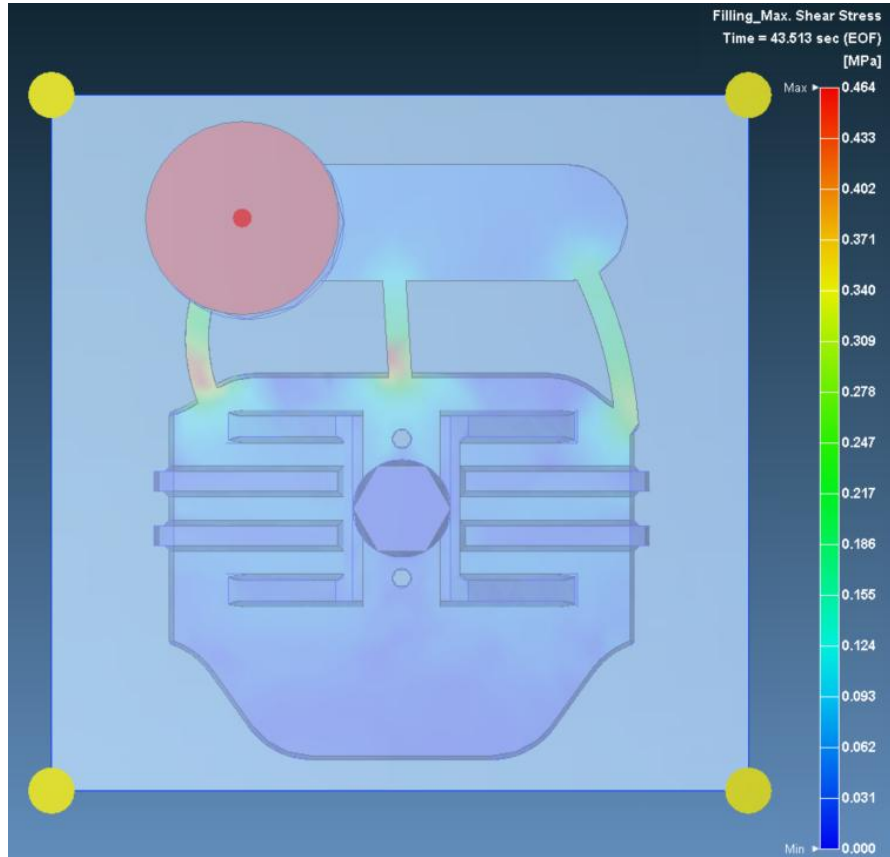


Fig. 11. Internal stresses of the casted brake pedal face

For the analysis results that not only is the maximum stress located outside the brake pedal face itself, it being located in the tunnel network used to ensure the proper fill of the cavity, but the value is only 0.5 MPa. The final brake pedal face, after the removal of the tunnel network, has a volume of only 95 cc which when considering the average density of aluminum, 2.7 g/cc, results in a weight of only 260 grams.

5 Implementation and integration of a variable brake balance using a stepper motor and two pressure sensors

The brake balance is defined as the distribution of braking force at the front and rear wheels. This balance is normally set before the usage of the single seater and rarely perfected due to being difficult to change, but by implementing this system the driver will be able to fine tune the brake bias from the comfort of the cockpit. Using a pair of two couplings and a twisted series of steel wires extracted from a drill attachment the stepper motor is connected to the threaded rod of the brake balancer assembly. The two

couplings are manufactured from C45 steel and present a series of threads that allow the fixture of the couplings to the twisted wires and to the stepper motor shaft and brake balancer threaded rod respectively. The stepper motor was a natural choice for such a system due to its precision and overall lightweight aspect but high torque output. The two pressure sensors are distributed one on the front brake lines and the other on the rear brake lines. The ratio between the outputs of these two sensors gives us the brake bias percentage that by pressing one of the two buttons on the steering wheel the driver can increase or decrease the percentage of the rear.

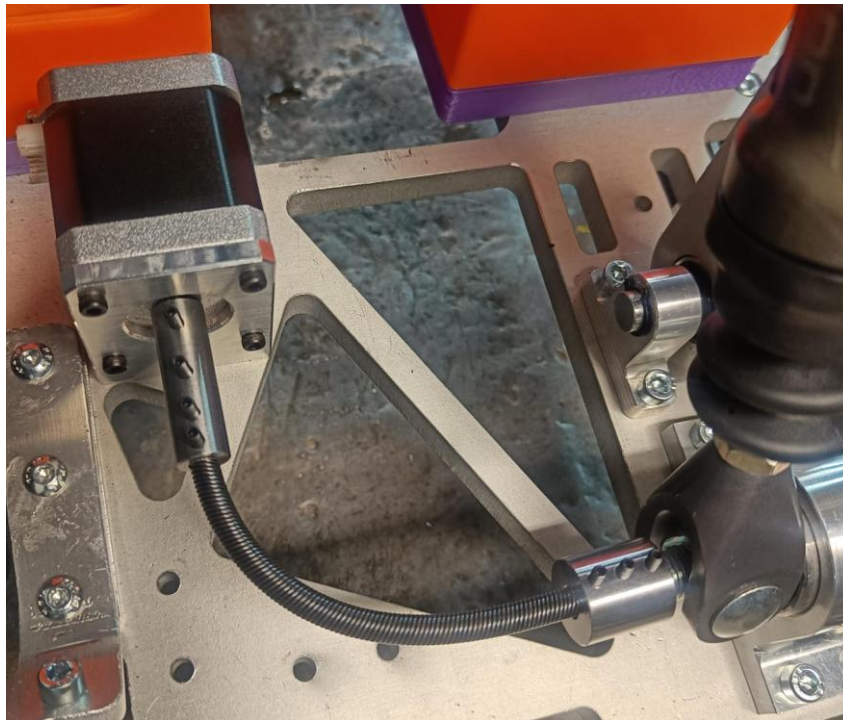


Fig. 12. Photo of the implementation of the system described above

6 Ergonomics and driver comfort [7,8]

The pedal box assembly has a series of adjustments that not only allow the pedal box to be utilized by a variety of drivers, from tall to short, but also to make the driving experience smoother. These adjustments include the indexed rails, that allow the pedal box's position relative to the driver to change, accommodating for the variation in height between different drivers. The heel rest are also mounted on two slots each and by losing the screws that fix the heel rest, it can glide through the slot allowing it to be brought closer or further from the driver. This aspect compensates for the difference between the geometry of the foot of different drivers.



Fig. 13. Photo of one of our drivers inside the single seater to test the of the pedal box

The combination of the factors presented above with the ability to change the brake bias with ease from the comfort of the cockpit had made a positive improvement on the overall ergonomics of the pedal box assembly.

7 Conclusions and final thoughts

The new improved design of the pedal box has a weight reduction of only 10%, while the expected reduction was around 15%. This difference is the result of the implementation of the indexed rails, this decision all though it increased the weight from the expected 4.9 kg to around 5.2 kg it made a positive impact on the overall ergonomics and viability of the pedal box assembly. The implementation of the stepper motor to change the brake bias from the cockpit electronically is an innovation in the Formula Student community, the others solution to this problem being a purely mechanical one, by wire, solution that comes with a large series of drawbacks.

In conclusion, by utilizing basic kinematics, finite element analysis simulations and a series of different manufacturing processes, from milling and turning to 3D printing and metal casting, the overall weight of the assembly was reduced from previous versions and the ergonomics, versatility and reliability were increased to heighten degree (see Table 2).

Table 2. Differences between the initial and new design

| | Initial design | New design |
|--|---|---|
| Total weight | 5.7 kg | 5.2 kg 10% lighter |
| Heel rests | Not included | 3D Printed from Fiber glass infused Nylon |
| Adjustable distance to pilot | Not included | Indexed rail FEA optimized |
| Distance between the centers of the gas and brake pedal | 120 mm Not comfortable for drivers | 160 mm More comfortable for drivers |
| Brake bias | Only changeable by moving a thread rod manually in the pedal box assembly | With stepper motor, changeable for the cockpit with 2 buttons |
| Integration with the board display in the cockpit | Not included | Real time brake bias and brake pressure information display |

References

1. Tilton brake controls. <https://tiltonracing.com/product-category/brake/>
2. Kourouzidis Ioannis "Design and Manufacturing of Formula SAE", T.E.I. of Western Macedonia, 2018
3. Zachary Demetriades "FSAE Zips Electric Racing Brake System Design", University of Akron Department of Mechanical Engineering, 2020
4. Formula Student Regulations 2024. https://www.formulastudent.de/fileadmin/user_upload/all/2024/rules/FS-Rules_2024_v1.1.pdf
5. Ansys Mechanical User Guide and INAS's Engineering Tomorrow course
6. Moldex 3D User Guide
7. Arshil Ahmad "Cockpit Design of a Formula Student Race Car: An Ergonomics Study", Aligarh Muslim University, 2021
8. Ameya Dabhade "Research on Brake Pedal and Mounting to Adjust Different Parameters for Maruti Tandem Master Cylinder", University of Duisburg-Essen, 2020

Study of Gas Exchange of a Supercharged, Two Stroke, Opposed Piston Engine

Costin Ene¹

Coordonator: Prof. Dr. Horia Abăitancei² and Prof. Dr. Sebastian Radu³
^{1,2,3} Transilvania University of Brasov, Braşov BV 500036, Romania
costin.ene@student.unitbv.ro

Abstract. The two-stroke engine has the potential of high-power density and will be always considered to be optimized based on its advantage. Further improvements can be obtained using the opposed piston principle having a common combustion chamber. The potential advantage of the solution is derived by the absence of the heat transfer at the cylinder head surface and an improved balancing output. The paper presents CFD simulation results for the described configuration of the two-stroke engine in order to identify pressure losses and turbulence generations during the gas exchange process. Based on a CAD model and using a Lattice-Boltzmann based CFD method the gas exchange processes inside the cylinder were analysed. The supercharging of the engine is also considered as a special flow analysis case to support scavenging and increased pressure at the end of the compression stroke. The supercharging parameters of the CFD simulation are computed based on a 1D thermodynamic analysis model of the engine. Two-stroke engines typically have highly dynamic gas exchange processes, such as scavenging, mixing, turbulence, and blowing, with moving walls (the piston) and changeable gas cross-sections acting as boundary conditions.

Keywords: CFD, 1D method, opposed piston engine.

1 Introduction

1.1 CFD analysis and 1D method

In the design and optimization of internal combustion engines, CFD (Computational Fluid Dynamics) simulations are essential. They efficiently facilitate the understanding of gas flow behaviour inside the cylinder and the evaluation of engine performance under different operating conditions

The Lattice Boltzmann Method (LBM) is a computational fluid dynamics (CFD) method that represents a paradigm shift in the way simulations are conducted, allowing for a wide range of applications previously inaccessible to traditional Navier-Stokes solvers.

The application of LBM has increased substantially due to its capabilities in managing complex flow scenarios and complex geometries. It has been used in various sectors, including aerospace, automotive, and architecture.

The Lattice Boltzmann Method (LBM) is a numerical method that simulates fluid dynamics at a macroscopic scale based on kinetic equations formulated at a mesoscopic scale. More precisely, it is "a parallel and efficient algorithm for simulating monophasic and multiphase fluid flows and for incorporating additional physical complexities." It is particularly useful for modelling complex boundary conditions and multiphase interfaces.

The 1D thermal calculation aims to find the parameters that characterize the thermodynamic processes of the engine and the energy balance parameters associated with useful power and efficiency. Based on thermodynamic calculations, the parameters of the energy balance are identified as a function of the crankshaft position, this making their graphical representation possible.

Based on the parameters determined according to the position of the crankshafts, the integral parameters of the engine are determined.

Ultimately, this information can be used to evaluate the main components of the engine in terms of durability. The thermodynamic calculation can be performed at different speeds and loads, resulting in the engine's characteristics

2. 1D method for thermodynamic analysis

Based on the thermodynamic equations, we were able to determine variations in the phenomena within the cylinder as a function of the crankshaft rotation.

$$\text{Energy Variation} \quad \dot{U} = \dot{W}_p + \dot{Q}_p + \dot{Q}_c + \dot{H}_a + \dot{H}_e \quad [1]$$

$$\text{Mechanical work} \quad W_p = p \cdot V = F \cdot d \quad [2]$$

Results are visible in the following graphs.

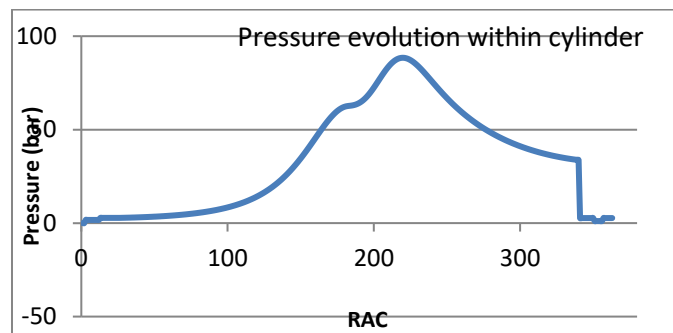


Fig. 1. Pressure evolution inside the cylinder in a full crankshaft rotation

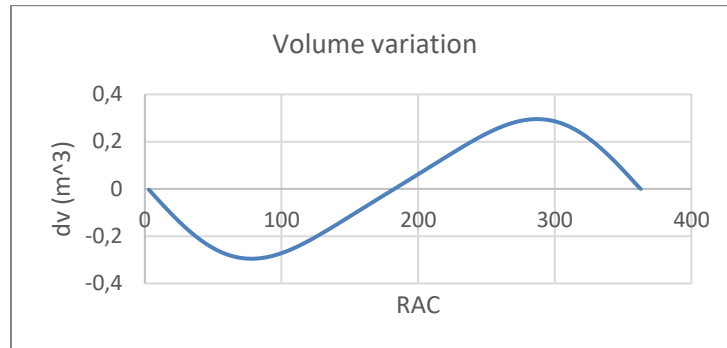


Fig. 2. Volume variation inside the cylinder

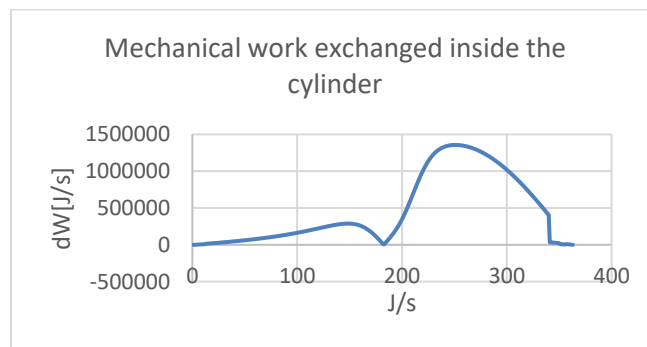


Fig. 3. Mechanical work exchanged inside the cylinder

2. CFD analysis

To perform the CFD simulation, it is necessary to capture the motion of the engine mechanism from a Multibody program, as well as a simplified geometry of the pistons. The simulation was performed for a single cylinder, thus facilitating the observation of gas exchange.

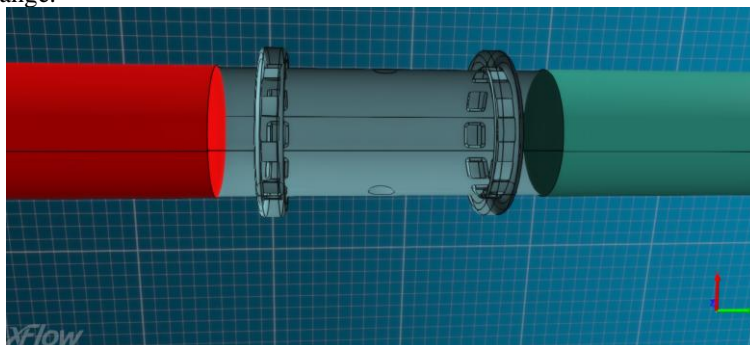


Fig. 4. Simplified geometry of the piston-cylinder assembly

Results of the simulation:

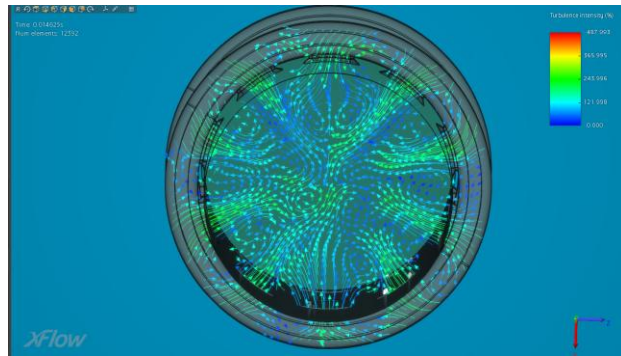


Fig. 5. Turbulences in the intake ports

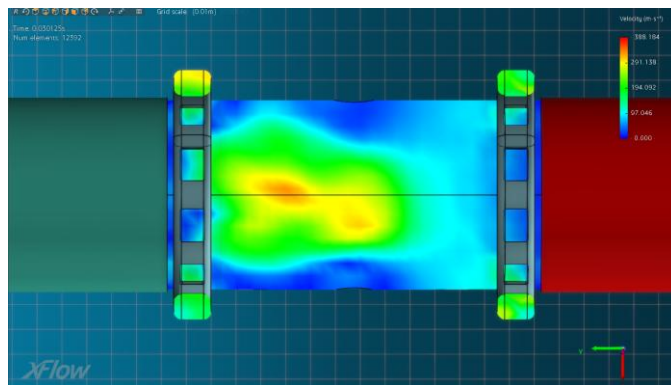


Fig.6. Velocity of the working fluid (intake and compression phase)

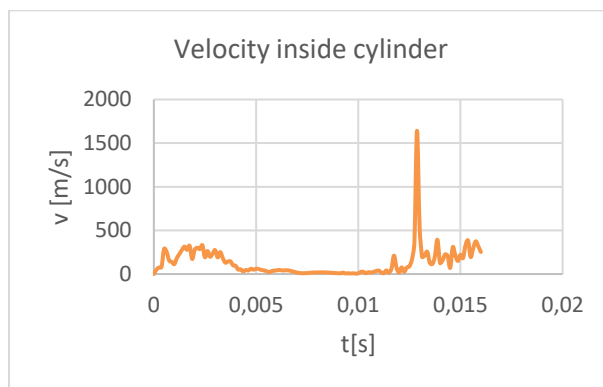


Fig.7. Velocity of the working fluid inside the cylinder in a full stroke at max rpm (7500 rpm)

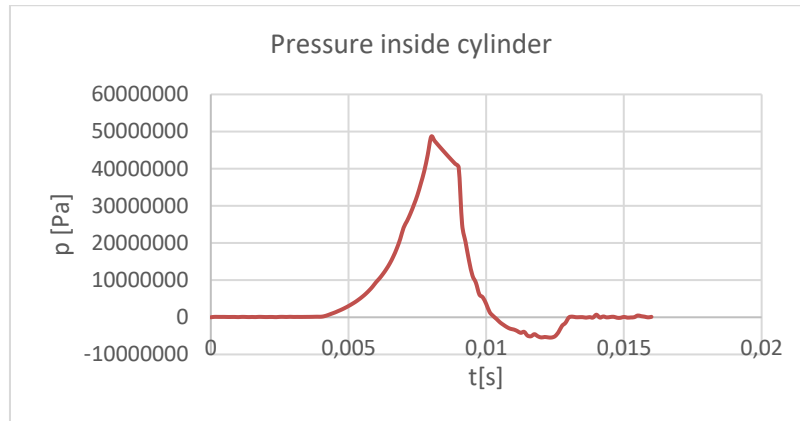


Fig. 8. Pressure of the working fluid inside the cylinder in a full stroke without combustion

3. Conclusions

The impact on the work using 1D method was significant, shaping the vision of the processes and the pre-dimensioning of the parts.

The simulation of the flow processes during admission shows an intense dynamic character both at the moment of the openings and throughout the gas exchange processes. The moment of the opening of the orifices, the pressure peaks, and the extreme speed that could favour or inhibit the quality of the gas exchange are highlighted. The comparison of pressures at the end of compression performed by the analytical method and CFD allows for the validation of results between the two methods, with an error of 1% at the maximum pressure value. The pressure evolution over time is similar for the two methods used.

References

1. Scheiterlein, A., Der Aufbau der raschlaufenden Verbrennungskraftmaschine, Springer-Verlag, Wien, 1964
2. Conf. Dr. ing. Corneliu Cofaru, Proiectarea motoarelor pentru autovehicule, 1997
3. Biezeno/Grammel, Technische Dynamik Zweiter Band Dampfturbinen und Brennkraftmaschinen, Springer-Verlag, Berlin-Heidelberg, 1971
4. Conf. Dr. ing. DAN ABĂITĂNCEI, Motoare pentru automobile, Editura didactică și pedagogică București

Design and Manufacturing of the Drive Shaft using CFRP for the Formula Student Car

Andrei Casian Borza¹, Andrei Tiberiu Borborean¹, Sergiu-Valentin Galațanu¹

¹Polytechnic University of Timișoara, Timișoara RO-300222, Romania

Abstract. In this paper, two drive shafts were developed, components of the UPT Racing Team's Formula Student car. This is a competition dedicated to students and it was initiated in the USA by the Society of Automotive Engineers (SAE). The main goal is to design and build an open-wheel formula race car. This work aims to lighten and improve the performance of the single-seater by reducing drive shafts' inertial and overall mass, using composite materials such as carbon fiber. The materials used for manufacturing the driving shafts are carbon fiber and epoxy resin (CFRP) for the hollow tube, aluminum for creating the shaft groove ends, and a high-strength adhesive used for bonding the carbon fiber components with the aluminum components. Initially, the tensile properties of the CFRP were determined. Using the properties from these tests, a simplified numerical model was used to determine the sizing of the parts, considering the engine's torque output and the competition regulation for 2024, following the execution phase. The expected results are a weight reduction of the driving shaft up to 40% compared to the previous iteration which was entirely made of steel.

Keywords: Formula Student, Drive Shaft, Composite Material.

1 First Section

Formula Student is an international program dedicated to students from worldwide higher education institutions who are passionate about engineering and motorsport. This project was founded in 1981 in the United States by the Society of Automotive Engineers (SAE) [1].

The objective of this project is to design, manufacture and compete with a single-seater race car that complies with the rules and restrictions of the competition regulations, at the Formula Student competitions [2].

To create the single-seater race car, the participating teams must first develop a detailed plan, allocating the team's resources efficiently. This step includes research, design, and finite element analysis of the components to ensure a valid and robust approach.

The next step is the physical construction of the single-seater car, which involves several manufacturing processes, such as welding, machining, composite material processing, electrical installation, and assembly. After these steps, the single-seater is tested to validate its functionality, followed by participation to competitions.

The competition comprises static and dynamic events. At the static events, teams present their car's design, cost management, and a business plan. The dynamic events test the car's performance, such as: acceleration, skid pad (cornering), autocross (handling), endurance, and fuel efficiency.

Drive shafts are essential components of transmissions generally used in the automotive industry, being responsible for transmitting the power flow generated by the engine to the vehicle's drive wheels, allowing it to move forward or backward.

For the same weight, driveshafts with a tubular cross-section are more rigid and can operate at higher speeds compared to those with a solid cross-section. In this work, the proper driveshaft, originally made of steel, was changed with a new concept driveshaft made of composite material and aluminum [3], [4].

Mosopefoluwa Samuel and Rostand B. Tayong presented in their study the benefits of using Carbon Fibre Reinforced Polymers (CFRP) for drive shaft manufacturing in automotive applications. Comparing CFRP with Steel and Aluminum, the results show that the CFRP drive shaft provides superior mechanical performance, better fatigue resistance, and weight reduction up to 79.6% [5].

C. Ramesh Kannan and I. Daniel Lawrence evaluated the fibre orientation and stacking sequence on the torsional stiffness, natural frequency, and buckling strength of composite drive shafts. This work highlights the benefits of composite materials like carbon and kevlar for weight reduction in the automotive industry, improving fuel efficiency without compromising performance. Finite Element Analysis shows that composite drive shafts reduce stress and weight effectively [6].

I.V.S. Yeswanth and A. Abraham Eben Andrews focused on replacing conventional steel drive shafts with composite materials like high modulus carbon/epoxy or E-glass polyester to reduce weight and improve strength. Using ANSYS and CATIA software, the analysis compares steel and composite drive shafts, optimizing parameters for torque, diameter, and natural frequency. Results show composites offer higher strength, lighter weight, and longer life [7].

G. Minak and S. Abrate examined the residual torsional strength of T300-carbon/epoxy tubes damaged by low-velocity impacts. Twenty-four specimens were impacted at 7 J under various torsional preloads. Different lamination sequences were tested, and FEM models analyzed impact-induced delaminations. Despite similar absorbed impact energy, results showed that torsional preload significantly affects residual torsional strength [8].

K. L. Alderson and K. E. Evans performed low-velocity impact and static tests on glass-fiber reinforced pipes with two support conditions: floor-supported and end-cradled. A backlighting technique was used to analyze failure and quantify damage. The failure process involves two stages: elastic behavior ends with an initial failure, followed by delamination until a second major failure, influenced by support conditions [9].

2 Materials and methods

2.1. Design of the drive shaft

This chapter presents the design of the planetary shaft assembly, aiming for a geometry as simple as possible to allow efficient manufacturing. The sizing of the components was done by considering the torsional strength of the carbon tube, the torque developed by the engine, and the distance between the tripod and the CV joint (transmission components) where the drive shafts were mounted. For the manufacturing process of the driveshaft ends, an exterior diameter of $29.92 (\pm 0.02)$ mm was considered at the joint with the carbon tube, thus achieving a clearance fit (H7). Following the analytical calculations, three design solutions were selected for the driving shaft assembly.

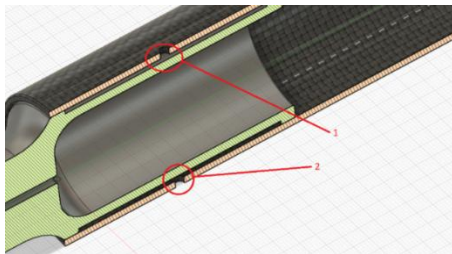


Figure 1 - Solution A

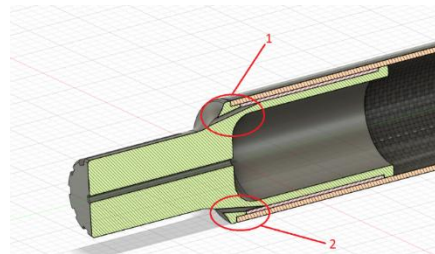


Figure 2 - Solution B

Solution A (figure 1) consists of the outer cylinder, the two driving shaft ends, and the adhesive layer between the components. The main element of this assembly is the carbon tube, which is joined to the splined driving shaft ends using a high-strength adhesive. To inject the high-strength adhesive into the cavity formed by assembling the composite material tube with the splined ends, four holes were executed in the carbon tube for the first design solution. Specifically, two holes with an offset of 180 degrees were made at each end.

The difference between Solution A and Solution B (figure 2) is the placement of the adhesive injection holes. In the second design solution, these holes are integrated into the driving shaft ends, unlike the first where they are in the outer cylinder. This prevents the degradation of the carbon fibers in the outer cylinder caused by the drilling process for creating the adhesive injection holes. Such a process negatively impacts the outer cylinder's resistance to torsional stresses.

Solution C presents a rough surface on the exterior of the driving shaft end on the area where the adhesive was applied. The rough surface was created by knurling the smooth surface. As a result of knurling the smooth surface, a larger and more adhesive surface was obtained, allowing for the application of high-strength adhesive.

2.2. The mechanical characterization of the CFRP

Dawon Jang and Min Eui Lee reviewed polyacrylonitrile (PAN)-based CFs, highlighting efforts to develop high-performance CFs through theoretical and experimental approaches, and addressing manufacturing defects. The theoretical tensile strength of CFs can be ideally up to 100 GPa with the perfectly developed graphitic structure and its orientation along the fiber direction. However, commercially available CFs reveal only a tensile strength of 7 GPa because of the existing defects. [10].

This chapter aimed to determine the properties and tensile strength of the composite material used in manufacturing the outer tube of the driving shaft assembly. To determine these properties, specimens were manufactured and experimentally tested.

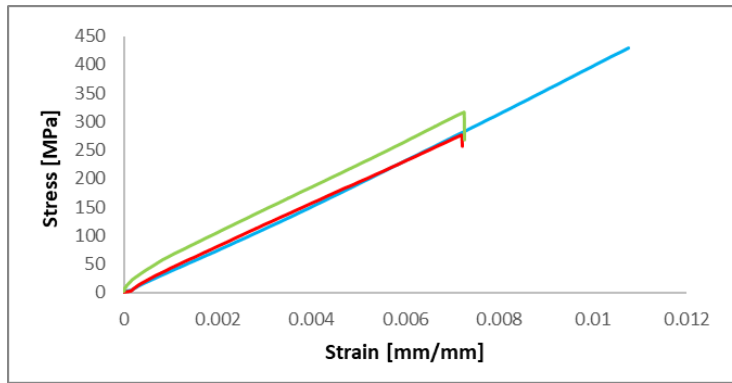


Figure 3 - Stress-strain diagram

The composite material specimens were subjected to axial loading through tensile testing. The main properties determined from the tests are Young's modulus (E) and the tensile strength (R_m).

The composite material specimens were tested using the ZWICK ROELL Z005 tensile/compression testing machine. For measuring the material displacement during testing, an extensometer was used, fixed along the specimen's length.

Using the force-displacement diagram, the longitudinal elasticity modulus (Young's modulus) was calculated, the result was an average value of 49602.2 MPa. In Figure 3, the stress-strain diagram for the specimens is presented. Here, the average ultimate tensile strength is 333.81 MPa.

2.3. Numerical analysis of the driving shaft

In this chapter, the numerical simulation of the driveshaft assembly (carbon tube-aluminum ends) and driveshaft components are presented. The maximum stresses occurring in the material and the maximum deformations were determined through finite element analysis of the component. The program used for finite element analysis of the drive shaft assembly was Abaqus CAE. The first step was assigning the materials and their properties determined from experimental testing. For the carbon tube, 26 layers

were assigned, at different orientations: 15, 30, and 45 degrees. The next step involved assigning boundary conditions, with the assembly subjected to a maximum torsional moment of 100 Nm. To apply a torsional load and record reactions, two control points were added to the surfaces at the ends of the tube. For geometry mash, 21245 nodes and 19312 shell elements with 4 nodes were used, considering the component as a deformable solid. The analysis yielded a maximum stress of 134.761 MPa (figure 4), which represents a singularity at the driving shaft end. The total deformation obtained from the analysis was 0.606 mm. (figure 5).

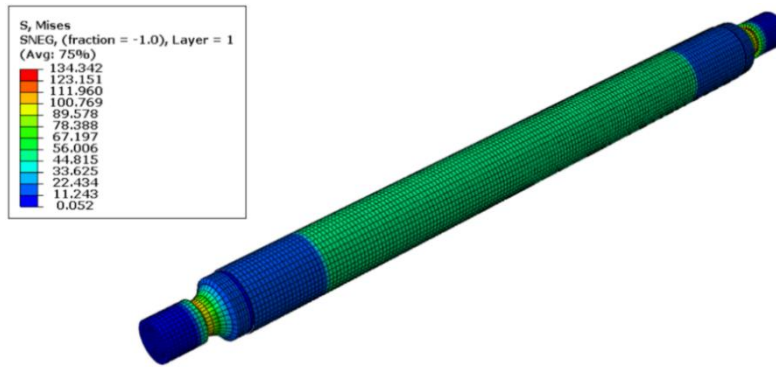


Figure 4 - Maximum stress

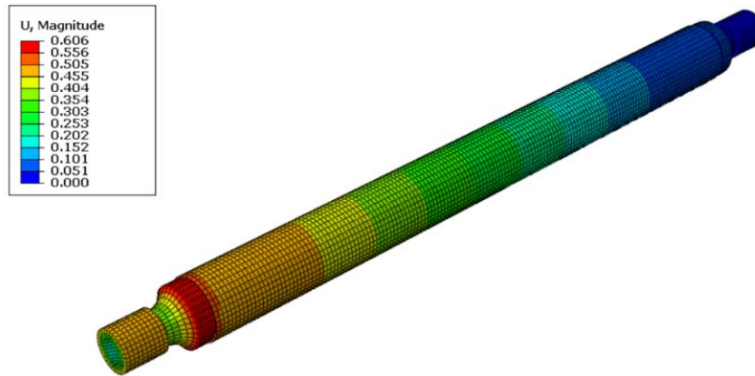


Figure 5 - Total deformation

The first and the second version of the drive shaft ends were numerically simulated, aiming to visualize the influence of stresses occurring on the adhesive injection holes area. Using Ansys structural solver, the material properties were assigned to components (aluminum 7075), with a longitudinal elasticity modulus (Young's modulus) of 70000 MPa and a transverse contraction coefficient (Poisson's ratio) of 0.33. For geometry mash, 46547 linear tetrahedral elements were used, for both versions, considering the components as a deformable solid. The analysis yielded maximum stress of

256,08 MPa and a total deformation of 0,084 mm for the first version, as represented in Figures 6 and 7 For the second version, the analysis yielded maximum stress of 258.95 MPa and total deformation of 0.085mm, as represented in Figures 8 and 9 Thus, it can be observed that the difference between the values obtained for the first version of the driveshaft shaft end, without injection holes, and the second version, with injection holes, is very small. These results favor the second design option. Due to the adhesive injection method, the integrity of the carbon tube was preserved.

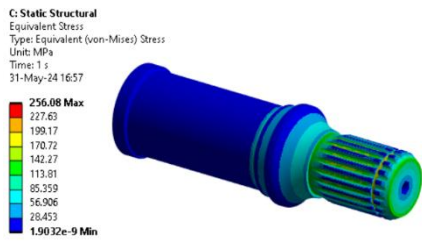


Figure 6 - Maximum stress

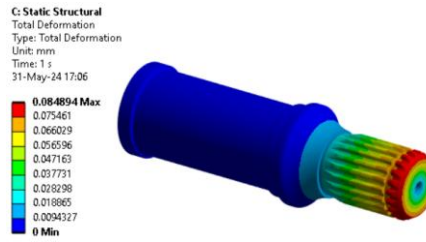


Figure 7 - Total deformation

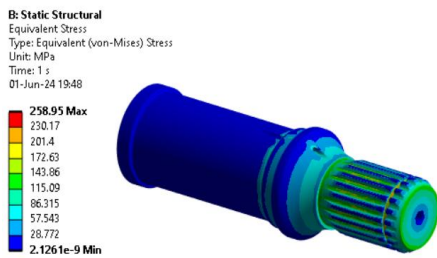


Figure 8 - Maximum stress

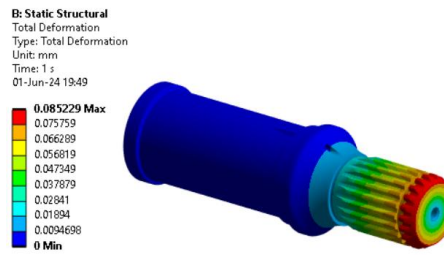


Figure 9 - Total deformation

2.4. Manufacturing of the drive shaft

The materials used for manufacturing the carbon tube included 500g of carbon fiber in ribbon form, 350g of epoxy resin, and 110g of hardener. For manufacturing the driving shaft ends, a 7000 series (7075) aluminum drawn bar with dimensions $\text{Ø}30 \text{ mm} \times 400 \text{ mm}$ was used.

The assembly of the drive shaft consists in: the CFRP tube, the two aluminum drive shaft ends, and a high-strength adhesive. The machine used for manufacturing the tube is an SN 400 lathe. For manufacturing the driveshaft ends, a CNC lathe, and a solid electrode EDM machine were used.

For the final assembly, the three components were cleaned using technical alcohol, for a better-quality bonding. The next step involved inserting the drive shaft ends into the composite material tube. The final step was injecting the adhesive through the holes integrated into the aluminum drive shaft end, with a curing time of 24 hours. The

adhesive used to bond the three components of the assembly has a shear strength of 31 MPa.

3. Results and discussions

Following the design of the three construction versions, the goal is to select the optimal version using a decision matrix. Each construction version is assigned a score based on criteria, and the version that receives the highest score will be chosen for implementation. Scores are assigned on a scale from one to five. Number one represents the minimum value, the least favorable, while number five represents the maximum value, the most favorable.

| Criteria | Solution A | Solution B | Solution C |
|---------------------------|------------|------------|------------|
| Manufacturing cost & time | 5 | 4 | 3 |
| Simplicity of geometry | 5 | 4 | 4 |
| Reliability | 2 | 3 | 5 |
| Torsional resistance | 3 | 3 | 5 |
| Total | 15 | 14 | 17 |

The first two criteria represent both the simplicity of the geometry, but also the cost and manufacturing time of the three design solutions. The highest score is attributed to solution A because it has a simpler geometry of the aluminum drive shaft ends.

The lowest score is attributed to variant C, representing the most complicated geometry, which includes the four adhesive injection holes and the knurled surface. The last two criteria represent the reliability and torsional resistance of the design solutions.

The highest score is attributed to variant C because it has a larger and more adhesive surface for component bonding. Additionally, the composite material tube of variant C does not have holes that could affect the fiber structure. The lowest score is attributed to variant A, as it has a less adhesive surface for component bonding, and the fiber structure of the outer tube is affected by the adhesive injection holes.

After tallying the scores assigned to each construction version, it was concluded that the third solution is the most feasible, as it is the one that has been manufactured.

4. Conclusions

The design and manufacturing process of the Formula Student single-seater driveshaft assembly highlights a comprehensive engineering approach that integrates advanced materials and precise manufacturing techniques. This project underscores the importance of meticulous planning, from the initial research and design stages through testing and manufacturing process.

Three design versions of the driveshaft were proposed and evaluated, with the third version being selected for implementation due to its superior performance characteristics. Using high-strength adhesive with knurled surfaces improved the bonding strength.

The selection of 7075 aluminum and carbon fiber for the driveshaft components reflects a strategic choice aimed at optimizing the strength-to-weight ratio, essential for high-performance applications. Detailed considerations of torsional strength, torque, and component sizing have been made to ensure the reliability and efficiency of the driveshaft assembly.

The result was a 42.3% reduction in the mass of the planetary shaft compared to the original steel version. The final weight of the planetary shaft made from composite material was approximately 375 grams.

References

1. Design of a Formula Student Race Car Spring-Damper System; P.C.M. van den Bos, 0576519; Technische Universiteit Eindhoven.
2. Analysis of Formula Student Race Car; B. Subramanyam, Mahesh Kollati, K. Praveen Kumar, Vishal; JNTU University, Hyderabad, India.
3. Ion Tabacu, *Transmisii Mecanice pentru Autoturisme*, Editura Tehnica, București 1999.
4. Harald Naunheimer, Bernd Bertsche, Joachim Ryborz, Wolfgang Novak, *Automotive Transmissions*, Springer-Verlag Berlin Heidelberg 1994, 2011.
5. 3D numerical analysis of the structural behavior of a carbon fiber reinforced polymer drive shaft; Mosopefoluwa Samuel, Rostand B. Tayong; Institute for Research in Applicable Computing (IRAC), School of Computer Science and Technology, University of Bedfordshire, Luton LU1 3JU, United Kingdom.
6. Design and Analysis of Composite Drive Shaft for Automotive Application; G. Kaviprakash, C. Ramesh Kannan, I. Daniel Lawrence, A. Prince Regan; Anna University Regional office – Madurai, Madurai, India.
7. PARAMETRIC OPTIMIZATION OF COMPOSITE DRIVE SHAFT USING ANSYS WORKBENCH 14.0; I.V.S. Yeswanth, A. Abraham Eben Andrews; Hindustan Institute of Technology and Science, Chennai, India.
8. Residual torsional strength after impact of CFRP tubes; G. Minak, S. Abrate, D. Ghelli, R. Panciroli, A. Zucchelli; Alma Mater Studiorum, Università di Bologna, Mechanical Engineering Department DIEM, viale del Risorgimento 2, 40136 Bologna, Italy; Department of Mechanical Engineering & Energy Processes, Southern Illinois University, Carbondale, IL 62901, USA; 2010.
9. Low velocity transverse impact of filament-wound pipes: Part 1. Damage due to static and impact loads; K. L. Alderson and K. E. Evans; Department of Materials Science and Engineering, University of Liverpool, PO Box 147, Liverpool L69 3BX, UK.
10. Strategies for the production of PAN-Based carbon fibers with high tensile strength; Dawon Jang, Min Eui Lee, Jiwon Choi, Se Youn Cho, Sungho Lee; Carbon Composite Materials Research Center, Institute of Advanced Composite Materials, Korea Institute of Science and Technology, 92 Chudong-ro, Bongdong-eup, Wanju-gun, Jeollabuk-do, 55324, Republic of Korea; Department of Quantum System Engineering, Jeonbuk National University, 567 Baekje-ro, Deokjin-gu, Jeonju, Jeonbuk, 54896, Republic of Korea; 2021.

Aerodynamics in Karting

George Octavian Onaca¹, Dragos Maxim¹, Florin Scurt¹ and Casian Alexandru Toth¹

¹ University of Oradea, Oradea, University St. no.1, Romania
www.uoradea.ro

Abstract. The paper targets aerodynamics in karting over the years and coming up with a new concept. The subject which was overlooked over the years and here we're going to compare old and contemporary fairings design with one another and with our take on kart fairings which developed and implemented for Kart Low Cost 2024 contest. We expect a significant improvement in downforce from our concept in comparison with the designs already on the market

Keywords: Karting, Aerodynamics, Ground Effect, Kart Low Cost, Down Force.

1 Introduction

Aerodynamics is a sub-field of fluid dynamics, primarily concerned over the drag, lift and downforce of a solid object, caused by air passing by and near the specified object. Aerodynamic rules show how an airplane can fly or how a car can create downforce and more grip through corners [1].

The air is a thin fluid that flows around and through bluff bodies, the road vehicle. Above certain speeds, the air flow that encounters the vehicle begins to have an impact on the acceleration, top speed, handling and fuel efficient [2].

The scopes of the vehicle aerodynamics are in close relation with the objectives set for the car (fuel economy or speed) and, for this reason, drag remains the main point of the vehicle aerodynamics [3].

Over the years, engineers discovered that aerodynamics can be the reason for winning not only a race, but also the championship. As in the pinnacle of motorsport, in Formula 1, the aerodynamics only started to play a significant role in the '60 when Lotus introduced the Lotus 49, the first car to feature a full aerodynamic package. They also had made the discovery of the ground effect in 1997 with the Lotus 78, the effect that gave such a big advantage that the Federation Internationale de l'Automobile banned the technology until 2022 [4].

In karting, the subject of aerodynamics was overlooked for years, but in recent years, from 2016 onwards, it has been increasingly researched by various manufacturers as the computational fluid dynamic studies became more and more accessible to engineers.[5]

As a matter of fact, it has been demonstrated that by taking care of the aerodynamics of a kart it is possible to obtain faster lap times, even by half a second, all this without any major costs.[5]

In practice, the fairings, which have evolved from a mere protective device, are the main reason that lead to the reduction of drag.

The first bodywork consisting of side fairings, front spoiler and front number plate was introduced in 1992, all having a rectangular shape with the front spoiler being proportioned to the kart, almost covering the front tires. This kit, having a square shape, made it clear that the aerodynamic research was unknown in the karting world, given the shape of the fairings. This kit was used in K.L.C. 2023 by U.O. K.L.C. Team, figure 1.



Fig. 1. University of Oradea kart with rectangular bodywork design

What is ground effect?

A down force exerted on a racing car by specially designed features such as a wing close to the ground that enables it to achieve higher speed through turns, increasing the grip of the car. To achieve ground effect on a racing car, there has to be a tunnel with such features and geometry that can create two effects that consolidates the ground effect:

- the venturi effect, in which the reduction in fluid pressure that results when a moving fluid speeds up as it flows through a constricted section of a pipe (tunnel), where on a racing car this effect creates suction to the ground when the pressure drops and the velocity increase in the constricted zone;[6]
- the coandă effect, that is the tendency of a fluid jet to stay attached to a convex surface, furthermore elongating the area of the downforce action on the tunnel, respectively on the car. [7]

2 Methods

Taking note of the of the K.L.C. 2024 regulation at the first meeting of U.O. K.L.C. Team, a loophole has been found in the fairings rules that let us develop them as we wished because there were only requirements for kart dimensions and this allow us to get creative with the design. With that in mind, we proceeded to study the ground effect concept and its application over the years in Formula 1, which was our inspiration.

Taking notes from Formula 1 cars, starting with the Lotus 79 designed by Colin Chapman and all the way to the RedBull RB 19 designed by Adrian Newey, the first sketches started to take contour and a design for the fairing with a inside Venturi Tube has been agreed by the team and the process continued with the 3D modelling of the kart in Catia V5 R19 where it started as a simple squared tube and evolved in more aerodynamical fairings to eliminate drag forces as much as possible, and little adjustments were needed to be able to manufacture the fairings. The final fairings design is presented in the figure 2.

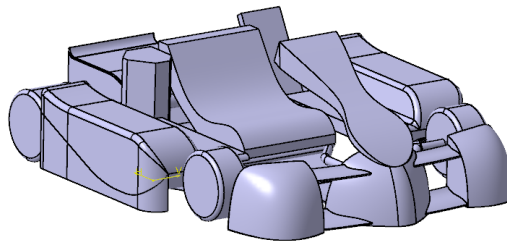


Fig. 2. Final 3D model of the U.O. K.L.C. Team kart

With the 3D model finished and the fairings symmetrical, only the right side was imported in Ansys 2022 Software. After the model has been verified, repaired and the enclosure that represents the wind tunnel created in Ansys Discovery, the fairing was imported in Ansys fluent for meshing and simulations.

The meshing consists of three refinement regions, one surrounding closely the modeled fairing with a mesh size of 16 mm, one more distant from the 3d model with the mesh size of 32 mm and one far with the mesh size of 64mm to gather all the necessary data.

Local sizing for the fairing has been set with the size control type Curvature, a local min size of 2 mm, max size of 16 mm and the curvature normal angle to 9 deg.

The surface mesh has been created with a minimum of 4 mm and a maximum of 256 mm size, growth rate of 1.2, curvature normal angle of 18 deg, cells per gap 1 and size functions Curvature & Proximity.

The volume mesh was generated with poly-hexacore fill with two buffer layers and one peel layer and the boundary layers have been updated accordingly to the inlet, outlet and the walls of the wind tunnel, symmetry and the fairings walls.

Continuing with the simulation, we will cover the drag force and downforce generated, the static pressure on the fairings, the air flow and air recirculation on three speed cases: at 15.65 m/s or 56 km/h representing a slow speed corner, at 23.62 m/s or 85 km/h, a medium speed corner and 36.12 m/s or 130 km/h representing the top speed of U.O. K.L.C. Team kart.

For all three of the cases the settings were identical, besides the value of velocity in the upper paragraph.

Physics settings starting with Viscosity to ensure that the simulation will give the results correlated to the real condition we need to select the most appropriate solver, in this case we need to determine the type of the flow by calculating the Reynolds Number:

$$\text{Re} = \frac{\rho \cdot v \cdot l}{\mu} \quad (1)$$

Where: - ρ – Density of fluid (kg/m³);
 - v – Velocity of fluid (m/s);
 - l – Characteristic length of Solid (m);
 - μ – Dynamic Viscosity (kg/m*s).

$$\text{Re} = \frac{1.293 \cdot 15.65 \cdot 0.7}{1.802 \cdot 10^{-6}} = 7.86 \cdot 10^6$$

Based on this Reynolds Number the flow is classified as turbulent and in Ansys Fluent the following settings have been made for the most accurate simulation:

The operating Pressure is set at 101325 Pa for the Viscosity reference values and Viscosity Model the base k-omega solver with the k-omega model GEKO (Generalized k-omega) with the default settings beside csep constant, with a range from 0.7 to 2.5 it is used to optimize flow separation from smooth surfaces, will be set at 1 for more accurate force predictions in this case and which provides the flexibility to tune the model for different type of flow.

As for the Material used the air has been defined with default properties from the software.

The Reference Values for the simulation were kept in default settings beside the Area that comes in direct contact with the flow, measured at 0.19 m², the length of the fairing, measured at 0.7 m and the Velocity set for each time for the tree simulation cases 15.65 m/s, 23.62 m/s and 36.12 m/s. The wind tunnel crated in Ansys Discovery has been assigned operating conditions, front wall as inlet with a turbulence intensity of 5% and Velocity Magnitude for fluid entering the enclosure set to each of the tree cases studied, back wall as outlet with Pressure Profile Multiplier set to 1, lateral walls and the ceiling of the enclosure set as stationary walls and the Sand-Grain Roughness Constant set to 0.5 and lastly the enclosure ground set as a moving wall relative to Adjacent Cell Zone and the speed specific to each case presented above.

Last but not least the report definitions were made for the drag force with the force vector set perpendicular to the front of the fairings and lift force with force vector set perpendicular to the ground with the rest of the parameters set to the default settings from Ansys Fluent 2022.

3 Results

The results were generated with Hybrid Initialization on Absolute Reference Frame and 10 iterations and finally the Run Calculations were made with Automatic Time Step Method and Time Scale factor set to 1 and on the Parameters side the Number of Iterations set to 5000 with the Reporting Interval and Profile Update Interval both set to 1.

The simulations were run only for the right side fairing of the aerodynamic module and the results are multiplied by 2, to represent the real fairings on the kart.

The results are presented in Tabel 1 through Tabel 6.

Table 1. Drag Force.

| Velocity [m/s] | Drag Forces [N] | Drag coefficient |
|----------------|-----------------|------------------|
| 15.65 | 14.6 | 0.25 |
| 23.62 | 29.3 | |
| 36.12 | 68.8 | |

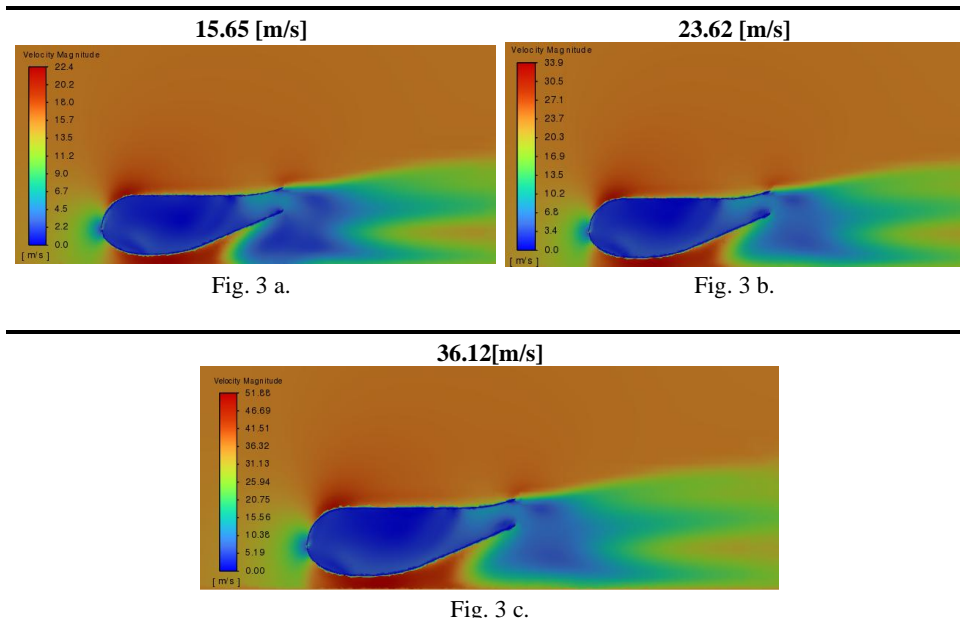
In the table above is presented the drag forces that acts perpendicularly on the front of the fairing for each of the three velocity cases studied. The drag coefficient of the fairings is 0.25 and the forces increase in relation with the velocity increase.

Table 2. Down Forces

| Velocity [m/s] | Down Forces [N] | Down Forces [kg] | Down coefficient |
|----------------|-----------------|------------------|------------------|
| 15.65 | -19.6 | 2 | 0.3 |
| 23.62 | -45.3 | 4.7 | 0.35 |
| 36.12 | -75 | 7.7 | 0.25 |

The result of interest are the down forces which proves that the concept is effective and generates negative lift even from a speed below 15.65 m/s and it is increasing exponentially at 23.62 m/s. The down force increase from a 23.62 m/s to a 36.12 m/s velocity is not as steep as from 15.65 m/s to 23.62 m/s and leaves room for improvement on the concept.

Table 3. Down Force visual.



In the table 3 is compared each case of the aerodynamic study over the velocity of the fluid, from 0.0 m/s, blue, to each case top speed, red. The most visible red zone is created by the ground effect which is imposed by the tear shape of the venturi tunnel of the fairing concept forcing the fluid to increase its velocity and creating a low pressure zone which results in a suction zone between the ground and the fairings. The low pressures zone as well as the high pressure zones are presented in the table 4, with the highest pressure is found on the front of the fairings, marking the zone with the peak drag forces and the low pressure zone is found in the venturi tunnel, marking the zone with the most down forces.

Table 4. Static Pressure.

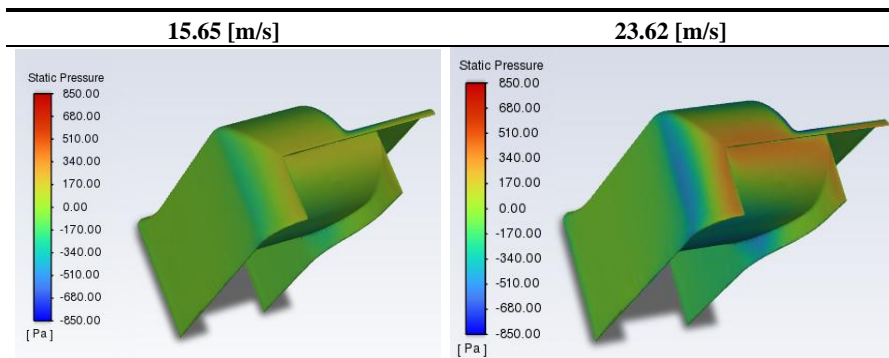


Fig. 4 a.

Fig. 4 b.

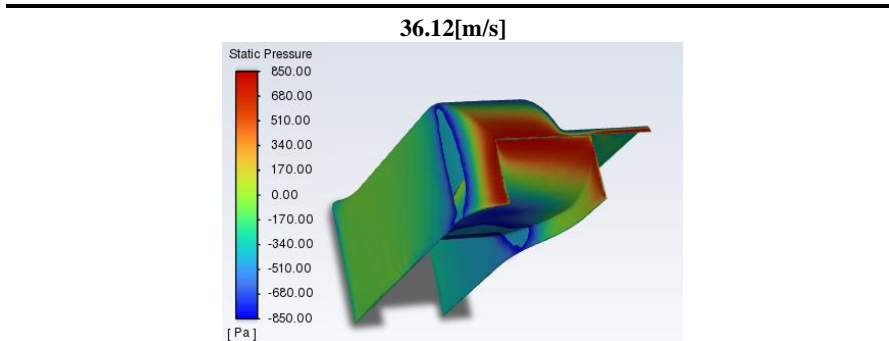
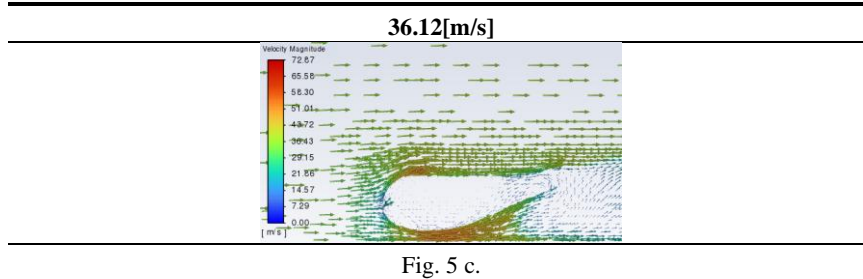
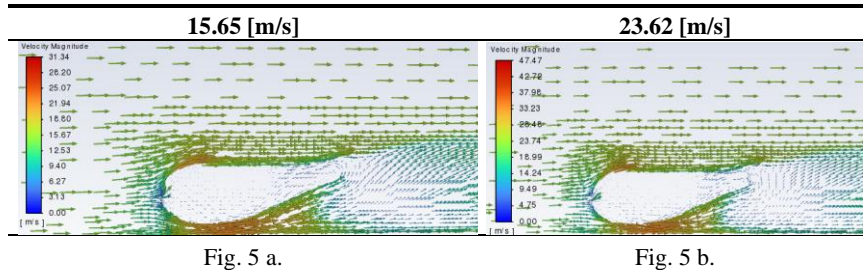


Fig. 4 c.

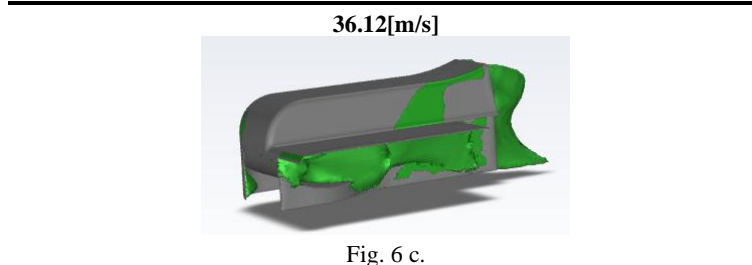
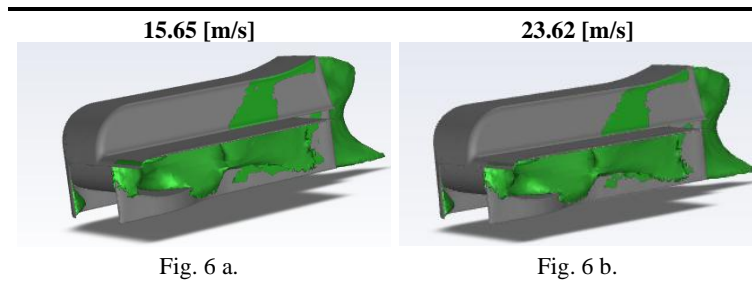
The air flow is consistent over all tree cases of the study as seen in the table 5 with little to no disruption with the increase of velocity. On the back side of the fairings the air flow can be seen recirculating inside the fairing, zone that needs to be addressed in order to fully benefit from the ground effect fairings.

Table 5. Air Flow.



The air recirculation is represented in the table 6 marking the zone where the improvement of the concept is needed in order to fully make use of all the potential performance and reduce at minimum possible the air recirculation of this concept, beginning with small changes in the front and big changes on the lateral side of the fairing and back side of ground effect tunnel.

Table 6. Air Recirculation.



The concept created and implemented works as intended creating in the venturi tunnel at the closes point from the ground a low pressure zone, as presented in the table 1 to table 6 and high velocity of the air generating, a substantial downforce even in low speed corners, giving an advantage to U.O. K.L.C. Team kart over the completion. The fairings have been manufactured for the K.L.C. 2024 contest from fiber glass to keep the cost low and to be as durable and light as possible and respecting the 3D model, presented in the figures 10 and 11.

The design shows more promising performance as the velocity increases. The concept leaves room to optimize the future generations of Ground Effect kart fairings at low and high velocity not by only solving the air recirculation zones but to improve the overall fairings with a more aerodynamic exterior.



Fig. 7. U.O. Kart with Ground Effect fairing



Fig. 8. Ground Effect fairing at Nevers

References

1. Aerodynamics course – Dr. Krishna Anand V G; 2023-2024
2. Automotive Aerodynamics - SAU1601 – Sathyabama Institute of Science and Technology
3. Aerodynamics of Road Vehicles – Wolf-Heinrich Hucho, Gino Sovran; 1993
4. <https://tkart.it/en/magazine/tech-talk/the-aerodynamics-of-a-kart-kg-otk-spoiler-drag-cx#1>
5. <https://tkart.it/en/magazine/special/evolution-kart-bodywork-kits#1>
6. Ground Effect Aerodynamics of Race Cars – Xin Zhang, Willem Toet, Jonathan Zerihan - 2006
7. An Overview of Scientific and Technical Literature on Coanda Effect Applied to Nozzles - Michele Trancossi – Universita di Reggio Eimglia; 2011

Efficiency of the Design of a Formula Student Chassis based on an Architecture in CATIA

Daniel Ursache¹, Alexandru George Pantiru¹, Robert Adrian Chiscop¹,
Ștefan Grigorean¹

¹Gheorghe Asachi Technical University of Iasi, Romania

ursache_daniel@yahoo.com
pantiru.alexandru77@gmail.com
robert_chiscop43@yahoo.com
stefan.grigorean@academic.tuiasi.com

Abstract. The use of design software is increasingly widespread among Formula Student teams. This work aims to present a CAD product, developed and used by the design department of the TUIASI Racing team, which has successfully streamlined the development of a virtual chassis. At its core is the CATIA V5 program, with which a smart architecture was created. This architecture has proven extremely useful in the context of the large number of components on the chassis

Keywords: Automotive Engineering, Computer Aided Design, CATIA.

1 Introduction

TUIASI Racing represents the team of the Gheorghe Asachi Technical University of Iași, and the single seaters developed by us have participated in the international Formula Student competition. As the name suggests, the competition is aimed at students, with a strong emphasis on innovation and strict regulations. The competition's rules impose a series of technical constraints, thus becoming a true challenge.

To be validated and accepted by the organizers, each Formula Student single-seater must adhere to specific constructive dimensions. Therefore, the design process represents the first significant step in the field of design and development.

Within our team, the use of CAD programs is essential as it accelerates the development process of the virtual model, saves money on the manufacturing process, and even allows us to optimize various components of the single seater. Additionally, CAD programs facilitate the easy creation of execution drawings, which are required by the organizers.

The TUIASI Racing team has adopted and currently uses CATIA V5 as the main design tool because it effectively organizes large assemblies, where hundreds of virtual components make up the racing single seater. This aspect of working with a very large number of parts represents a true challenge, and thus our team had to find a solution.

The keyword is “CAD architecture.” The architecture is an internal product developed by the team’s design department and created in CATIA V5. This approach helps us structure the virtual model into class levels, starting with sub-products, sub-sub-products, down to the final level where we find simple components such as screws, nuts, washers, etc. Additionally, the architecture locates each part and each sub-assembly in a determined position, thus preventing the accidental movement of elements within the model

Besides its organizational role, the CAD architecture was initially created to be user-friendly, to respond quickly to design updates or parameter changes. The architecture is a scalable, stable, yet flexible product. As the virtual model expanded, the architecture gradually incorporated new functions such as DMU Kinematics, Section View, and Clash Analysis, among others.

These capabilities assist us in the development process of the chassis, suspensions, steering system, and braking systems. We periodically test the architecture’s functions to ensure that the latest improvements do not affect the functionality of the entire virtual model. In the next chapter, we will delve deeper into the details of the architecture, exploring its components and how it operates.

2 Definition of a CAD architecture

As mentioned earlier, this CAD architecture is a proprietary creation of the TUIASI Racing team and is, moreover, a relatively recent implementation. Additionally, we view it as an application that requires constant updates.

2.1 Main product and its items

Our product is named TUIASI_242_Full_Assembly and has the following significance: TUIASI is the acronym for the Technical University of Iași, 242 represents the competition number of the racing car, and Full Assembly denotes the main product in CATIA. This product contains 10 items, including a part named TUIASI_242_0000_VEHICLE_ARCHITECTURE, 8 other sub-products, and finally, a set of geometric constraints.

Figure 1 shows the CATIA feature tree with the structure of the main product, and we observe that at the highest level, we find only the important systems (e.g., the front and rear axles, the chassis with the body, the powertrain, etc.).

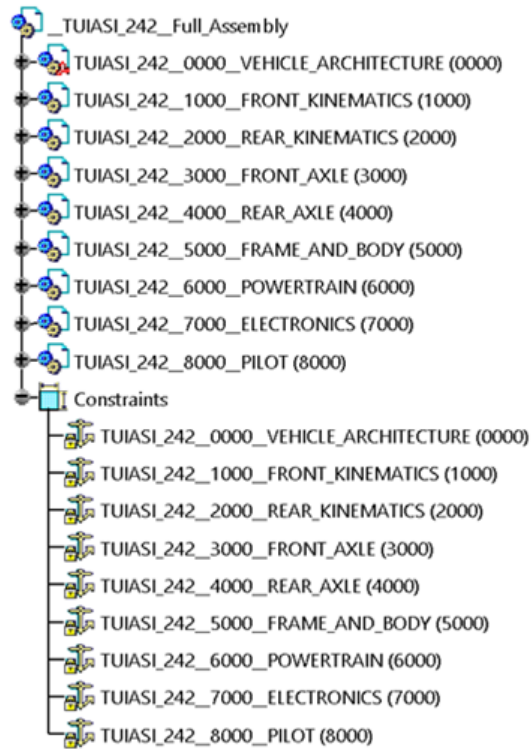


Fig. 1. CATIA feature tree and the structure of the main product.

2.2 The elements of the vehicle architecture

TUIASI_242_0000_VEHICLE_ARCHITECTURE serves as a linking part between all virtual components, regardless of their level in the structure. Its name is specific and has the following significance: TUIASI is the acronym for the Technical University of Iași, 242 represents the competition number of the racing car, 0000 represents the part number, and finally, VEHICLE_ARCHITECTURE denotes the part name.

One important aspect to mention about the part number format is that it consists of only four characters because our racing car does not have more than 9999 main components. However, if the design of more than 10,000 parts is desired, the solution is to add a fifth digit at the end of the part number.

Inside the Vehicle Architecture part, there are three working planes (XY, YZ, ZX), a set of axis systems, a set of variable parameters, a list of calculation relationships between parameters, six geometric sets or folders, a workspace, and a list of publications (see Fig. 2).

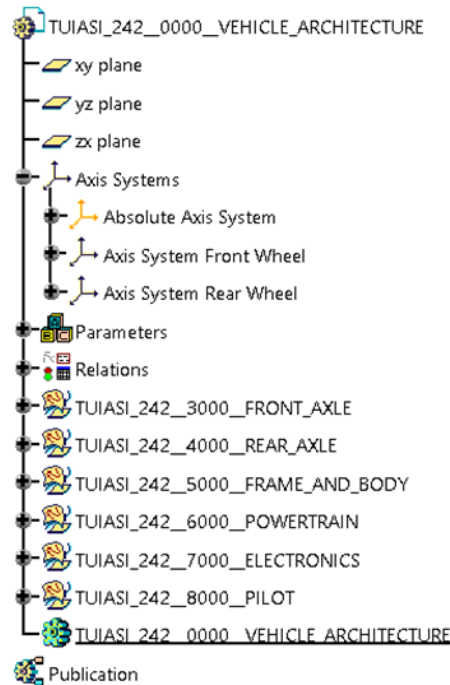


Fig. 2. CATIA feature tree and the structure of the architecture.

Default working planes

The three working planes XY, YZ, and ZX are automatically introduced by the CATIA tool each time a new Part file is created. These planes cannot be deleted or modified, and they are found in the tree structure in the first three positions, immediately below the Part title (see Fig. 2). The intersection of these three planes generates a coordinate point $\{0.0, 0.0, 0.0\}$ known as the absolute origin.

In our case, we will not use these working planes because we employ another method that involves creating an absolute fixed axis system.

The set of axis systems

The CATIA user has the ability to define one or more axis systems to be used according to the design requirements. In our case, we created a primary axis system called Absolute Axis System with the following properties: the origin of the axis system is exactly the intersection point of the aforementioned planes, and the orientations of the axes have been correlated with those in the MSC ADAMS Car tool.

The X-axis is positive from the front of the racing car to the back, the Y-axis is positive from the left side of the racing car to the right side, and the Z-axis is positive from the ground surface towards the sky.

This Absolute Axis System can still be moved even though it is constrained by the absolute origin point, with translation being done in the previously mentioned working planes.

Two other defined axis systems are Axis System Front Wheel and Axis System Rear Wheel, which have the following properties: they are relative axis systems linked to the Absolute Axis System, their origins are the center points of the front and rear wheels, respectively, and their orientations are identical to those of the Absolute Axis System.

2.3 Parameters and Relations

Parameters and relations are elements that allow users to make certain features or geometry visible in a CAD model to facilitate collaboration and reuse in other modules or applications. Publications are used to create interfaces between components, ensuring that important parts of the model are accessible to other users or CATIA modules without exposing the entire structure. Typical uses of publications are described in the next paragraph.

In assemblies (Assembly Design), publications provide easy access to specific parts of a piece (e.g., mounting holes) to create links between components or to define constraints between them.

In collaboration contexts, if multiple people or teams are working on the same project, publications allow them to share only the relevant information for their tasks, keeping the rest of the model private.

For data exchange with other applications: Publications facilitate the integration of CATIA with other design or analysis programs.

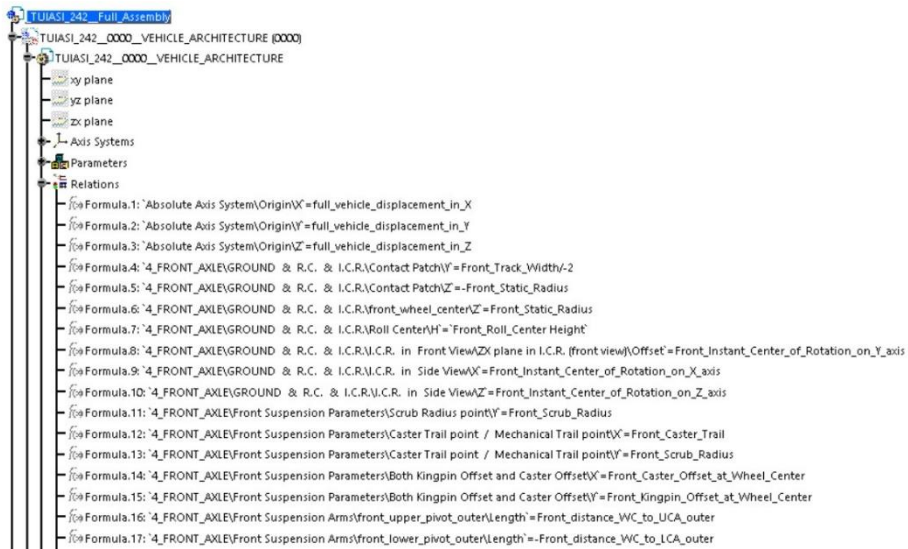


Fig. 3. Example of relations used in the architecture.

2.4 Geometric sets

In CATIA V5, a Geometrical Set is used to organize and manage wireframe and surface entities (curves, lines, planes, points, surfaces, etc.). It helps maintain clarity and order within the model, especially in complex projects. Geometrical Sets do not contain solid bodies but are exclusively intended for non-solid geometric entities.

One of the key features of a geometric set is hierarchical structure. Geometrical Sets can be grouped into a hierarchical structure, allowing geometric entities to be organized on multiple levels, based on their functionality and use within the model. For example, in a complex model, points, curves, and surfaces that are part of a specific section of the design can be placed in one Geometrical Set, while entities from another section can be placed in a different set.

Designers can toggle the visibility of an entire Geometrical Set, making only the elements in that set visible or invisible in the graphical model. This helps manage the complexity of the model, allowing users to focus on specific parts of the geometry without being distracted by other elements.

Geometrical Sets are usually independent of the solid modeling history. This means that changes made within a set do not directly affect the solid body, unless there are direct references between them (e.g., using a curve from a Geometrical Set to extrude a solid).

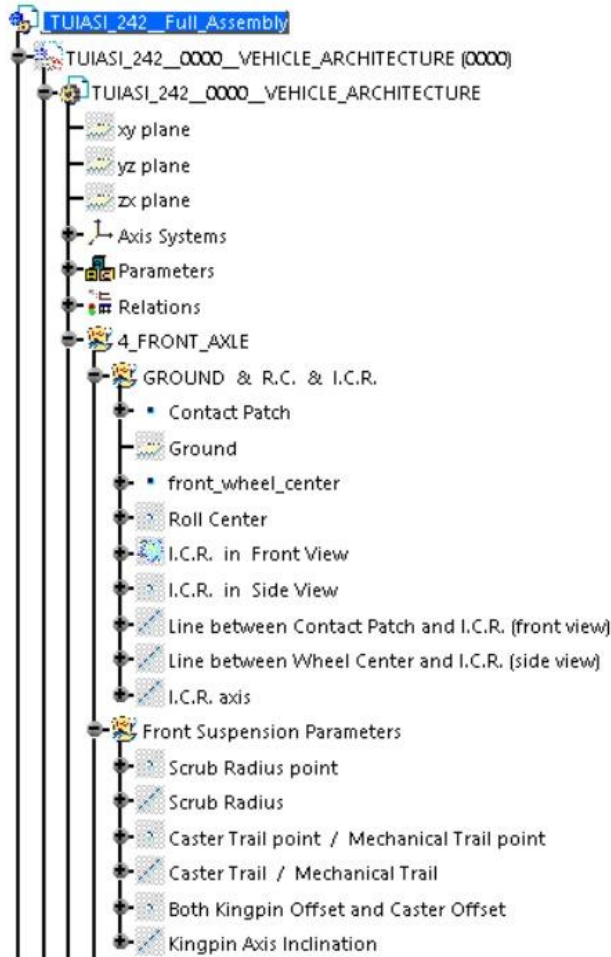


Fig. 4. Geometrical sets used in the architecture of the suspension

2.5 Publications

Publications are elements that allow users to make certain features or geometry visible in a CAD model to facilitate collaboration and reuse in other modules or applications. Publications are used to create interfaces between components, ensuring that important parts of the model are accessible to other users or CATIA modules without exposing the entire structure.

The main advantage of publication is the collaboration between teams: Publications allow the sharing of certain geometries (such as points, edges, surfaces, bodies, etc.) with other teams or designers without providing access to the entire model.

Simplify model reuse: If a certain element of the model is published, it can be accessed and reused by other functions or modules without the need to redefine or recreate that geometry.

Optimize interactions between modules: In CATIA, there are many modules (Design, Assembly, Analysis, etc.), and publications allow the geometry created in one module to be visible and usable in another module.

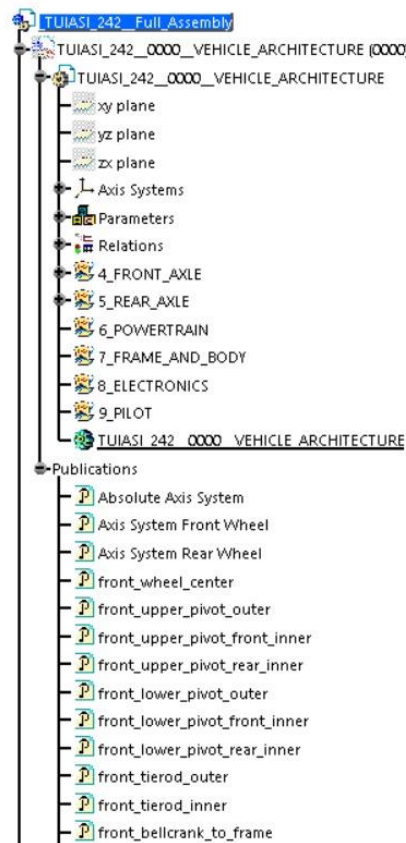


Fig. 5. Example of publication used in the architecture

3 Chassis development

The chassis of the race car is a component that requires a well-defined design methodology to minimize difficulties that may arise as the assembly becomes complete. The time allocated for design and development is also a factor with a major impact on the vehicle's performance. Thus, by introducing architecture as a design methodology, design time and errors have decreased considerably.

The Formula Student chassis is constrained by a set of rules that govern both the positioning of the tubes and their minimum dimensions to meet the minimum safety and strength requirements for the forces encountered during circuit running. Thus, each roll hoop requires a bracing, bracing support, and diagonal members that must be

properly triangulated. The chassis has two roll hoops, Main Hoop and the Front Hoop, a Side Impact Structure and a Front Bulkhead that serves as a support for the impact attenuator.

In order to simplify the design phase, we divided the chassis in three sections. The front section represented by the space between the Front Bulkhead and the Front Hoop, the middle section constrained by the Front Hoop and the Main Hoop and the rear section which begins at the Main Hoop and ends at the rear of the vehicle, depending on the team design.

3.1 Chassis front section

The front section of the chassis is built from the Front Bulkhead, Front Hoop, Front Bulkhead Support and the Front Hoop Bracing. The main components of the car that are within this section are the front suspension, pedal box group and the steering assembly.

The first step to design this section is to establish and freeze the design of the front suspension. The front suspension dictates how the Front Bulkhead Support is designed in order to accommodate the pickup points. From this point the architecture begins to have a major role in the overall design method. All the suspension pickup points are used as an external reference for the chassis, therefore the design of the members that support the suspension is constructed using a connexion between the architecture and the chassis (see Figure 3.). This link between components do not seem useful on the first build, but with the next project, when all the links are already in place the designer can adjust the chassis members fast and check wit ease if the distance allows the built of the brackets. Furthermore, the same principle applies to other components that are within the chassis front section.



Fig. 6. Example of the external references used

3.2 Chassis middle section

The middle section of the chassis consists of the Front Hoop, Main Hoop, Side impact structure, Shoulder Harness Bar, and additional, if it is necessary, the seat support structure. This part of the chassis has a direct influence on the driving position due to space specified between the Roll Hoops. To design this section the team has to determine the best driving position with the respect of the 95th percentile man rule and also in accordance with the available drivers. As seen in the previous images, in the architecture the pilot has a separated folder.

This approach was chosen due to the connections that are required to other assemblies. The pilot determines the position of the steering wheel, thus of the steering assembly and of the pedal box. Using these links, the driving position offers the position of not only the Main Hoop and Shoulder Harness Bar, but also of the Front Hoop and the Front Bulkhead.

3.3 Chassis rear section

The last section of the chassis consists of only three elements that are required by the rule book, the Main Hoop, Main Hoop Bracing and Main Hoop Bracing Support. This fact permits a free design of the rear part of the chassis on which the rear suspension is mounted.

The rear section is the most complicated one due to the fact that there is a big number of parts that are dependent such as the rear suspension, transmission and engine bay

area which includes catch cans, fuel tank, air intake assembly, etc. The complexity of this section is that the designer can not make chassis members dependent on certain components. This happens due to changes that appear every year with a new vehicle.

In this section the architecture has a major role in the connection with the rear suspension, because contains the powertrain with the drive shaft and the differential. These parts need to be mounted on a high stiffness structure that also respect the space for other components.

4 Conclusion

The adoption and utilization of this strategy through the implementation of a CAD architecture have proven to be efficient in the design process with CATIA. This is because it allows us to avoid incorrect positioning of parts or sub-assemblies, prevent accidental collisions between two or more components, avoid situations where the space between two parts is too small, and prevent the design of technically incorrect components.

Additionally, we can export data from CATIA to other types of programs (e.g., MSC ADAMS, ANSYS, etc.), perform real-time measurements directly on the CAD model, and, last but not least, work with revisions and variants of the same part. This capability helps us track the evolution of the design of the same component from one project to another.

The CAD architecture has significantly streamlined the design process. It emerged as a response to the challenge posed by working with large assemblies. However, it also has a less favourable aspect: it takes a considerable amount of time to complete, and using the architecture requires a certain level of discipline in CATIA design. Nevertheless, this does not deter us from continuing to use the architecture, as the advantages far outweigh the disadvantages

References.

1. Formula Student Rules 2024 v1.1, <https://www.formulastudent.de/fsg/rules/> , last accessed 2024/10/6
2. Mononen J., Bachelor's Thesis, Industrial Vehicle Engineering, Tampere University of Applied Sciences (2023)
3. Baker C.S., Dissertation, Mechanical Engineering, University of Southern Queensland (2004)
4. Krunal K, Aditya V, Rushang B, Jayendra V., Design and Development of Formula Student Chassis, IJERT, Volume 10, Issue 5 (2023)
5. Shobhit A, Prashant A., Tarun S., Mukul K., Vishal J., Design and Analysis of Spaceframe Chassis for FSAE Vehicle, IJERT, Volume 9, Issue 3 (2020)

Fixed Air Quality Monitoring Station in Road Traffic

Sorin Ionascu¹, Alexandru Şopron¹, Cosmin Hâncu¹ and Robert Perianu¹

Coordinator: Prof. Dr. Eng. Dumitrescu Valentin Marius

¹Ovidius University of Constanţa

Abstract. Air quality monitoring in road traffic is an important component of air quality monitoring efforts in general because road traffic is one of the main sources of air pollution in urban areas. The present work, which is part of the complex project called SMART AIR, presents the technical solutions, compatible with IOT, for the realisation and the implementation of a fixed station for monitoring air quality in road traffic in our city. The fixed station is a device strategically placed in an area with heavy traffic to measure and monitor air pollution values generated by road traffic.

Keywords: Air, Station, Traffic.

1 Objectives

Development of the air quality monitoring system: the system uses the Arduino Nano development board as a central platform for collecting data from various sensors.

2 System architecture

2.1 Components of the monitoring platform Arduino Nano:

The Arduino Nano development board is a platform equipped with an ATMEGA 328 microprocessor, with the ability to integrate different sensors.

Sensors:

The component sensors of the system, initially pre-calibrated by the manufacturer, are compatible with I2C communication for an easier implementation. In addition, they have a low consumption of electricity, a necessary attribute in the operation of the battery-powered system.

- BH1750 - Digital light sensor
- MAX9814 - Microphone amplifier module
- HMC5883L - Magnetometer
- SGP30 air quality sensor: Measures the concentration of volatile organic compounds (VOC).
- HTU21D humidity sensor: Measures relative humidity.

2.2 System structure

The monitoring station is built around the Arduino Nano development board, which collects data from sensors via the I2C bus and transmits it via a communication module using the ESP8266 Wi-Fi module to a web server. The data can be processed in real time or can be stored in a database, with the possibility to synchronize the collected data with the information provided by a GPS system, the result being the overlay of the recorded data on a digital map.

2.3 The principle of operation of the platform

Data Collection: Arduino Nano polls the sensors at regular time intervals and collects the data.

Data transmission: Using a communicating module (e.g. ESP8266), the Arduino Nano transmits the collected data to a web server.

Data storage: Data is stored in a database, allowing access and subsequent analysis.

The system architecture is presented in fig.1, and the prototype of the monitoring system is shown in Fig.2.

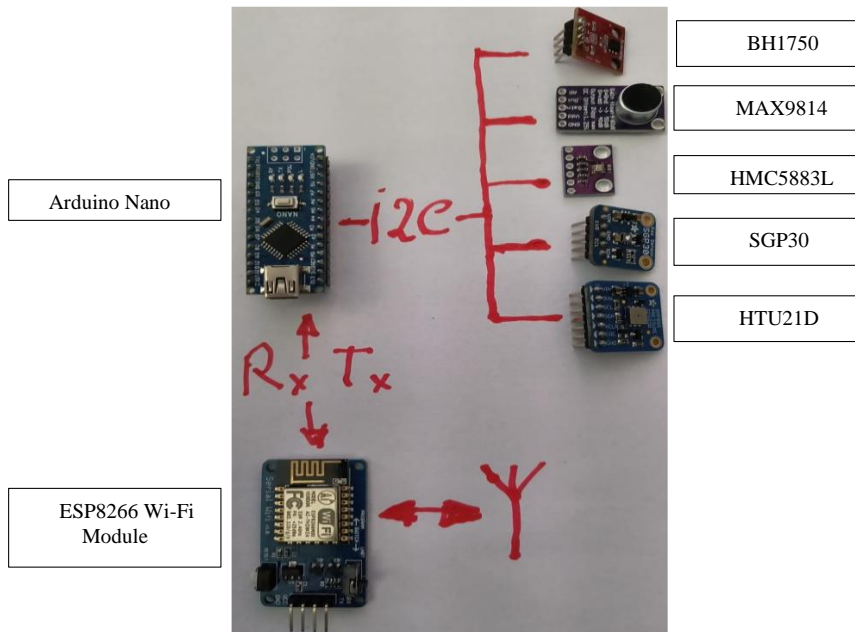


Fig 1. The system architecture.

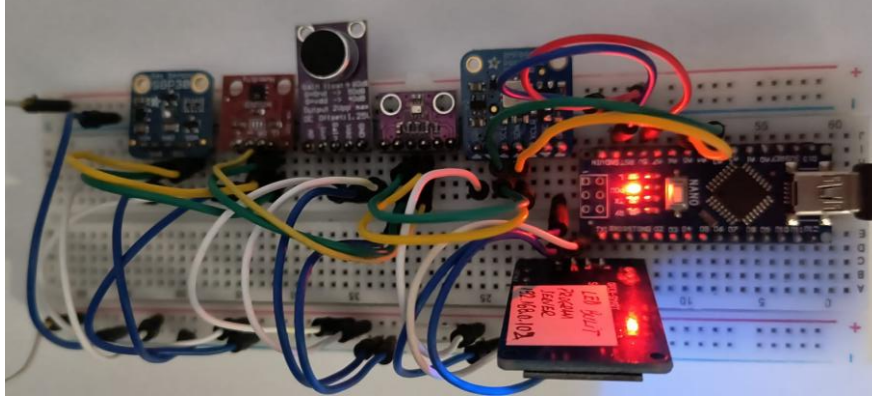


Fig 2. System prototyping.

2.4 Software used:

Arduino Nano Firmware: The microcontroller software was written using the Arduino IDE platform. It includes the libraries required for interfacing with sensors and for Wi-Fi connectivity.

CoolTermWin64Bit is a graphical serial terminal. It is used to communicate with devices that have a serial interface, such as microcontrollers (e.g. Arduino) and other equipment that use RS-232 serial ports.

Web Server: The web server is implemented using a framework, which handles requests from the Arduino Nano and stores the data in a database.

3 Results

The monitoring system was initially tested in the laboratory, and after the completion of the prototyping, the platform will be tested in the field.

The data collected demonstrated the effectiveness of the project.

An example of collected data is shown in fig.3, where VOC stands for ‘Volatile Organic Compounds’, being an important indicator in air quality assessment. The concentration of VOCs is expressed in ‘parts per million’ (PPM). These data were recorded in traffic at an interval of 2s. The reason of choosing such short interval is to show how efficient, in collecting data, the system is.

| VOC (ppm) | Temp (°C) | Humidity (%) |
|-----------|-----------|--------------|
| 17281 | 28.6 | 90.5 |
| 17174 | 28.6 | 90.4 |
| 17132 | 28.6 | 90.3 |
| 17055 | 28.6 | 90.3 |
| 16994 | 28.6 | 90.2 |

| | | |
|-------|------|------|
| 16889 | 28.6 | 90.2 |
| 16823 | 28.6 | 90.1 |
| 16699 | 28.6 | 90.0 |
| 16403 | 28.6 | 90.0 |
| 16758 | 28.6 | 90.1 |
| 16863 | 28.6 | 90.7 |
| 17303 | 28.7 | 91.4 |
| 18311 | 28.6 | 91.6 |
| 19920 | 28.7 | 91.4 |
| 20819 | 28.6 | 91.1 |
| 21264 | 28.7 | 91.0 |
| 21556 | 28.6 | 90.7 |
| 21845 | 28.7 | 90.3 |
| 22046 | 28.6 | 89.9 |
| 22210 | 28.6 | 89.7 |

Fig 3. Example of collected data

4 Conclusions

The fixed air quality monitoring station based on Arduino Nano proved to be an ideal solution for real-time monitoring of air quality in traffic areas.

The information collected by this fixed monitoring station will be used to assess air quality, identify areas with pollution problems and take corrective measures to improve air quality. This data can be used to inform the public about pollution levels and to encourage more responsible behavior regarding air pollution.

References

1. Arduino - <https://www.arduino.cc/en/Reference/Libraries>
2. Bosch sensor - <https://www.bosch-sensortec.com/products/environmental-sensors/pressure-sensors/bmp280/>
3. Gas sensor - <https://www.sensirion.com/en/environmental-sensors/gas-sensors/sgp30/>
4. Microphone module - <https://www.maximintegrated.com/en/products/analog/audio/MAX9814.html>
5. Esp8622 - <https://www.espressif.com/en/products/socs/esp8266/resources>
6. Air pollution - <https://www.who.int/airpollution/ambient/health-impacts/en/>

Implementation and Evaluation of the Bearing Monitoring System in the EV Field using Vibrations Sensors in the Context of Maintenance Engineering

Dumitrel Barbu¹, Raul Ferchiu¹ and Valentin Silivestru¹

Coordinator: Prof. Dr. Eng. Panait Paula

¹Ovidius University of Constanța

Abstract. A common technology in the electric's actuators field, are electromotors controlled in frequency. These are used on a wider scale in the automotive industry for being easy to adjust the power, torque, and direction of rotate. This kind of control is made through adjusting the current frequency supply of the motor. The basic principle of frequency control is that the speed of an engine is directly proportional with the frequency supply current and backwards with the number of motor pols pairs. Therefore, through changing the supply current frequency, we can control the motor speed and direction of rotation, without being necessary to change mechanical equipment. Regular maintenance of bearings that equips an electric motor, is a real requirement that will ensure proper operation of the equipment for a longer period. A common problem with electric motors that equip electric vehicles is the appearance of wear of the bearings that support the axis of the electric motor. The consequence is destruction of these bearings and the complete destruction of the electric motor, and the repair is very expensive. In this case, our work presents the conception, implementation, and evaluation of a monitoring system for bearings used in the EV field, to detect anomalies occurred during the operation of the electric motor.

Keywords: Bearing, Engineering, Monitoring.

1 Components used:

a. DC electric motor

This is a direct current electric motor with a nominal voltage of $U_n=12V$ and a maximum absorbed current $I_{max}=7A$. This electric motor has a ball bearing as a component.

b. Sound sensor

The sensor is a RobotDyn Sound Detector type (Fig.1)

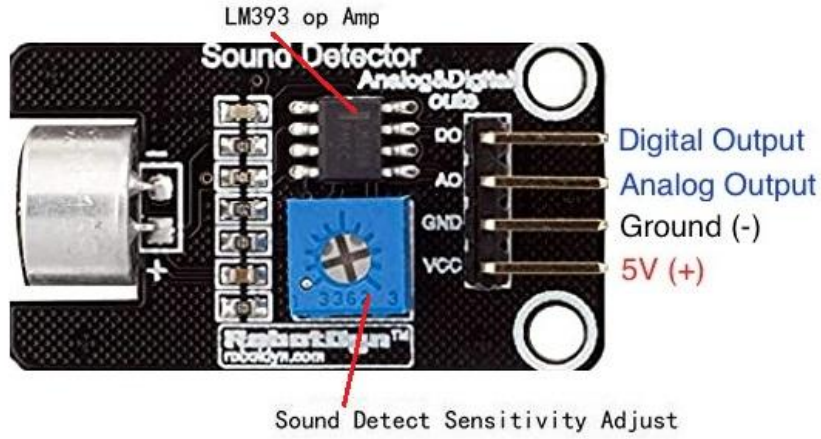


Fig 1. RobotDyn Sound Detector.

The RobotDyn Sound Detector Module uses a microphone and a power amplifier to detect sounds and output a digital or analog signal.

The digital signal output can be adjusted with an onboard potentiometer to set the trigger sound level.

The analog signal output is a real time output of the microphone input(fig.2). It will be glued to the DC motor, so that the microphone is permanently in contact with the analyzed bearing housing.

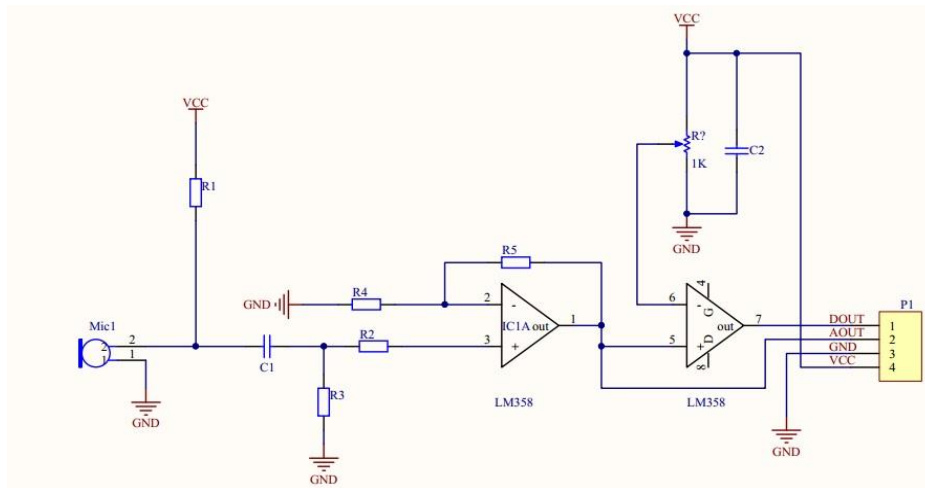


Fig 2. Schematic RobotDyn Sound Detector.

c. DS18B20 temperature sensor

The DS18B20 communicates over a 1-Wire bus that requires only one data line (and ground) for communication with central microprocessor-by definition.

In addition, the DS18B20 can drive power directly from the data line (“parasite power”), eliminating the need for an external power (fig.3)



Fig 3. Temperature sensor DS18B20.

d. Arduino board

Arduino Uno is a microcontroller board based on the ATmega328P(datasheet).

Is a 14 digital input/output pins (of which 6 can be used as PWM outputs), 6 analog inputs, a 16 MHz ceramic resonator (CSTCE16M0V53-R0), a USB connection, a power jack, an ICSP header and a reset button (fig.4).

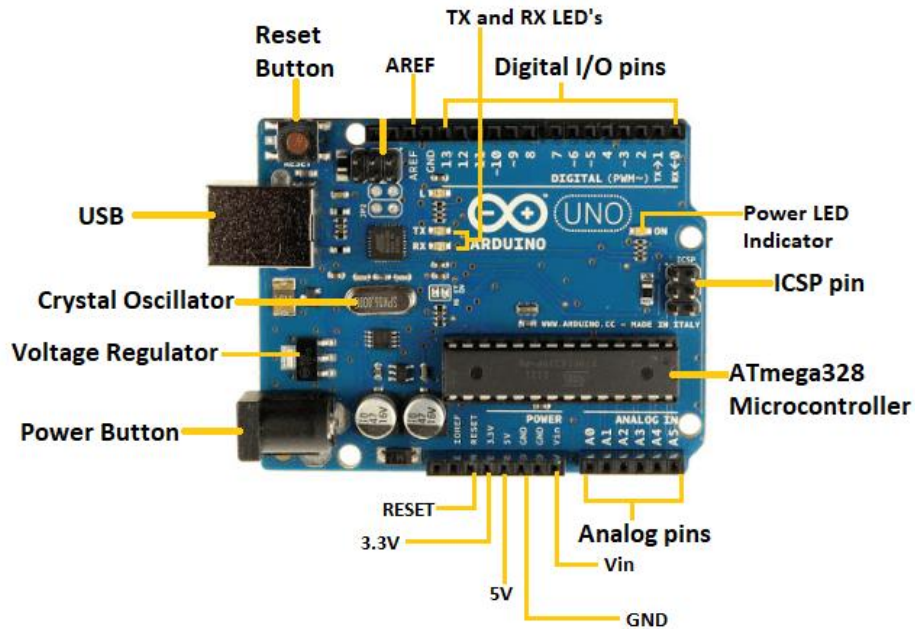


Fig 4. Arduino Uno.

e. Oscilloscope for the signal viewing.

2 Arduino Uno Software and Programming

Libraries used (One Wire, Dallas Temperature).

Programming the Arduino consisted of writing the source codes for the sound and temperature sensors.

- Sound reading code (demonstrative code provided by the sensor manufacturer):

```
//Define the sound pin const int sound
SensorPin=A0; void setup(){
//Initialize serial communication at 9600 baud
Serial.begin(9600);}void loop(){
//Read the analog value from the sound sensor
Int soundValue=analogRead(soundSensorPin);
//Sendingthe read value via serial
Serial.print(soundValue);
//500ms pause between readings
```

```
Delay(500);}

```

- Temperature reading code (demonstrative code provided by the sensor manufacturer):

```
#include <OneWire.h>
#include <DallasTemperature.h>
// Pin definition for DS18B20 sensor
#define ONE_WIRE_BUS 2
// Initialize OneWire instance and DallasTemperature
OneWire oneWire(ONE_WIRE_BUS);
DallasTemperature sensors(&oneWire);
void setup() {
  // Initialize serial communication at 9600 baud
  Serial.begin(9600);
  // Start the temperature sensor
  sensors.begin();
}
void loop() {
  // Request temperature data
  sensors.requestTemperatures();
  // Reading the temperature in Celsius degrees
  float temperatureC = sensors.getTempCByIndex(0);
  // Send temperature over serial
  Serial.print("Temperature: ");
  Serial.print(temperatureC);
  Serial.println(" °C");
  // 1 second pause between readings
  delay(1000);
}

```

3 Data visualization

To carry out the experiment regarding the simulation of bearing wear, its anti-dust protection was removed.

To collect and interpret the data with the help of oscilloscope, the following stages were completed:

Step 1: The first determination of the signal generated by the Sound Detector sensor was made with the electric motor powered at the nominal voltage of 12V.

Step 2: The same measurements as in step 1 were repeated, the only difference being that a few grains of sand were added to the bearing.

Step 3: The same determinations were repeated but with a larger amount of sand grains.

The results recorded and displayed by the oscilloscope can be observed in the three cases in fig.5.

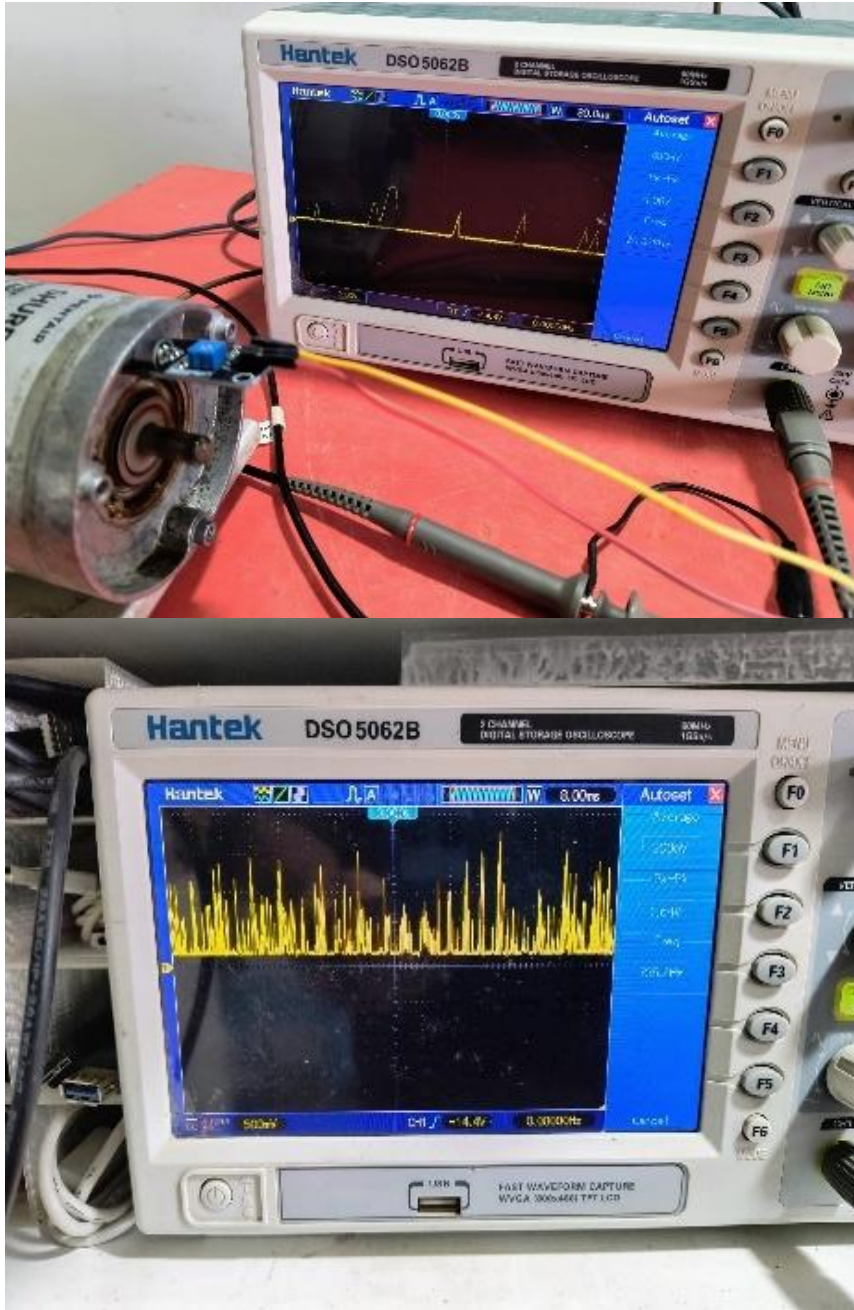




Fig 5. Visualization of the wear stage of the bearing.

Using the Arduino serial monitor to display the noise produced by the bearing (fig.6):

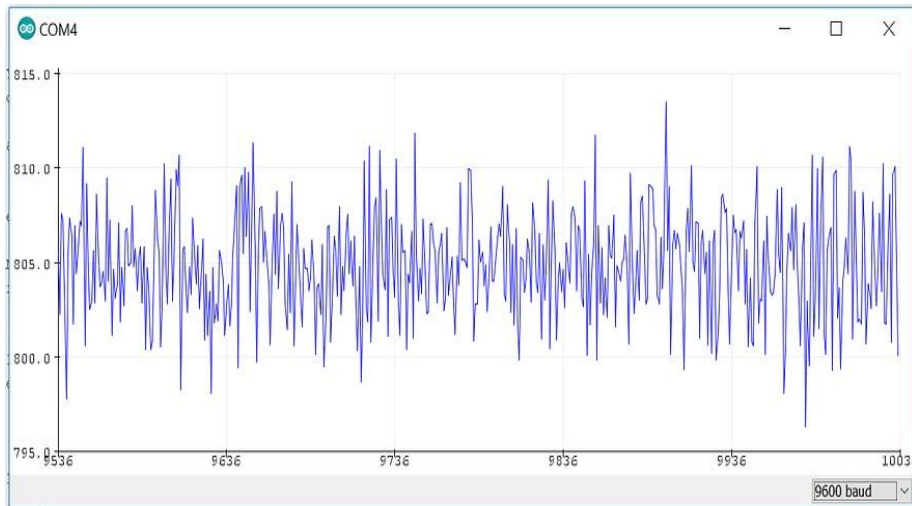


Fig 6. Display of bearing noise.

Using the Arduino serial monitor to display the temperature (fig.7):

| Temperature (°C) |
|------------------|
| 30.27 |
| 30.76 |
| 30.76 |
| 29.79 |
| 30.27 |
| 30.27 |
| 29.79 |
| 29.30 |
| 30.27 |
| 30.27 |

Fig 7. Temperature display.

4 The results obtained in the project card

Several test sessions were carried out under controlled and variable conditions to simulate different operating scenarios of the bearings.

The conclusions were the following:

Sound sensor:

- During the tests, the sound sensor was able to detect variations in the intensity and frequency of the sound produced by the bearing. In particular, an increase in the noise level and the appearance of abnormal sounds were observed in the case of defective bearings.
- The data was visualized using an oscilloscope.

Temperature Sensor DS18B20:

- The temperature sensor constantly monitored the bearing temperature. In case of defects, the temperature showed a significant increase due to the additional friction between the bearing elements.
- Temperature data was collected and displayed in real-time via Arduino's serial monitor, showing variations correlated with the bearing's operating condition.

Anomaly detection

To detect anomalies in the operation of the bearings, simple methods of signal analysis were used:

- Sound analysis:

Intensity and frequency thresholds were identified and established to differentiate normal sound from abnormal ones. For example, sounds above certain threshold of frequency and intensity were considered indicators of defects.

- Temperature analysis:

A sudden and sustained increase in temperature has been correlated with a possible malfunction.

5 Conclusions

Following the development and testing of the sound and temperature monitoring system for the detection of bearing defects, the following key conclusion were reached:

1. **Anomaly Detection Effectiveness:** The system has demonstrated a high ability to identify specific sounds of faulty bearings.
2. **Temperature Monitoring:** The DS18B20 temperature sensor provided accurate and consistent bearing temperature measurements.
3. **Hardware and Software Integration:** The use of the Arduino board facilitated the integration of data from sensors and their transmission through serial communication.
4. **Visualization and Analysis of Data:** Visualization of sound signals on the oscilloscope allowed a clear interpretation of the behavior of the bearings during the period of operation of the motor. The Arduino serial monitor provided an efficient method of displaying and recording real-time data.

The proposed system represents an important step towards efficient and automatic monitoring of the bearing condition. Early detection of defects can not only prevent major failures, but also significantly reduce maintenance costs and operational downtime. With further improvements, this system can become an essential tool in industrial predictive maintenance.

References

1. RobotDyn - <https://www.addicore.com/products/robotdyn-sound-detector#:~:text=The%20RobotDyn%20Sound%20Detector%20Module,output%20of%20the%20microphone%20input>.
2. Arduino - <https://store.arduino.cc/products/arduino-uno-rev3>
3. Sound code - <https://randomnerdtutorials.com/guide-for-microphone-sound-sensor-with-arduino/>
4. Temperature sensor code - <https://randomnerdtutorials.com/guide-for-ds18b20-temperature-sensor-with-arduino/>

Global Positioning and Data Synchronisation System

Aurora Țurcanu¹, Cristina-Corina Chihaiia¹ and Ruben Drăgan¹

Coordinator: Prof. Dr. Eng. Tudor Camil

¹Ovidius University of Constanța

Abstract. Urban transport system facing significant challenges related to traffic efficiency, pollution, and road safety. The S.M.A.R.T. AIR project developed within the “Ovidius” University Constanta - Faculty of Mechanical Industrial and Maritime Engineering, aims to improve these aspects by integrating advanced tracking and monitoring technologies in urban electric vehicles. S.M.A.R.T. - Sistem Mobil Avansat de Recunoaștere a Traficului (Advanced Mobile Traffic Recognition System). This paper presents the development and testing of a global localization and data synchronization system for urban electric vehicles, part of the S.M.A.R.T. AIR project. The data is displayed on a 12C display and transmitted to a U-Center2 digital map, ensuring real-time monitoring of the collected information. This project is the testing phase for installation on an urban vehicle.

Keywords: GPS, System, Air.

1 Objectives

The main objective of this project is the development of a localization and data synchronization system that allows real-time monitoring of urban electric vehicles. The system will help optimize traffic and increase safety by providing accurate and up-to date data.

2 System architecture

2.1 Platform components

- VK2828U7G5LF GPS module: Uses GNSS technology to provide accurate location data (Fig.1). The features of this module are the following:
- Industry standard GPS antenna of 25*25*4mm, with high sensitivity
- Optional interface: UART/TTL, RS232
- High-precision TCXO of KDS 0.5PPM
- Built-in LNA
- Optional frequency of data refreshing: 1Hz-10Hz

- Supports A-GPS service: Assist Now Online and Assist Now Offline
- Hybrid engine: GPS, GALILEO, SBAS (WAAS, EGNOS, MSAS, GAGAN)

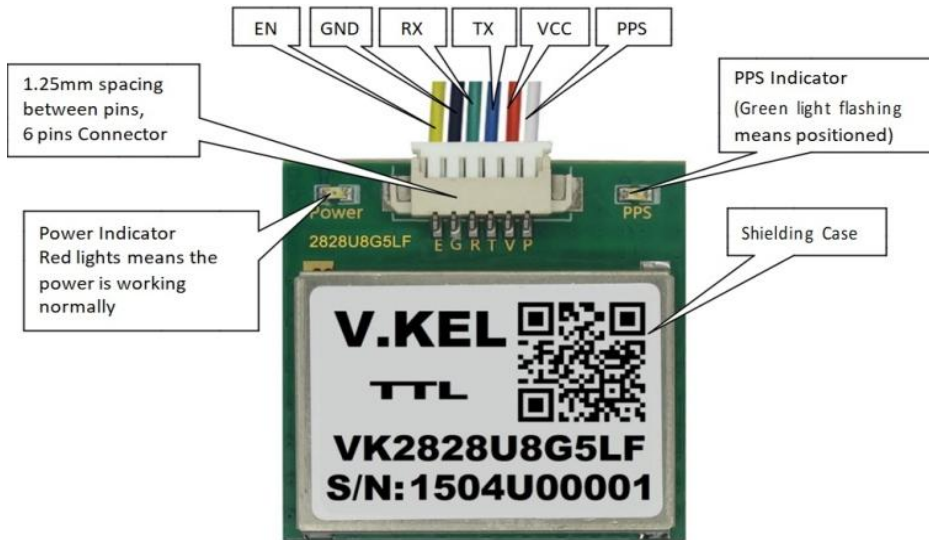


Fig. 1. VK2828U7G5LF GPS module.

| Name | Function Description |
|------|---|
| PPS | Output time pulses (pulses per second) |
| VCC | The main power supply is +3.3V~+5V, and the power consumption is 50mA in one hour |
| TX | UART/TTL interface, and RS232_TXD is optional |
| RX | UART/TTL interface, and RS232_RXD is optional |
| GND | Connect to the ground |
| EN | Power Enable: high level means the module works, low level means the modules is closed. |

- **Arduino Uno:** The open-source module used for data processing and transmission.
- **I2C compatible display:** Displays data in real time.

- **u-center2 software:** Allows viewing and analysis of location data on a digital map.

2.2 Hardware connections

The VK2828U7G5LF GPS module is connected to the Arduino Uno as follows (Fig.2). The I2C display is connected to the SDA and SCL pins on the Arduino (Fig.3).

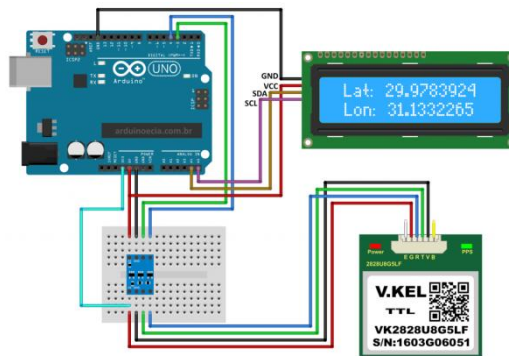


Fig. 2. System overview.

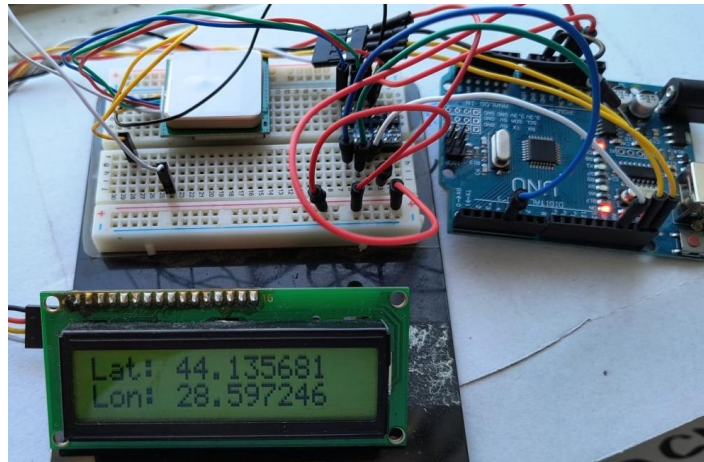


Fig. 3. I2C display.

2.3 Software configuration

The code on the Arduino board is written to read the GPS data and transmit it to the I2C display and U-Center2 software. The libraries necessary to compile the TinyGPS++, SoftwareSerial, LiquidCrystal_I2C software were used.

3 Results

After making the connections and writing the codes, a series of tests were carried out to verify the system.

3.1 Testing and validation

The system was tested in a controlled environment to verify the accuracy of the location data and the functionality of the I2C display. The data was successfully transmitted to U-Center2, where it was visualised on a digital map, in real time (Fig. 4)

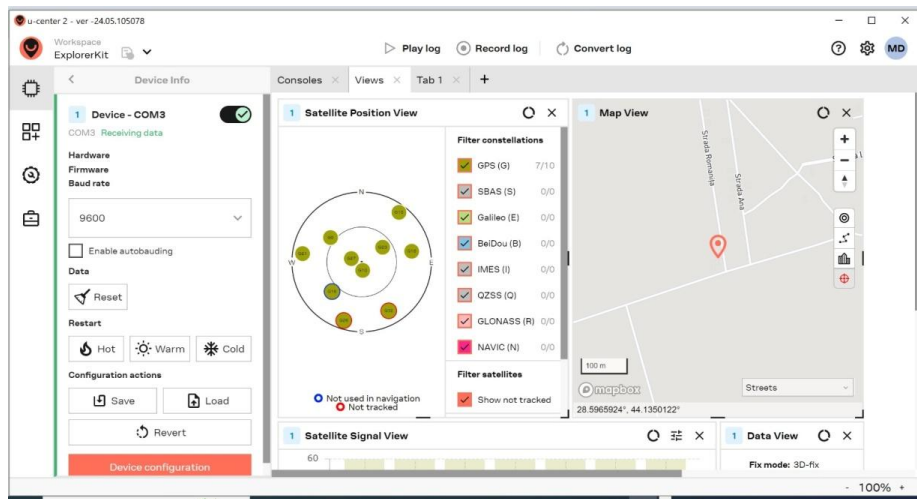


Fig. 4. U-Center2 interface.

3.2 System performance

Initial results indicate that the system can receive and transmitting location data with a high degree of accuracy.

The precision of the system is actually 7 decimals (fig. 2 and 5). According to Wikipedia.org, 1 degree in latitude means 111.111m (111km), so we can deduce that 7 decimals are equivalent to 1,1cm accuracy. The fact that in the fig. 3 are shown 6 decimals is because the limit of how many decimals that specific display can show. Data integrity and response time conform to project requirements.

4 Conclusions

This location and data synchronization system is an important step towards optimizing urban traffic and increasing road safety. By integrating IoT and GNSS technologies,

the S.M.A.R.T. AIR demonstrates the potential to transform the way urban electric vehicles are managed.

The project will continue with field testing of the system and its integration with other components of smart urban infrastructure. Possibilities will also be explored to expand the system's functionalities to include the monitoring of other parameters relevant to urban traffic. The final package composed of the aggregation of several research projects (Global localization and data synchronization system, Road traffic and air quality monitoring system in traffic, system for generating local maps with pollution and traffic values) will be implemented on an urban electric vehicle (fig. 6, fig. 7) to monitor and manage road traffic dynamically, with the goal of improving road safety and traffic efficiency.

References

1. U-center - <https://www.u-blox.com/en/u-center-2>
2. Arduino - <https://www.arduino.cc/>
3. https://www.researchgate.net/publication/335911298_Molybdenum_Car-bide_as_an_Efficient_and_Durable_Catalyst_for_Aqueous_Knoevenagel_Condensation

Outriggers for Vehicle Testing and Concepts of Lateral Stability

Elena-Dorina Dumitru¹

¹National University of Science and Technology POLITEHNICA Bucharest, Romania
elena.dumitru0306@stud.trans.upb.ro

Abstract. This paper aims to analyze existing design solutions for outrigger systems used in vehicle testing. Additionally, fundamental concepts of lateral stability in automobiles will be explored, focusing on the dynamic challenges vehicles encounter during testing. The study provides an in-depth examination of current outrigger technologies and their role in improving vehicle safety and performance by enhancing stability during dynamic maneuvers.

Keywords: Vehicle Testing, Lateral Stability, Outriggers.

1 Introduction

The stability of vehicles, particularly in lateral motion, has become a critical focus in the automotive industry. With the growing demand for safer and more efficient vehicles, researchers have explored a wide range of solutions aimed at improving vehicle stability during complex maneuvers.

At the same time, understanding the fundamental dynamics of vehicle motion remains essential. Forces acting on a vehicle, such as those generated by acceleration, braking, or external disturbances like wind, directly influence its stability. Lateral stability, in particular, is critical in ensuring that vehicles can maintain their intended trajectory, especially when navigating turns or avoiding obstacles. The analysis of these forces, combined with the implementation of advanced stabilization technologies, forms the backbone of modern vehicular safety strategies.

This research explores both the theoretical aspects of vehicular stability and the practical solutions developed to enhance it, with a focus on lateral stabilization systems. By combining theoretical dynamics with cutting-edge technology, this study aims to provide a comprehensive overview of the current advancements and challenges in ensuring vehicle stability while testing them.

2 Fundamentals of Handling and Stability of Passenger Cars

Lateral stability is crucial for ensuring that passenger vehicles maintain control during cornering and other maneuvers. Understanding the dynamics of lateral stability involves analyzing the various forces acting on a vehicle and how they contribute to the

risk of rollover or loss of traction. This chapter delves into the complexities of lateral stability, presenting the relevant equations and graphical representations to illustrate the concepts.

2.1 Lateral Stability Dynamics

The loss of lateral stability can occur either through the skidding of the vehicle or through lateral rollover under the action of the transverse component of the centrifugal force that arises during turning maneuvers or due to the component parallel to the road of the vehicle's weight when it moves on a road with a significant transverse incline. Additionally, the transverse component of wind speed plays an important role in lateral stability.

2.2 Determination of Transverse Stability Parameters for Skidding

Considering that the vehicle's speed v and the turning radius R are constant, the condition for maintaining lateral stability against skidding (Fig. 1) is:

$$\mu_y \cdot (Z_{1,3} + Z_{2,4}) > Y_{1,2} + Y_{3,4} \tag{1}$$

Taking into account the expression for the transverse inertia force, the limiting angle for the road's transverse inclination β_d at which lateral stability is on the edge of skidding can be calculated as:

$$\beta_d = \arctan g \frac{\frac{v^2}{R} - \mu_y \cdot g}{g + \mu_y \cdot \frac{v^2}{R}} \tag{2}$$

where μ_y is the coefficient of lateral friction.

Assumptions:

- The wheels lift off the ground simultaneously;
- The suspension is locked;
- Tire stiffness is not considered.

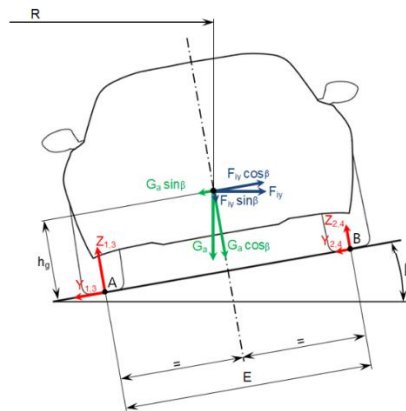


Fig. 1. The forces and moments acting on the vehicle on a road with a transverse inclination, after [2].

Notations:

- β - angle of transverse inclination of the road;
- CG - center of gravity;
- h_g - height of the center of gravity;
- E - wheel track of the vehicle;
- F_{iy} - transverse inertia force;
- θ - steering angle of the front wheels;
- $Y_{1,3}$ and $Y_{4,2}$ - lateral reactions of the road on the vehicle's wheels (transverse components of the friction force);
- $Z_{1,3}$ and $Z_{4,2}$ - normal reactions of the road on the vehicle's wheels, on the left and right sides, respectively.

The limit speed of a vehicle turning on a road with transverse inclination, at which slipping (lateral sliding) does not occur but may begin, is given by the relation:

$$v_{cr,d} = \sqrt{\frac{g \cdot R \cdot (\mu_y + tg\beta)}{1 - \mu_y \cdot tg\beta}} \quad (3)$$

Observations:

- With the increase in the angle β of the transverse inclination of the road, the limit speed $v_{cr,d}$ will also increase;
- At $tg\beta = \frac{1}{\mu_y}$ will result that $v_{cr} \rightarrow \infty$, without the possibility of slipping occurring;
- $\beta = 0 \Rightarrow v_{cr,d} = \sqrt{\mu_y \cdot g \cdot R}$ [m/s].

Considering that the slipping of the vehicle is not as dangerous as overturning, based on the condition that lateral sliding occurs before lateral overturning ($v_{cr,d} < v_{cr,r}$ or $\beta_d < \beta_r$), we obtain:

$$\mu_y < \frac{E}{2 \cdot h_g} \quad (4)$$

Relation (4) is always true, even at high values of μ_y . Consequently, the loss of lateral stability of the vehicle is most commonly characterized by lateral sliding rather than lateral overturning.

2.3 Determination of Transverse Stability Parameters for Rollover.

To establish the criteria for transverse stability, the vehicle is considered in a turn on a road with a transverse inclination β . Lateral rollover occurs around point B (Fig 3.1). Considering that the vehicle's speed v and the turning radius R are constant, based on the moment equation relative to the overturning point B , taking into account the expression for the inertia force F_{iy} , the condition for maintaining lateral stability at the limit of overturning ($Z_{1,3} = 0$) yields the limit angle of transverse inclination of the road β_r , at which lateral stability against overturning is at its limit, making the beginning of the vehicle's overturning possible at any moment from this angle.

$$\beta_r = \arctg \left(\frac{\frac{v^2}{g \cdot R} \frac{E}{2 \cdot h_g}}{1 + \frac{v^2}{g \cdot R} \frac{E}{2 \cdot h_g}} \right) \quad (5)$$

where:

v [m/s] is the speed of the vehicle;

g [m/s²] is the acceleration due to gravity;

h_g [m] is the height of the vehicle's center of gravity;

R [m] is the turning radius;

E [m] is the wheel track.

The limit speed of a vehicle turning on a road with transverse inclination, at which lateral overturning may begin, is given by the relation:

$$v_{cr,r} = \sqrt{\frac{g \cdot R \cdot \left(\frac{E}{2 \cdot h_g} + tg\beta \right)}{1 - \frac{E}{2 \cdot h_g} tg\beta}} \quad (6)$$

Observations:

- In the case of lateral stability against the overturning of the vehicle, it is noted that as the limit angle of transverse inclination β of the roadway increases, the critical speed of the vehicle also increases;
- At $tg\beta = \frac{2 \cdot h_g}{E}$ will result that $v_{cr} \rightarrow \infty$, without the possibility of slipping occurring;
- Transverse inclination, with a slope toward the outside of the curve, is applied in the construction of modern roads;
- At $\beta = 0$, it results that $v_{cr} = \sqrt{\frac{g \cdot R \cdot E}{2 \cdot h_g}}$ [m/s].

Lateral overturning of the vehicle is possible under the conditions mentioned above, provided it is not preceded by lateral sliding (slipping).

The conditions for lateral stability are valid in situations where no tangential traction or braking forces act on the vehicle's wheels. In reality, lateral sliding of the vehicle occurs at lower speeds than those obtained under the respective conditions.

2.4 Special Cases in Horizontal Curve Driving

When a vehicle moves on a flat road in a circular trajectory with a radius R , the inertia force (F_{iy}), the lateral reactions ($Y_{1,3} + Y_{2,4}$), and the normal reactions on the road acting on the wheels ($Z_{1,3} + Z_{2,4}$) and the vehicle's weight G_a act on the vehicle (Fig. 2).

Hypotheses:

- The suspension is locked;
- The tires do not deform;
- The wheels on the same side lift off the ground simultaneously;
- The angle formed by the vehicle's body with the roadway at the moment the wheels lift off the ground is very small due to the static radius of the tires lifting off the ground.

To prevent slipping, it is necessary to fulfill the condition:

$$F_{iy} \leq (Y_{1,3} + Y_{2,4}) \tag{7}$$

At the limit, the relationship is:

$$R = \frac{v^2}{\mu_y \cdot g} \tag{8}$$

$$v_{cr,d} = \sqrt{\mu_y \cdot g \cdot R} \tag{9}$$

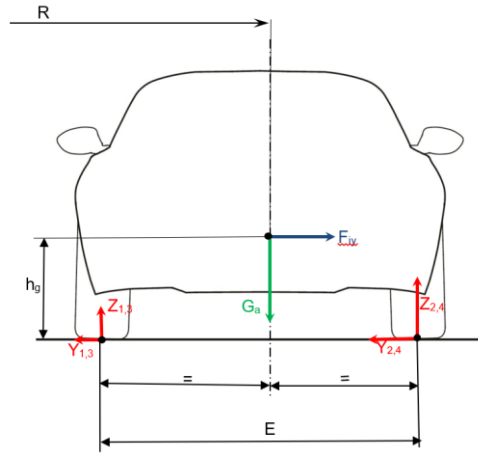


Fig 2. The forces acting on the vehicle when turning on a flat road, after [2].

The inner wheels lift off the road when the normal reaction and the lateral reaction in the contact patch become zero (Fig. 3):

$$Z_{1,3} = 0 \text{ and } Y_{1,3} = 0 \tag{10}$$

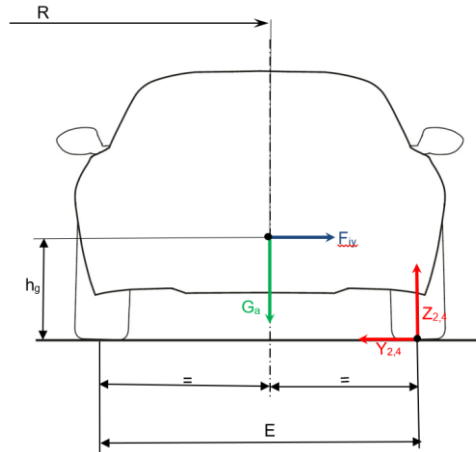


Fig. 3. The forces acting when the inner wheels lift off the road during turning, after [2].

By taking the sum of moments around the point of application of the reaction forces on the outside of the curve, the speed and turning radius at which the wheels lift off the ground can be obtained:

$$v_{cr,r} = \sqrt{\frac{g \cdot R \cdot E}{2 \cdot h_g}} \text{ [m/s]} \quad (11)$$

$$R = \frac{2 \cdot v^2 \cdot h_g}{E \cdot g} \text{ [m]} \quad (12)$$

At this moment, if the speed decreases or the turning radius increases, the vehicle will return to its normal position, with all wheels in contact with the ground. However, if the speed increases or the turning radius decreases, the moment generated by the transverse inertia force will be greater than the moment generated by the vehicle's weight, leading to overturning.

$$v_{cr,r} > \sqrt{\frac{g \cdot R \cdot E}{2 \cdot h_g}} \text{ [m/s]} \quad (13)$$

$$R < \frac{2 \cdot v^2 \cdot h_g}{E \cdot g} \text{ [m]} \quad (14)$$

It should be noted that overturning can occur even without lateral sliding taking place, as the phenomenon of sliding is directly affected by the coefficient of friction between the road surface and the contact patch of the tire.

The condition for slipping to occur, but not for overturning, is:

$$v_{cr,d} < v_{cr,r}$$

By comparing (9) and (13), we obtain:

$$\mu_y < \frac{E}{2 \cdot h_g} \quad (15)$$

This ratio significantly influences stability against overturning, as observed from equation (13). It can be used to assess stability against overturning.

The ratio $\frac{E}{2 \cdot h_g}$ is referred to as the vehicle's transverse stability coefficient.

The average values of this coefficient are as follows [1]:

- For passenger cars: 1.00 - 1.40;
- For trucks: 0.60 - 0.90;
- For buses: 0.60 - 0.70.

These values correspond to overturning angles of over 32° , exceeding typical transverse inclinations. It is noted that condition (15) is satisfied for passenger cars since, in practice, $\frac{E}{2 \cdot h_g} < 1$. However, for other types of vehicles, even on regular roads, this condition is no longer met, which can lead to the possibility of overturning.

The real danger of overturning is even greater when considering the rolling motion manifested in the case of unblocked suspensions and deformable tires. The lateral displacement of the center of mass can reach considerable values and is favored by the strong deformation of the tires. The actual overturning speed represents between 75% and 85% of the overturning speed calculated according to equation (11).

It can be observed that increasing the wheel track has a similar effect to reducing the height of the center of mass on increasing the overturning speed.

Overturning is also favored by increasing the steering angle of the front wheels. Furthermore, it must be taken into account that road irregularities, especially transverse ones, can significantly contribute to overturning, particularly when the road's coefficient of friction is high [1].

3 Constructive Solutions of Existing Outriggers

Outriggers play a critical role in vehicle stability, especially in preventing rollover during dynamic driving tests. Over the years, engineers have refined outrigger systems to accommodate different types of vehicles, focusing on reducing mass, improving structural integrity, and ensuring ease of installation and adjustment. This chapter provides an overview of the existing outrigger designs, with an emphasis on their mechanical functionality and contributions to vehicle handling safety.

3.1 Handling Tests

Handling tests are essential for evaluating a vehicle's stability under various dynamic conditions. These tests simulate real-world scenarios where rapid steering or sharp turns may induce lateral forces, causing potential instability. The outrigger systems, specifically designed to support the vehicle in such instances, act as a fail-safe to prevent the vehicle from tipping over. By using sensors and adjustable components, the modern outrigger ensures that the vehicle remains on a stable path without compromising its original dynamics.

Common handling tests include the “double lane change” and “fish hook” tests, where the vehicle must navigate sudden directional changes at high speeds. The design of the outrigger in these scenarios focuses on minimizing impact on the vehicle’s natural behavior while providing sufficient lateral support. For instance, systems equipped with adjustable supports (as shown in Figure 4) enable engineers to fine-tune the outrigger to suit specific vehicle models and test conditions.

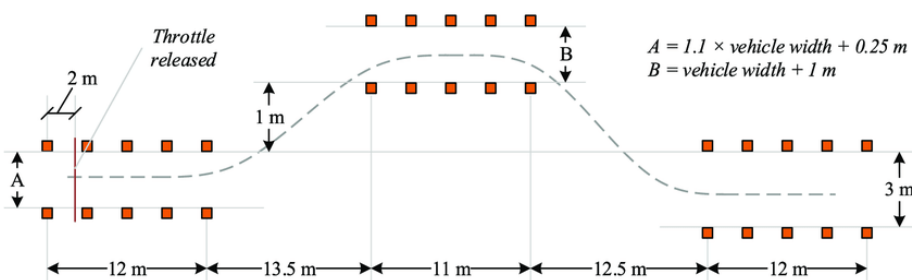


Fig. 4. Diagram of a double lane change test trajectory [3].

3.2 Previous Achievements

The evolution of outrigger designs has been shaped by several key innovations aimed at improving both performance and safety. One of the earliest iterations, developed in the 1960s, included a triangular lower frame with a damping device to absorb lateral impact forces. Over time, these designs have been modified to include modern materials and improved attachment systems that allow quick installation and removal without altering the vehicle's structure [4].

The modern outrigger system features components like telescopic tubes and reinforced joints, allowing for adjustable height and enhanced durability. These elements contribute to reducing the system's overall weight while maintaining its ability to absorb shocks and prevent vehicle rollovers.



Fig. 5. Illustration of an early outrigger design with triangular support frames and damping mechanisms [4].

In the current outrigger configurations, the primary focus has been on reducing the system's moment of inertia and ensuring it doesn't interfere with the vehicle's inertia during tests. These systems are typically used in both front and rear support setups, utilizing rollers or sliders as points of contact with the road. This method minimizes friction and ensures the vehicle can perform critical maneuvers without unwanted drag [4].



Fig. 6. Schematic of a modern outrigger system with adjustable height and low-inertia rollers [4].

After a detailed investigation, it seems that there is a wide range of constructive solutions utilized by vehicle testing institutes. These solutions vary significantly in design and implementation, reflecting the diverse requirements and challenges faced in the field of vehicle testing and safety assessment. For a better understanding of the presented constructive solutions, it is useful to schematicize them.

Figure 7.a) illustrates the principle scheme of the triangular spatial frame solution. This solution, utilized pivoting wheels for contact with the roadway in the past, while currently, sliding elements made of plastic materials are used. The spatial frame consists of three bars, one of which is fixed to the roof frame using a relatively complex system that may include a volume-variable chamber element (damper) for adjusting the height of the system. The other two bars are articulated to the vehicle's threshold (at the bottom) via hinges [4].

In Figure 7.b), the constructive solution with a planar triangular frame [8] is schematically represented. This solution was used during the stability test of a minibus, utilizing pivoting wheels as contact elements with the road. The mounting method on the vehicle is not detailed in the studied source; however, for the solution to be functional, the upper mounting must be of the fixed type, similar to the assembly of the previous support system to the vehicle body [5].

In Figure 7.c), the constructive solution with front-rear beams is schematically illustrated. This support system can be equipped with either pivoting wheels as contact elements with the roadway or with sliding elements, and it consists of two horizontal beams. The beams are mounted on the front and rear cross members of the vehicle, requiring the removal of the protective bumpers in these areas. The mounting is rigid, with threaded assembly, using intermediate elements, which allow for adjusting the height of the contact element relative to the ground [6].

In Figure 7.d), the principle scheme of the support system with lateral beams at the rear doors is presented. Here, plastic sliding elements are used as contact elements with the road. The solution consists of two beams, one on each side of the vehicle, and two perforated square-profile bars, which are used to adjust the height of the sliders relative to the ground. To mount this system on the vehicle, it is necessary to remove the rear doors, as the fixation is done through an intermediate frame mounted in place of the door [7].

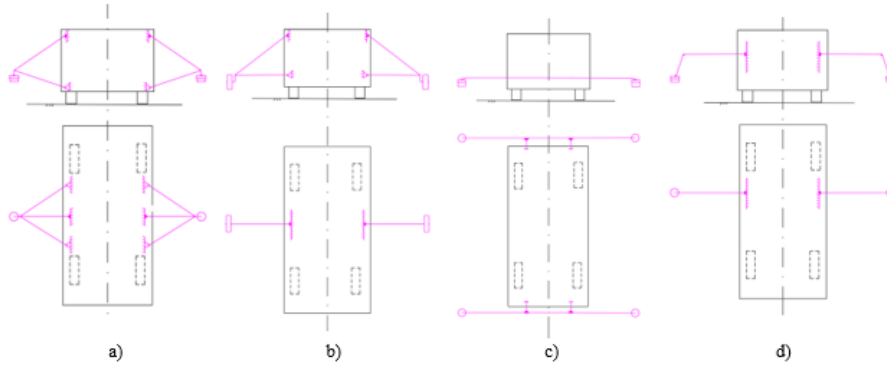


Fig. 7. Principle Schemes of the Studied Constructive Solutions

3.3 Requirements for the Designed Support System

The support system must be designed to:

- Ensure the safety of the driver during the testing process;
- Maintain the integrity and operational condition of the vehicle;
- Alter the dynamic characteristics of the vehicle as little as possible;
- Be easily transportable to the testing location;
- Be installable on multiple types of vehicles;

4 Conclusions

To draw meaningful conclusions regarding the various constructive solutions studied, a thorough analysis from multiple perspectives is essential. This evaluation should consider factors such as safety, functionality, ease of implementation, cost-effectiveness, and long-term reliability. By examining these aspects in detail, it becomes possible to identify the strengths and weaknesses of each solution, ultimately leading to more informed decisions in the design and implementation of vehicle testing systems.

Table 1. Centralized Table for Comparing Solutions

| Criteria | 3.3.a) | 3.3.b) | 3.3.c) | 3.3.d) |
|---|--------|--------|--------|--------|
| Modification of Inertia Properties | - | 0 | -- | 0 |
| Added Mass | - | - | -- | 0 |
| Irreversible Modification of the Body | -- | - | 0 | 0 |
| Capacity to Absorb Contact Forces Between the Support System and the Road | + | - | + | - |
| Possibility of Placement on Other Vehicles | - | -- | ++ | + |
| Ease of Equipping the Vehicle | -- | - | + | - |

In the overall system of supports used to prevent lateral rollover during lateral stability tests of vehicles, there are two types of support elements: pivoting wheels and plastic slides. Compared to older solutions, such as pivoting wheels, slider elements made from plastic materials (UHMW) have become increasingly common in modern solutions. There are advantages and disadvantages associated with each type of contact element (Table 2).

Pivoting wheels tend to better absorb the initial shock of contact with the ground surface and provide good stability. They do not induce an additional moment of rotation, which can be beneficial during lateral stability tests. However, they may be less reliable over time and may require periodic maintenance to ensure proper functioning. On the other hand, slides made from ultra-durable plastic materials can offer greater wear resistance and a longer lifespan than pivoting wheels. They may be less prone to damage over time and require less maintenance. However, sliders can introduce moments of rotation, which could affect the vehicle's stability during tests. Additionally, being made from plastic materials, they introduce vibrations into the vehicle-support system when in contact with the road surface. These vibrations can severely alter the information obtained from a data acquisition system during testing.

Most testing institutes prefer the use of sliders, as they are often considered more reliable and can be used for a greater number of tests compared to pivoting wheels, despite their disadvantages.

Table 2. Advantages and Disadvantages of Sliders and Pivoting Wheels

| | Slider | Pivoting Wheel |
|---------------|--|---|
| Advantages | <ul style="list-style-type: none"> – Easier; – Simpler; – Reliable ; | <ul style="list-style-type: none"> – Easy to procure; – Does not negatively affect the vehicle dynamics; – Irregularities in the road surface do not significantly influence the results; – Can withstand relatively large loads; |
| Disadvantages | <ul style="list-style-type: none"> – Requires a road surface with very good flatness; – Negatively affects the vehicle dynamics; – Introduces vibrations into the system through a stick-slip effect. | <ul style="list-style-type: none"> – Lower reliability; – Requires intermediate elements for mounting to the support system. |

References

1. Untaru, M., Poțincu, G., Stoicescu, A., et al: Dinamica autovehiculelor pe roti (1981)
2. Anghelache, G. : Dinamica autovehiculelor I și II, note de curs. UPB (2022)
3. Passenger cars–test track for a severe lane-change manoeuvre–Part 2: obstacle avoidance. ISO 3888-2 (2011)
4. Automotive Testing, INC. Documentation of Automobile Performance. (n.d.). The design of ATI's outriggers, Report No. 03013.
5. Kryaskov, V., Vashurin, A., Tumasov, A., Vasiliev, A.: Designing of Outriggers for the Needs of the Vehicles Stability Testing. Applied Mechanics and Materials 875:71–76 (2018).
6. Phillip, D.: NHTSA launches new tests to measure, rate light-vehicle rollover risk. autonews.com (2018)
7. Staff C., Toyota RAV4: Is Now Much Safer Thanks To One Simple Fix (2020)
8. Todoruț, A., Cordoș, N., Barabás, I.: Elemente de dinamica autovehiculelor (2021)

Construction and Mechanical Design of a Four Rotor Wankel Engine

Mihai Bălășescu¹

Coordonator: Prof. Dr. Horia Abăitancei² and Prof. Dr. Sebastian Radu³

^{1,2,3} Transilvania University of Brasov, Brașov BV 500036, Romania

Abstract. This paper presents the design and development of a four-rotor Wankel engine with a displacement of 2616 cubic centimetres and an output of 300 kW. The design includes an overview of the engine's working principles, component details, calculations, and construction using CATIA V5 software. By addressing some common challenges of rotary engines, the work aims to enhance the Wankel engine's potential in high-performance applications.

Keywords: Rotary engine, ICE, Rotational kinetic energy.

1 Introduction

The Wankel rotary engine, invented by Felix Wankel, represents a unique approach to internal combustion. Unlike conventional piston engines, it uses a triangular rotor that rotates within an epitrochoidal housing, converting combustion pressure into rotational motion. This design allows for fewer moving parts and a high power-to-weight ratio but has faced challenges in terms of fuel efficiency, emissions, and durability.

2 Working Principle of the Wankel Engine

The Wankel engine operates on a four-stroke cycle: intake, compression, power, and exhaust. These strokes are achieved through the rotation of the rotor inside the housing.

As the rotor turns, its apexes continuously maintain contact with the housing, creating three distinct working chambers. Each chamber goes through the four-stroke cycle in one rotor rotation, while the output shaft completes three rotations during the same time. This arrangement allows the Wankel engine to produce more power strokes per rotation compared to traditional engines.

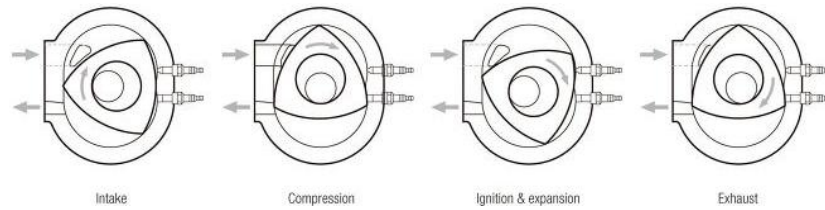


Fig. 1. Generated epitrochoid shape.

3 Engine Components

The key components of the four-rotor Wankel engine include:

- Rotor: The rotor has a triangular shape with curved sides and is fitted with apex, side, and corner seals to maintain compression. The design of the rotor's recess determines the engine's compression ratio and combustion efficiency.

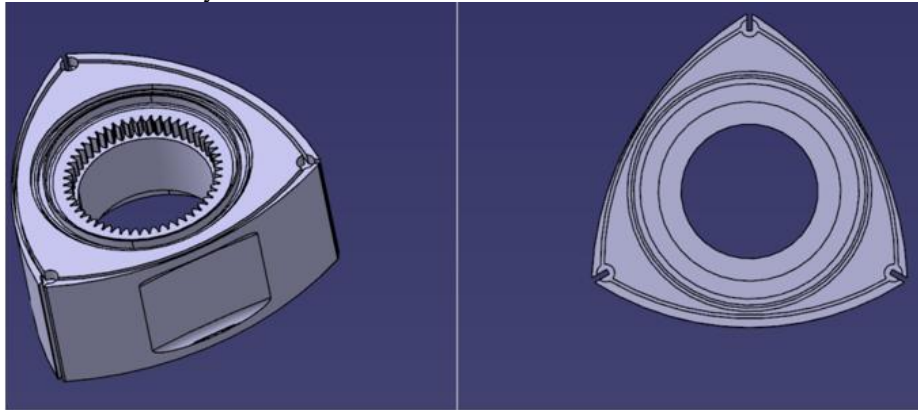


Fig. 2. Rotor.

- Rotor Housing: This part forms the epitrochoidal chamber within which the rotor moves. It includes cooling passages, spark plug mounts, and intake/exhaust ports, making it critical for managing heat and gas exchange.

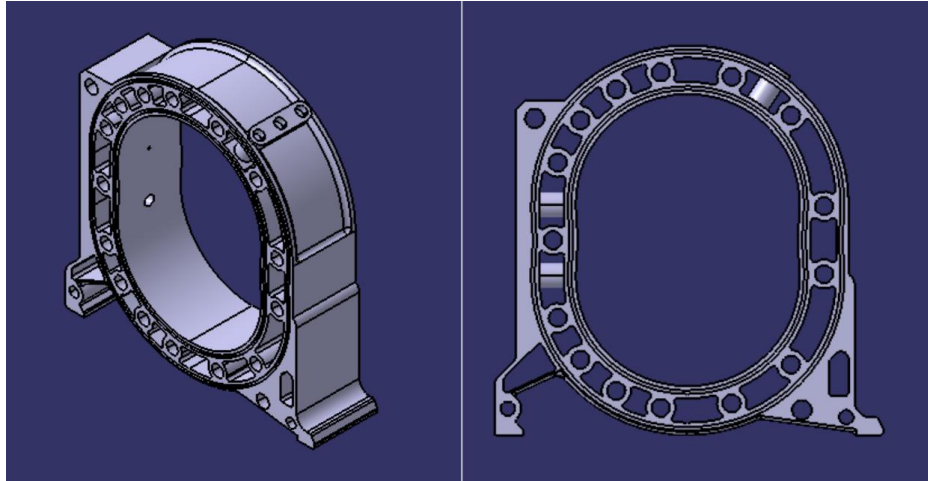


Fig. 3. Rotor Housing.

- **Sealing Mechanism:** The apex seals, side seals, and oil seals ensure gas tightness and proper lubrication, which are essential for the engine's performance and longevity.

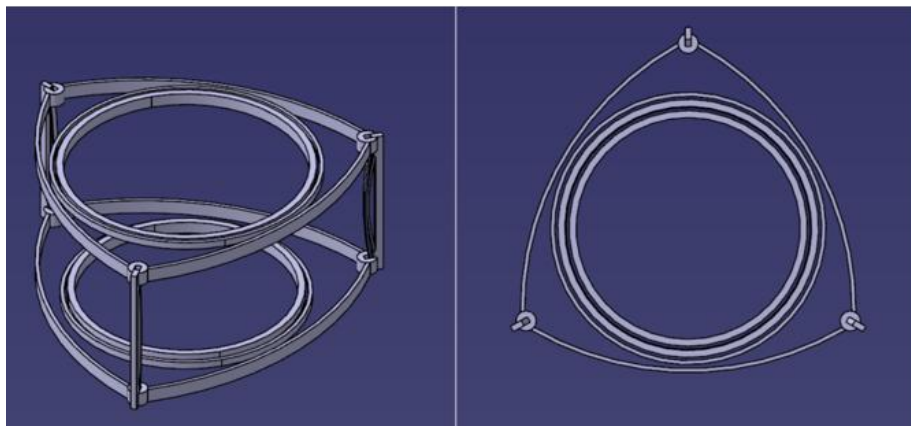


Fig. 4. Rotor Seals.

- **Phasing Gear Mechanism:** The phasing gear, or synchronization gear, is crucial for maintaining the correct timing between the eccentric shaft and the rotors. It comprises of a ring, attached to the rotor and an outer stationary gear fixed to the housing. This mechanism ensures that the rotor

maintains the correct angular position relative to the housing, enabling smooth and consistent operation throughout the engine cycle.

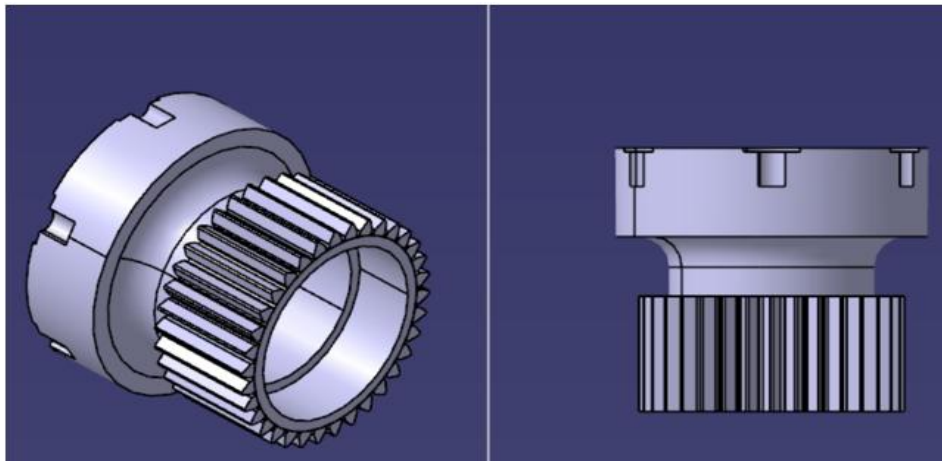


Fig. 5. Inner stationary gear.

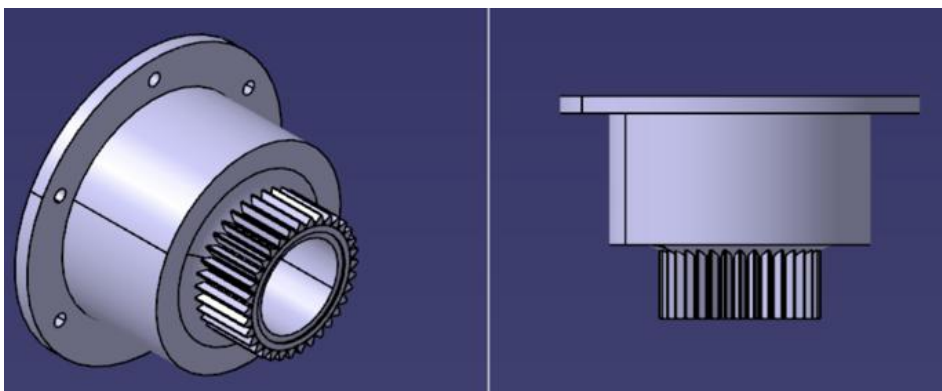


Fig. 6. Outer stationary gear.

Eccentric Shaft: Analogous to a crankshaft in piston engines, it supports the rotors and converts the rotor's movement into rotational output. In this design, the shaft features removable journals for easier assembly.

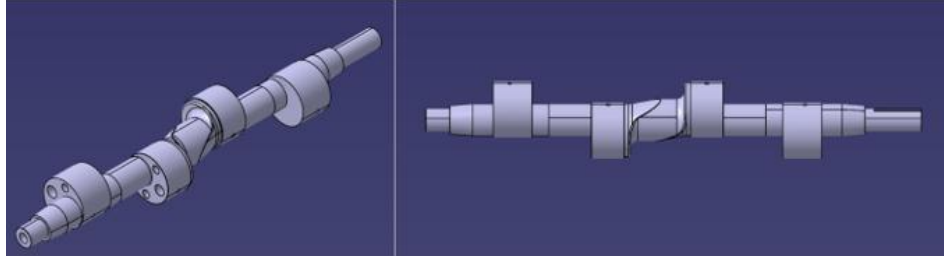


Fig. 7. Mounted eccentric shaft.

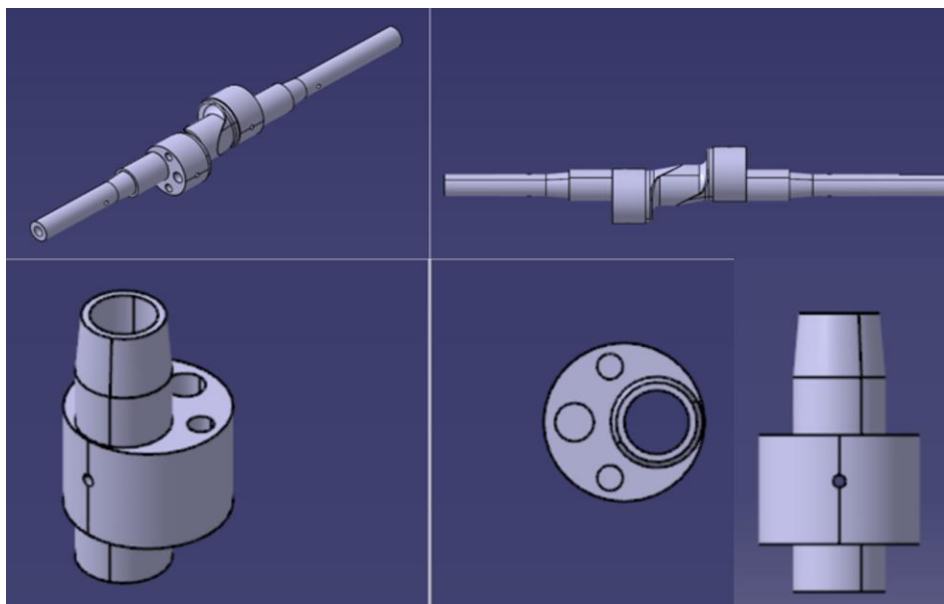


Fig. 8. Eccentric shaft. Removable Journals.

4 Geometrical and Thermodynamic Calculations

The design calculations involved determining the geometry of the rotor and housing using peritrochoid equations. The key parameters included:

Eccentricity (e): Determines the distance between the rotor's center and the shaft, influencing displacement and compression ratio.

Trochoid Constant (K): A ratio between the generating radius and eccentricity that affects the engine's compression characteristics. A value of 7 was used to balance efficiency and power.

Volume Calculations: The working chamber's volume change was calculated across the four strokes, impacting the engine's power output and thermodynamic efficiency.

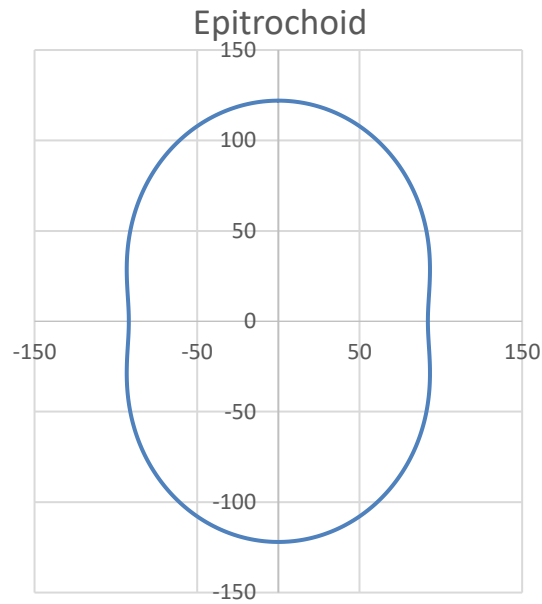


Fig. 9. Generated epitrochoid shape.

The thermodynamic cycle was analyzed by considering the variations in pressure, temperature, and volume during each phase of the engine's operation. Heat transfer coefficients were calculated for cooling and exhaust gases to optimize thermal management

Starting from the energy variation equation :

$$U = (W_p) + (Q_p) + (Q_c) + (H_a) + (H_e)$$

and the calculus model, the thermodynamic cycle of the engine was calculated.

(W_p) = variation of mechanical work [J]

(Q_p) = variation of heat transmitted through the walls [J]

(Q_c) = variation of heat transmitted through the cylinder [J]

(H_a) = variation of enthalpy transmitted through the walls [J]

(H_e) = variation of enthalpy transmitted through the cylinder [J]

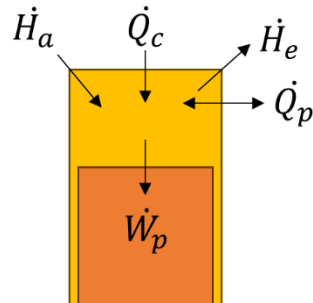


Fig. 10. Energy variation diagram.

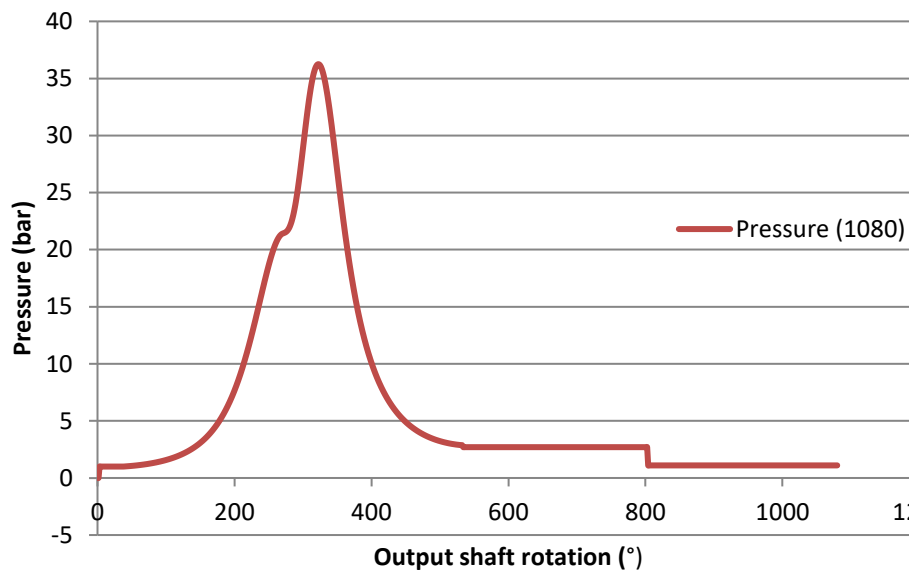


Fig. 11. Combustion chamber pressure.

5 CAD Construction Using CATIA V5

The engine was modeled in CATIA V5, with detailed 3D models of each component. Key steps in the CAD modeling process included:

Rotor and Housing design: The peritrochoid-shaped rotor housing and rotor were modeled to accommodate sealing and cooling features.

Designing the Eccentric Shaft: Implementing a shaft with removable journals for ease of assembly, using finite element analysis (FEA) to assess stress and deformation.

Integrating Cooling and Lubrication Systems: Ensuring cooling passages were appropriately placed in the rotor housing. Three oil supply channels were strategically placed within the rotor housing to ensure proper lubrication.

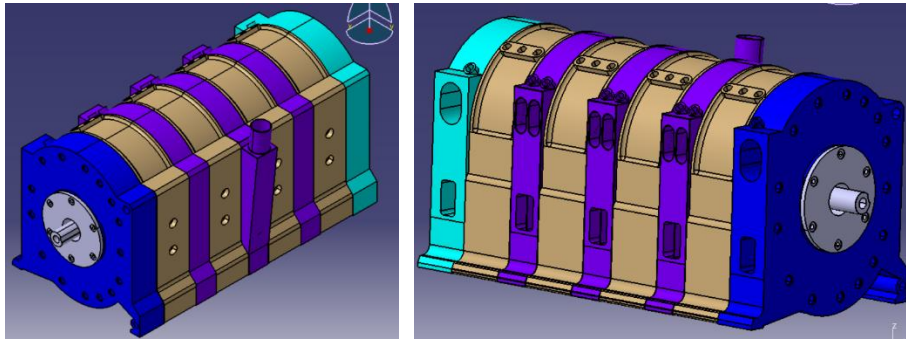


Fig. 12. Assembled four rotor engine: A. Spark plug side; B. Intake/Exhaust ports side.

6 Conclusion

This study successfully designed a high-performance four-rotor Wankel engine with potential applications in motorsports and other high-power requirements. The detailed calculations and CAD modeling provide a foundation for further development, potentially including hybridization to further enhance efficiency and emissions performance.

References

1. Yamamoto, K. (1971). Rotary Engine.
2. Yamamoto, K. (1981). Rotary Engine.
3. Ansdale, R. (1968). The Wankel RC Engine, Design and Performance.
4. Bensinger, W.-D. (1973). Rotationskolben-Verbrennungsmotoren.
5. Hege, J. B. (2001). Wankel Rotary Engine.
6. <https://www.autoguide.com/auto-news/2017/05/mazda-s-rotary-engine-celebrates-50th-birthday.html>

Study of Gas Exchange and Acoustical Supercharging of the Wankel Engine

Maria Dimache¹

Coordonator: Prof. Dr. Horia Abăitancei² and Prof. Dr. Sebastian Radu³

^{1,2,3} Transilvania University of Brasov, Braşov BV 500036, Romania

Abstract. The CAD model of the gas exchange system effectively simulates the intricate flow dynamics and diffusion processes involved in gas exchange. By visualizing the design, it provides valuable insights into optimizing the system's efficiency and improving its performance. This tool allows engineers to predict system behavior under different conditions, minimizing trial-and-error during the actual implementation phase. The developed CAD model successfully demonstrates the structural layout and functional components of the gas exchange system. It enhances the understanding of gas flow pathways, pressure regulation, and heat transfer processes. This digital representation is a vital step in refining the system design, ensuring it meets the necessary operational and safety standards, while reducing development costs and time.

Keywords: Rotary engine, ICE, Wankel

1 Introduction

1.1 3D analysis of the gas exchange

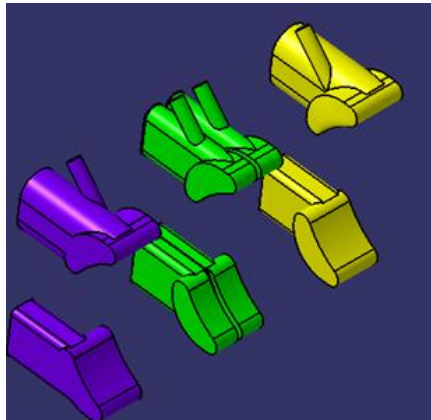


Fig. 1. 3D CAD negative model of front plate, center plate and end plate for gas exchange system.

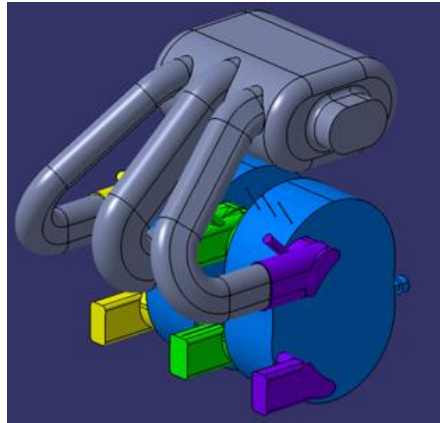


Fig. 2. Complete 3D CAD negative model of gas exchange system of a two rotor Wankel engine.

The application of Computational Fluid Dynamics (CFD) in the analysis of gas exchange processes within engines represents a significant advancement in engineering design and performance optimization. CFD allows for a three-dimensional examination of the fluid dynamics involved in the intake, compression, combustion, and exhaust phases of an engine's operation. By simulating these processes, it gains a detailed understanding of how gases move and interact within the engine, providing insights that are not easily obtainable through experimental methods alone.

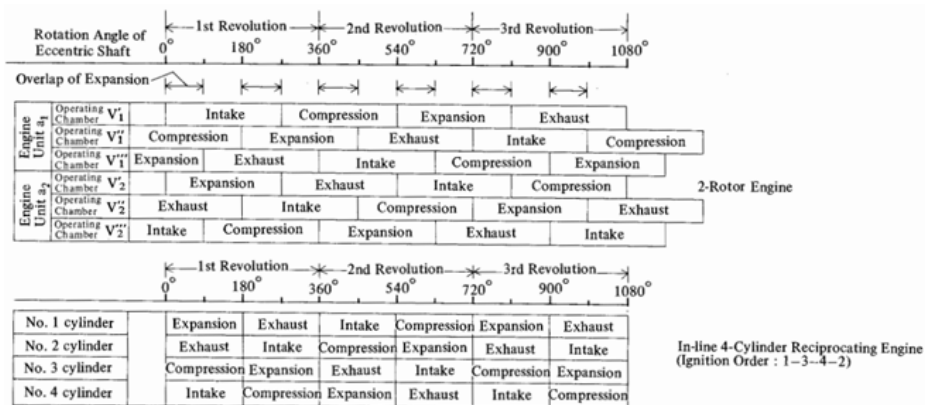


Fig. 3. Comparison of engine working conditions.

CFD analysis for gas exchange is an ability to visualize and quantify complex flow patterns and turbulence within the engine. In a Wankel engine, the unique rotary design creates distinctive fluid dynamics that can significantly influence performance. CFD

simulations can capture these dynamics in great detail, allowing engineers to identify areas where airflow can be optimized to enhance volumetric efficiency. By adjusting parameters such as intake port design, rotor geometry, and chamber volume, the CFD analysis helps in fine-tuning the engine for better performance.

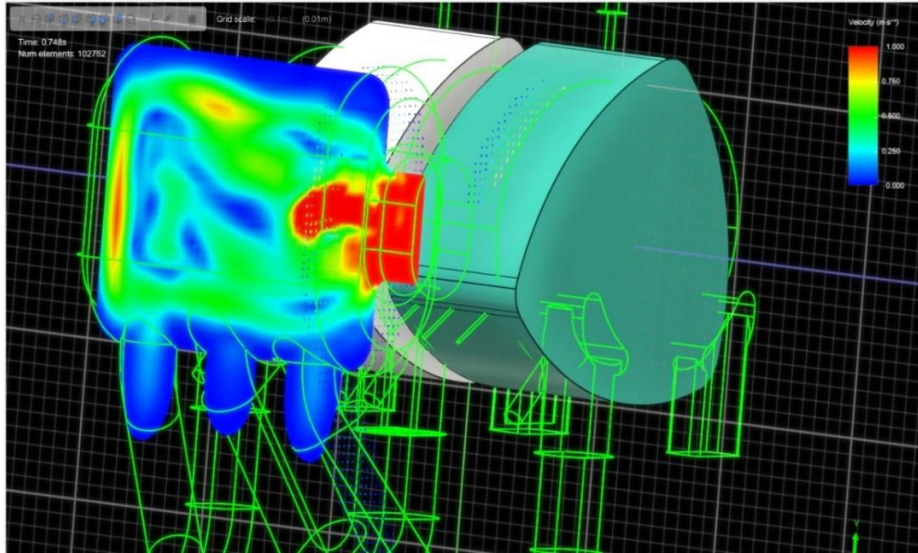


Fig. 4. 3D gas exchange system analysis – view on Z axis.

XFlow is one of the best software used for CFD dynamic simulation of the fluids. We modified the CAD parts only for the flow of the gases. It was selected a face of the 3D CAD model where the pressure inlet is acting. This view is obtained by cutting the model with a plan on the X axis, using the vectorial visualization method.

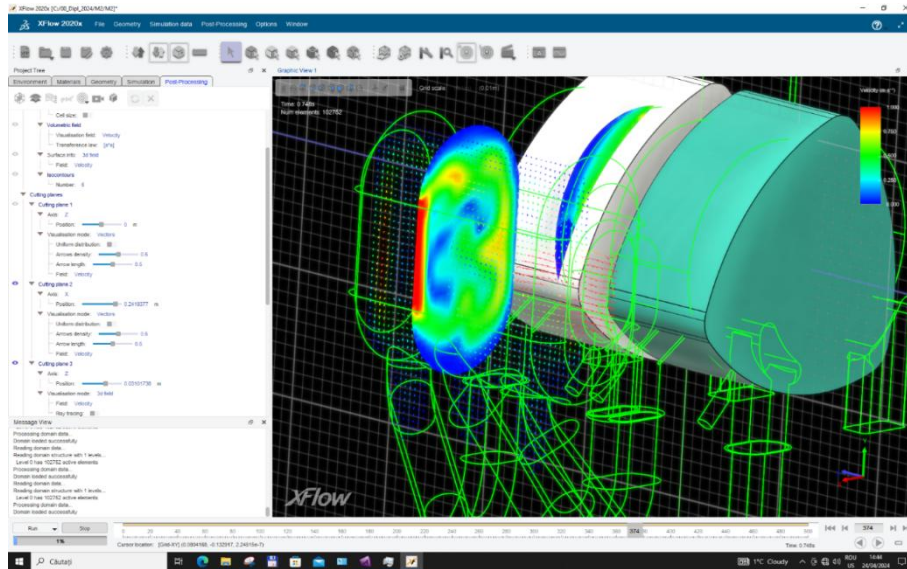


Fig. 5. 3D gas exchange system analysis – view on X axis.

CFD analysis enables the examination of the effects of various physical and thermal conditions on the gas exchange process. Factors such as wall temperature, cooling fluid temperature, and wall thickness can be systematically varied in the simulations to observe their impact on engine performance. This capability is crucial for optimizing thermal management and ensuring that the engine operates efficiently under different operating conditions. The insights gained from these simulations can lead to design modifications that improve overall engine efficiency and reliability.

The use of CFD analysis in the 3D examination of gas exchange processes is a powerful tool that significantly contributes to the advancement of engine technology. By offering detailed insights into the fluid dynamics within the engine, CFD helps engineers to optimize design, improve efficiency, and innovate with confidence.

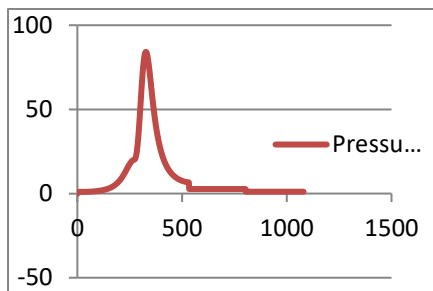


Fig. 6. The pressure for a complete rotational cycle.

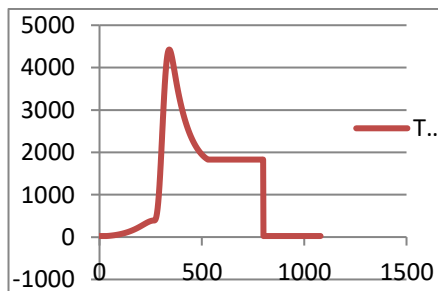


Fig. 7. The temperature for a complete rotational cycle.

2 The intake system as Helmholtz resonator

Supercharging is the technique of utilizing a device known as a supercharger to increase the air intake pressure of an internal combustion engine. More air than atmospheric pressure would permit is forced into the engine's cylinders by this device. Usually, a belt, gear, or chain drive connects the engine's crankshaft to the supercharger, providing mechanical power. Supercharging enhances engine performance by increasing the density or pressure of air entering the combustion chamber through the following mechanisms:

Ram induction charging will produce an improvement in volumetric efficiency at certain engine speeds by means of individual cylinder induction pipes or tracts. The extra charging effects are due to the inertia and elasticity of the charge in the inlet tract and cylinder. For slow-speed heavy-duty engines, which may have a maximum engine speed of only 2000 rev/min, the individual induction tract length would be far too long, so that it would be very difficult to accommodate.

An alternative and more compact induction system known as the Helmholtz resonator tuned induction is sometimes used on large diesel engines in the single stage form or in the dual and triple stage configuration for some high-performance petrol engines.

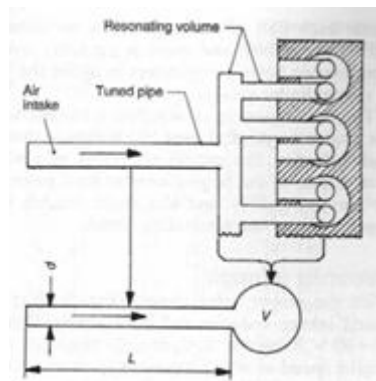


Fig. 8. Comparison of the Helmholtz resonator with tuned manifold system.

The Helmholtz resonator originally simply consisted of a spherical chamber with a pipe projecting from it (Fig. 6.14), the chamber being the equivalent of the manifold gallery and branch pipes in addition to the inlet valve ports and cylinder, whereas the pipe projecting from the chamber becomes the tuned induction tract.

The operating principle of the Helmholtz resonator is as follows: air filling any given sized chamber, when shaken, will oscillate to and from at its own unique frequency—known as its natural frequency of vibration. If now the unique chamber was connected almost directly to an inlet valve port and the open-ended pipe becomes the air intake tract, then every time the inlet valve opened a negative pressure-wave pulse would disturb the air in the resonator chamber and pipe. Now, if the engine's speed is increased

until the pressure-wave pulse frequency corresponds to the natural frequency of the air in the resonator chamber, then the air in the system will be excited into a state of resonance at which the amplitude of the pressure-wave moving through the incoming air stream produces a series of pressure-waves or jolts. If properly timed, these waves will bombard the cylinder with surges of compressed air towards the end of the induction period when the piston is moving against the incoming mixture and, as a result, more charge will be crammed into the cylinder before the inlet valve closes.

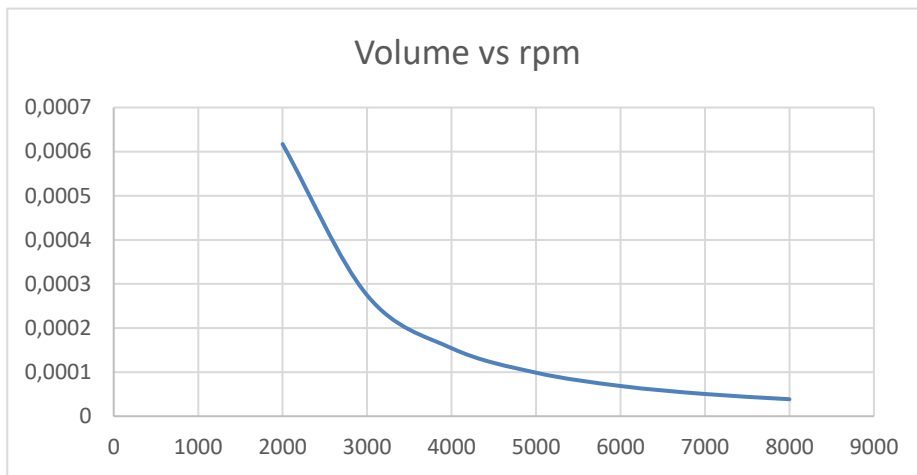


Fig. 9. Volume vs RPM

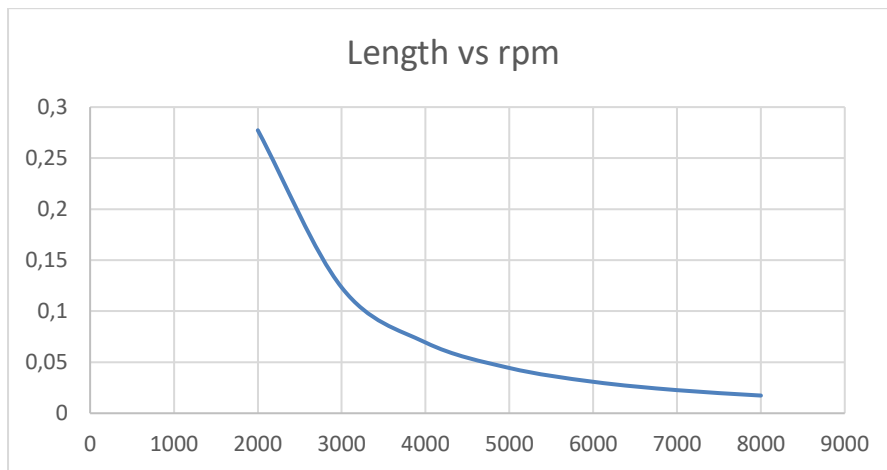


Fig. 10. Length vs RPM

3 Conclusion

The CAD model of the gas exchange system effectively simulates the intricate flow dynamics and diffusion processes involved in gas exchange. By visualizing the design, it provides valuable insights into optimizing the system's efficiency and improving its performance. This tool allows engineers to predict system behavior under different conditions, minimizing trial-and-error during the actual implementation phase.

The developed CAD model successfully demonstrates the structural layout and functional components of the gas exchange system. It enhances the understanding of gas flow pathways, pressure regulation, and heat transfer processes. This digital representation is a vital step in refining the system design, ensuring it meets the necessary operational and safety standards while reducing development costs and time.

4 Optimization ideas

4.1 Port Geometry Adjustment

Fine-tuning the intake and exhaust port geometry can optimize airflow and reduce pressure losses. Adjustments to the shape and size of these ports are essential to better align the gas exchange processes with the engine's operational requirements.

4.2 Rotor Design and Chamber Volume Tuning

Modifying rotor geometry and optimizing combustion chamber volume can help reduce turbulence, improve fuel mixing, and lead to more consistent combustion. These improvements will boost both power output and fuel efficiency.

4.3 Thermal Management Optimization

By optimizing wall thickness and cooling fluid temperatures, heat dissipation can be better controlled, enhancing the engine's thermal efficiency. Effective thermal management will ensure the engine operates efficiently under varying conditions.

4.4 Helmholtz Resonator Tuning

Further refinement of the Helmholtz resonator design could enhance its resonance effect, increasing the amount of compressed air entering the cylinder. This tuning should focus on adjusting chamber dimensions and pipe lengths for specific RPM ranges to improve volumetric efficiency.

References

1. Yamamoto, K. (1971). Rotary Engine.

2. Yamamoto, K. (1981). Rotary Engine.
3. Ansdale, R. (1968). The Wankel RC Engine, Design and Performance.
4. Bensinger, W.-D. (1973). Rotationskolben-Verbrennungsmotoren.
5. Hege, J. B. (2001). Wankel Rotary Engine.
6. <https://www.autoguide.com/auto-news/2017/05/mazda-s-rotary-engine-celebrates-50th-birthday.html>

Analysis of Brake Energy Recovery Potential in Flywheels

Mânza Radu-Cristian¹

Coordonator: Prof. Dr. Horia Abăitancei² and Prof. Dr. Sebastian Radu³

^{1,2,3} Transilvania University of Brasov, Braşov BV 500036, Romania

Abstract. The paper presents a comprehensive analysis to identify the brake energy recovery potential of the mechanical principle, based on a flywheel. The flywheel solution is considered working under open air conditions and a numerical simulation is carried out. It is emphasized to identify the influence of moment of inertia and angular velocity of the mass on stored energy. The analysis is performed using an analytical model and a numerical model, computed for different moments of inertia. The recovery potential is analyzed considering one braking event coming to a full stop. The study is applied to a mid-size vehicle.

Keywords: Flywheel, Energy storage device, Rotational kinetic energy.

1 Introduction

1.1 Motivation

To raise the overall efficiency of current day vehicles, attention to the energy losses during different driving moments becomes of importance. Therefore, the most notable periods of energy loss are the braking and deceleration. With the help of braking energy capture devices and storage systems the ability to reduce the losses to a very minimum appears, and to repurpose the stored energy for other driving moments, such as hard acceleration and starting for a dead stop.

For a mechanical system, the capturing and storing devices are all in one, becoming the most convenient one in terms of dimensions. For a flywheel the energy is stored in the form of rotational kinetic energy by utilizing the flywheel's moment of inertia and angular velocity. For the moment of inertia, the mass of the flywheel is of value, such as the radius of rotation about a chosen axis.

The flywheel can be coupled with multiple vehicles having different propulsion systems. For example, on an electric vehicle the storage device can be linked to an electric generator to store and release energy. On the other hand, on an ICE equipped vehicle, the flywheel can be connected to the conventional motor using a clutch, offering the possibility of mechanical decoupling. In both cases, the flywheel can serve as an energy consumption and charging damper, being able to minimize the consumption curve during transient driving conditions. On the combustion engine the flywheel serves also as a mechanical damper, reducing the shocks from the ignition stroke.

2 Potential Brake Energy Recovery

2.1 Driving cycle.

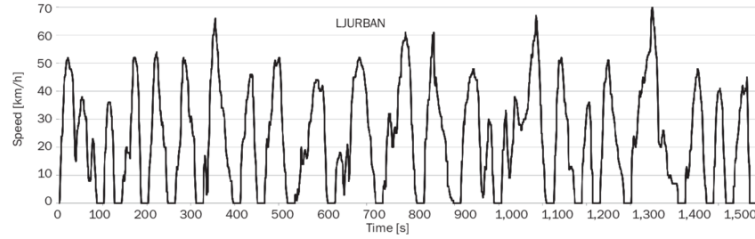


Fig. 1. Urban driving cycle in the city of Ljubljana [5].

For a better understanding of the advantages given by storing braking energy in flywheel it will be consider a driving cycle in the city Ljubljana.

The above graph shows the dynamic analysis of a vehicle driving in an urban cycle in the city of Ljubljana, the capital of Slovakia. An analysis has taken place considering the initial speed, deceleration, time, and distance. Therefore, resulting linear kinetic acceleration, with which incipient dimensions of the flywheel can be found.

First, we start with an example: The chosen vehicle is a Renault Clio 2 Phase III 1.5dci with a mass of 970kg, the tire specification of 185/55r15. During braking, from a velocity of 18.4m/s to a standing still in 41s, the resulting deceleration is found with the following formula:

$$a_x = \frac{V_f - V_i}{\Delta t} = \frac{-V_i}{\Delta t} = -0.45 \cdot \frac{m}{s^2} \quad (1)$$

To find the traveled distance during braking with constant deceleration from the initial speed can be found using the Newton's Equation of Motion:

$$x_f = x_i + V_i \cdot \Delta t + \frac{a \cdot (\Delta t)^2}{2} = V_i \cdot \Delta t + \frac{a \cdot (\Delta t)^2}{2} = 375.8 \cdot m \quad (2)$$

Computing with mass, acceleration and distance the resulting deceleration work is found:

$$W_d = m \cdot a \cdot s = 163013.9 \cdot Ws = 45.3 \cdot Wh \quad (3)$$

For the wheel angular velocity, it is necessary to find the free radius of the wheel from the tire's dimensions 185/55r15:

$$r_{wheel} = \frac{AR \cdot W}{100} + \frac{D}{2} = 292.25 \cdot mm \quad (4)$$

Therefore, the angular velocity of the wheel will become:

$$\omega = \frac{V_i}{r_{wheel}} = \frac{18.4}{0.29225} = 62.7 \cdot \frac{rad}{s} \quad (5)$$

2.2 Dimensioning of the flywheel

By using an amplifier for the angular speed resulting from the traction wheels, the dimensions of the flywheel can be reduced but also keep the energy storage capacity. Therefore, the following dimensions result.

$$\omega' = 50 \cdot \omega = 3136.6 \cdot \frac{rad}{s} \tag{6}$$

$$E = \frac{1}{2} \cdot I \cdot \omega'^2 \Rightarrow I = \frac{E \cdot 2}{\omega'^2} = 0.033 \cdot kg \cdot m^2 \tag{7}$$

$$m(mass) = \frac{I \cdot 2}{r_{flywheel}^2} = 6.63 \cdot kg \tag{8}$$

$$V(volume) = \frac{m}{\delta} = \frac{6.63}{7800} = 8.497 \cdot 10^{-4} \cdot m^3 \tag{9}$$

$$D(diameter) = 2 \cdot r_{flywheel} = 0.2 \cdot m \tag{10}$$

$$A(area) = \frac{\pi \cdot D^2}{4} = 0.03142 \cdot m^2 \tag{11}$$

$$h(thickness) = \frac{V}{A} = 27.05 \cdot mm = 0.027 \cdot m \tag{12}$$

2.3 Simulation model

For a better view of the phenomenon, a numerical processing application has been used such as AMESim.

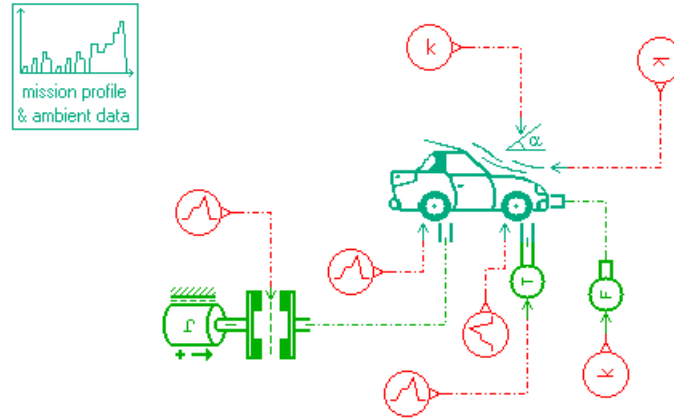


Fig. 2. AMESim simulation scheme of a vehicle having a rotational mass.

In the workspace there has been created a simplified model of a vehicle going with a velocity of 18.4m/s, to which is applied a rotational mass with initial moment of inertia of 82.9 kgm². With this example it is demonstrated that the vehicle velocity supports considerable deceleration. For analysis a batch with different moments of inertia has been created.

Table 1. Batch of different moments of inertia used during simulation.

| ID | Value |
|-------|-------|
| Set 1 | 82.9 |
| Set 2 | 55 |
| Set 3 | 25 |
| Set 4 | 5 |
| Set 5 | 0.033 |

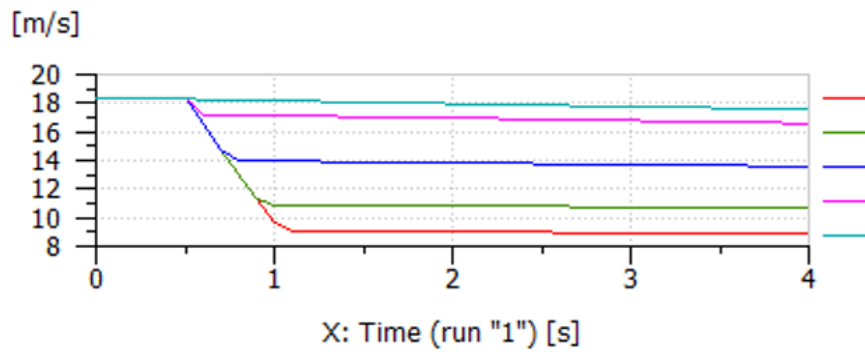


Fig. 3. Vehicle velocity.

Depicted in the Fig.4 is the vehicle velocity plot, where the deceleration occurs when the clutch is coupled. The biggest deceleration appears when the moment of inertia is the largest. As it is reduced the deceleration decreases.

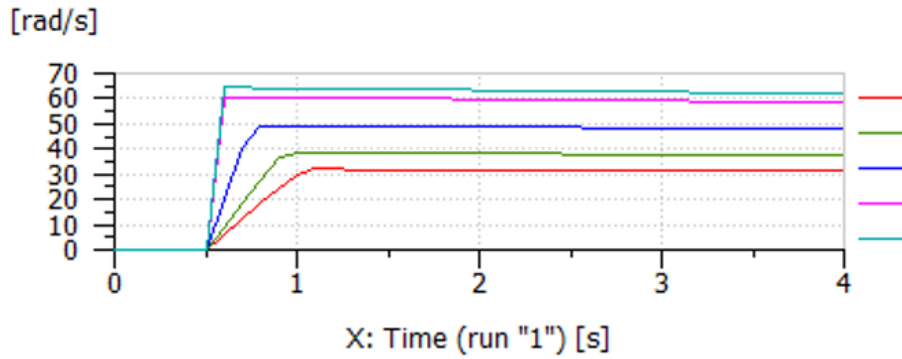


Fig. 4. Flywheel rotational speed.

For Fig. 5 the rotational speed of the flywheel has been plotted. Here the flywheel of the highest mass of inertia has the lowest rotational speed. Simultaneously the flywheel with lowest moment of inertia achieves the highest rotational speed.

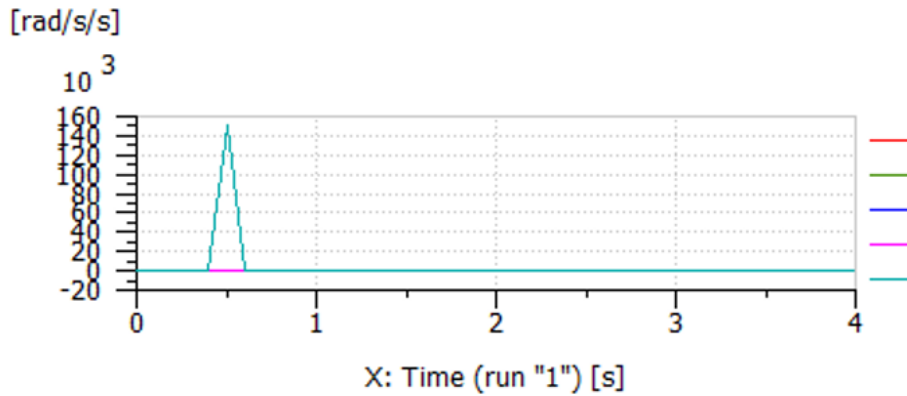


Fig. 5. Flywheel rotational acceleration.

Because the flywheel with the lowest moment of inertia has the highest rotational speed its acceleration is the most powerful of the selected batch.

2.4 Technical implementation

As mentioned before, the flywheel has the advantage of being able to be coupled with various propulsion systems. In Fig.6 it is represented such an option for implementation with an internal combustion engine, where the flywheel is paired with a variable ratio coupling connected to the drivetrain using a clutch.

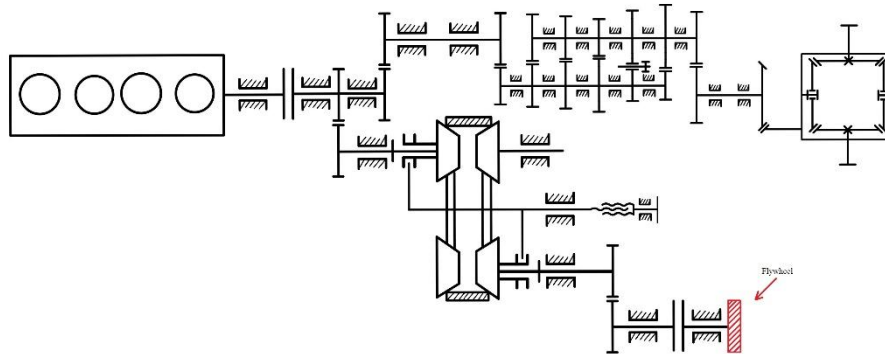


Fig. 6. Basic scheme for implementation with an ICE.

3 Conclusion

Ultimately the paper intends to show the advantages of using flywheels as energy storage devices for automotive use during fast recovery events. The first advantage that a flywheel present is the ability to be paired with a range of different propulsion systems such as internal combustion engines and hybrid/electric driving systems, where it could serve as a damper for charging and discharging, protecting the lifetime of the battery and other electrical components that do not support sudden energy transfers. Secondly by using an amplifier the dimensions of the flywheel can be easily managed, being able to be fitted with ease to different size and classes of vehicles. Finally, the flywheel can prove efficiency in terms of fuel consumption, and it can also minimize the wear on the braking components, therefore being possible to reduce maintenance cost and time.

References

1. Emad Airoud Basmaji: Flywheel Energy Storage System. 24th December 2018 https://www.researchgate.net/publication/332061263_Flywheel_Energy_Storage_System
2. Armin Buchroithner, Michael Bader: History and development trends of flywheel-powered vehicles as part of a systematic concept analysis. In: European Electric Vehicle Congress At: Brussels, Belgium. November 2011 https://www.researchgate.net/publication/278020316_History_and_development_trends_of_flywheel-powered_vehicles_as_part_of_a_systematic_concept_analysis
3. Chunhui Liu and Kun Zhang 2021 J. Phys.: Conf. Ser. 2030 012003 <https://iopscience.iop.org/article/10.1088/1742-6596/2030/1/012003>
4. Richard Stephan, R. de Andrade Jr, Guilherme Goncalves Sotelo: Third Generation of Flywheels: A Substitute to Batteries. In: Congresso Brasileiro de Eletrônica de Potência, COBEP-2007 At: Blumenau, SC – Brazil Volume: 1. DOI:10.13140/2.1.1627.2324 September 2007

- https://www.researchgate.net/publication/267625785_Third_Generation_of_Flywheels_A_Substitute_to_Batteries
5. Peter Lipar, Irena Strnad, Martin Česnik, Tomaž Maher: Development of Urban Driving Cycle with GPS Data Post Processing. In: Promet-Traffic & Transportation. August 2016
https://www.researchgate.net/publication/312052301_Development_of_Urban_Driving_Cycle_with_GPS_Data_Post_Processing
 6. **: Automotive Handbook. Robert Bosch Gmbh, Stuttgart (1996)

Lithium Iron Phosphate Battery Pack for Hybrid Drive Applications

Andrei Cristian Grigore¹, Jan-Alexandru Văduva¹

¹ National University of Science and Technology Politehnica Bucharest, Splaiul Independenței
Nr. 313 Sector 6 060042 Bucharest
andrei.grigore2712@stud.etti.upb.ro, jan.vaduva@upb.ro

Abstract. Formula Student is an international engineering competition where students design, develop, and race single-seater race cars, with a strong emphasis on engineering innovation. This paper presents the development of a traction battery pack for a hybrid powertrain combining gasoline and electric propulsion. As Formula Student competitions increasingly promote the transition towards fully electric vehicles (EVs), the development of such battery packs represents a critical step in this shift. The design process familiarizes students with key EV architectures, industry-standard practices, and essential concepts in electric mobility. The battery pack described in this study was designed and constructed using in-house resources and accessible tools. The results demonstrate the feasibility and reliability of the proposed battery pack architecture, contributing to the broader goal of enhancing hybrid and electric vehicle technologies in Formula Student.

Keywords: LiFePO₄, battery pack, feasibility study, hybrid powertrain.

1 Overview of Hybrid Drive Systems

1.1 General Aspects

When designing a battery pack architecture for either a Battery Electric Vehicle (BEV) or a Hybrid Electric Vehicle (HEV), the initial step involves analyzing the power demands and load requirements the battery will need to support. In the case of BEVs, the battery capacity, voltage, and power output are typically much higher compared to low-voltage battery packs (those under 60V), often used in hybrid systems.

For low-voltage battery packs, a modular approach can be applied, where the battery is divided into smaller, individual modules. Each module operates under 60V, which is the threshold between low-voltage and high-voltage direct current (DC) systems. These modules are then connected in series and/or parallel configurations to optimize the overall performance of the battery pack, tailoring its specifications to meet the specific requirements of the intended application.

This modular approach enables greater flexibility and scalability, particularly in hybrid systems where the power requirements may vary based on the interaction between the internal combustion engine and the electric drive [14].

1.2 Motor Selection and Battery Constraints

While there is a broad range of low-voltage traction motors available on the market, the specific requirements of motorsport applications, particularly for Formula Student teams, significantly narrow the available options. The most critical factors to consider when selecting a motor for a Formula Student single-seater race car include weight, dimensions, power, torque, and RPM output, cost and ease of use in the vehicle [11].

For this project, the motor selected is the **Motres CIAG100-30**, due to its favorable balance between performance and suitability for a Formula Student vehicle [12], [13]. Its key parameters are as follows:

- Continuous power: 3 kW
- Peak power: 5 kW
- Efficiency: 94%
- Rated voltage: 50 V
- Weight: 1.7 kg
- Phase current: 110 A

Following the motor selection, the next step is to determine the appropriate battery pack chemistry and architecture. This process is guided by the regulations outlined in the Formula Student Germany rulebook [1], which are adhered to by most European competitions.

A key design constraint imposed by the rulebook is the strict limit on battery pack weight, which must not exceed 3 kg. This limit applies solely to the weight of the battery cells, excluding auxiliary components such as interconnecting cables and busbars. After careful evaluation of various options, the **LithiumWerks ANR26650** cells were chosen for the battery pack [6], [7]. These cells offer an excellent balance of performance, weight, and cost. Moreover, they are based on LiFePO₄ (Lithium Iron Phosphate) chemistry, which is known for its robustness. These cells are certified to endure harsh operating conditions, mechanical damage (including impact and penetration), and improper use without posing significant risks to the safety of users [2], [18].

1.3 Battery Pack Configuration and Design Trade-offs

The 3 kg battery weight limit, as stipulated by the Formula Student rulebook, and the individual cell weight of 76 grams, allow for a maximum of 39 cells within the battery pack. This limit directly informs the battery pack's design and configuration [3].

Since the battery pack is meant for tractive applications, it's desirable to maximize the battery pack energy storage capacity so that the hybrid vehicle can rely on the electric powertrain for as long as possible, thus decreasing fuel consumption. Therefore, it is imperative that we use 39 cells. Then, it's a matter of figuring out how to use them.

We must decide on a tradeoff here, since there is no way to obtain both high voltage (close to 60V) and high current output. This decision was simple to make, as it is well known that combustion engines burn a lot of fuel when accelerating from a standstill. Additionally, the low-speed nature of formula student tracks means that high motor rpm is not that relevant, while high torque (implying high current) output is desirable [5].

It is known that, to obtain high current output, cells must be placed in parallel. Given the fact that each cell is capable of 50A output continuously and the motor requires 100A for its peak power, it can be deduced that at least two groups of cells must be used in parallel. However, to put less strain on the individual cells, it's better to increase the number of parallel groups. This helps by decreasing equivalent resistance, which in return decreases temperature rise and improves charging / discharging current capabilities as well.

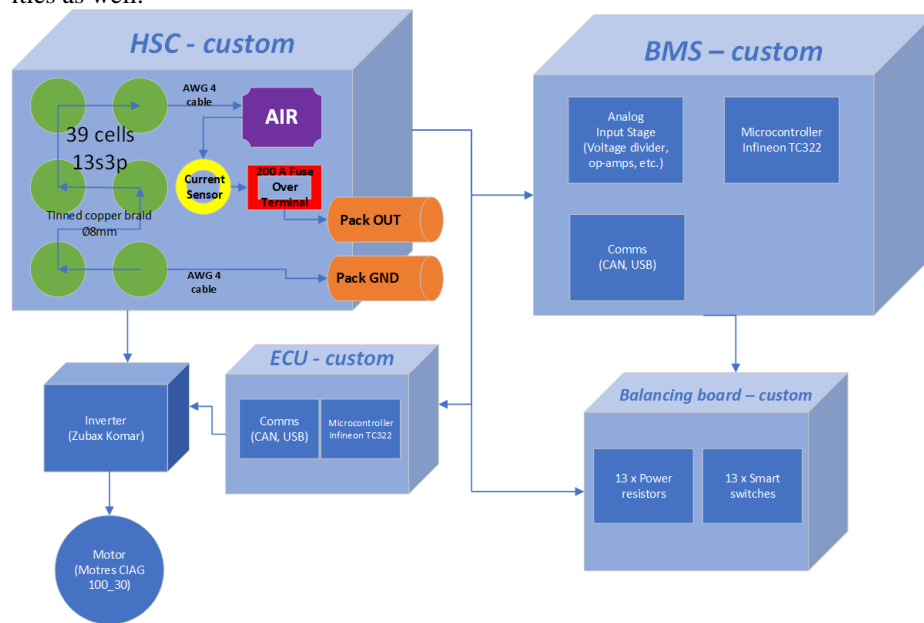


Fig. 1. Overall hybrid system proposed architecture.

Using three groups in parallel helps increase the overall safety factor of a parallel. However, that limits the number of series connections. By simple math we can deduce that we can develop a 13 series, 3 parallel configurations (13s3p).

2 Assembling the battery pack

2.1 Battery Pack Shape and Layout

The battery pack is designed to be integrated into a Formula Student single-seater race car [19], where volumetric constraints are a critical consideration in determining the pack's shape and layout. Given the limited space available within the vehicle, the shape of the battery pack had to be carefully optimized to fit within the structural confines of the chassis.

For enhanced safety and ease of access, the battery pack was strategically positioned beneath the driver's seat, secured behind a protective firewall. This placement not only provides additional safety in the event of a thermal event or impact but also ensures a

compact and efficient use of space. However, the unique shape of the chassis significantly influenced the final design and geometry of the battery pack, necessitating a custom configuration to accommodate the available space without compromising safety or performance.

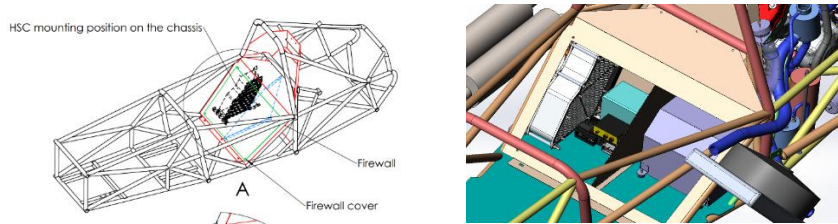


Fig. 2. Hybrid System Container (HSC) location in the vehicle chassis.

The technical drawing details the internal components and layout of a small-scale vehicle, focusing on design choices to optimize performance. Key elements include 3mm steel mountings with gussets for structural integrity, a hydraulic steering column (HSC) secured by M5x110 bolts, and radiator vanes for heat transfer. The Battery Management System (BMS) indicates integration with hybrid or electric vehicle systems.

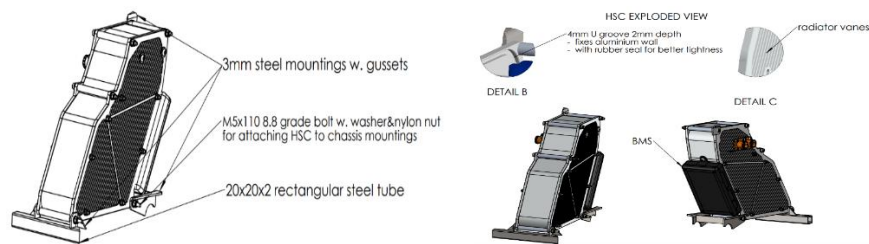


Fig. 3. HSC shape, cooling and chassis mounting specifications.

The custom-made ABS spacer serves as a structural component within the battery pack, organizing and securing the cells while also contributing to its durability and resilience. ABS was chosen for its high impact resistance and thermal stability, making it suitable for the demanding environment of motorsport applications.

2.2 Interconnecting the cells

The technique used to interconnect battery cells is a critical aspect of battery pack design, as improper connections can lead to conductive losses, which in turn can cause several undesirable effects. These include temperature rise, inaccurate voltage readings by the Battery Management System (BMS), and premature wear of conductive elements or contact points.

To mitigate such risks, the use of low-resistance conductors is essential. Traditionally, spot-welded copper polygons are employed to interconnect cells due to their low

electrical resistance. However, for this project, an alternative interconnection method was developed and adopted due to budgetary constraints.

Tinned copper braid with an 8mm diameter was used to connect the cells. The copper braid was secured to each battery terminal using 0.15mm nickel ribbon strips, which were spot-welded in place. Before connecting the cells in parallel, a preliminary voltage matching process was conducted to ensure that the voltage of each cell was sufficiently close, reducing the risk of damaging the cells due to voltage imbalances.

The use of copper braid in an elliptical pattern offered a dual benefit: it not only served as an efficient conductor but also contributed to thermal management. The braid facilitates the extraction and distribution of heat generated by the cells, directing it towards the aluminum casing, which functions as a heatsink to dissipate heat effectively.



Fig. 4. Assembled pack with thermistors and cell voltage readout cables, high voltage terminal.

Additionally, thermistors and cell voltage readout cables were integrated within the battery pack and connected to the BMS, ensuring real-time monitoring of cell temperatures and voltages for optimal performance and safety. High current output terminals were used to connect the cells within the battery pack to the high-power wiring harness.

2.3 Cooling concept

Once the cells are interconnected, the battery pack is placed inside the HSC (Housing Structure Casing), where it is positioned between two silicone pads. These pads are thermally conductive yet electrically insulating, providing an effective means of dissipating heat while ensuring electrical isolation.

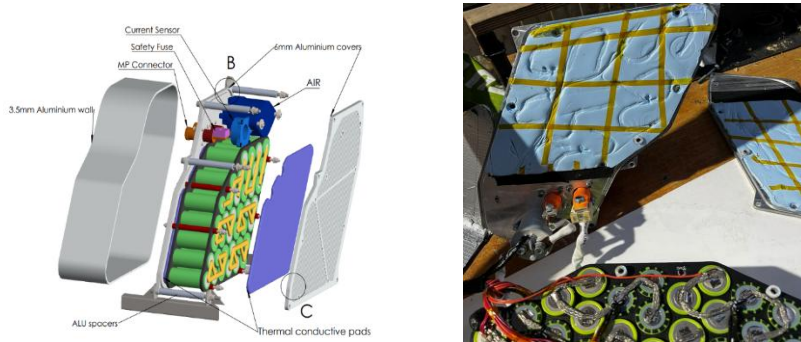


Fig. 5. Pack assembly within HSC, silicone thermal pad inside battery pack casing.

This arrangement enhances the thermal management of the battery pack, contributing to improve cooling and overall system efficiency.

3 Testing the battery pack

3.1 Testing precautions and setup

Before assessing the battery pack's output performance, several safety precautions were implemented. Initially, the Battery Management System (BMS) was used to measure the open-circuit voltage of the series groups and determine the state of charge. The battery pack was then charged, and any necessary cell balancing was performed. Mechanical connections between high-current conductors were also thoroughly inspected to ensure their reliability and stability [15], [16].

During testing, key parameters such as pack voltage, current, temperature, and state of charge were continuously monitored. A thermal camera was employed to detect any potential hotspots within the battery pack, ensuring proper heat distribution.

3.2 Light load test

The initial test involved connecting four 12V, 55W H4 lightbulbs in series, creating a total load of approximately 220W.

The battery pack had no difficulty powering the bulbs, and thermal camera imaging revealed an even heat distribution, indicating successful performance during this preliminary test.

3.3 Intermediate, variable load test

Subsequent testing was conducted with the aid of a Keysight 350W electronic load. This equipment allowed us to simulate real-world dynamic conditions by incrementally increasing the load current from zero to the maximum allowable value. The electronic load provided valuable data under these dynamic conditions.

Additionally, the electronic load was used for cycle testing, performing ten charging/discharging cycles to observe battery performance across a range of conditions and identify the optimal operational parameters. After each full discharge, the battery pack was recharged using a bench power supply.

3.4 Heavy resistive load test

A stress test followed, using a setup of five 4.7-ohm power resistors wired in parallel, resulting in an equivalent resistance of approximately 0.9 ohms. The battery pack was tested from full charge to complete depletion under conditions like those of the electronic load.



Fig. 6. 0.9-ohm resistive power load test setup.

The average power output during this test was around 1.6 kW, with a discharge current of approximately 40A, which exceeds the average values the battery would experience under race conditions.



Fig. 7. Battery pack temperature heat distribution at the end of the test.

Several observations were made:

- Heat distribution was uniform, with no significant hotspots detected.
- The cells effectively conducted heat through their terminals, dissipating it via the copper braid interconnecting the cells.
- The temperature rise after the test was measured at 15°C.
- The observed pack capacity was approximately 10% lower than expected (290Wh versus 320Wh), likely due to the intense load and low ambient temperatures, in sync with the findings from [10].

3.5 Heavy tractive motor test

The most extensive test involved using an oversized motor rated at 8 kW. The test setup utilized an electrified, decommissioned Formula Student car [20], allowing for motor swapping between the oversized motor and the hybrid system motor.

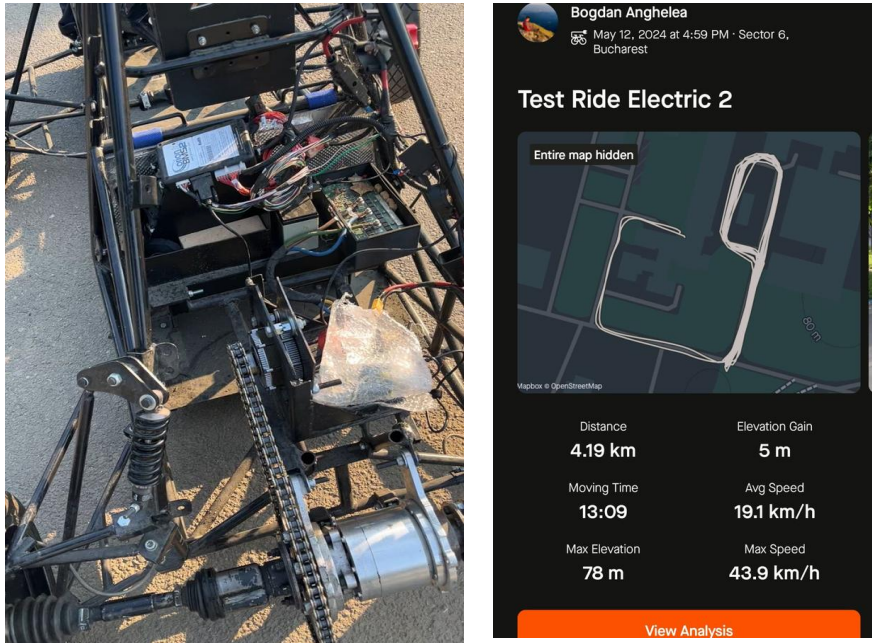


Fig. 8. Electric motor test setup, circuit and results of a typical run.

The vehicle's total weight, including the battery pack, was approximately 120 kg, with test pilot weights ranging from 70 to 85 kg. These tests aimed to determine the usable range of the battery pack, which was evaluated on a predefined circuit at varying speeds.

The battery pack provided a range of 2 to 5 km, depending on acceleration intensity and top speed, with a maximum speed of 62 km/h recorded during testing. The results exceeded expectations, with the energy stored in the battery pack being equivalent to approximately 35 ml of gasoline.

4 Results

The battery pack testing yielded highly favorable results, confirming that Lithium-Werks ANR26650 cells are a reliable choice for tractive system battery packs. The cells performed as expected and aligned with their datasheet specifications. A particularly noteworthy observation was the cells' ability to maintain stable voltage across most of their state of charge, even under heavy loads. This stability is crucial as the battery pack voltage directly influences the motor's maximum RPM, ensuring a consistent and reliable setup.

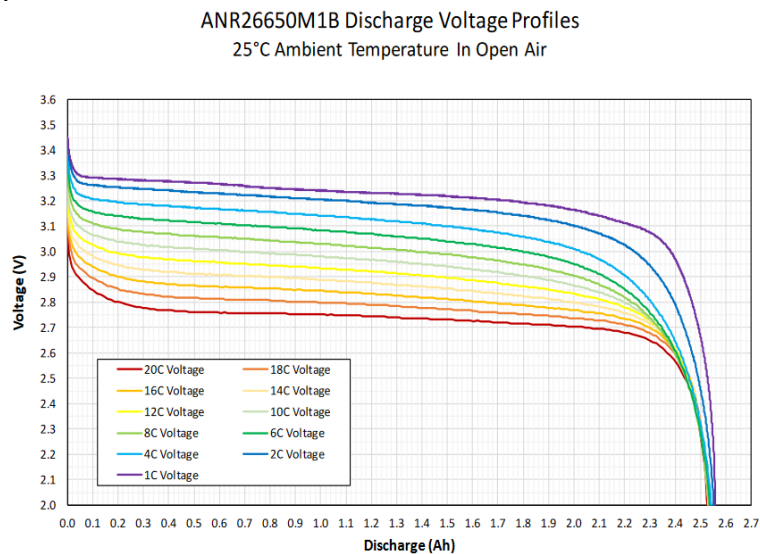


Fig. 9. ANR26650 discharge profiles [2].

The results of the battery pack testing demonstrated its robustness and effectiveness in tractive applications, particularly for a Formula Student vehicle [17].

5 Future Steps

While the experiments were successful, several areas warrant further investigation:

- A simpler interconnection technique could be explored, as the current method, although effective, is labor-intensive and time-consuming.
- A second battery pack with the same design has been produced. Testing the two packs in series would allow for the evaluation of their performance in a high-voltage setup for driving a fully electric powertrain.
- Exploring forced air or liquid cooling systems may prove beneficial. Although this was beyond the scope of the current study, considering the strict limit of maintaining cell temperatures below 60°C, forced cooling may become essential in summer race conditions where track temperatures often exceed 40°C.

References

1. Formula Student Rules 2024. https://www.formulastudent.de/fileadmin/user_upload/all/2024/rules/FS-Rules_2024_v1.1.pdf. Accessed: 2024-10-05.
2. LithiumWerks ANR26650M1B Datasheet. <https://lithiumwerksbatteries.com/lithium-werks-anr26650m1b-3-3-v-2-6-ah-lithium-iron-phosphate-lifepo4-battery-pre-order/>. Accessed: 2024-10-05.
3. Emadi, A. *Handbook of automotive power electronics and motor drives*. CRC press, 2017
4. Emadi, Ali. *Advanced electric drive vehicles*. CRC Press, 2014.
5. Hannan, Mahammad A., F. A. Azidin, and Azah Mohamed. "Hybrid electric vehicles and their challenges: A review." *Renewable and Sustainable Energy Reviews* 29 (2014): 135-150.
6. Ehsani, Mehrdad, et al. "State of the art and trends in electric and hybrid electric vehicles." *Proceedings of the IEEE* 109.6 (2021): 967-984.
7. Masias, Alvaro, James Marcicki, and William A. Paxton. "Opportunities and challenges of lithium ion batteries in automotive applications." *ACS energy letters* 6.2 (2021): 621-630.
8. Luo, Fang Lin, Hong Ye, and Muhammad H. Rashid. *Digital power electronics and applications*. Elsevier, 2010.
9. Song, Ziyu, et al. "A comparison study of different semi-active hybrid energy storage system topologies for electric vehicles." *Journal of Power Sources* 274 (2015): 400-411.
10. Lux, Gerhard, et al. "Thermal Management of Hybrid Electric Vehicles." *Hybrid and Electric vehicles, energy storage technologies and control systems*. 2008.
11. Markel, Tony, and Andrew Simpson. "Cost-benefit analysis of plug-in hybrid electric vehicle technology." *World Electric Vehicle Journal* 1.1 (2007): 294-301.
12. Heidari, Hamidreza, et al. "A review of synchronous reluctance motor-drive advancements." *Sustainability* 13.2 (2021): 729.
13. Donaghy-Spargo, C. M. "Synchronous reluctance motor technology: opportunities, challenges and future direction." *Engineering & technology reference* (2016).
14. Vaduva, J. A., Curteanu, D. F., & Rughinis, R. 2016. REAACT: Testbed for Virtual Vehicles. *UPB Scientific Bulletin, Series C: Electrical Engineering and Computer Science*, **78**, 207–214.
15. Perisoara, L. A., Săcăleanu, D. I. 2022. Automotive Ethernet Architecture for the Connected Dacia Logan Electric Vehicle. *14th International Conference on Development and Application Systems*, 121–126.
16. Perisoara, L. A., & Guran, I. C. 2018. A Passive Battery Management System for Fast Balancing of Four LiFePO4 Cells. *IEEE 24th International Symposium on Design and Technology in Electronic Packaging*, 92–97.
17. Chang, Ikwhang, et al. "Designing and manufacturing of Formula SAE-Hybrid racecar for a new engineering education program." *2010 IEEE Vehicle Power and Propulsion Conference*. IEEE, 2010.
18. Makhija, Gagan, et al. "Design and Optimization of Powertrain Using Hybrid Planetary Gearbox for Formula Student Vehicle." *International Design Engineering Technical Conferences and Computers and Information in Engineering Conference*. Vol. 57205. American Society of Mechanical Engineers, 2015.
19. Birut, Aleksandra, et al. "Performance analysis of electric motor for Formula Student race car." *Combustion Engines*.
20. White, Darris, J. E. McKisson, and William Barott. "Organization Of A Multi Disciplinary Capstone Design Project For The Sae Formula Hybrid Competition." *2007 Annual Conference & Exposition*. 2007.

Evaluation of the Tire Influences on the Dynamics of a Formula Student Type Single-Seater

Bogdan-Tudor Gal¹ and Adrian Todoruț¹

¹Technical University of Cluj-Napoca, Cluj-Napoca, Romania

gal.fl.bogdan@student.utcluj.ro

adrian.todorut@campus.utcluj.ro

Abstract. The objective of the paper is to examine how tire behavior affects vehicle dynamics in competition events. Tire dynamics represent a starting point in understanding vehicle behavior and in further developing systems such as the suspension, steering and tractive system. The tire is the point of contact between the vehicle and the road thus it is the point in where forces and moments are applicable. Longitudinal and lateral forces generated at the tire contact patch are traction, braking and lateral forces that influence the handling and stability of the vehicle. To develop these characteristics in tires there is also a power loss due to rolling resistance that generates resistive forces. By considering the tire a unitary elastic element, the deformations and the vertical rigidity are key factors for defining the tire contact patch under certain load conditions. For the ART TU Cluj-Napoca car the cases in which the tire dynamics are taken into consideration are acceleration, braking and cornering which are specific for the Formula Student competitions. Analyzing the tire behavior is accomplished by modelling the tire and then simulating the tire for characteristics and behavior in a full vehicle model. The tire is modeled using the Magic Formula, implemented in MATLAB and Simulink, where the general tire behavior is generated based on load and inflation pressure and then integrated into a multibody full vehicle model in ADAMS, here the vehicle is simulated in the dynamic events to analyze the impact on the dynamic behavior of the Formula Student vehicle.

Keywords: Tire Dynamics, Formula Student, Vehicle Simulation.

1 Introduction

The tires bear a vertical load given by the weight of the race car, but in addition to these loads, aerodynamic forces and forces arising from the lateral inclination of the contact surface are also applied. The interaction between the tire and the track generates most of the forces and moments. The arrangement of forces and moments will follow the SAE standard for axis representation. By the direction of the forces, the arrangement of the forces is longitudinal, lateral and vertical. These forces are to be separated in their individual axis system for a better understanding.

The normal force, or tire load, represents the influence of all forces and moments that occur at the contact point between the tire and the track. Thus, any load transmitted through the rim to the tire will deform it, giving rise to reaction forces, specifically the normal force. As the load on the wheel increases, the tire will deform more, increasing its contact area with the surface. For this reason, the load on a set of tires will determine the acceleration characteristics, both longitudinally and laterally [3,5].

The deformation mechanism of the tire defines a characteristic called vertical stiffness, and for race cars, the ratio between the tire's vertical stiffness and the suspension springs' stiffness typically ranges from 2 to 3. In the case of an uneven road surface, both components will experience approximately equal displacement, making the tire an important part of the suspension system as well. Overloading the tire will lead to significant deformation in the contact patch area, thus increasing the temperature with each wheel rotation. Gradually, these deformations become larger, and the contact point between the tire and the road surface is compromised, which negatively affects the race car's dynamic performance [5].

To accelerate or brake a vehicle, it is necessary to generate a longitudinal force between the tire and the road surface. The traction force acts in the same direction as the vehicle's movement, while the braking force acts in the opposite direction. Due to the elasticity of the tire, when the tread enters the contact area with the road surface, it is subjected to tangential compression and is stretched as it leaves this area. The braking force that appears at the contact patch, as a result of the braking moment, tends to shift the patch towards the rear of the axle, compressing the elastic elements of the tread in this direction[5,6].

An important notion for the longitudinal forces generation is the longitudinal slip. Longitudinal slip represents the ratio between the speed of a point on the tread, located at a radius equal to the dynamic radius, and the translational speed of the tire.

The longitudinal characteristic of a tire describes two distinct areas, the stable area where the tire has grip and provides traction, and the unstable area, where after a certain limit of the longitudinal force the tire cannot provide the characteristics of traction and slip occurs (Fig 1)[5].

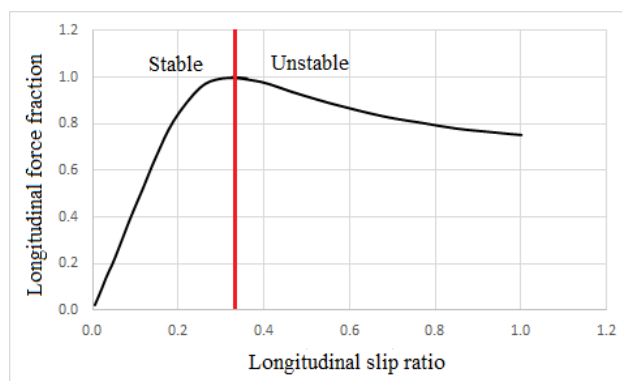


Fig. 1. Tire longitudinal behavior.

At the contact point between the tire and the road surface, there is also a force that is perpendicular to the direction in which they are oriented. This force is important for the dynamic capabilities of a vehicle because it allows for maneuvering during turns. The mechanisms for generating these forces are through the development of a slip angle or through the generation of a reaction force when a camber angle is applied to the wheel. The slip angle occurs due to the elastic properties of the tire. During cornering, the steering wheels will be tangent to the circle that describes the turn, but at the contact point between the tire and the road surface, the tread will deform according to an angle formed between the initial direction of travel and the direction in which the wheel is pointed (Fig. 2)[3,4,5].

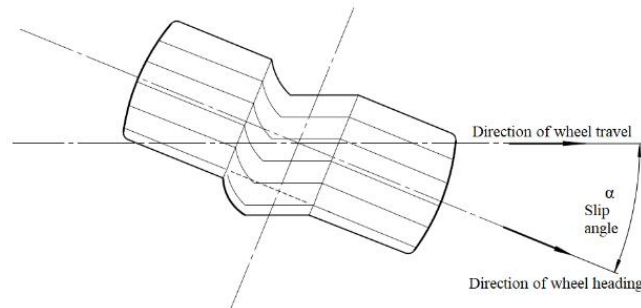


Fig. 2. Slip angle for a steered wheel.

The tire characteristic for the lateral force maintains the same tendencies as in the longitudinal case. The lateral force increases with the slip angle until a certain limit is reached, from there onwards the tire is in an unstable behavior zone even if the slip angle continues to increase. In the unstable zone the lateral tire force decreases and the effect is tire slip (Fig. 3)[3,4,5].

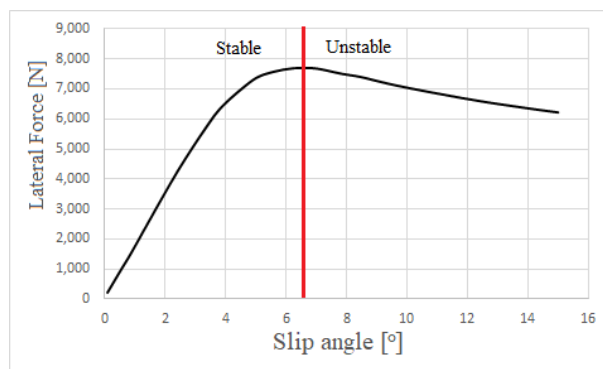


Fig. 3. Lateral force characteristic.

2 Mathematical modelling of the tire

2.1 Tire variant and simulation cases

For the mathematical modeling of Continental 205/510R13 tires, aimed at determining the forces that arise at the contact point between the tire and the road surface during the movement of the ART TU Cluj-Napoca team's race car on specific dynamic test routes, a series of equations known as the Magic Formula is used. The mathematical model is based on experimental data obtained from tests conducted at Calspan Corp. for tires intended for Formula Student competitions at various inflation pressures ranging from 0.069 MPa up to 0.096 MPa.

The specific dynamic events in which the behavior of the tires is analyzed are the acceleration and Skidpad events (Fig. 4)[8].

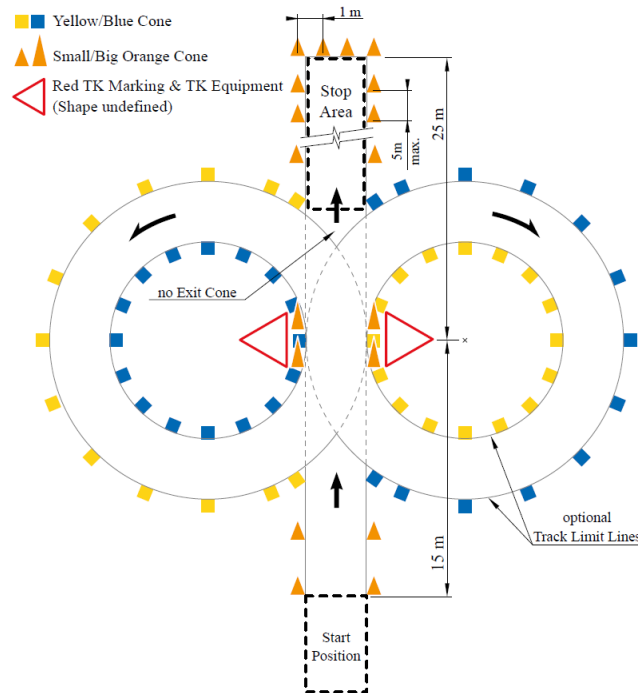


Fig. 4. Skidpad track.

The skid pad course consists of two concentric circles arranged in the shape of an figure eight with centers 18.25 meters apart. The inner circle has a diameter of 15.25 meters, and the outer circle has a diameter of 21.25 meters. The start and finish lines are represented by the median line between the centers of the circles, and the timed lap will be the second lap around the circle[8].

The acceleration track consists of a straight 75 meter acceleration zone and another straight 75 meter slowdown zone. After passing through the acceleration zone, the race car reaches a speed of approximately 100 km/h, so the course includes a deceleration zone where the car must stop within a distance of no more than 75 meters (Fig. 5)[8].

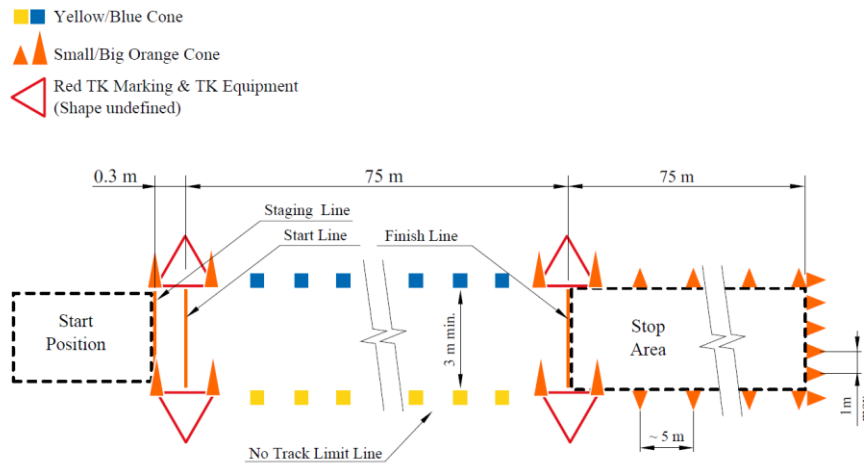


Fig. 5 Acceleration track.

2.2 Modeling the force system

The forces generated at the contact point between the tire and the road surface, specifically the longitudinal and lateral forces, are proportional to the wheel load. To ensure accuracy in tire modeling results, the loads on each wheel during dynamic tests like acceleration and skid pad are taken into account. These loads consist of a static component, the weight of the race car, and a dynamic component, a load due to acceleration. To determine the loads, the Simulink extension of the MATLAB program is used, incorporating the technical data gathered by the ART TU Cluj-Napoca team regarding vehicle weight, wheel base, wheel track and the position of center of gravity.

The modeling begins by defining individual cases in which mass transfer occurs as a result of acceleration. These cases account for how the vehicle's weight shifts between the wheels during different dynamic events, such as acceleration, braking, and cornering.

The static load on each axle is determined using the following equations [7]:

$$G_1 = \frac{b}{A} \cdot G_a, [N] \tag{1}$$

$$G_2 = \frac{a}{A} \cdot G_a, [N] \tag{2}$$

Longitudinal acceleration causes a mass transfer toward the rear axle, increasing the load on the rear wheels and reducing the load on the front wheels. This effect is reversed during braking, where the mass shifts toward the front axle, loading the front wheels and unloading the rear wheels. For these effects the following equations were used to determine the load on each wheel [4]:

$$F_{z_f} = \frac{1}{2} \cdot m \cdot g \cdot \frac{b}{A} - \frac{1}{2} \cdot m \cdot a_x \cdot \frac{hg}{A}, [N] \tag{3}$$

$$F_{z_r} = \frac{1}{2} \cdot m \cdot g \cdot \frac{a}{A} + \frac{1}{2} \cdot m \cdot a_x \cdot \frac{hg}{A}, [N] \tag{4}$$

While driving on the Skidpad circuit during the timed lap, the vehicle is considered to maintain a constant speed, meaning the race car only accelerates in the lateral direction. This lateral acceleration results from the forces needed to keep the car on the curved path, influencing the tire loads and overall handling. The wheel loads were obtained using the equations [4]:

$$F_{z_{fr}} = \frac{1}{2} \cdot m \cdot g \cdot \frac{b1}{w} + \frac{1}{2} \cdot m \cdot a_y \cdot \frac{hg}{w}, [N] \tag{5}$$

$$F_{z_{fl}} = \frac{1}{2} \cdot m \cdot g \cdot \frac{b2}{w} - \frac{1}{2} \cdot m \cdot a_y \cdot \frac{hg}{w}, [N] \tag{6}$$

$$F_{z_{rr}} = \frac{1}{2} \cdot m \cdot g \cdot \frac{b1}{w} + \frac{1}{2} \cdot m \cdot a_y \cdot \frac{hg}{w}, [N] \tag{7}$$

$$F_{z_{rl}} = \frac{1}{2} \cdot m \cdot g \cdot \frac{b2}{w} - \frac{1}{2} \cdot m \cdot a_y \cdot \frac{hg}{w}, [N] \tag{8}$$

The equations were then implemented in Simulink to obtain the tire forces system (Fig. 6)

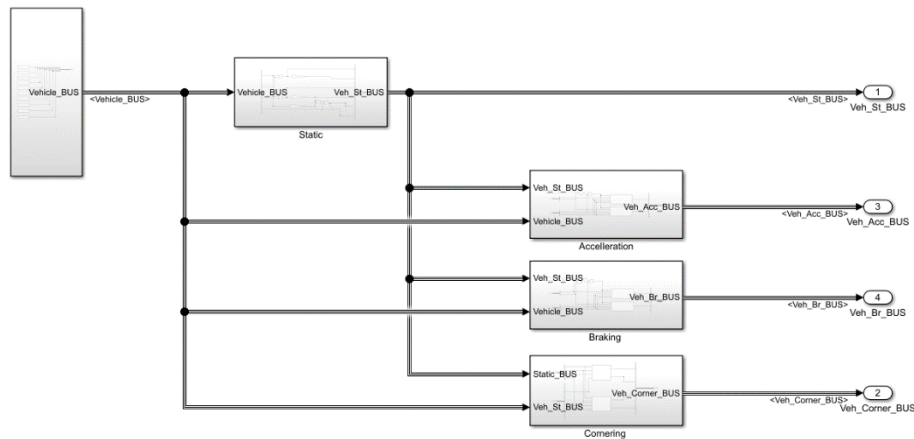


Fig. 6. The tire forces system modeled in Simulink.

The simulation results for the model used to determine the wheel loads in the proposed cases are presented in Table 1. These results show the distribution of loads on each wheel under various dynamic conditions, providing crucial data for analyzing the vehicle's performance during acceleration, braking, and cornering.

Table 1. Tire load on each wheel

| Tire | Tire load [N] | | | |
|---------------------|---------------|-------------|-----------|------------|
| | Front-Left | Front-Right | Rear-Left | Rear-Right |
| Case | | | | |
| Static | 913,3 | 913,3 | 950,6 | 950,6 |
| Acceleration | 768,1 | 768,1 | 1096 | 1096 |
| Braking | 1198 | 1198 | 666 | 666 |
| Skidpad – left turn | 596 | 1258 | 628,8 | 1272 |

2.3 Magic Formula modeling

The mathematical modeling of the tires is based on a semi-empirical model widely used to determine the forces at the contact point between the tire and the road surface, aimed at advancing vehicle dynamics, known as the Magic Formula. The semi-empirical nature of the model comes from the use of dimensionless parameters p and r , along with a scaling factor λ , which are obtained experimentally [1,2].

For the implementation of the model in MATLAB Simulink, experimental data are read from files provided by the Formula SAE Tire Test Consortium platform. The mathematical equations are then implemented in Simulink using function blocks. For the front wheels only the lateral behavior is modeled, since they are not traction wheels (Fig. 7).

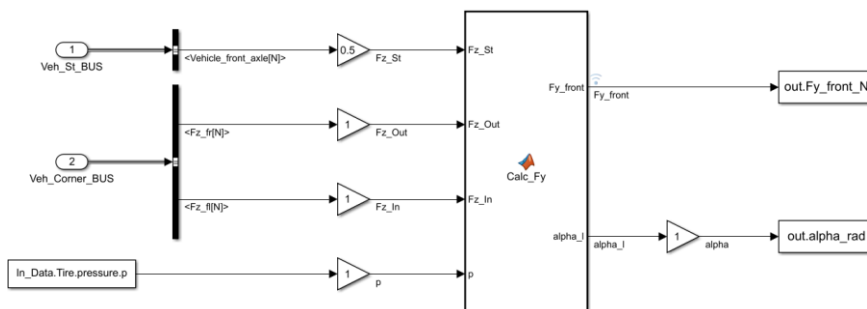


Fig. 7. Magic Formula implementation for the front tires considering only the lateral case.

Given the configuration of the ART TU Cluj-Napoca team's race car, with the rear axle being the driving axle, both the determination of the longitudinal force and the lateral force, which result from the tire-road contact, are key points of interest for analyzing the car's dynamic behavior. For the rear tires, both the lateral and longitudinal behaviors is modeled, as depicted in figure 8. and figure 9.

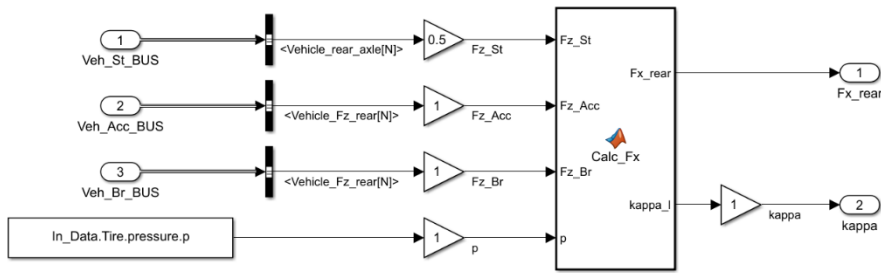


Fig. 8. Magic Formula implementation for the rear tires in the longitudinal case.

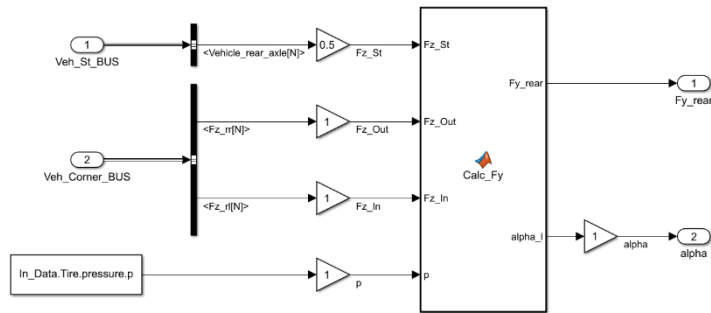


Fig. 9. Magic Formula implementation for the rear tires in the lateral case.

3 Tire simulation

To analyze the real-time behavior of the tires during a specific dynamic event in the Formula Student competition, the ADAMS Car module of the ADAMS software is used. For tire modeling in the ADAMS Car – Builder module, data provided by the Formula SAE Tire Test Consortium platform are utilized, which are delivered in files compatible with the modeling module. This allows for accurate simulation and assessment of tire performance under various conditions [1].

The full vehicle model, depicted in figure 10, is tested in the acceleration and skid pad events. The conditions and data for each test comply with the dynamic event regulations. For each test scenario, the model configuration allows for three variants of the Continental tire, where the inflation pressures are: 0.069 MPa, 0.083 MPa, and 0.096

MPa. Therefore, in the acceleration test simulations, three different configurations of the race car are obtained, as seen in Table 2, while in the skid pad event simulations, nine configurations are generated as seen in Table 3.

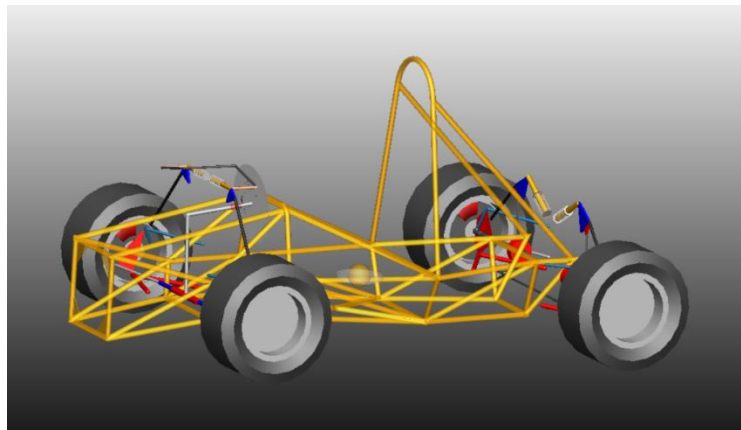


Fig. 10. Full vehicle model in ADAMS Car.

Table 2. Acceleration tire pressure configuration

| Acceleration event | | | |
|---------------------------|-----------------|-------|-------|
| Inflation pressure, [MPa] | | | |
| | Rear Axle Tires | | |
| 0,096 | 0,069 | 0,083 | 0,096 |

Table 3. Skidpad tire pressure configuration

| Skidpad event | | | |
|---------------------------|-----------------|-------|-------|
| Inflation pressure, [MPa] | | | |
| Front Axle Tires | Rear Axle Tires | | |
| 0,096 | 0,069 | 0,083 | 0,096 |
| 0,083 | 0,069 | 0,083 | 0,096 |
| 0,069 | 0,069 | 0,083 | 0,096 |

The simulations of the race car's dynamic behavior consider the impact of tire inflation pressure on rolling resistance. Lower pressures increase tire deformation and contact area, raising rolling resistance. To minimize this in the acceleration event, the front tires are set to 0.096 MPa in the simulations due to the high load on the ART TU Cluj-Napoca car.

For the Skidpad test, the cornering behavior is analyzed by having the race car follow half of the track, specifically a single circle with a constant radius, at a constant speed, as in the timed lap. The speed for this test is set at 40 km/h, considering the car's weight and its aerodynamic features.

4 Results

4.1 Mathematical model results

The tire analysis was performed for the available inflation pressures of 0.069 MPa, 0.083 MPa, and 0.096 MPa, under varying wheel load conditions. This includes scenarios of wheel loading and unloading during acceleration and braking, as well as a case where the car moves at a constant speed.

The maximum values of longitudinal forces for the three configurations occur at the same longitudinal slip values. However, as inflation pressure decreases, the tire deformation varies for the same load, resulting in an increased contact patch area. This is reflected in the increase of longitudinal force as inflation pressure decreases for each loading case. The tire characteristics for the longitudinal force are depicted in figure 11, figure 12 and figure 13.

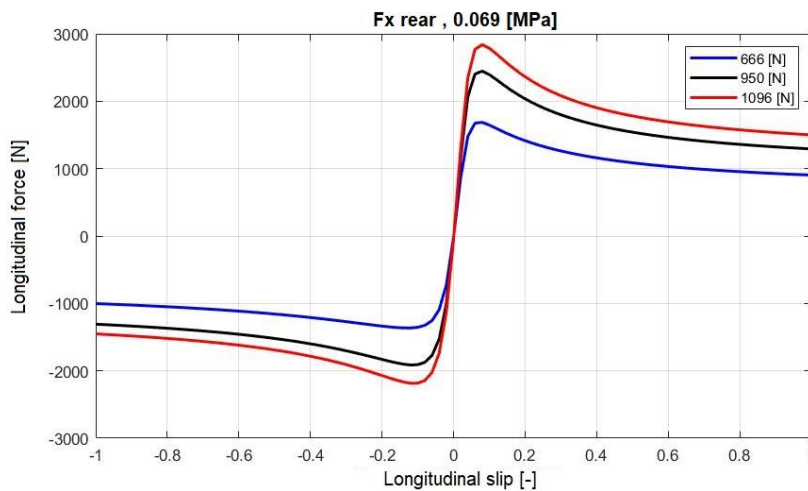


Fig. 11. Longitudinal tire force characteristic – 0.069 MPa.

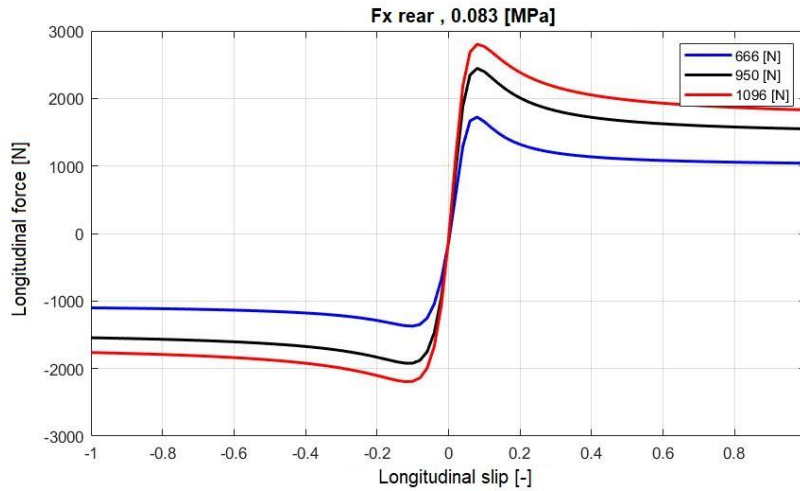


Fig. 12. Longitudinal tire force characteristic – 0.083 MPa.

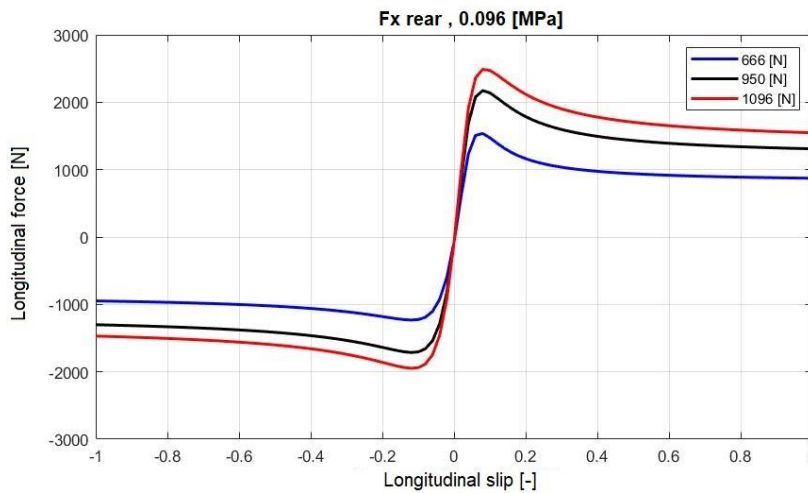


Fig. 13. Longitudinal tire force characteristic – 0.096 MPa.

In the analysis of lateral forces for the tires on both axles, the dependence on tire inflation pressure is similar to that of longitudinal forces for each loading case. However, as the wheel load increases, the lateral slip angle at which the maximum longitudinal force is achieved also rises. Thus, at higher loads, the tire maintains stable behavior at a larger lateral slip angle. The inner tire during a turn, which experiences unloading, will behave unstably at the same lateral slip angle as the outer tire. This instability can lead to a loss of stability and maneuverability for the race car, resulting in a faster

degradation of the inner tires. The lateral tire force characteristic for both front and rear tire are depicted in figure 14 through figure 19.

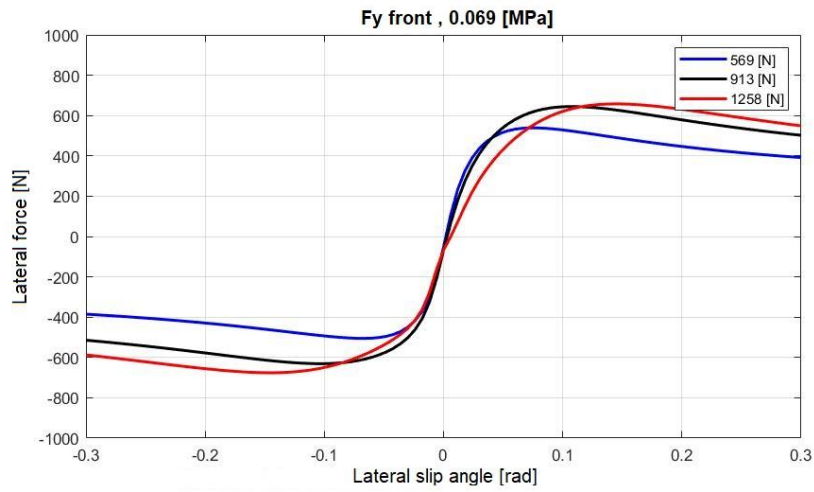


Fig. 15. Lateral tire force characteristic, front – 0.069 MPa.

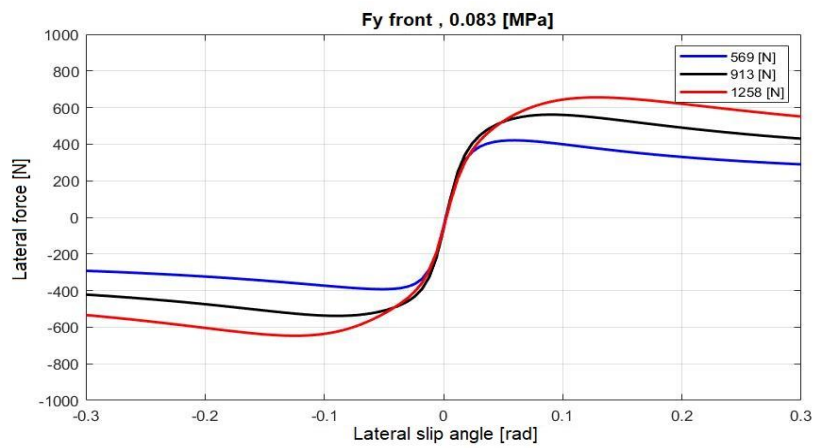


Fig. 14. Lateral tire force characteristic, front – 0.083 MPa.

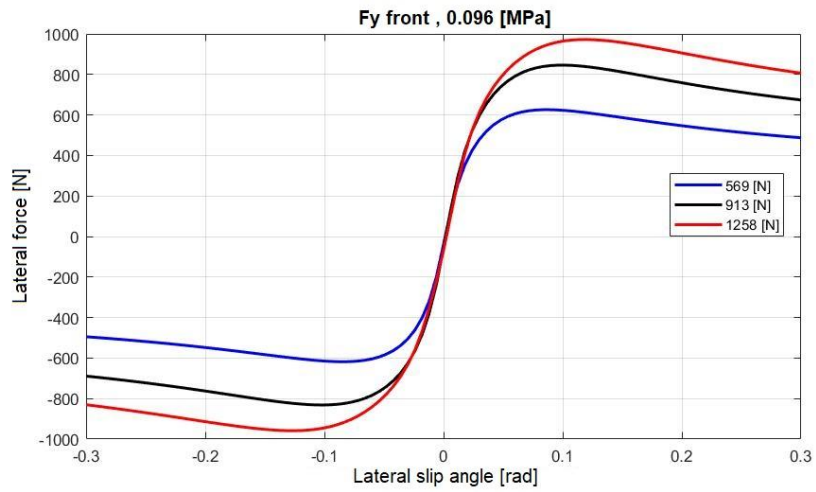


Fig. 16. Lateral tire force characteristic, front – 0.096 MPa.

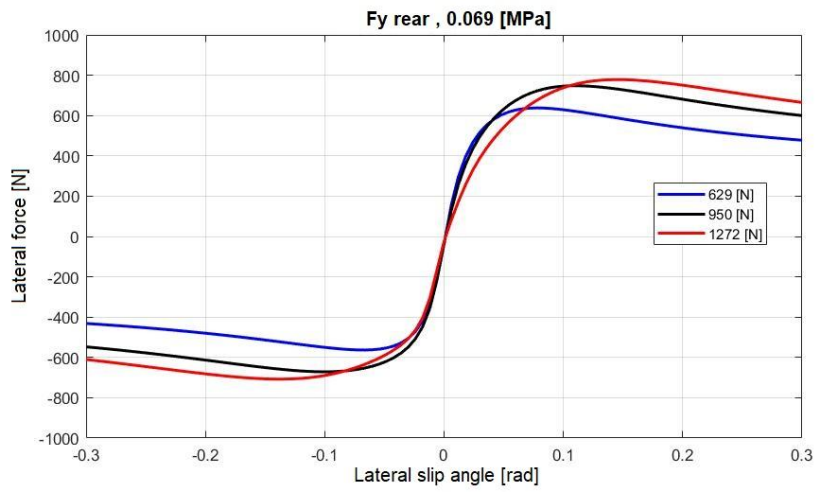


Fig. 17. Lateral tire force characteristic, rear – 0.069 MPa.

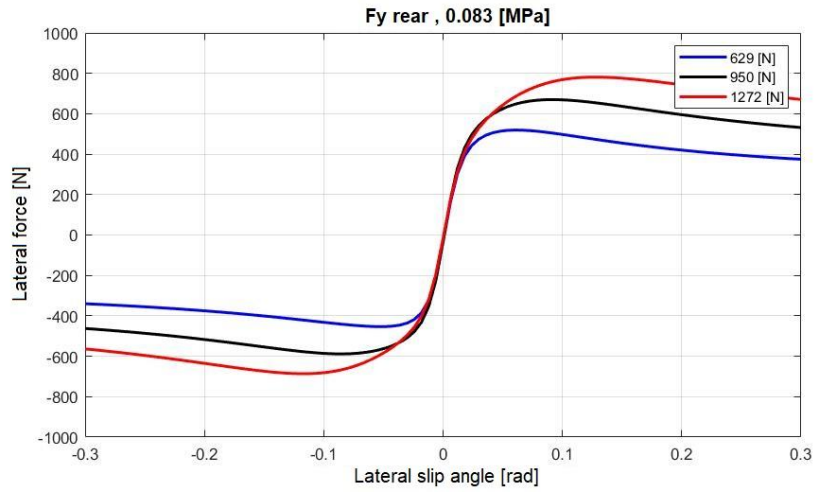


Fig. 19. Lateral tire force characteristic, rear – 0.083 MPa.

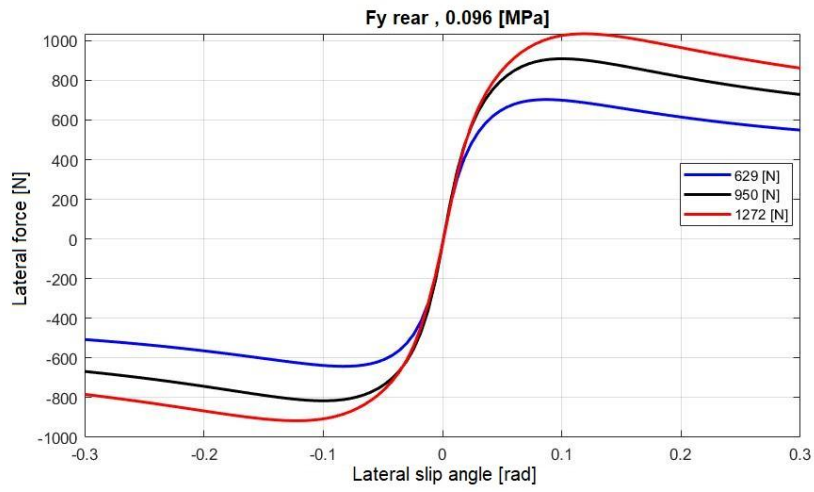


Fig. 18. Lateral tire force characteristic, rear – 0.096 MPa.

4.2 Tire simulation results

The simulation results, presented in graphical form, illustrate the race car's behavior during the acceleration test. In the graphical representation shown in Figure 4.4, the acceleration of the race car is noted for each inflation pressure of 0.069 MPa, 0.083 MPa, and 0.096 MPa, with the corresponding acceleration values being 0.703 m/s², 0.701 m/s², and 0.7 m/s², respectively (Fig. 20).

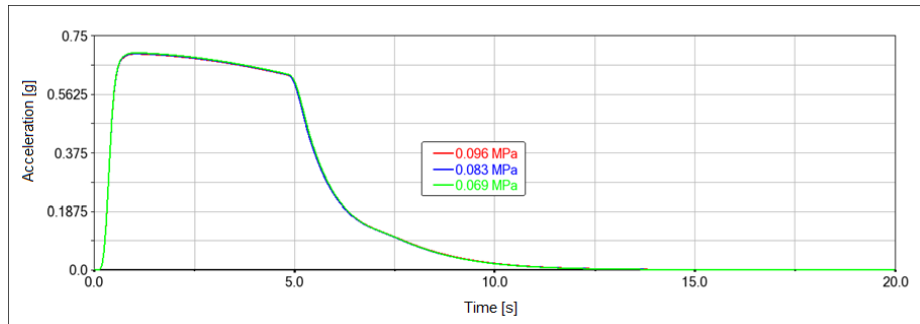


Fig. 20. Longitudinal acceleration of the vehicle.

In the analysis of longitudinal force on the driving axle tires (Fig. 21), the maximum value for a tire is reached at 1140 N for an inflation pressure of 0.069 MPa, 1137 N for 0.083 MPa, and 1135 N for 0.096 MPa. The observed trend of increasing longitudinal force with decreasing tire pressure is attributed to greater deformation of the tire at lower pressures, resulting in a larger contact patch between the tire and the road surface.

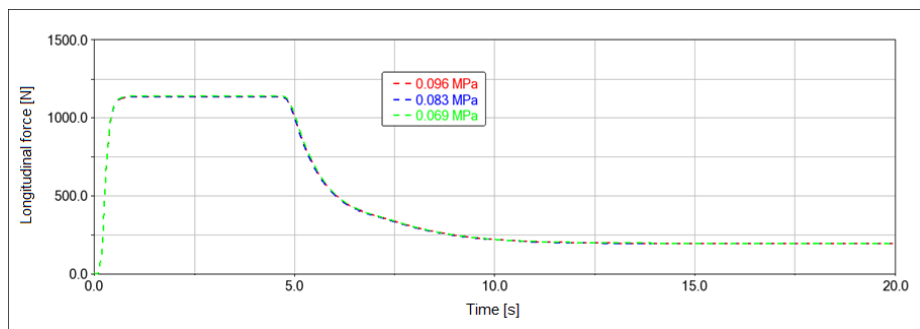


Fig. 21. Longitudinal tire force for the rear tires.

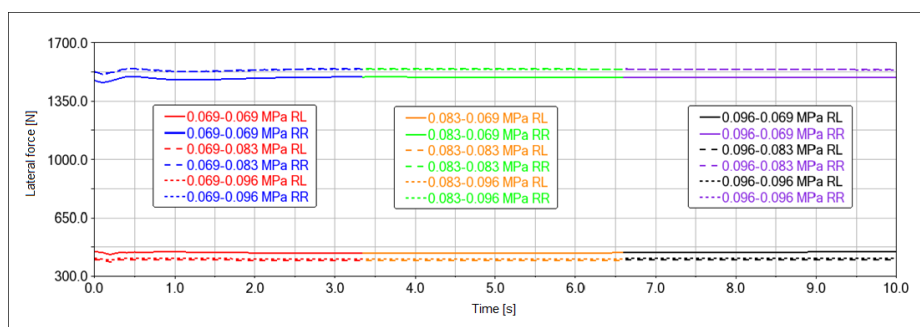


Fig. 22. Lateral tire force for the front tires.

The analysis of tire behavior during the Skidpad test examines the variation of lateral force at the contact patch between the tire and the road surface for all available tire inflation pressure configurations. The highest lateral force value for the front axle tires is 1453.4 N, observed for the outer tire during cornering, with a pressure of 0.096 MPa for the front tires and 0.069 MPa for the rear tires (Fig. 22).

The configuration that produces the highest lateral forces is analyzed at a speed of 40 km/h, corresponding to a lateral acceleration of 13.5 m/s². To assess the potential for performance improvement in this test, the lateral slip angle at which these lateral forces are achieved is examined (Fig. 23).

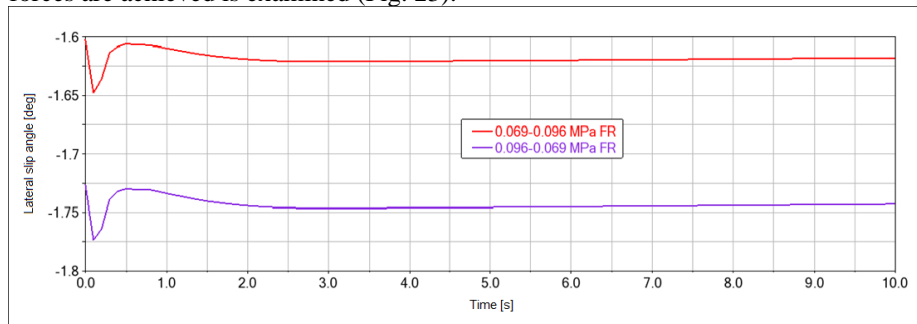


Fig. 23. Lateral tire slip at the front tires for the proposed configurations.

5 Conclusions

Following the mathematical modeling of the tires in Simulink, a comprehensive model was developed to describe tire behavior based on the specific test undertaken by the ART TU Cluj-Napoca race car team. The tire inflation pressure significantly influences the maximum values of both longitudinal and lateral forces, enabling the tire to adjust its contact patch due to deformation at each pressure level. Additionally, maintaining stability and maneuverability is achieved by increasing the load on the tires inside the turn, which can be accomplished by adding aerodynamic elements that provide additional downforce.

The behavior of the tires during the acceleration and Skidpad tests was analyzed through the modeling of the ART TU Cluj-Napoca race car in the ADAMS engineering software, specifically in the Car module. Simulations were conducted by varying the tire inflation pressure based on values provided by Calspan Corp. via the FSAE Tire Test Consortium. In the acceleration test, all tire pressure configurations achieved a maximum acceleration of 0.7g. The optimal configuration was found to be with the front tire pressure set at 0.069 MPa, as the increased contact patch due to greater deformation resulted in a 35% lower longitudinal slip compared to the configurations with pressures of 0.083 MPa and 0.096 MPa.

After the tire modeling and simulation, both the mathematical model and the simulation are

Disclosure of Interests. The authors have no competing interests to declare that are relevant to the content of this article.

References

1. Bruce P. Minaker, *Fundamentals of Vehicle Dynamics and Modelling: A Textbook for Engineers with Illustrations and Examples*, 1 ed, 2019
2. Hans B. Pacejka, *Tire and Vehicle Dynamics*, Elsevier, 2012 DOI: 10.1016/C2010-0-68548-8.
3. James Balkwill, *Performance Vehicle Dynamics*, Elsevier, 2018 DOI: 10.1016/C2016-0-03741-5.
4. Jazar R.N., *Advanced Vehicle Dynamics*, Cham, Springer International Publishing, 2019 DOI: 10.1007/978-3-030-13062-6.
5. Milliken W.F., Milliken D.L., *Race Car Vehicle Dynamics*, SAE International, 1995.
6. Nakajima Y., *Advanced Tire Mechanics*, Singapore, Springer Singapore, 2019 DOI: 10.1007/978-981-13-5799-2.
7. Todoruț A., Cordoș N., Barabaș I., *Elemente de dinamica autovehiculelor*, Cluj-Napoca, U.T. Press, 2021.
8. Formula Student Rules 2023.

Development of an Electric Powertrain for a Formula Student Vehicle

Ionuț-George Moldovan¹ and Mihai-Alexandru Bilici¹

¹ Technical University of Cluj-Napoca, Cluj-Napoca, Romania
moldovan.ga.ionut@student.utcluj.ro
mihai.bilici@campus.utcluj.ro

Abstract. The present paper addresses the challenges encountered by the ART TU Cluj-Napoca team in developing electric powertrains for a Formula Student single-seater race car. With limited prior experience, the team aims to create a revised vehicle for the 2024 competition. The primary objective is to design, develop, and manufacture a rule-compliant tractive system, enabling participation in dynamic events. The project emphasizes optimizing electrical and mechanical configurations using modern design tools and methodologies. The electrical design focuses on selecting, implementing, and testing components, including the high-voltage circuit and safety systems. The mechanical design section highlights the powertrain component packaging and manufacturing processes. A functional and compliant system was achieved, though final validation awaits technical inspections.

Keywords: Formula Student, Tractive System, Electric Powertrain.

1 Introduction

Formula Student is an international competition where university students design, build, and race single-seater formula-style cars. Established in the 1980s in the United States, it has become a prestigious event held globally, offering students practical experience in automotive engineering, project management, and teamwork [1].

The main goal of this project is to develop a functional and rule compliant tractive system. To achieve this, various components of the powertrain system need to be developed, reconfigured, or redesigned. The accumulator unit, a source of past issues due to incomplete or flawed designs, will be a primary focus, with efforts directed towards creating a fully rule-compliant, lightweight, and compact unit. The redesign of the chassis and structural elements aims to improve the vehicle's layout and dynamics by optimizing space usage. Additionally, a compliant electrical configuration will require thorough research, testing, and implementation of safety and auxiliary systems, with some components reused and others newly designed or selected through extensive research.

2 Electrical Design

2.1 High Voltage Circuit

The high voltage circuit of the tractive system is defined by the path the high current takes while powering the electric powertrain. This circuit starts in the Tractive System Accumulator Container (TSAC) and extends all the way to the electric motors. It consists of several components such as the cells, main fuse, relays, connectors, cables and can be distinguished in Figure 1.

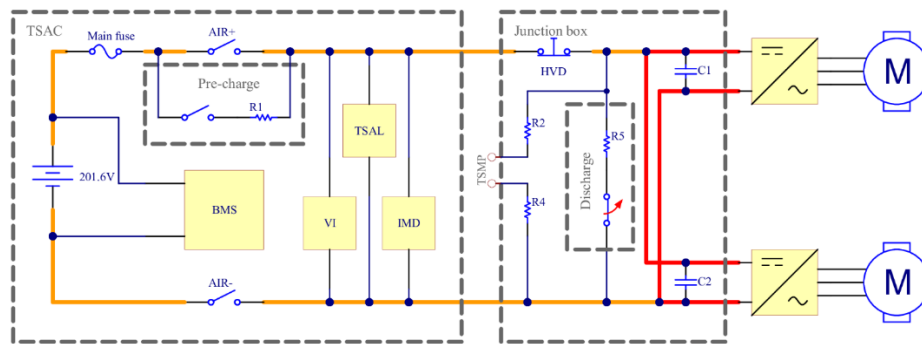


Fig. 1. Simplified schematic of the tractive system.

While part of these components will be reused from the previous iterations of the tractive system in order to save some costs, several new components are selected to better suit the needs for the system that runs this year.

Cells. This year's accumulator will reuse Enepaq VTC6 modules due to their high cost. Each module contains 10 Sony 18650 lithium-ion cells (US18650VTC6) wired in parallel, with threaded terminals for easy assembly and wiring. Each module has two sensors in contact with the negative poles of two adjacent cells and wire fuses on each cell for secondary protection in case of failure [2].

Main fuse. Although multiple active overcurrent protection systems exist in the high current path, a fuse is essential as a redundant safeguard against short circuits. The appropriate fuse was selected according to two parameters: the lowest continuous current limit of the components and the theoretical short circuit current. The model Little-fuse SPFJ100 was selected with a breaking current limit of 20 kA, opening the circuit for a current of 200 A in about 250 s and 400 A in 3 s respectively.

Relays. An Accumulator Isolation Relay (AIR) is a normally-open contactor controlled by the vehicle's shutdown circuit, designed to disconnect both poles of the tractive system and prevent high voltage at the accumulator output. The model GV200BBC-1 from GIGAVAC was selected based on operating voltage, switching cycles, continuous

current capacity, and coil voltage. Additionally, the relays are equipped with insulated auxiliary contacts to monitor the mechanical state of the main contacts, indicating whether they are open or closed, which helps detect potential malfunctions.

Pre-charge and Discharge Circuits. According to the operating manual, the inverters driving the rear motors require additional DC-link capacitors on the high-voltage line to smooth voltage ripples caused by cable length. To prevent damage to the AIRs or capacitors from high current spikes during direct contactor closure, a pre-charge circuit is used. This circuit includes a relay and series resistor that bypasses the AIR on the positive side of the tractive system.

A discharge circuit is also necessary to safely discharge the DC-link capacitors when the system is off, preventing high voltage on the vehicle side of the AIRs. This circuit includes a power resistor connected by an NC relay to the TS lines, housed in the junction box. The resistors were dimensioned according to the required pre-charge and discharge times that can be observed in Figure 2.

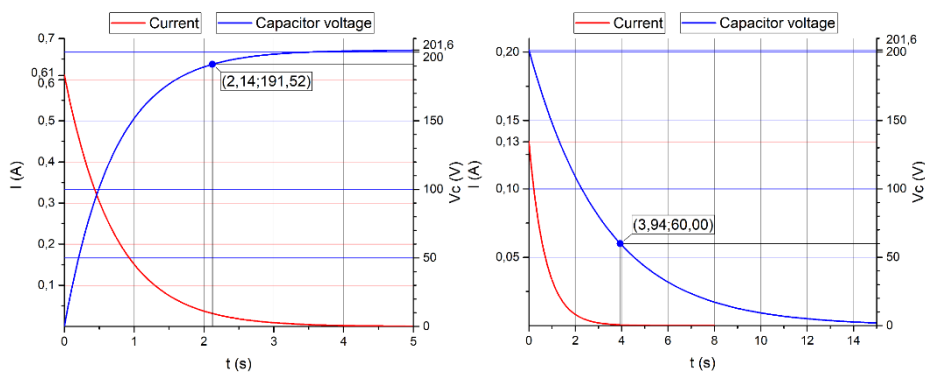


Fig. 2. Pre-charge (left) and discharge (right) current and capacitor voltage drop variation in time.

Cables and Connectors. The continuous current limit for the tractive system is 200 A, requiring cables that can handle this load. As shown in Figure 1, the high-voltage circuit carries the full current upstream of the DC-link capacitors and splits into two branches downstream, supplying the motor inverters. To comply with regulations, shielded cables will be used for external wiring, while unshielded cables will be used inside enclosures to prevent shield grounding.

A main connector is required on the accumulator container for disconnecting the battery when removed or connected to a charging station. The TE Connectivity HVP800 model meets the required specifications. For the junction box, Amphenol pass-through housings (HVPT2A50 for 50 mm² cables and HVPT2A25 for 25 mm² cables) are used, as easy disconnection is not necessary.

2.2 Safety Systems

In a high-voltage electric powertrain, multiple active and passive safety systems are used to prevent accidents during operation or maintenance. These systems are strictly regulated by the FSG rule book and must meet high standards, as their functionality is rigorously inspected before competitions. Key systems include the Shutdown Circuit (SDC), Brake System Plausibility Device (BSPD), Battery Management System (BMS), Insulation Monitoring Device (IMD), Tractive System Active Light (TSAL), Voltage Indicator (VI), and High Voltage Interlocks (HVIL).

Shutdown circuit. The Shutdown Circuit (SDC) is a series connection of components that supply power to the AIRs and the pre-charge/discharge circuits. Its primary function is to deactivate the tractive system by cutting power to the AIRs when a fault occurs. While master switches, interlocks, and the BOTS directly open the SDC, certain elements like the IMD and AMS trigger a special circuit called a power stage, which keeps the contacts open until the faults are cleared and manually reset.

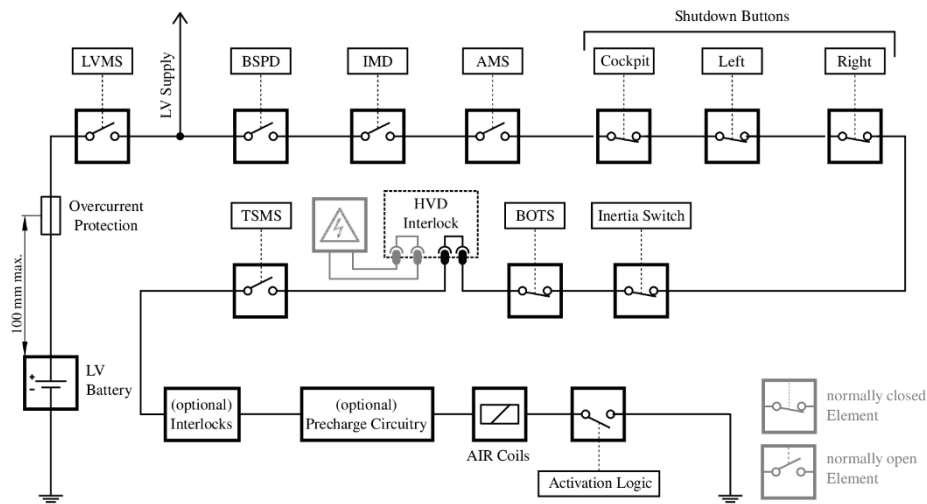


Fig. 3. Explanatory example schematic of the required SDC [3].

Battery Management System. The Battery Management System (BMS), referred to as the Accumulator Management System (AMS) in the rulebook, is the most crucial active safety feature in the tractive system. It continuously monitors and protects the battery from electrical and thermal misuse during operation [4], [5]. For the 2023-2024 season, the Orion BMS 2 from Ewert Energy Systems will be reused to save costs. This unit, previously purchased, is configured to monitor up to 72 cells and 88 thermistors when paired with the Thermistor Expansion Module (TEM).

Insulation Monitoring Device. The Insulation Monitoring Device (IMD) is a key safety feature in electric vehicles, monitoring the insulation between the tractive and low voltage systems. It triggers a fault signal when the resistance between these circuits drops below a set threshold, opening the shutdown and high-voltage circuits. As part of a sponsorship program, the Bender A-ISOMETER® IR155-3204 (Figure 4) was selected. The response value (R_{an}) is calculated based on the required 500 Ω/V and the tractive system's maximum voltage, with a final value of 300 k Ω chosen to accommodate potential future increases in TS voltage.



Fig. 4. Bender A-ISOMETER® IR155-3204 Insulation Monitoring Device.

Tractive System Active Light. The Tractive System Active Light (TSAL) is a mandatory visual indicator that displays the status of the tractive system. It is a very important safety feature that functions as long as the low voltage system is powered and must light up according to the following states (Table 1):

Table 1. TSAL states.

| Condition | Green light | Red light |
|---|-------------|-----------|
| $V_{TS} < 60$ VDC and all relays are open | ON | OFF |
| $V_{TS} > 60$ VDC | OFF | Flashing |
| LVS OFF or safe state | OFF | OFF |

Two common methods for measuring the tractive system voltage are using a Hall effect sensor or a voltage divider. The voltage divider was chosen for its simplicity and proven reliability. This setup involves a resistive voltage divider connected to the positive and negative poles of the tractive system, outputting a lower signal directly proportional to the system's voltage.

With the rulebook requiring signal integrity checks and constraining the voltage measurement locations, the following architecture for the TSAL was deemed to be the best option:

- 1 Red light voltage measurement PCB located in the junction box;
- 1 Green light voltage measurement PCB located in the TSAC, identical to the board above;
- 1 TSAL Main PCB, located in the TSAC;
- 1 TSAL Main Hoop PCB located on the main hoop;
- 1 TSAL Indicator PCB mounted in the cockpit of the vehicle.

2.3 Electric Motors and Inverters

Part of the final stage of the electric powertrain are the electric motors with their respective inverters, these components dictating the maximum performance that the vehicle can reach.

Electric Motors. The powertrain is configured to independently drive each rear wheel, enabling torque vectoring, a technology that dynamically distributes torque between wheels to improve handling, stability, and traction [6]. For this, two Plettenberg Nova 30-50-A4 S P50 WK electric motors (Figure 5.a) are reused from the previous racecar. These BLDC in-runner motors deliver 30 kW peak power each, with a maximum rotation speed of 7000 RPM and up to 80 Nm of torque. Compact and lightweight, they are water-cooled and equipped with temperature sensors [7].

Inverters. The chosen inverter for our application is the model MST 400-200 WK from Plettenberg (Figure 5.b). It was strongly recommended by the manufacturer as it is designed specifically for the Nova series of BLDC motors and in this way the highest system efficiency can be achieved. This model has a maximum continuous power output of 70 kW, maximum voltage of 370 V and maximum current of 200 A. The heat is dissipated through a water-cooling loop that is common with the motors [8].

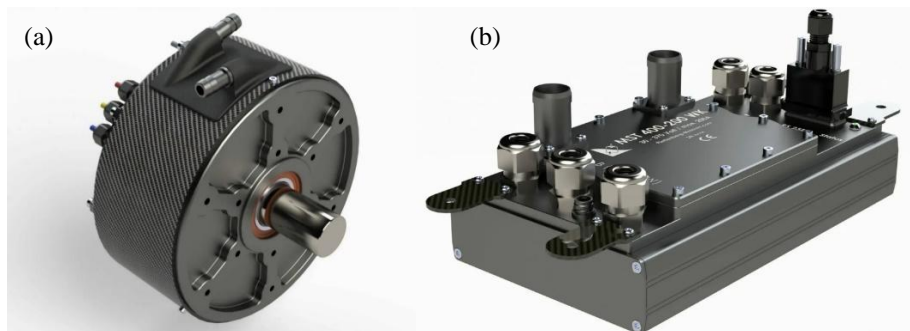


Fig. 5. (a) Plettenberg Nova 30-50-WK electric motor and (b) MST 400-200 WK inverter [7], [8].

3 Mechanical Design

3.1 Packaging

With the chassis being revised in the 2023-2024 season, the packaging for the powertrain components will also be revisited. The configuration for the tractive system consists of the Tractive System Accumulator Container (TSAC), junction box, traction motors and inverters (Figure 6).

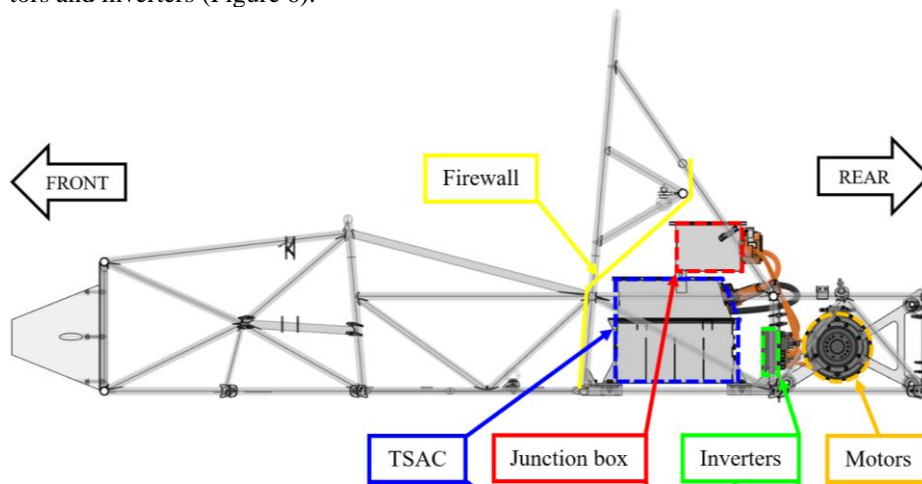


Fig. 6. The 2024 tractive system layout within the chassis.

3.2 Tractive System Accumulator Container

The Tractive System Accumulator Container (TSAC) houses the tractive system accumulator and must protect the cells and electrical components while securely attaching to the vehicle. It also provides electrical insulation from high-voltage parts to ensure safety during use and maintenance. To comply with regulations and improve access for maintenance, the container was divided into two compartments (Figure 7).

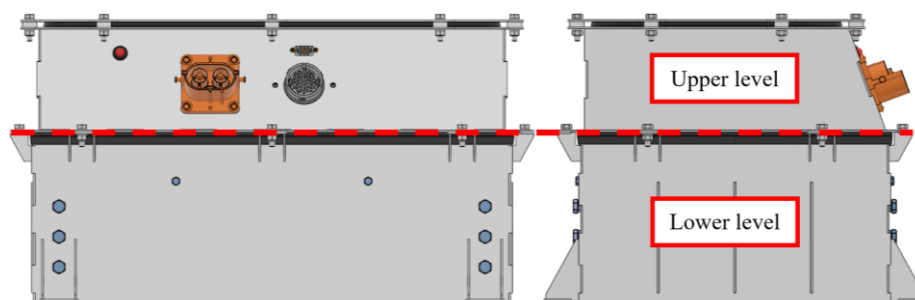


Fig. 7. Side views and compartmentation of the TSAC.

Lower Level. The lower level is primarily designed to house and secure the cell modules and is subject to numerous restrictions from the Formula Student ruleset. All of the walls for the lower level of the TSAC are fabricated from 2 mm thick S355 sheet metal steel while the four segments that mount in the TSAC are separated by insulating, fire-retardant barriers made from FR4 [9].

Cell segments. A segment is defined as a sub-division of the cells that constitute the battery pack. A final segment configuration was obtained of 12s10p cells, or 2 rows of 6 cell modules wired in series and positioned longitudinally within the construction (Figure 8).

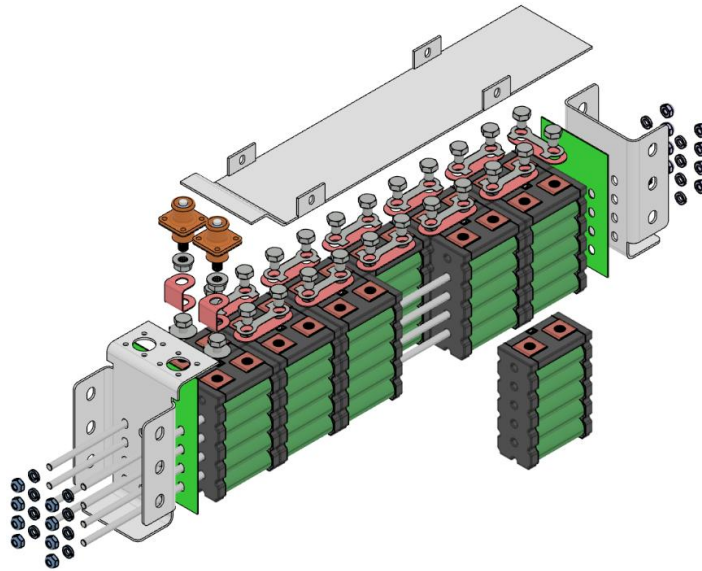


Fig. 8. Accumulator segment exploded view.

Upper level. The upper level is a compartment mounted at the top of the tractive system accumulator container and is designed to house a good portion of the components in the high voltage circuit and safety systems.

3.3 Junction Box

The junction box is a chassis-mounted enclosure that houses high-voltage components that cannot or should not be placed in the TSAC. These include DC-link capacitors, discharge circuitry, the TSAL red light measurement circuit, tractive system measuring points, and components like the BSPD current sensor and data logger. To optimize space and avoid additional enclosures, the HVD, low voltage, and tractive system master switches are also housed here. All components are insulated and protected against water ingress.

4 Conclusions

The project met its primary goal of creating a functional tractive system and correcting previous design flaws while ensuring the implementation of critical safety measures. Additionally, the comprehensive documentation of the design process provides a valuable reference for future powertrain developments within the team.

Making use of advanced design tools such as 3DEXPERIENCE CATIA, Fusion 360, and Altium Designer, the project optimized both the electrical and mechanical configurations, applying principles like Design for Manufacturing (DFM) to enhance resource efficiency and streamline low-volume production. The electrical systems, including the high-voltage circuit and active safety systems, were individually developed and tested, although full functionality will be confirmed upon the assembly of the complete system. Mechanically, the tractive system layout was significantly improved, enabling a more compact design with a reduced wheelbase.

Future research in this area could focus on enhancing the accumulator's energy capacity, integrating active cooling systems for better performance, and adopting regenerative braking technology. Additionally, developing a more advanced accumulator charging system will address current limitations, ultimately pushing the vehicle's performance and reliability to new levels.

Disclosure of Interests. The authors have no competing interests to declare that are relevant to the content of this article.

References

1. "Formula Student Germany, About-Concept." Accessed: Jul. 04, 2024. [Online]. Available: <https://www.formulastudent.de/about/concept/>
 2. "Li-ion building block with Sony/Murata VTC6 datasheet." Accessed: Jan. 07, 2024. [Online]. Available: www.enepaq.com
 3. "Formula Student Rules," vol. Version 1.1, 2024, Accessed: Dec. 09, 2023. [Online]. Available: https://www.formulastudent.de/fileadmin/user_upload/all/2024/rules/FS-Rules_2024_v1.1.pdf
 4. "Orion 2 BMS Wiring & Installation Manual." Accessed: Mar. 15, 2024. [Online]. Available: www.orionbms.com
 5. "Orion 2 BMS Operation Manual." Accessed: Apr. 20, 2024. [Online]. Available: www.orionbms.com
 6. S. Pillai and S. Thale, "Design and Implementation of a Three Phase Inverter for Renewable Energy Source with Unified Control Strategy," in *Energy Procedia*, Elsevier Ltd, Dec. 2016, pp. 673–680. doi: 10.1016/j.egypro.2016.11.236.
 7. "Plettenberg NOVA 30 Operating Manual." Accessed: Jun. 24, 2024. [Online]. Available: <https://plettenbergmotors.com/>
 8. "Operating Manual MST 400-200 WK." Accessed: Jun. 28, 2024. [Online]. Available: https://plettenbergmotors.com/wp-content/uploads/2023/01/OM_MST_400-200_V8.10_EN-1.pdf
- R. Sallai, "Proiectarea și realizarea unui modul de alimentare pentru un monopost categoria formula student," 2023.

